Hétérostructures supraconductrices et isolants topologiques

Oliver Hijano Cubelos

NTT: 2015SACLS247

Université Paris-Sud

Ecole Doctorale ED564 : Physique en Île-de-France
Laboratoire de Physique des Solides

Discipline : Physique

Thèse de doctorat

Soutenue le 15 décembre 2015 par

Oliver Hijano Cubelos

Hétérostructures supraconductrices et isolants topologiques

Directeur de thèse : M. Marc Gabay — Professeur (Laboratoire de Physique des Solides)

Composition du jury :

Président du jury :	M. Philippe Lecoeur	Professeur (Institut d'Electronique Fondamentale)
Rapporteurs :	Mme. Roser Valentí	Professeur (Institut für Theoretische Physik)
	Gervasi Herranz	Directeur de Recherches (ICMAB-CSIC)
Examinateurs :	M. Andrés Santander-Syro	Maitre de Conférences (CSNSM, Univ. Paris Sud)
	Mme. Claudine Chopin-Noguera	Directrice de Recherche (Université Pierre et Marie Curie)

Contents

1 - Introduction

The study of transition metal oxide interfaces has generated a large interest in the research community since a two-dimensional electron gas (2DEG) was found in the atomically abrupt heterointerface of $LaAlO_3/SrTiO_3$ grown along the (001) orientation of the $SrTiO_3$ (STO) structure by Ohmoto and Hwang in 2004 [37]. Since then, several other 2DEGs have been found at the interfaces of $LaAlO_3/SrTiO_3$ grown along the (110) and (111) orientations and in various polar/non-polar interfaces ($LaTiO_3-STO$, $CaTiO_3-STO$, $GdTiO_3-STO$...) [9, 13, 30]. A lot of effort has been devoted to reveal the origin of such 2DEG. In the case of polar interfaces, the alternating polarity of atomic layers forces the electric charges to reconstruct at the interface in order to avoid a divergent electrostatic potential [56]. The presence of Oxygen vacancies can also create metallic states at the interface, even with non-polar interfaces [34, 65, 66]. There are also suggestions that the cationic intermixing at the interface can result in the interfacial metallicity [22].

The study of these two-dimensional electron gases in transition metal oxides (TMOs) is crucial. TMOs can behave as insulators, semiconductors or even metals. Ferroelectricity, metal to insulator transitions, magnetism and high temperature superconductivity are some of the many physical phenomena that can be found in these systems. The complexity of their electronic structure is responsible for most of the relevant physics. This makes these materials very rich and promising for practical applications. It can be argued that the discovery of the conducting interface between a (001)$SrTiO_3$ surface and a $LaAlO_3$ film [37] triggered the large interest in the understanding of these 2DEGs, both theoretically and experimentally.

These 2DEGs do not only appear at the interface of two TMOs, they can also be found at the bare surface of $SrTiO_3$ [43], $KTaO_3$, and other transition metal oxides [5, 6, 9]. One of the goals of this thesis is the study of the 2DEG that can be found at the (001) surface of $SrTiO_3$. This 2DEG shows signs of several physical phenomena such as spin-orbit induced spin textures or superconductivity [15, 14, 20, 31]. The properties of the 2DEG strongly depend on the crystallographic direction of the surface [15], on the surface termination, and on the potential Oxygen deficiencies induced at the surface. TMO crystals usually present oxygen vacancies (or other cationic vacancies), point defects, planar dislocations and other structural defects, however their location within the crystal lattice is difficult to control. It has been confirmed that the intrinsic n-type interfaces are conducting [41,42]. However, the carrier density and its spatial distribution are not fully understood yet. The

majority of doped electrons are supposed to be confined within a few layers from the interface.

This particular work will focus mainly on the properties of Strontium Titanate. In this chapter we will review some of the properties of $SrTiO_3$ and we will introduce the mathematical model that we will use for our calculations. In chapter 2 we will study the crystal when it is cut along the (111) direction and we will take a look at the potential existence of topological states and their properties. In chapter 3 we will show the cluster that we will use to study the (001) surface of STO and we will explain the importance of understanding the impact of Oxygen vacancies in the system. In chapter 4 we will show the electronic structure of the cluster and we will study the impact of Oxygen vacancies and surface termination. We will show further results in Appendix C. We will make some comments on DFT calculations in chapter 5. Finally, we will make a summary of our results in chapter 6.

There are several reasons for the choice of this particular material. Firstly, $SrTiO_3$ has very flat surfaces that can be controlled chemically, making it very attractive for experimental research [20]. It is actually the father of a whole new generation of materials used to engineer new electronic components. Secondly, we are interested in the interfaces of TMOs, and the simplest interface that one can find is that between a transition-metal oxide and vacuum. Moreover, as we will see in the next chapter, the charge gap of this insulator separates Oxygen $2p$ and Titanium $3d$ states, so that when the material is doped, part of the $3d$ states will be occupied and new electronic properties will appear. Of course and alternative choice could have been the study of the interface of $LaAlO_3/SrTiO_3$ [13, 30], however this system is much more complicated to study theoretically due to the non-neutral layers LaO^+ and AlO_2^-. More information about the $LaAlO_3/SrTiO_3$ interface is given in chapter 6.

The study of two-dimensional electron gases or, in general, transport in confined geometries is essential for the development of the current technology [5, 6]. One of the current goals in the industry is to increase the density of transistors per volume on electronic chips in order to increase the efficiency of electronic devices. This, in principle, could be achieved using confined geometries instead of the prototypic 3D semiconductors. Moreover, the appearance of new quantum states that give rise to new phenomena lay the foundations for the research of new promising technologies. Thus, the potential ability to change $SrTiO_3$ crystals into metals is a very important subject towards future electronic applications.

Silicon-based semiconductors are reaching their limits. It is no longer possible to

reduce the size of en electronic system or increase its power by some orders of magnitude. From a technological point of view, $SrTiO_3$ has around ten times larger dielectric constant at room temperature and could be used to build electronic devices and used as a substitute of conventional semiconductors, allowing even smaller devices. One of the main advantages of this material is the carrier concentration, found to be up to two orders of magnitude larger than that of a MOSFET. On the other hand, it has been mentioned that the band gap is around 3.2 eV, which is much larger than the electronic gap of Silicon, around 1.1 eV. This is a disadvantage in terms of energy cost and mobility.

There is plenty of experimental research already done on the surface of $SrTiO_3$. Theoretical studies are still limited. One of the key questions is what is the difference between the two possible terminations of $SrTiO_3$ (SrO and TiO_2) when Oxygen vacancies are introduced. We will address this and other questions throughout this study and we will compare some of our results with DTF calculations.

1.1 $SrTiO_3$ structure and properties

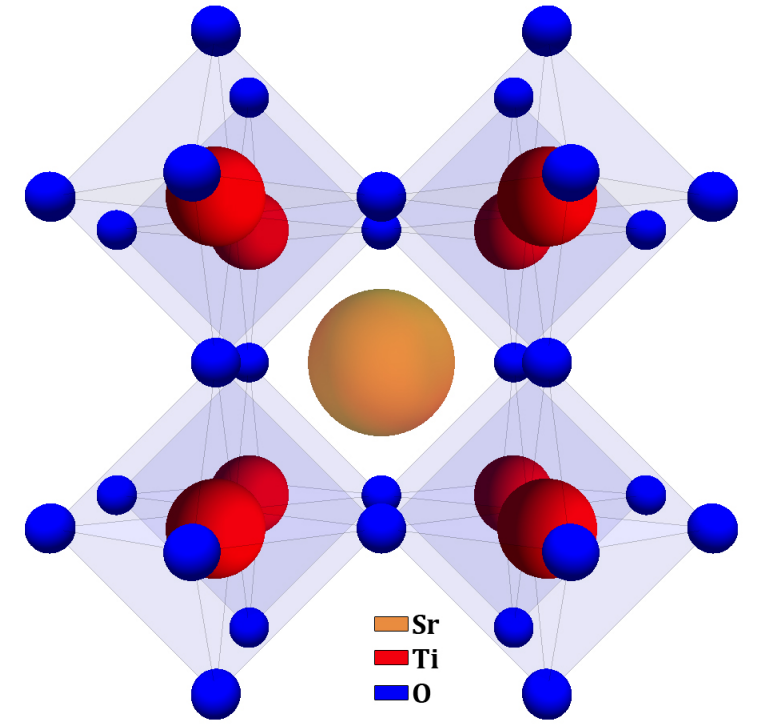

Figure 1.1: $SrTiO_3$ structure.

Most complex transition-metal oxides with the generic ABO_3 formula have a cubic perovskite structure at room temperature. This is indeed the case of $SrTiO_3$. The basic cubic cell can be constructed by placing Strontium atoms in the corner, Oxygen atoms in the center of each face, and one Titanium atom at the center of the cube. This means that each Titanium atom is surrounded by an octahedron of six Oxygen atoms, and each Strontium atom will be at the center of a cube where eight Titanium atoms (and their corresponding octahedron) are placed at the corners (see Fig. 1.1). Along the (001) direction it can be seen as a stacking of neutral SrO and TiO_2 layers.

Titanium is an element belonging to the transition metal series. These elements usually have d states that are rather close in energy to the valence s states. The d states are actually closer to the nucleus than the s states. This means that one can treat the d electrons as localized electrons, because the overlap interaction between

s electrons forces neighboring atoms to be sufficiently far from each other so that the overlap of d electrons is very weak. For this reason, in section 1.2 we justify the treatment of d electrons as point particles sitting on the nucleus of Ti atoms when using the tight binding model.

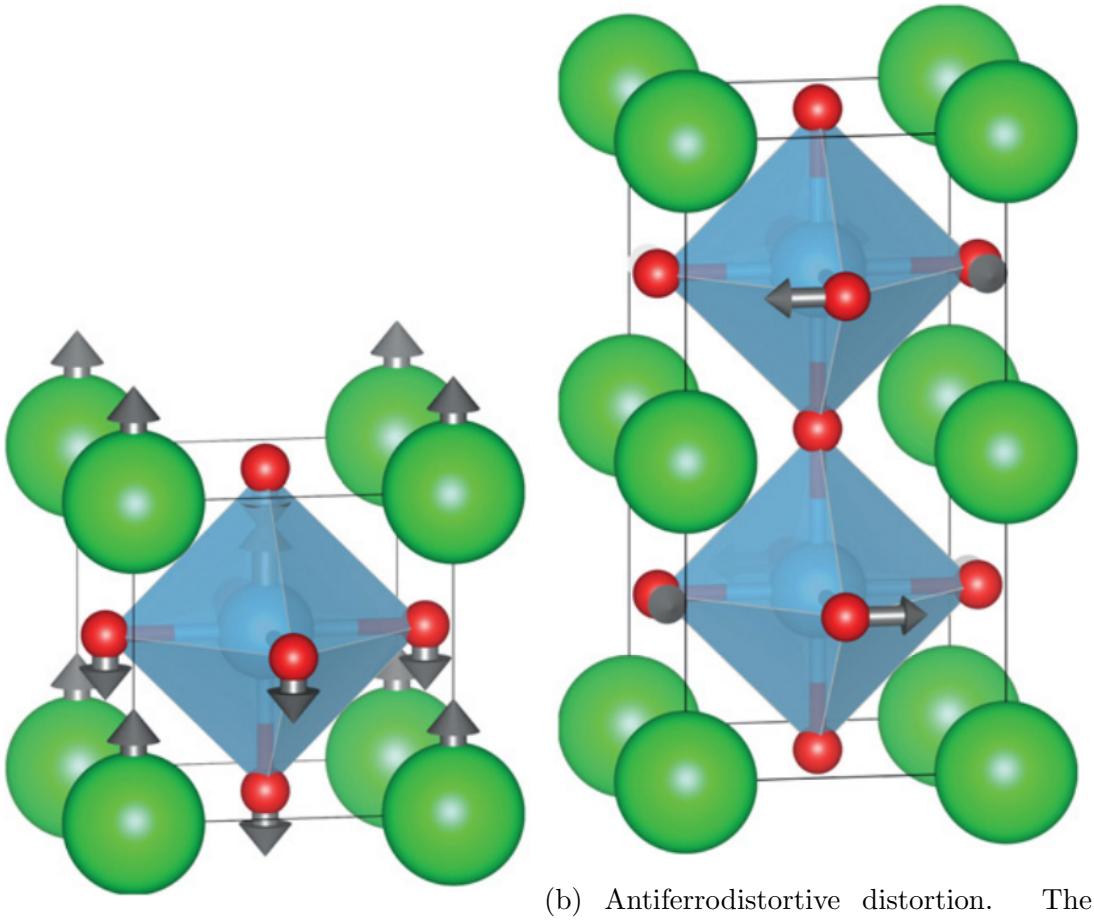

(a) Ferroelectric distortion. The Titanium and Oxygen sublattices get displaced.

(b) Antiferrodistortive distortion. The Oxygen octahedra rotate around the central Titanium atom.

Figure 1.2

Possible distortions of this perfect crystal structure can occur if the TiO_6 octahedron rotates around the Titanium atom at the center (antiferrodistortive distortion, AFD) or when there is a polar displacement of some ions in the crystal (ferroelectric distortion, FE) [50, 17, 71]. The rotations of the Oxygen octahedra reduce the Ti-O-Ti angle, strongly modifying the transport and magnetic properties of this compound.

At the critical temperature of $Tc \approx 105K$ $SrTiO_3$ undergoes a cubic to tetragonal transition [17, 70]. These are AFD rotations where the TiO_6 octahedra rotate around the z axis (see Fig 1.2b), and the rotations in successive layers are out of phase. This distorsion changes the lattice parameters and bond angles of the crystal. The a and b (horizontal lattice distances) decrease whereas the c (vertical lattice parameter) increases with the distortion angle. The idea is to keep the volume of the bulk unit cell constant, so smaller horizontal lattice distances imply larger vertical one. Thus, the ratio c/a increases with the AFD angle. Around $65K$ there is an orthorhombic transition [50].

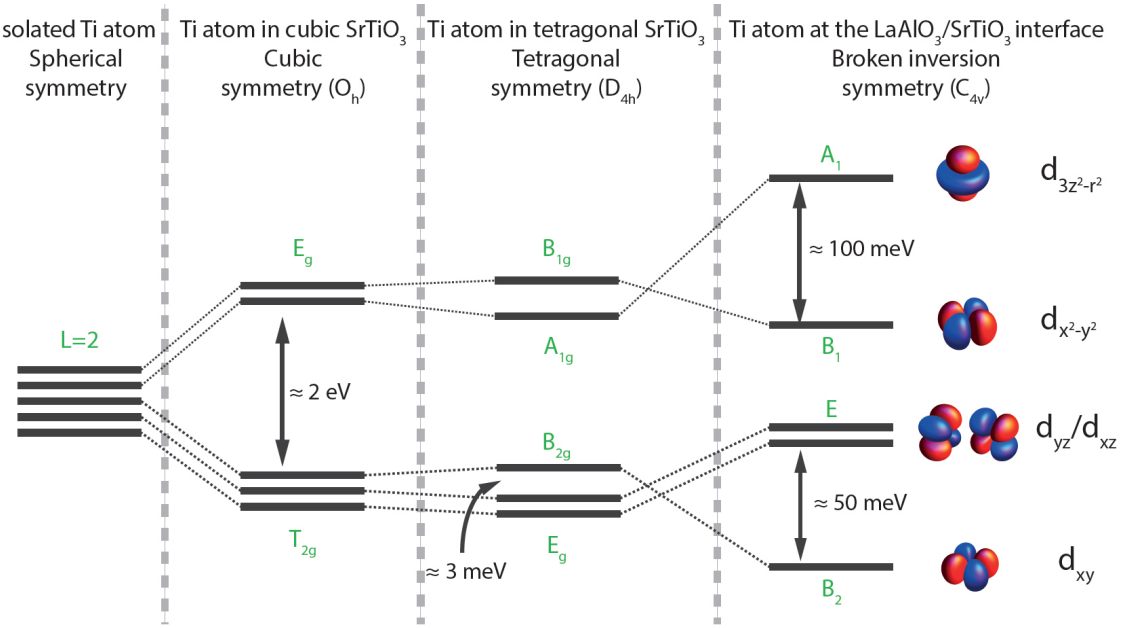

Figure 1.3: The degeneracy of the five Ti $3d$ orbitals is lifted depending on the crystal field surrounding the Titanium atom. This Figure shows the relative energy levels of these orbitals in a spherical, cubic, tetragonal and non inversion-symmetric tetragonal environment.

In general, the effective potential at an atomic site has the same symmetry as that of the crystal structure. This symmetry is usually non-spherical (i.e., different than that of vacuum), meaning that the degeneracy of the atomic levels will be lifted. By looking at the symmetry of the crystal field we can already make predictions on the degree of orbital degeneracy of the system. Figure 1.3 shows the corresponding energy levels of the Titanium $3d$ orbitals depending on the crystal field felt by the Titanium atom. The five $3d$ orbitals are degenerate in energy when the atom is in

the vacuum and there is spherical symmetry. The cubic symmetry splits the levels into two groups. The t_{2g} group ($\Gamma_{25'}$, composed by d_{xy}, d_{xz} and d_{yz}) is lower in energy compared to the eg group (Γ_{12}, $d_{x^2-y^2}$ and d_{z^2}). The degeneracy of these two groups can be split again when the $SrTiO_3$ has a tetragonal structure at lower temperatures.

In this work we will focus on the cubic structure of $SrTiO_3$. This is because in the 2DEG all the relevant energy scales (sub-band splitting, spin-orbit interaction, exchange constants) are far larger than the 2-3 meV caused by the AFD transition. The Oxygen p-orbitals (p_x, p_y, p_z) remain degenerate within this structure, because the system has cubic-symmetry. However, this symmetry partially lifts the degeneracy of the Titanium d-orbitals, as shown in Figure 1.3.

$SrTiO_3$ is known to have exceptional dielectric properties. The dielectric constant of strontium titanate is around 300 times larger than that of the vacuum at room temperature. This value can rise up to 24000 at low temperatures.

$SrTiO_3$ is a non-polar pseudo-cubic band insulator with an electronic gap of ~ 3.2 eV. The valence band is dominated by Oxygen $2p$ orbitals, and the conduction band is dominated by Titanium $3d$ orbitals. The crystal field split the $t2g$ and the eg bands by ~ 2.5 eV. When doped, this compound can be used as an n-type semiconductor.

1.2 Tight binding model

There is plenty of evidence showing that the tight binding model is a very good approximation to study the electronic structure of some TMOs [23, 43]. Usually the nearly free electron model is very suitable for delocalized electrons in simple metal thin films or even semiconductor heterostructures. This model suggests that the electrons are free to move with the usual parabolic dispersion relation. However, this is not true for perovskite oxides where the d electrons are confined within a small radius from the nucleus of the transition-metal ion sites and the electron is forced to hop through intermediate Oxygen sites. Thus, a tight binding model is a better approach to study the physical properties of perovskite oxides in general and $SrTiO_3$ in particular.

In the case of $SrTiO_3$, the d electrons are confined within a few unit cells. This confinement is responsible for the appearance of orbital-selective quantum well states, which have been experimentally observed for several heterostructures with ARPES (Angular Resolved Photoemission Spectroscopy) [38].

All the calculations and simulations made for this work assume the following:

- The role of Strontium atoms is neglected. Only Titanium and Oxygen atoms are taken in consideration. The electron structure of Strontium is [Kr] $5s^2$, with two electrons outside its krypton-like core.
- Only the five d orbitals play a role in the Titanium atoms (s and p orbitals are neglected). The electron structure of Titanium is [Ar] $3d^2$ $4s^2$, with four electrons outside its argon-like core.
- Only the three p orbitals play a role in the Oxygen atoms (s orbitals are neglected). The electron structure of Oxygen is [He] $2s^2$ $2p^4$.
- Titanium atoms can only interact with the nearest surrounding Oxygen atoms (six in the absence of vacancies) and the six nearest Titanium atoms (see Figure 1.1).
- Oxygen atoms can only interact with the nearest neighbor Oxygen atoms (eight in the absence of vacancies) and the two nearest Titanium atoms.

Two neighboring atoms separated by the Euclidean vector $\vec{v}_{ab}$ will then interact with each other. The interaction term in the tight binding Hamiltonian between these two neighboring atoms describes an electron jumping from one particular orbital of the second atom (orb_b) to one particular orbital of the first atom (orb_a). This interaction

term has the following form:

$$H_{int}(\vec{v}_{ab}, orb_a, orb_b) = t_{(\vec{v}_{ab},orb_a,orb_b)} e^{i\vec{k}\vec{v}_{ab}} A^{\dagger}_{orb_a} B_{orb_b}$$

where $t_{(\vec{v}_{ab},orb_a,orb_b)}$ is the corresponding amplitude of any particular interaction. This amplitude depends on the two orbitals involved in the interaction and on their relative spatial position. This amplitude can be calculated using the Slater-Koster rules. A more extensive explanation on how to compute this amplitude can be found in *Appendix A*. $A^{\dagger}_{orb_a}$ is the creation operator. It creates an electron in the orbital orb_a on site a. B_{orb_b} is the corresponding annihilation operator (orbital orb_b, site b). The spin dependence of the electron is implicit in the definition of orb_a and orb_b.

This somewhat simplified tight binding model is more than enough to recreate plenty of calculations made on $SrTiO_3$ and to obtain some of its physical properties. Once the Hamiltonian of the model is built (see sections 2.2 and 3.1), we can already compute the energy bands in the bulk of $SrTiO_3$. Figure 1.4a shows the band structure of the perovskite at several points along the Brillouin zone calculated by Piskunov [16]. This figure is in perfect agreement with other theoretical DFT calculations and experimental observations [11]. Figure 1.5 shows again the band structure of $SrTiO_3$. This second plot has been calculated using the tight binding model proposedat the begining of this section. There are several parameters that need to be tuned in the model of $SrTiO_3$. These parameters are summarized in Table 1.

Table 1: Tight-binding parameters (in eV).

On-site energies	d-d interactions	p-p interactions	p-d interactions
$E_{d_{xy}}$=$E_{d_{xz}}$=$E_{d_{yz}}$ = −11.04	$dd\sigma = 0$	$pp\sigma = 0.0381$	$pd\sigma = -2.1225$
$E_{d_{x^2-y^2}}$=$E_{d_{z^2}}$ = −8.54	$dd\pi = 0$	$pp\pi = -0.02177$	$pd\pi = 1.0381$
E_{p_x}=E_{p_y}=E_{p_z} = −14.13	$dd\delta = 0.00136$		

The simple cubic Bravais lattice of $SrTiO_3$ gives rise to a Brillouin zone with simple orthorhombic lattice (see Fig. 1.4b) where the Titanium atoms are placed in sites with full cubic symmetry and the Oxygen atoms in sites with tetragonal symmetry.

We can clearly differentiate two types of bands in the plot. The valence bands are mainly Oxygen-p states, which are completely occupied in $SrTiO_3$. The Titanium-d states give rise to the conduction bands, that are completely empty. The Fermi level is located in the gap. Since the unit cell of the bulk contains one Titanium atom

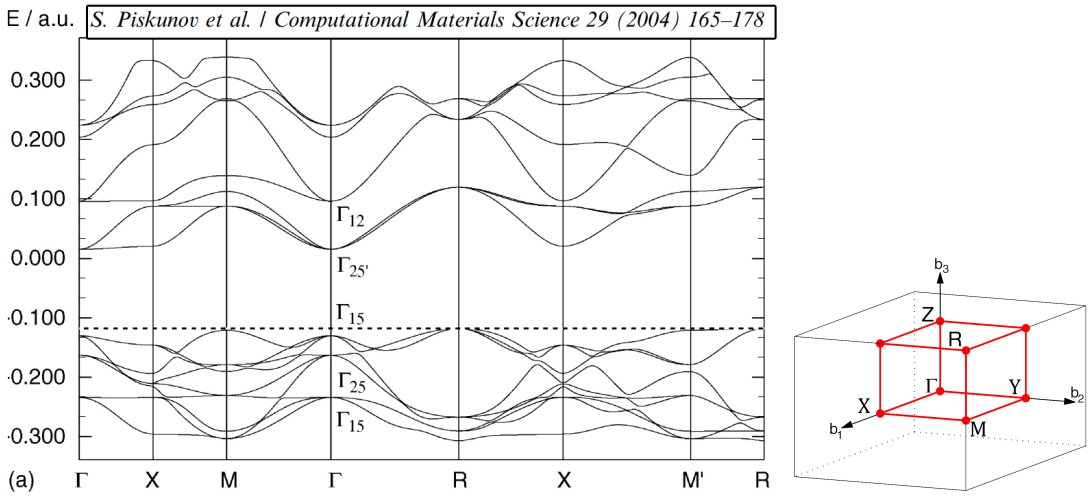

(a) Piskunov *et al.* calculate the bulk electronic structure with HF/DFT [16] (energy scale in atomic units).

(b) Simple orthorhombic lattice Brillouin zone.

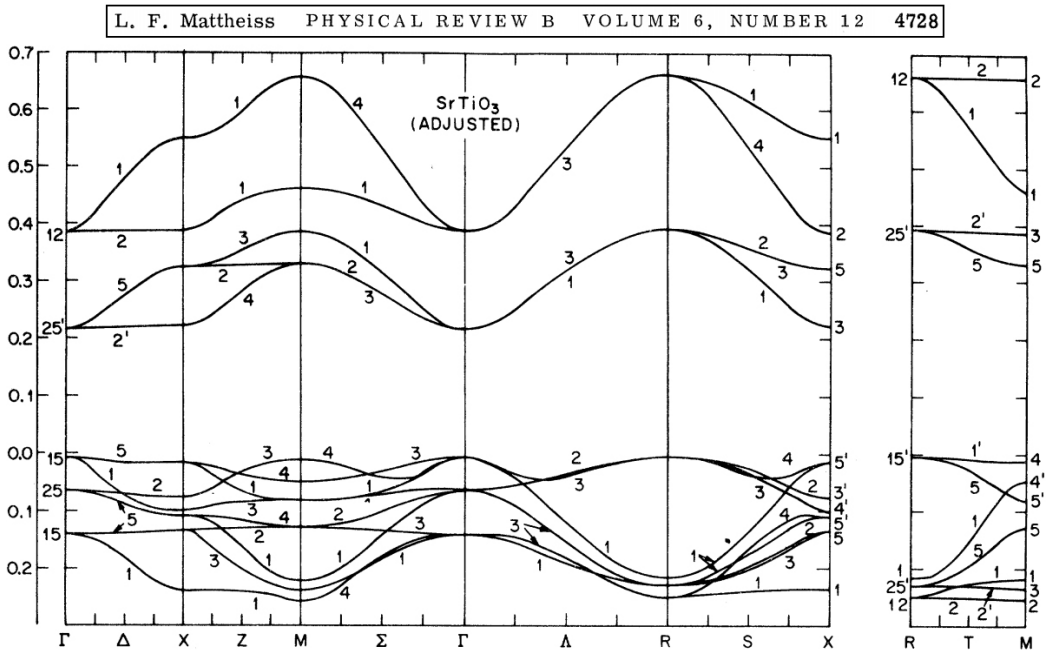

(c) Mattheiss. Bulk electronic structure, adjusted LCAO [11] (energy scale in Ry).

Figure 1.4: Bulk structure of $SrTiO_3$.

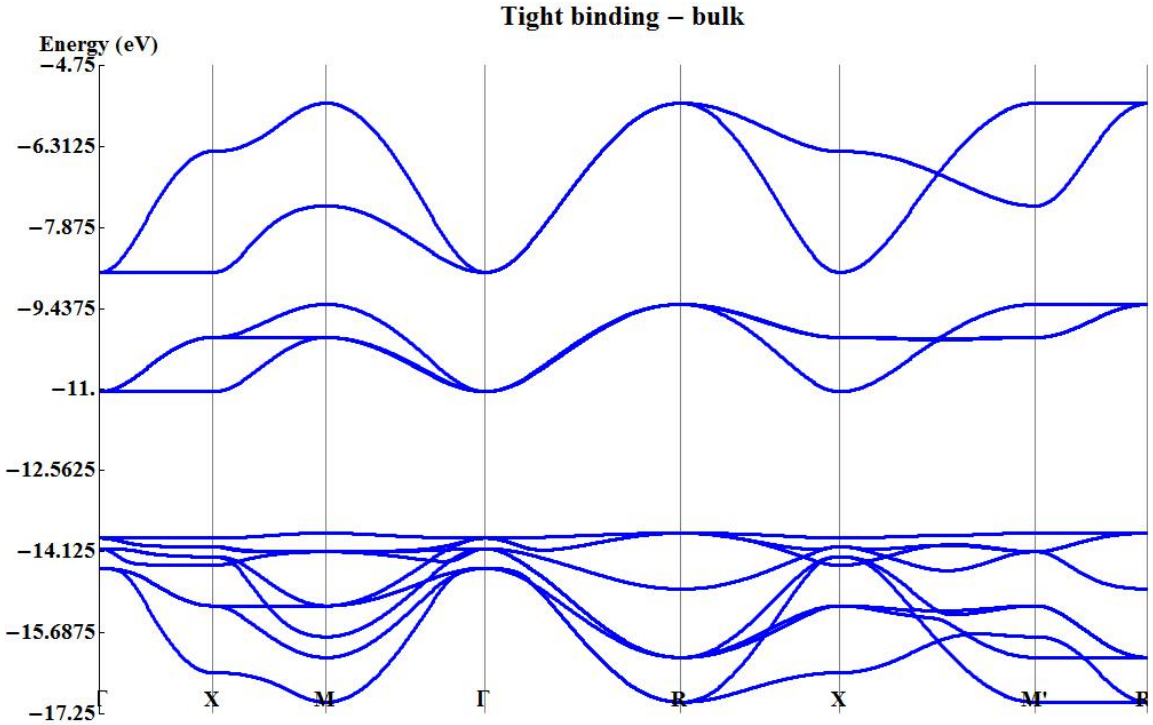

Figure 1.5: Bulk structure of $SrTiO_3$ calculated with our tight-binding model.

and three Oxygen atoms, we expect $1 \times 5 + 3 \times 3 = 14$ bands in the bulk. More precisely, five conduction bands coming from the five d orbitals of the Titanium atom and nine valence bands coming from the p orbitals of the Oxygen atoms. One of the main differences between the two figures is that in Figure 1.5 there are only two branches of bands in the conduction part, whereas there are several more bands in the conduction part of Figure 1.4a. This is because in our model we neglected the role of strontium atoms. Those bands belong to strontium-s states that are a bit higher in energy compared with the Titanium-d states.

d-bands

As we stated before, in $SrTiO_3$ the Fermi energy is within the gap that separates valence and conduction bands. Thus, it would be interesting to understand the properties of the conduction bands that will host any extra electron that is added to the system. At the Γ point we can observe the degeneracy of the three t_{2g} and two

e_g states described in the previous section.

- When we move from Γ to X, we see that one of the t_{2g} states does not disperse. We identify this state with the d_{yz} orbital. The other two states remain degenerate and they disperse. These are d_{xy} and d_{xz} states. Regarding the e_g states, we see that one of them does not disperse along this direction (this is the d_{z^2} state), but the other does. This second e_g band belongs to the $d_{x^2-y^2}$ orbital.

- Going from X to M we see that the d_{yz} state now disperses, as expected. Similarly, the degeneracy of the d_{xy} and d_{xz} bands is broken, since now d_{xz} does not disperse and remains flat, but d_{xy} does. It is interesting to note that at M the d_{yz} and d_{xz} states are now degenerate again. Similarly, now both d_{z^2} and $d_{x^2-y^2}$ disperse.

- All the bands disperse along the path $M - \Gamma$, as expected. In the end we recover the t_{2g}-e_g symmetry at the Γ point. This band structure can be easily ploted by just analyzing the symmetry and degeneracy of the orbitals at different points of the Brillouin zone and then connecting the dots.

The characterization of the valence p states is a bit more difficult because of the hybridization of the p-states. In any case, one can see that some bands disperse more than others at different parts of the Brillouin zone, so one could in principle guess the contribution of the p_x-p_y-p_z orbitals to these bands.

2 - The (111) bilayer

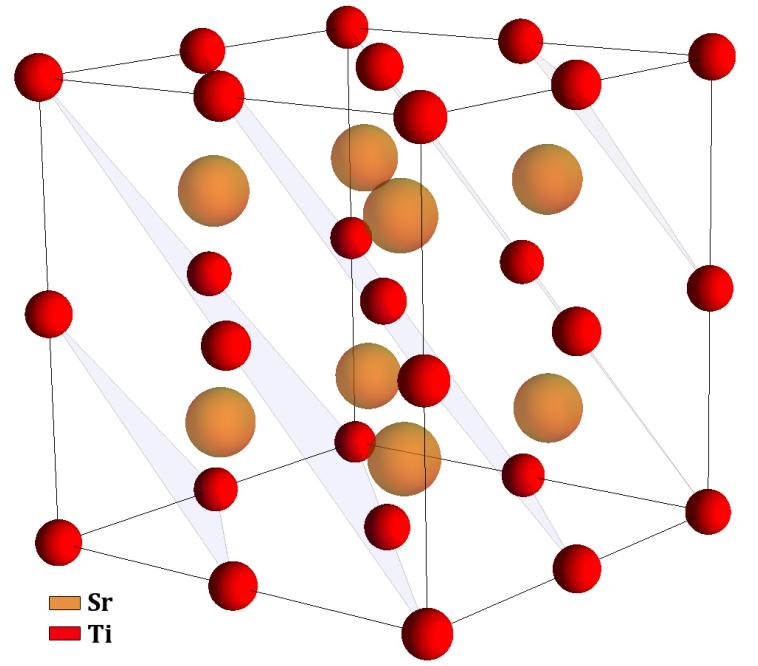

Figure 2.1: When $SrTiO_3$ is cut along the (111) direction, we obtain alternate layers of Ti and Sr atoms.

Since it is at the surfaces and at the interfaces of TMOs that the 2DEGs can be found, it is necessary to study different terminations to investigate the electronic properties of these 2DEGs. It has been suggested that some TMOs with perovskite structure might give rise to particularly interesting phenomena. For example, previous works show magnetic and topological phase transitions in (111) bilayers of some transition metal oxides with perovskite structure [44]. Part of this work consists on the study of the (111) surface of $SrTiO_3$ and on the search of new possible topological states.

Along the (111) direction the $SrTiO_3$ structure can be seen as stacking $(SrO_3)^{4-}$ and Ti^{4+} layers. In Figure 2.1 we can see that the Ti atoms form a triangular lattice. Thus, two consecutive (111) Ti planes form a honeycomb lattice.

A topological insulator is essentially a material that behaves just like a conventional insulator in the bulk, but that behaves quite differently on the surface, potentially showing conducting states [53, 60, 61]. The bulk gap is usually generated by the

spin-orbit interactions. At the surface, this bulk-gap can disappear and gapless surface states can be found. These surface states (or edge states) have properties different from the other electronic states in the material. They are protected by the time-reversal symmetry of the material.

In the coming sections we will study the electronic properties of the (111) bilayer and we will investigate the appearance of several edge states.

2.1 The honeycomb structure

In addition to the properties of the two-dimensional electron gases at transition-metal oxide interfaces we are also interested in the study of boundary states in topological insulators. The honeycomb-lattice geometry possibly gives rise to topologically protected spin-polarized bands in the presence of bulk spin-orbit interactions [18, 47, 54]. This is a general feature of TMOs with perovskite structure, but the properties of these states depend on the physical properties of the crystal. In order to recover a honeycomb geometry, we need to have strong enough confinement of the 2DEG, ideally two unit cells. $SrTiO_3$ (111) confines but $KTaO_3$ (111) is expected to confine even more due to the stronger polar charge of the layers. There have been some experimental results studying the surface of $KTaO_3$ that show that the 2DEG confined between two layers of Ta atoms (forming a honeycomb lattice) could lead to a topological metal [19].

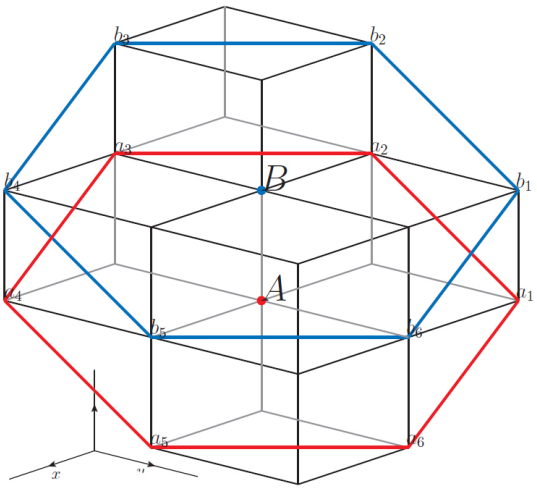

(a) Two (111) layers cut in the $SrTiO_3$ cubic structure.

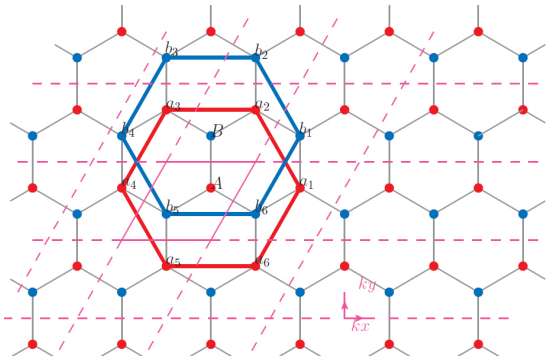

(b) Honeycomb lattice. In red, Ti atoms of the first layer. In blue, Ti atoms of the second layer.

Figure 2.2: Two (111) layers of a perovskite structure give rise to the honeycomb lattice.

Both $SrTiO_3$ and $KTaO_3$ are insulators with similar band gaps and they both can be made into n-type semiconductors when doped going from a transparent and colorless sample to darker and opaque one (see Fig. 2.3) [18, 19]. There are however several differences between $SrTiO_3$ and $KTaO_3$. One of them is that the bulk

spin-orbit coupling is considerably larger in $KTaO_3$. Also, the lattice parameter of $SrTiO_3$ ($\sim 3.905\mathring{A}$) is slightly smaller than that of $KTaO_3$ ($\sim 3.9885\mathring{A}$). The charge distribution and the polar character of the surface are also different. At the beginning of this chapter it was stated that the $SrTiO_3$ structure can be seen along the (111) direction as a stacking of $(SrO_3)^{4-}$ and Ti^{4+} layers. In the case of $KTaO_3$ these are $(KO_3)^{5-}$ and Ta^{5+} layers. In terms of crystal structure, we described in section 1.1 how $SrTiO_3$ undergoes several structural transformations at different temperatures including a cubic to tetragonal transformation around $110K$. However $KTaO_3$ seems to remain cubic even at $1K$.

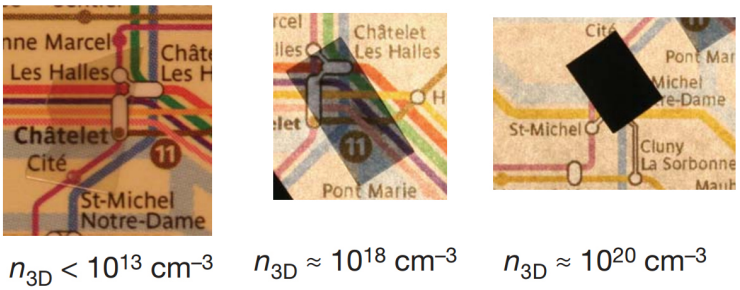

Figure 2.3: Photographs of $SrTiO_3$ samples at different bulk dopings [26].

When the STO crystal is cut along the (111) direction, the Titanium atoms of each layer create a two-dimensional triangular lattice. If we look at the first two (111) layers, as shown in Figure 2.2a, both lattices superpose and the hexagonal honeycomb lattice is recovered (Figure 2.2b).

There are two Titanium atoms per unit cell, each one coming from one of the (111) layers. The crystallographic symmetries of the 2DEG plane have an impact on the symmetry of the electronic structure of the system. The (111) plane has 6-fold symmetry. This means that, when viewed along a direction normal to the plane, all the t_{2g} orbitals are equivalent modulo a rotation of 120°.

2.2 The Hamiltonian

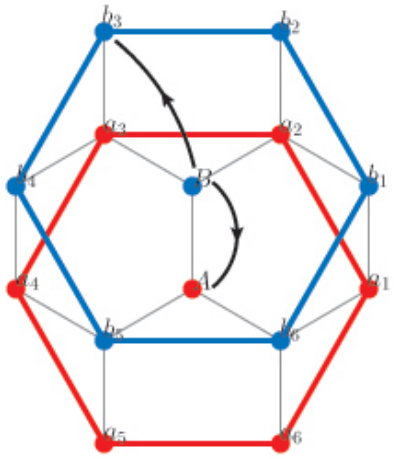

Figure 2.4: Red nodes represent Titanium atoms that belong to the first (111) layer. Atoms of the second layer are represented in blue. This figure illustrates that the nearest neighbors of any particular Titanium atom are the three closest Titanium atoms of the opposite layer. The second nearest neighbors would be the six nearest Titanium atoms belonging to the same layer.

The physical properties of the (111) bilayer can be mathematically described using the following Hamiltonian:

$$H = H_o + H_{1st} + H_{SO} + H_{trig}$$

where:

$$H_o = \sum_i \sum_{d_a,d_b} \sum_{\sigma=\uparrow,\downarrow} E_{d_a} A^\dagger_{i,d_a,\sigma} A_{i,d_a,\sigma} + E_{d_b} B^\dagger_{i,d_b,\sigma} B_{i,d_b,\sigma}$$

H_o denotes the on-site energies of the different orbitals. $A_{i,d_a,\sigma}$ is the annihilation operator that removes an electron of the first layer located at the position i with spin σ in the orbital d_a. The sum spans all the sites of the lattice and is extended to all the orbitals involved. Similarly $B_{i,d_b,\sigma}$ acts on the second layer.

$$H_{1st} = -t \sum_{<i,j>} \sum_{d_a,d_b} \sum_{\sigma=\uparrow,\downarrow} e^{i\vec{k}\vec{v}_{ij}} A^\dagger_{i,d_a,\sigma} B_{j,d_b,\sigma} + e^{-i\vec{k}\vec{v}_{ij}} B^\dagger_{i,d_b,\sigma} A_{j,d_a,\sigma}$$

H_{1st} represents the nearest neighbor interactions (see Fig. 2.4). The hopping amplitude is independent of the orbitals involved in the interaction because only the three t_{2g} orbitals are taken into account and they are equivalent in the honeycomb lattice (see section 2.1). The e_g doublet is much higher in energy. The hopping amplitudes between the e_g doublet are significantly smaller compared with the interactions between the t_{2g} triplet. Even though we do not include them in this model, we can still extract the main physical properties of the system. In reality the Titanium atoms *talk* to each other through the Titanium-Oxygen-Titanium interaction. The parameter t takes into account this interaction.

$$H_{SO} = \lambda \vec{L} \cdot \vec{S}$$

$$H_{trig} = \Delta \sum_{i} \sum_{d_1,d_2} \sum_{\sigma=\uparrow,\downarrow} A^{\dagger}_{i,d_1,\sigma} A_{i,d_2,\sigma} + B^{\dagger}_{i,d_1,\sigma} B_{i,d_2,\sigma}$$

Spin-orbit interaction is included in H_{SO} and H_{trig}. It is included to lift the spin-degeneracy in the 2DEG. Rashba splitting is generated when one considers on-site spin-orbit interactions (H_{SO}) together with processes in which the electrons change orbital character when they hop between two neighboring metal sites. The latter process is described by the trigonal field H_{trig}. A full description of the spin-orbit Hamiltonian is given in *Appendix B*.

2.3 Infinite vs finite size

Much in the same way as people investigated edge states in the 2D fractional quantum hall effect (FQHE) [68], we may ask whether the 2DEG displays interesting features at its boundary. For the FQHE, these special states are detected when the *bulk* is insulating, since the edge is conducting. There is one notable exception for the $\nu = 1/2$ FQHE when the *bulk* is metallic. In that respect we are considering the 2DEG counterpart of the $\nu = 1/2$ case.

Several physical properties of the (111) bilayer can be studied using the tight-binding Hamiltoninan described in the previous section. The Hamiltonian describes a two-dimensional infinite system with no spatial limitations. Figure 2.5 illustrates the energy bands of the Ti bilayer for two different values of the spin-orbit coupling parameter.

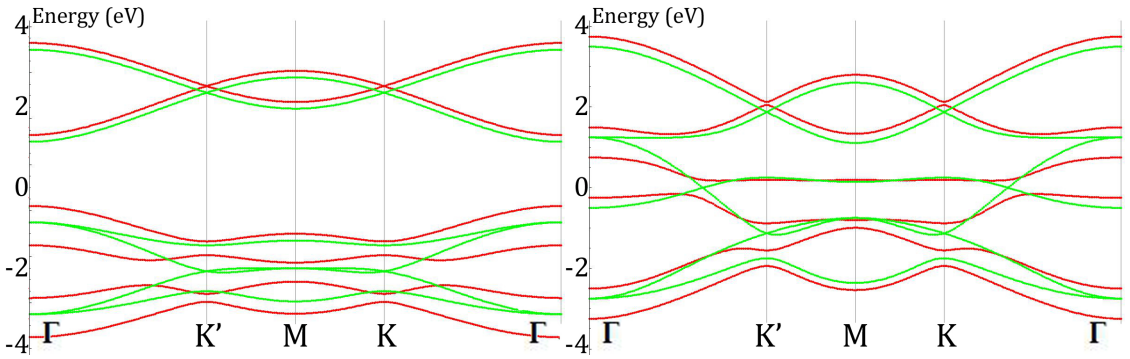

(a) Strong SO coupling ($\lambda = 5\ eV$). (b) Weak SO coupling ($\lambda = 1.5\ eV$).

Figure 2.5: Energy bands of the infinite (111) bilayer

As stated in the begining of this chapter, one can clearly differentiate between the valence and conduction states in the presence of strong spin-orbit coupling. The gap closes as this interaction is removed.

Once the $SrTiO_3$ crystal has been cut along the (111) direction, one recovers an infinite surface with honeycomb structure. In order to look for edge states, the idea is to limit the size of this system in one of the spatial directions and study its electronic structure. Figure 2.2b shows the unit cell of the crystal (containing two Titanium atoms that belong to the two (111) layers). This unit cell is replicated

[1] one of the two primitive vectors of the hexagonal lattice, the other being $(\frac{1}{2}, \frac{\sqrt{3}}{2})$

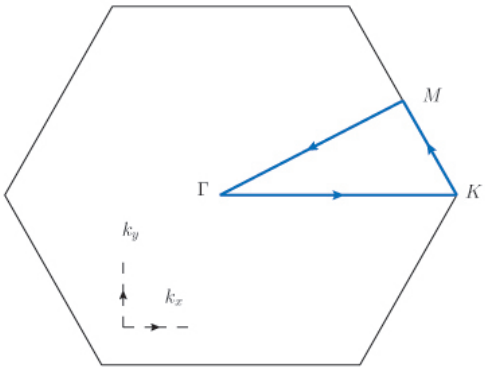

Figure 2.6: The first Brillouin zone of the honeycomb lattice has this particular hexagonal form. Different physical properties of the lattice may be different at different points along the Brillouin zone. Usually by looking at the Γ, M and K points (and the paths connecting them) one can recover all the information about the electronic structure of the system.

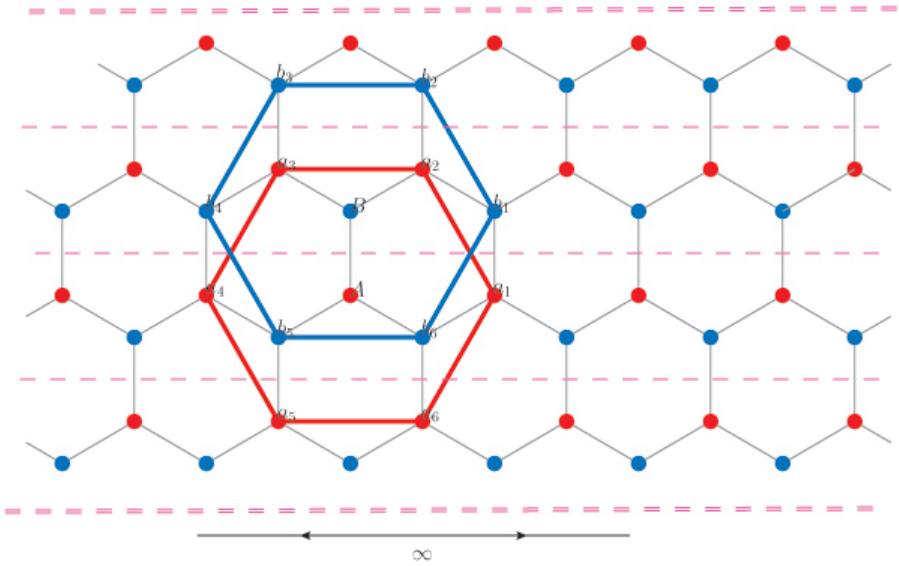

Figure 2.7: If the unit cell is replicated along the $(1, 0)$ direction[1], then one obtains an infinite horizontal strip made of an alternating zig-zag pattern of Ti atoms. This figure illustrates the hexagonal lattice limited in the y-direction to four strips.

along the primitive translation vectors. If the system is to be limited in size, the replication of the unit cell has to be limited as well. The idea is to let the system

be infinite in the x-direction but to have a limited size in the y-direction. To do so, the number of (infinitely long) horizontal strips is then a finite number. Figure 2.7 shows an example when the system is limited to only four strips.

The Hamiltonian has to be modified a bit in order to study finite size effects, because now the unit cell contains $2\times N$ Titanium atoms, where N is the number of strips considered. This unit cell is then repeated along the x-direction. Thus, the Hamiltonian is now dependent on the number of strips studied.

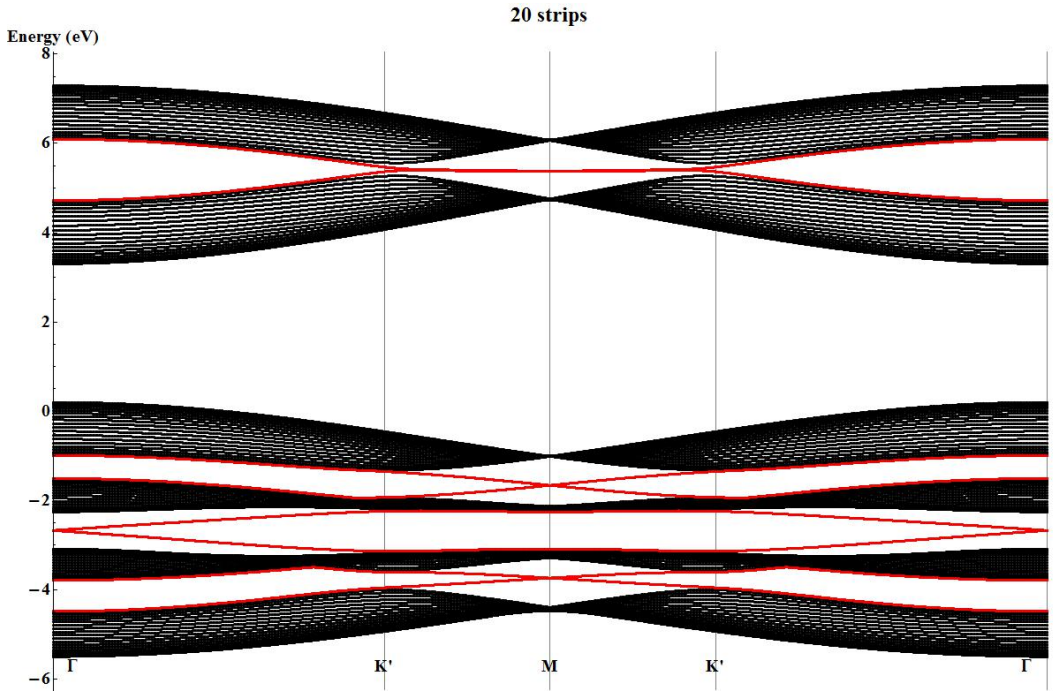

Figure 2.8: Energy bands of 20 strips. Strong spin-orbit coupling ($\lambda = 5\ eV$).

The energy spectrum of the finite-size system is a bit different than that of the infinite bilayer. A number of 20 strips is already enough to clearly see the effects of the limitation in size. Figures 2.8 and 2.9 show the energy bands for different values of the spin-orbit coupling.

In Figure 2.8 the valence and conduction parts are clearly differentiated (similar to 2.5a). At the Γ point the top of the valence band is at 0.3 eV and the bottom of the conduction band can be found at 3.26 eV. This means that at Γ there is a band gap of 2..96 eV. This gap is larger at other points in the Brillouin zone. We can also differentiate two kinds of bands in the spectrum. Some bands are grouped

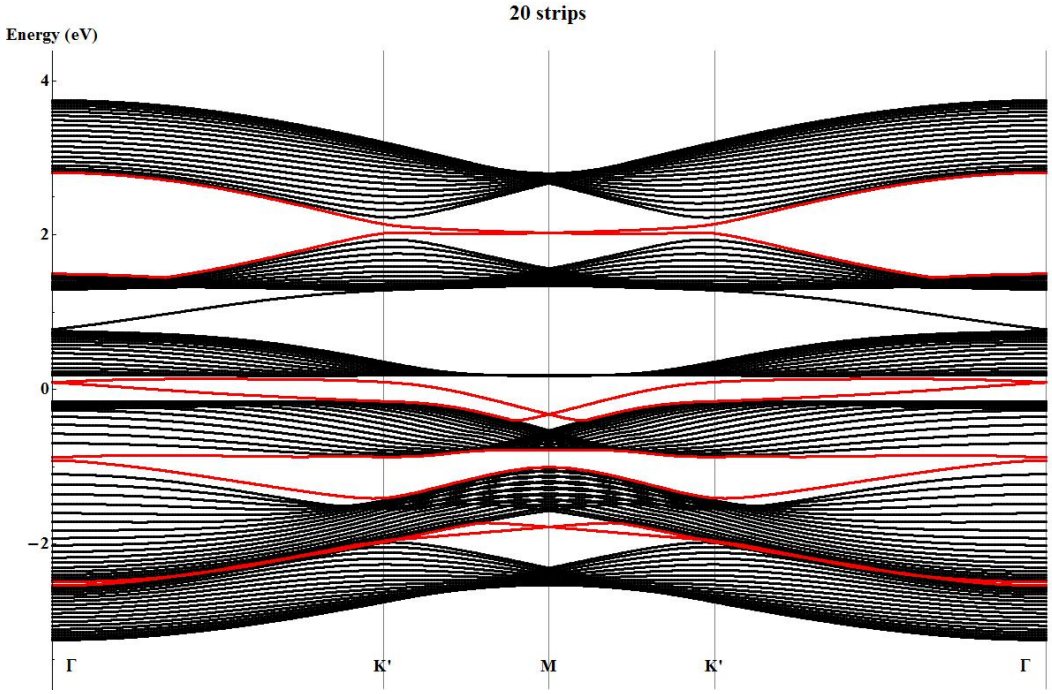

Figure 2.9: Energy bands of 20 strips. Weak spin-orbit coupling ($\lambda = 1.5\ eV$).

together along the Brillouin zone (in black). Some other bands (in red) are single bands that split from the previous branch at some points in the Brillouin zone. These single bands are the potential candidates for the edge states that we are looking for. Similar results can be retrieved when the spin-orbit coupling is rather weak. In this case the gap separating the conduction and valence parts shrinks, but similar single edge states can be found. In section 2.4 we will study the physical properties of these single bands and we will identify their origin.

Note that the values of the spin-orbit coupling parameter λ are quite large (5 eV and 1.5 eV respectively). Usually the measured values of this interaction are around 30-50 meV for $SrTiO_3$ and around 0.45 eV for $KTaO_3$. We decided to exagerate this value in order to fully appreciate the appearance of the edge states. This effect can be particularly seen when comparing Figures 2.8 and 2.9. Strong spin-orbit coupling interaction let us see more clearly the appearance of these edge states and makes it easier to study their properties (that we analyze in the next chapter). Realistic values of λ would make it harder to find and study these edge states.

2.4 Edge states

As a rule of thumb, a topological insulator is characterized by the existence of edge (or surface) states that, due to time-reversal symmetry, cannot be adiabatically connected to the other bulk states [47, 53, 60]. Historically, the first example of a state of matter which was topologically different than the other known states of matter was the Quantum Hall state [54]. In a 2D sample, the electric current is carried only along the edge of the sample, leaving the bulk insulating.

In Mathematics, the idea of topological invariance is generally used to classify objects depending on their geometry. For instance, two-dimensional surfaces can be classified by the number of holes in them, i.e. the *genus*. A key concept is that two objects are topologically equivalent if one can be *smoothly deformed* into the other. As an example, one can look at the famous comparison between a donut and a cup of tea, both of them containing just one single hole.

In Physics we can also classify systems depending on their topology. A key concept is that of *smooth deformation*. In the previous example the word *smooth* refers to the fact that you are changing the shape of the tea-cup without creating any more holes in the deformation process. In Physics, we can use this deformation process if we look at the energy spectrum of a particular system. For instance, in an insulator one can find some states (valence) separated from others (conduction) by a gap. A *smooth deformation* in the Hamiltonian would be one that leaves this gap untouched, and the gap is not closed. Thus, if we have two systems belonging to the same topological class and we put them in contact, the interface can show gapless states, but it is not a requirement. However, if the two systems belong to different topological classes, then new gapless states will appear at the interface.

In section 2.3, where we studied finite width system consisting of 20 strips, we saw that, depending on the band filling, edge states could be found. (Figures 2.8 and 2.9). Usually these states exhibit some peculiar properties at some points in the Brillouin zone. In this section we will study the properties of these candidates. To do so, we will study the parity and the evolution of the wave function of several states along the Brillouin zone.

2.4.1 Parity

Figure 2.2 shows that the system is composed by two types of atoms, those that belong to the first layer and those that belong to the second layer. This means that any eigenvector can be written as a linear combination of the spin dependent orbitals of the two atoms:

$$\Psi = \sum_{\sigma,orbs} \alpha_{\sigma,orb} + \beta_{\sigma,orb}$$

where α and β are the eigenfunctions representing the two types of atoms. The eigenvector Ψ is said to be even if after the interchange of the two atoms Ψ remains invariant. It is odd when the eigenvector changes sign.

$$Even : \Psi \xrightarrow{\alpha \leftrightarrow \beta} \Psi$$
$$Odd : \Psi \xrightarrow{\alpha \leftrightarrow \beta} -\Psi$$

When we look at the parity of the lowest band in the bulk, we observe that its parity changes along the Brillouin zone. We find that the lowest state is even at the Γ point and at two M points but it becomes odd at the third M point, as illustrated in Fig. 2.10.

This means that the point M_2 is isolated from the rest of the points, which means that it is not possible to *smoothly* connect it with Γ or the other two M points. This will cause the appearance of edge states when we limit the system in size. This is precisely the reason why we obtain single isolated bands in the electronic structure of the 20-strips system (Figure 2.8).

We have found one M point due to a particular choice of the lattice vectors. An alternative choice that is not orthogonal but that conforms to the rotational symmetry of the lattice would give three odd M points. This does not change anything in terms of topology, since what counts is the product of the parities at the four time reversal invariant points, Γ and M.

2.4.2 Localization

There are plenty of bands in Figure 2.8. The number of bands depends on the number of strips considered. If we choose one of these bands, we can study its wave function

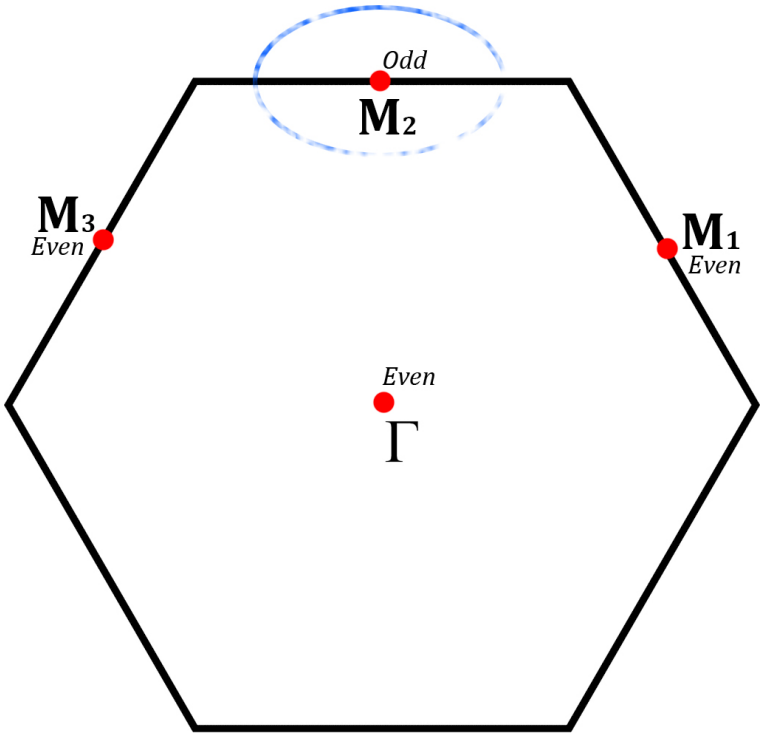

Figure 2.10: Parity of the lowest band at different points in the Brillouin zone.

along the Brillouin zone. The wave function contains all the information about that particular band. Part of this information is the localization of the band. That is, we can see what particular atoms (and strips) are contributing to that band at any point in the Brillouin zone. Most of the bands do not show any particular feature, one can simply see that all the strips are contributing more or less following some distribution. However, this is not the case with edge states. These states are usually localized on the surfaces of the system. Thus, it would be interesting to see the strip contribution of one of these states.

Figure 2.11 shows the localization of the wave function of the highest edge state candidate (red bands in Fig. 2.8). It can be clearly seen that at the M point the wave function is completely localized on one of the edges of the system, in strip number 1 (2.11d). As soon as we move away from M towards Γ, this localization disappears (2.11e - 2.11l). This is in perfect agreement with what can be seen in the band structure. At M the highest edge state is completely isolated from the rest of the states (between the two conduction branches). This state remains separate from

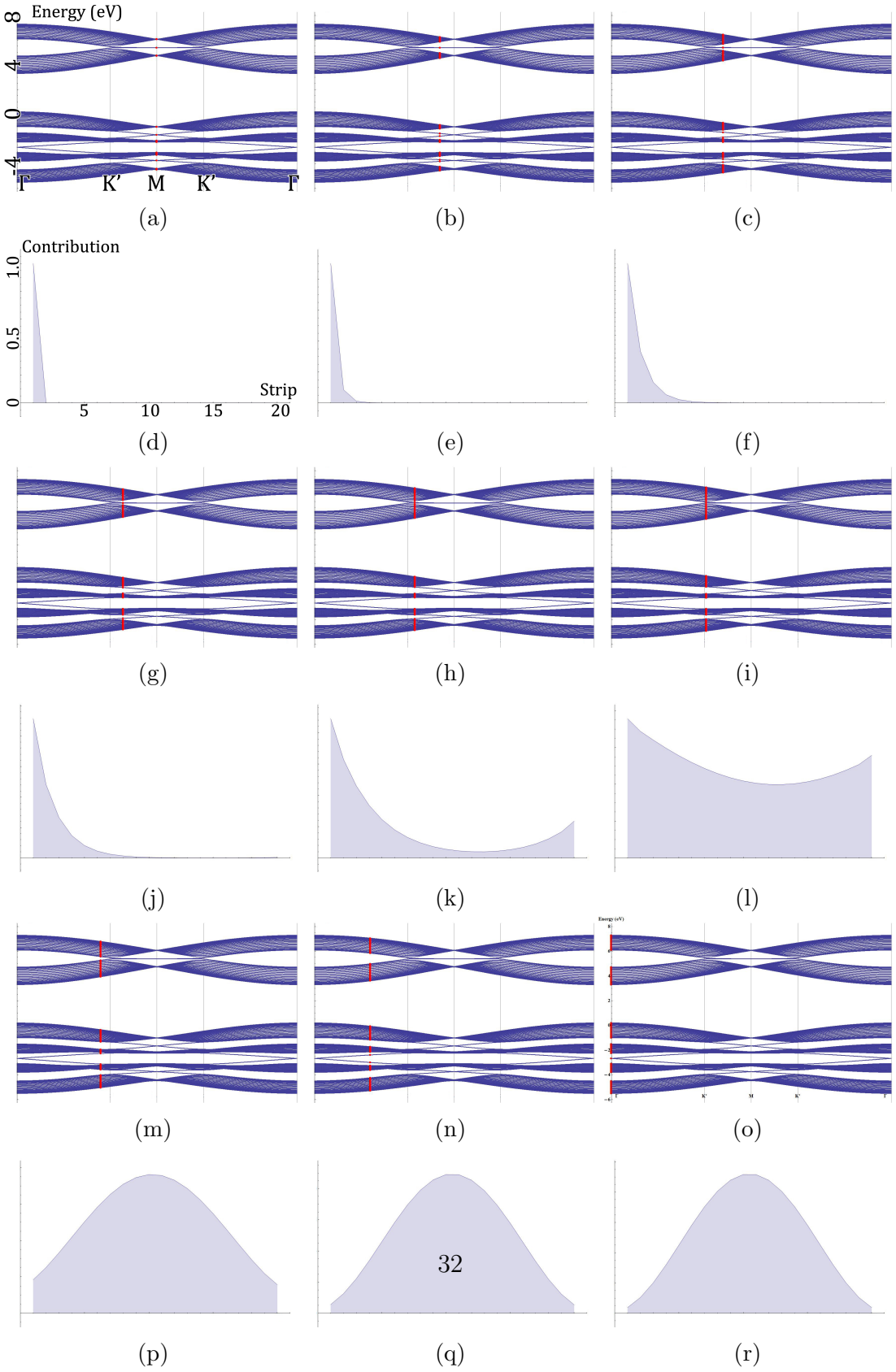

Figure 2.11: Evolution of the spatial distribution of the wave function along the Brillouin zone.

the rest until the K point, where it merges with the two conduction branches and delocalizes (2.11i).

When we look at the strip-distribution of any other *normal* band (the ones shown in black in Fig. 2.8), we see that is is like 2.11r at any point in the Brillouin zone. That means that is is completely delocalized. In summary, we have two types of bands. The first type of bands is always delocalized and its parity does not exhibit any special behaviour. The second type of bands (shown in red in Fig. 2.8) are different in the sense that they are strongly localized on one of the edges of the system at particular points in the Brillouin zone and their parity is not the same everywhere.

Experimental observations show that the measured thickness of the 2DEG appears comparable for $KTaO_3$ (111) and $SrTiO_3$ (111) [18, 19]. The band filling and spin-orbit energies are such that topological effects might show more easily in the case of $KTaO_3$, without requiring electrostatic doping to get close to the M points.

2.5 Polarity

$SrTiO_3$ seen along the (111) direction displays polar surfaces. In the introduction of this chapter we mentioned that we would find alternating $(SrO_3)^{4-}$ and Ti^{4+} layers. Thus, the *unit cell* in the stacking sequence bears a non-zero dipole moment. These dipoles are not a surface phenomenon, they can be found in the bulk of STO as well [76]. One could argue that the existence of a macroscopic dipole moment would generate an infinite surface energy. This situation can be avoided after surface reconstructions or if compensating charges are introduced in the surface. This means that in the end the surface configuration is different than that of the bulk. These changes have a deep impact on the surface electronic structure.

In the previous sections we have shown the electronic structure of the (111) bilayer of $SrTiO_3$ and we have studied the properties of the edge states that arise when the bilayer is limited in size. In the Hamiltonian we denoted the on-site energies of the atomic orbitals belonging to the two layers as E_{d_a} and E_{d_b}. For simplicity, in our calculations we consider these two values to be equal. That is, we consider that both layers are equivalent.

In a more realistic model, these two layers are not strictly equivalent. The first layer would have as neighbors the second layer and the vacuum, whereas the second layer would be placed between the first layer and the bulk of $SrTiO_3$. We should either implement surface reconstruction (affection the on-site energies of the atoms) and consider the charge distribution of the layers.

The implementation of polarity in our model would change the electronic structure of the system. However, we would find similar edge states (this is what is actually experimentally found [18]). The localization of these states would be very similar. A more in-depth study on the parity of these states would be required, since the interchange of the two layers can no longer be made.

3 The (001) surface of $SrTiO_3$

In previous chapters we reported that experimental results show that the behaviour of the surface of $SrTiO_3$ is different than that of the bulk. This is why it is important to study doped $SrTiO_3$ and the effect that the doped layers have on the surface. This can be done mainly either by atomic substitutions of certain atoms in the crystal (such as replacing Sr with a $d1$ transition metal like La or replacing Ti with a $d3$ transition metal such as Nb), or by reducing the Oxygen content introducing Oxygen vacancies. Our work will focus on the latter case.

The presence of Oxygen vacancies at the surface of the crystal can be the source of the metallic state and might be responsible for the different physical properties of the material, such as magnetism, if they manage to break the time-reversal symmetry of the crystal. In principle they can give an explanation of the two-dimensional electron gas found at the surface of $SrTiO_3$ and other transition metal oxides. One of the purposes of this work is to study the specific role that these vacancies play in the formation of the observed 2DEG.

The electronic structure of $SrTiO_3$ is affected not only by the density of these Oxygen vacancies but also by their relative position and arrangement in the crystal. Thus, we will investigate different arrangements of single and pairs of vacancies for the two possible surface terminations of the crystal. A single vacancy is the minimum number of vacancies that we can introduce in the system. Di-vacancies are specially interesting, since they might be able to explain the in-gap states observed experimentally around $-1.3\ eV$ below the Fermi energy. Three or more vacancies would produce Oxygen vacancy concentrations much higher than those found in STO. The Oxygen atoms populate the crystal structure as neutral atoms. When one Oxygen atom is removed, the two electrons used to fill the $2p^6$ orbital can be returned to the crystal. Thus, the Oxygen vacancy can be considered as a double donor impurity, as shown in Figure 3.1.

One possible approach to study the role of these vacancies is density functional theory (DFT). As an example, in [65] several slab configurations are analyzed, focusing on cases where two Oxygen vacancies can be found near the surface. Using a 3x3x4 slab, they find that these vacancies promote new in-gap states in the electronic structure of $SrTiO_3$.

Another approach is to build a theoretical model of these slabs for different arrangements of Oxygen defects and extract the band structure and other physical properties

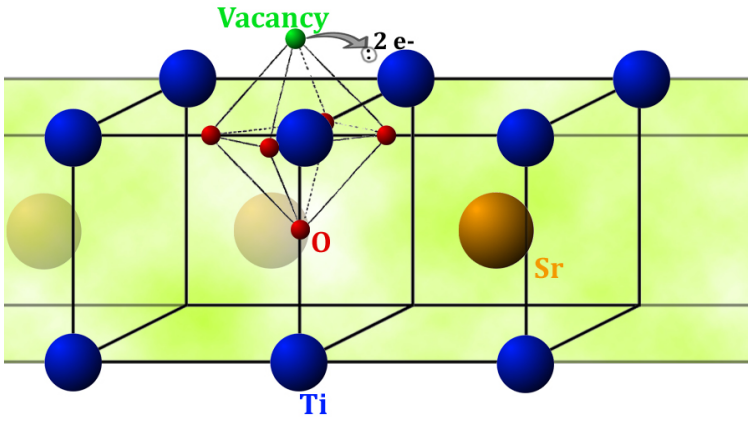

(a) Each Oxygen atom contributes with 2 electrons that need to be placed somewhere in the crystal.

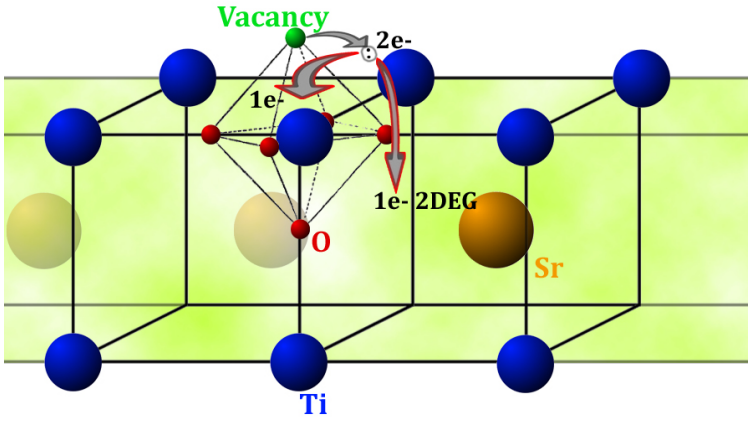

(b) One electron can be captured by the neighboring Ti atom. The other electron can be placed between the TiO_2 layers contributing to the formation of the 2DEG.

Figure 3.1: Possible explanation of the coexistence of superconductivity and magnetism in the presence of Oxygen vacancies.

of the system out of this model. The main advantage of this approach is that it allows us to track the origin of new electronic states and it makes it very easy to analyze the orbital character of the new states, as well as their location within the slab.

We will use a $2 \times 2 \times 4$ cluster for our calculations. There are a total of 68 atoms in the cluster (16 Titanium atoms and 52 Oxygen atoms).

The Figure shows a cluster that is SrO-terminated. The termination of the top layer plays an important role in the calculations and some electronic states present different properties depending on the termination of the surface. This is why it is not only important to study the role of the existence of vacancies and their position, but also on the termination of the surface. Study of this cluster with a TiO_2 layer surface can be done if we consider that the top four Oxygen atoms can be removed. We can consider them as *"vacancies"* (in addition to whatever vacancies are studied within the cluster).

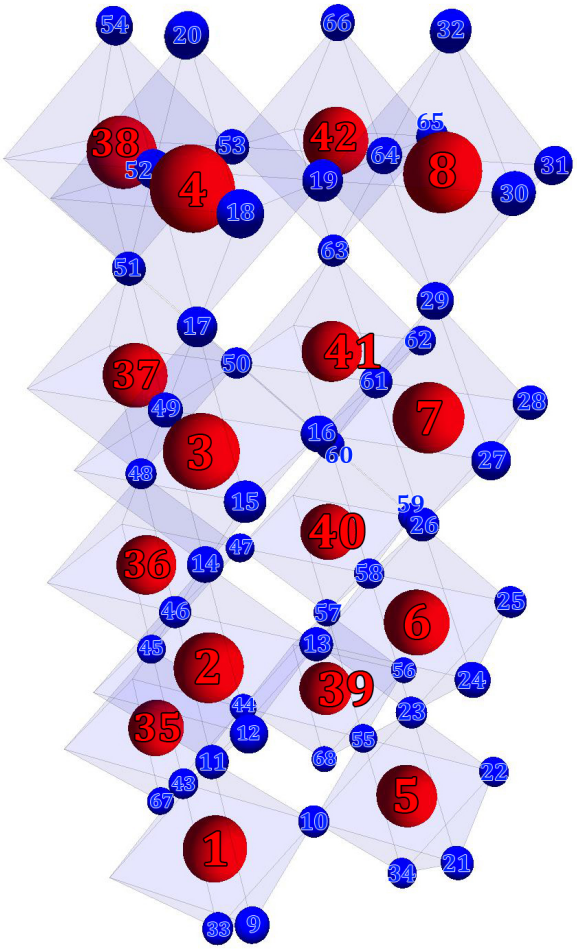

Figure 3.2: The $2 \times 2 \times 4$ cluster. In red, Ti atoms, surrounded by an octahedra of O atoms in blue. The existing atoms have been numbered so that the data shown in the coming chapters can be interpreted.

This cluster can be used to study the bulk of $SrTiO_3$ or the (001) surface in contact with vacuum. The cluster is periodic in the xy plane (that is, Ti atom 1 is also connected to O atom 22, Ti atom 35 is connected to O atom 9, etc.). The bulk can be analyzed imposing periodic boundary conditions. This means that O atoms 33, 34 67 and 68 are the same as O atoms 20, 32, 54 and 66, respectively. The surface of (001) can be studied by breaking the symmetry along the z-axis, so that the O atoms mentioned before are no longer equivalent.

Technically, if periodic boundary conditions are used along x and y this cluster can be simplified to a $1 \times 1 \times 4$ cell. Thus, a simplified unperturbed cluster would

show the same electronic structure and properties than that of the $2 \times 2 \times 4$ cell (see section 4.1). However, we will not give results for the $1 \times 1 \times 4$ system for several reasons. First of all, such cell does not allow the study of antiferrodistortive distortions, because when one octahedron rotates clockwise, the adjacent octahedra in the xy plane have to rotate counter-clockwise, and this cannot be implemented in a periodic xy system with a single column. Secondly, the study of Oxygen vacancies is rather difficult because one single vacancy would already yield a big density of Oxygen defects much higher than what is experimentally observed. Finally, a single column of Titanium atoms is not enough to study different relative positions of di-vacancies. For these reasons, we will continue our study using the $2 \times 2 \times 4$ cell for all the calculations.

The size of the cluster is big enough to obtain relevant data about the surface of $SrTiO_3$. We know that most transition-metal perovskites can accommodate a high density of Oxygen vacancies, and even when we introduce two vacancies in the TiO_2-terminated cluster the effective stoichiometry of the system is $SrTiO_{2.875}$.

3.1 Mathematical model

In the study of the $2 \times 2 \times 4$ cluster there are a total of 68 atoms (16 Titanium atoms and 52 Oxygen atoms, see Figure 3.2).

Taking into account that any single orbital can hold up to two electrons (spin up and down), there are a total[2] of $2 \times (16 \times 5 + 52 \times 3) = 472$ individual *spin-orbitals* to be taken into account.

The Hamiltonian has the following form:

$$H = H_o + H_{int} + H_{SO}$$

where

$$H_o = \sum_{i(Ti)} \sum_{d} \sum_{\sigma=\uparrow,\downarrow} E_d A^{\dagger}_{i(Ti),d,\sigma} A_{i(Ti),d,\sigma} + \sum_{j(O)} \sum_{p} \sum_{\sigma=\uparrow,\downarrow} E_p B^{\dagger}_{j(O),p,\sigma} B_{j(O),p,\sigma}$$

H_o is a diagonal matrix that contains the information of the on-site energies of the different atomic orbitals. $A_{i(Ti),d,\sigma}$ is the annihilation operator that removes an electron of the orbital d of the Titanium atom in position i(Ti) with spin σ. $B_{j(O),p,\sigma}$ is the annihilation operator that removes an electron of the orbital p of the Oxygen atom in position j(O) with spin σ. $A^{\dagger}_{i(Ti),d,\sigma}$ and $B^{\dagger}_{j(O),p,\sigma}$ are their counterpart creation operators. The first sum spans all the Titanium sites (16 in total) of the cluster and the five d orbitals (see section 1.2). Similarly the second sum spans all the Oxygen sites (52 in total) of the cluster and the three p orbitals.

$$\begin{aligned} H_{int} = & \sum_{<i(Ti_1),j(Ti_2)>} \sum_{d_1,d_2} \sum_{\sigma=\uparrow,\downarrow} T_{d_1,d_2,i(Ti_1),j(Ti_2)} e^{i\vec{k}\vec{v}_{i(Ti_1)j(Ti_2)}} A^{\dagger}_{i(Ti_1),d_1,\sigma} A_{j(Ti_2),d_2,\sigma} \\ & \sum_{<i(Ti),j(O)>} \sum_{d,p} \sum_{\sigma=\uparrow,\downarrow} T_{d,p,i(Ti),j(O)} e^{i\vec{k}\vec{v}_{i(Ti)j(O)}} A^{\dagger}_{i(Ti),d,\sigma} B_{j(O),p,\sigma} \\ & \sum_{<i(O_1),j(O_2)>} \sum_{p_1,p_2} \sum_{\sigma=\uparrow,\downarrow} T_{p_1,p_2,i(O_1),j(O_2)} e^{i\vec{k}\vec{v}_{i(O_1)j(O_2)}} B^{\dagger}_{i(O_1),p_1,\sigma} B_{j(O_2),p_2,\sigma} + H.C. \end{aligned} \tag{1}$$

[2]There are two spins (up-down), five d orbitals for the Titanium atom and three p orbitals for the Oxygen atom. That is: spin×(#Ti×#d-orbs+#O×#p-orbs) $= 2 \times (16 \times 5 + 52 \times 3) = 472$

H_{int} represents the nearest neighbor interactions. The most general case involves interactions between neighboring Titanium atoms (first term), interactions between neighboring Titanium-Oxygen atoms (second term) and interactions between neighboring Oxygen atoms (third term). When the Hamiltonian of the (111) bilayer was introduced in section 2.2, the hopping amplitude between any two atoms was always $-t$ because the symmetry of the system allowed it. This is no longer the case. Now the five d orbitals are not equivalent and this hopping amplitude depends on the relative position and the orbitals of the two atoms involved in the interaction. The calculation of this amplitude can be done using the Slater-Koster rules (see *appendix A*).

$$H_{SO} = \lambda \vec{L} \cdot \vec{S}$$

H_{SO} introduces spin-orbit coupling into the system. This term lifts the degeneracy of the spin up-down orbitals. We explain the physical meaning of this term and we show how to compute it in *appendix B*.

3.2 Oxygen vacancies

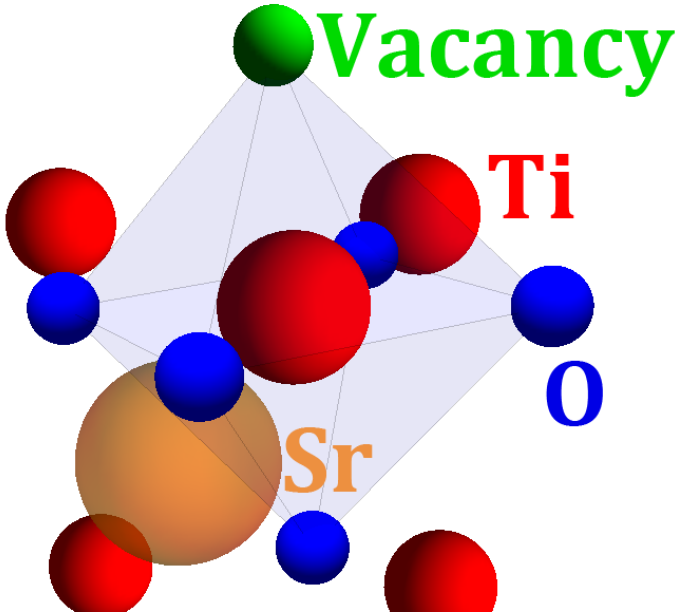

Figure 3.3: Representation of a single vacancy above a Titanium atom. The Ti atom will only interact with the five remaining Oxygen atoms.

The presence of Oxygen vacancies can be implemented in the model described in the previous section. To do so, the hopping amplitudes between the atoms near to the vacancy have to be tuned, as well as the on-site energies of these atoms. Relaxation can be simulated by displacing the Titanium atoms close to the vacancy.

Hopping amplitudes

In the previous section the Hamiltonian of the cluster was introduced using the tight binding model. It was stated that the interactions between any two atoms depended on their relative position and on the orbitals involved. Before removing the Oxygen atom to create a vacancy, the interaction between that Oxygen atom and a neighboring Titanium atom was proportional to the hopping amplitude $T_{d_a,p_b,i(Ti_a),j(O_b)}$. Once the Oxygen is removed, the possibility of an electron hopping from the Titanium atom to the Oxygen atom has to be removed. To do so, this hopping amplitude must be zero. Setting all the hopping amplitudes in the interaction between any kind

of atom with the Oxygen to be removed to zero is the first step to simulate a vacancy in the Hamiltonian. That is, if the Oxygen atom in position $m(O)$ is going to be removed, then

$$T_{d,p,i(Ti),m(O)} = 0$$

$$T_{p_1,p,i(O_1),m(O)} = 0$$

for all possible d and p orbitals, and for all possible $i(Ti)$ and $i(O_1)$ positions.

Relaxation

One way to simulate relaxation is by displacing the Titanium atoms. Normally the position of the Titanium atom is such that the overall energy of the atom is minimized. When the Titanium atom is surrounded by six Oxygen atoms, its *natural* position is in the middle of the octahedron, equidistant from all the surrounding Oxygen atoms. When one (or more) of the Oxygen atoms is removed, the Titanium atom needs to find a new stable position.

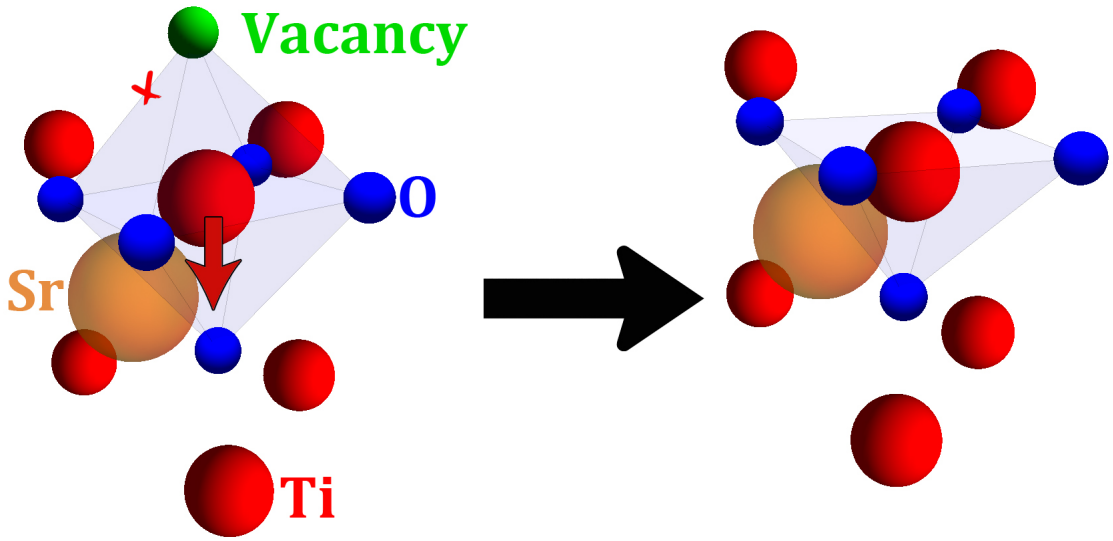

Figure 3.4: Removing an Oxygen atom changes the local crystal field of the neighboring atoms. On-site energies, hopping amplitudes and position of the atoms have to be adjusted.

Figure 3.4 shows the displacement of the Titanium atom when the Oxygen atom above it is removed. In this particular case, the Titanium atom would go down to

a new stable position. The displacement is not so strong in this case (around 4% of the Ti-O distance), but the impact on the Hamiltonian and the electronic structure is critical. Once again, the hopping amplitude between the displaced Titanium atom and its neighboring atoms depends on their relative position from each other. If the position of one of the atoms is modified, so is the hopping amplitude. This means that the hopping amplitudes $T_{d_1,d_2,i(Ti_1),j(Ti_2)}$ and $T_{d,p,i(Ti),j(O)}$ in (1) have to be recalculated.

On-site energies

The five d orbitals are degenerate in vacuum, and so are the three p orbitals. This is not the case with the perovskite structure. As we mentioned in section 1.1 the five d orbitals split into the t_{2g} triplet and the e_g doublet. The degeneracy of these two sets can be split again if we introduce Oxygen defects in the crystal. As a first approximation we can consider that the six Oxygen atoms surrounding any Titanium atom are responsible for the local crystal field felt by the Titanium atom. If we remove any of those Oxygen atoms, we change this crystal field, such that the cubic symmetry is broken. In the following sections we will show how the on-site energies of some particular orbitals change depending on the presence and position of one or more Oxygen vacancies.

4 Impact of Oxygen vacancies on the (001) surface of $SrTiO_3$

As mentioned before, the appearance of the two-dimensional electron gas found at the (001) surface of $SrTiO_3$ can be explained by the presence of Oxygen vacancies at the surface of the crystal. The density and relative position of these vacancies can have an impact on the physical properties of such 2DEG. In this chapter (and in *appendix C*) several configurations of the cluster will be presented.

The (001) surface has two possible terminations. One of them is the TiO_2 terrace and the other one is the SrO terminations. Their electronic structure is quite similar but there are slight differences that we will comment in the following sections.

Thanks to the fact that we are modeling the problem by means of a Hamiltonian we can use a simple mathematical trick to access states that are not experimentally realized and also that require elaborate schemes to be stabilized in DFT calculations. This trick consists on removing the Oxygen atom *smoothly*, so that there is a continuous transition between the cluster with all the Oxygen atoms in place and the cluster with one or more vacancies. This can be easily done by introducing a parameter α that regulates the existence of vacancies. More precisely, if $\alpha = 0$ then the Oxygen atom is removed and there is a vacancy in the cluster. If $\alpha = 1$ then the Oxygen atom has not been removed and there are no vacancies in the cluster. An intermediate value of α has no physical interpretation but it helps to understand the emergence of new electronic states that might give rise to the observed 2DEG.

In section 3.2 it was stated how the hopping amplitudes between atoms, the position of the atoms and their on-site energies depended on the existence and position of the vacancies. Using this parameter α all these physical quantities can be *smoothly* regulated. That is, if the real hopping amplitude between an Oxygen atom and a Titanium atom is t_o, then the mathematical amplitude would be αt_o, so that the amplitude is t_o when $\alpha = 1$ and the Oxygen atom is in the cluster, and it becomes 0 when $\alpha = 0$ and the Oxygen atom has been removed. Similar linear transformations can be done with the position of the atoms and their on-site energies.

Figure 4.1 can be helpful to visualize this trick. The Figure shows the energy states (y-axis) at the Γ point of the cluster for different values of α (x-axis). α regulates the existence of one of the Oxygen atoms on the top SrO layer. On the far right of the picture it can be observed that all the states are grouped in either the bottom

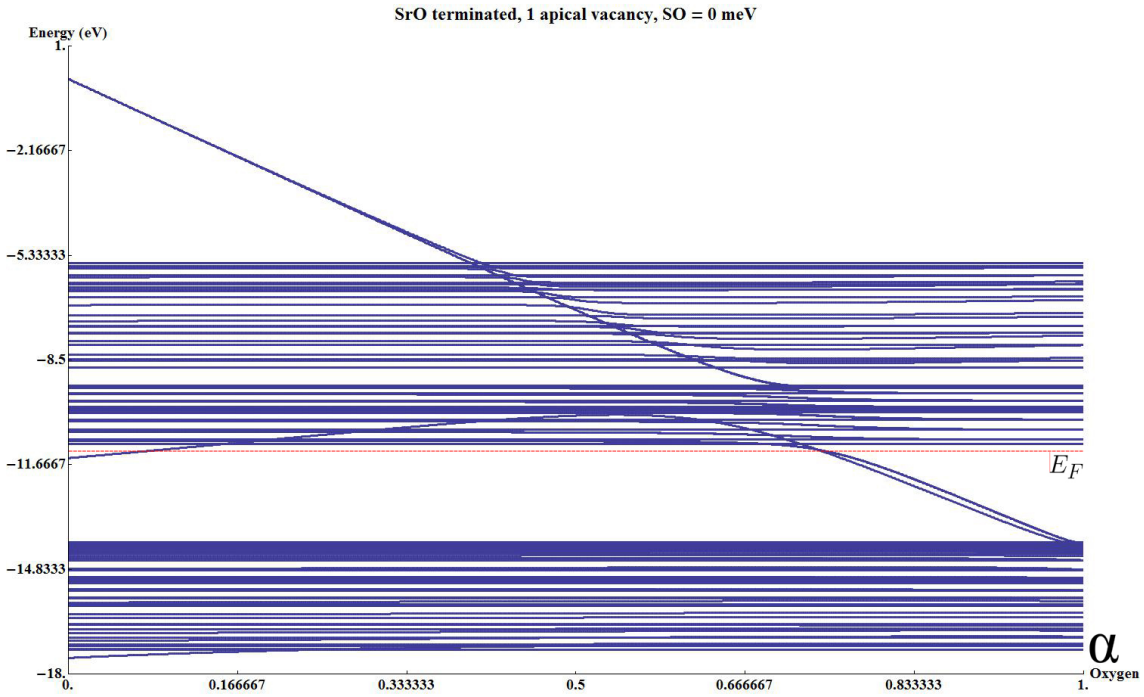

Figure 4.1: The horizontal axis denotes the *presence* of the Oxygen atom (it is the parameter α mentioned in the introduction of this chapter). On the far right, we can see the energy states at the Γ point when the Oxygen atom is still present. Thus, we can see the usual insulating case where the valence and the conduction states are separated by a large gap. On the left, we see the energy states when the Oxygen atom is not present, meaning that the system has one Oxygen vacancy. The smooth transition between the two cases helps us visualize the origin of the new states created both in the gap and within the conduction part.

of the figure (valence states, the top of the valence part is at $-14.05\ eV$), or in the top (conduction states, the bottom of the conduction bands is at $-11.04\ eV$). On the far left of the picture there are also states that belong to the valence and conduction bands, but there are also two new types of states. Firstly, there are states at $0\ eV$ These states represent the vacancy. Where there was an Oxygen before with an on-site energy of around $-14\ eV$ there is vacuum now. The site occupied by the Oxygen is now empty, and this site has a on-site energy of $0\ eV$ and there is no hopping amplitude connecting this site with any other atom. These states are completely orthogonal to the rest of the states. Secondly, there are new (degenerate) states in the gap that separates the valence and the conduction part, at around

$-11.5\ eV$. In the next sections we will study the particular properties of these new in-gap states. Finally, some of the conduction states have changed. We will also pay attention to some of the new conduction states appearing above the bottom of the conduction part.

In the model used to calculate the bulk electronic structure of $SrTiO_3$ there were several parameters that needed to be tuned (see Table 1). These parameters are still present for this model of the $2 \times 2 \times 4$ supercell. The numerical values that were tuned for the bulk will be the same in this case. However, since now we are introducing the possibility of Oxygen vacancies and Titanium displacements, there are new parameters that need to be tuned.

In the perfect cubic lattice we know that the d orbitals split into two groups, the e_g and the t_{2g}. This means that $E_{d_{xy}}$=$E_{d_{xz}}$=$E_{d_{yz}}$ and $E_{d_{x^2-y^2}}$=$E_{d_{z^2}}$. This is no longer the case in the presence of Oxygen vacancies. When an Oxygen atom is removed, its neighboring Titanium atom is surrounded by a slightly different crystal field that will split this degeneracy. As an example, let us suppose that we remove the Oxygen atom that is above a Titanium atom in the z-axis. In this case, the d_{xy} and $d_{x^2-y^2}$ do not feel the difference, but there will be a change in the on-site energies of the d_{z^2} and d_{xz}-d_{yz} orbitals, lifting the e_g and t_{2g} degeneracies.

Another set of parameters that needs to be tuned is the position of some of the atoms within the cluster. In the example mentioned before (see Fig. 3.4), the Titanium atom would be shifted along the z axis a modest 4% of the original Ti-O distance.

4.1 SrO-termination. No vacancies.

The $2 \times 2 \times 4$ cluster was already introduced in chapter 3. Before evaluating the electronic properties of the cluster with Oxygen vacancies, it is important to evaluate them when all the Oxygen atoms are present.

As a reminder, there are 68 atoms in the cluster (16 Titanium atoms and 52 Oxygen atoms). Figure 4.2 shows all the existing atoms, that have been numbered so that the data shown in the coming chapters can be interpreted.

The slab is periodic in the XY plane, whereas the symmetry in the z direction has been broken imposing surface terminations. Even though there are slight differences between the atoms close to the surfaces and the atoms in the bulk of the slab, we consider the symmetry of the system to be perfectly cubic. All the p orbitals of all the Oxygen atoms are considered degenerate in energy, as well as the t_{2g} triplets and the e_g doublets of the Titanium atoms.

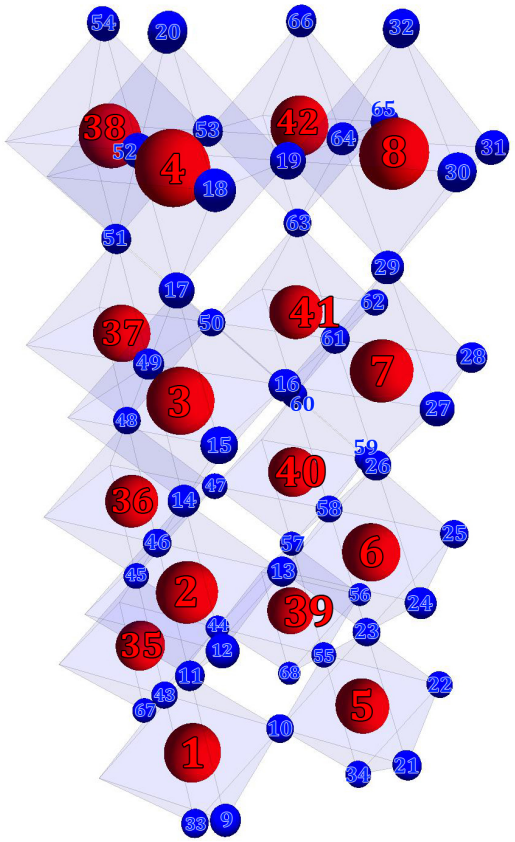

Figure 4.2: $2 \times 2 \times 4$ supercell with no vacancies.

In this section we will study the energy states at the Γ point and we will show the orbital and site character of the bottom of the conduction band (above the Fermi energy) before any Oxygen atom is removed. We will also show the energy bands along the Brillouin zone. These results will be used as a benchmark for the results that we obtain when we introduce Oxygen vacancies in the system.

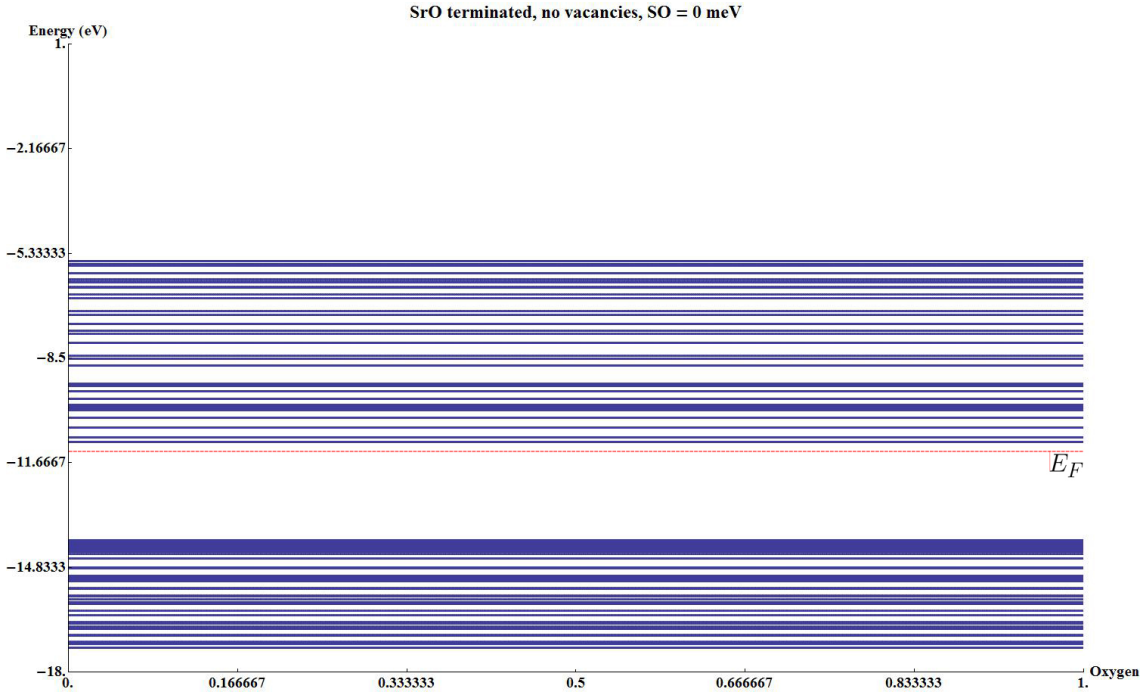

Figure 4.3: Electronic states at the Γ point of the $2 \times 2 \times 4$ cluster.

Figure 4.3 shows the energy states at the Γ point. Since we want to study the electronic structure of the cluster without Oxygen vacancies first, the states appear flat because no Oxygen atom is being removed at all. It can be clearly seen the two groups of states, one representing the valence part and the other one the conduction part. The gap is around 2.96 eV.

When we introduce Oxygen vacancies, there will be new in-gap states close to the conduction part. In order to make a comparison, we will show the character of the electronic states at the bottom of the conduction bands.

Several degenerate states can be found there. Figure 4.4a shows that the first conduction state has mostly d_{xy} character (slightly mixed with the other t_{2g} orbitals due to the small spin-orbit coupling). Figure 4.4b indicates the site contribution of this particular state (check Figure 4.2 to see the numbers of the atoms). It is quite clear that this state is located mostly on the eight Titanium atoms in the middle of the supercell, and there is a small contribution coming from the eight Titanium atoms close to the surfaces (illustrated in Figure 4.6a).

Some of the other degenerate states at the bottom of the conduction band have the

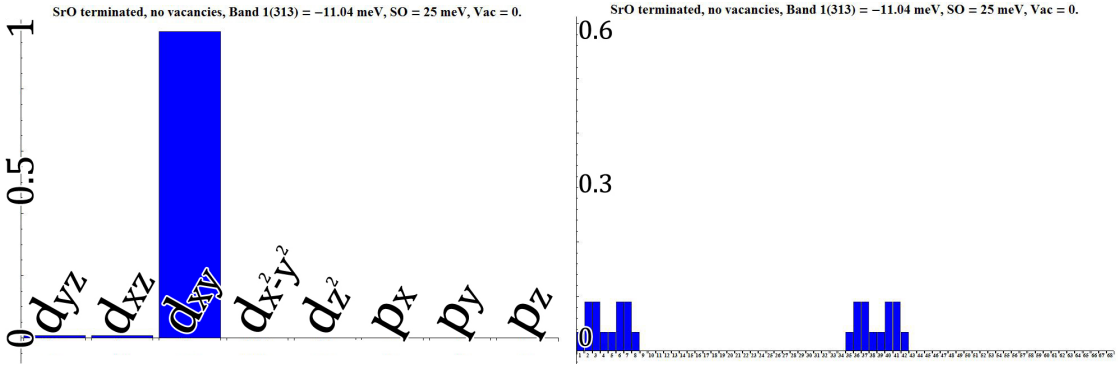

(a) Orbital (b) Sites

Figure 4.4: Orbital/site character of the electronic states at the bottom of the conduction band (I).

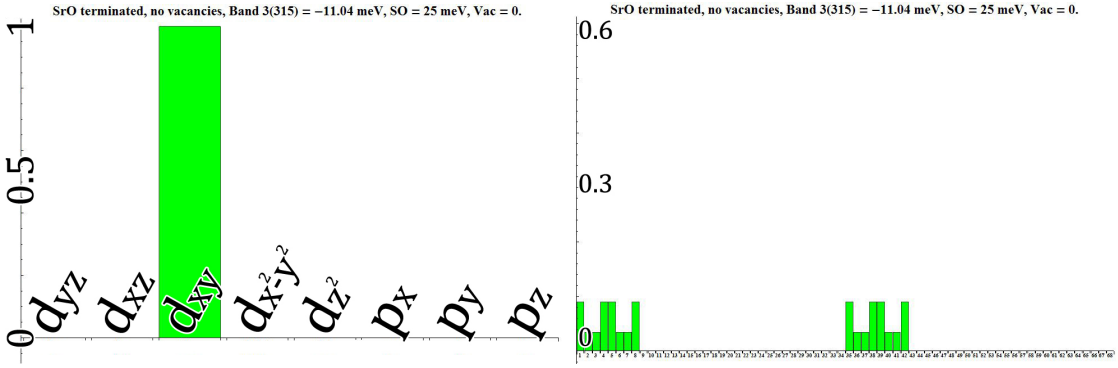

(a) Orbital (b) Sites

Figure 4.5: Orbital/site character of the electronic states at the bottom of the conduction band (II).

profile shown in Figure 4.5. Again it is a d_{xy} state, but now (as seen in Figure 4.5b) it is located on the surfaces of the cluster, mostly. There is a slight contribution coming from the Titanium atoms on the bulk of the supercell but it is the surface Titanium atoms the ones that contribute most (see Figure 4.6b).

The energy states shown in Figure 4.3 are calculated at the Γ point. Figure 4.7 shows the energy states at different points in the Brillouin zone.

Figures 4.3, 4.5 and 4.6 show properties of the eigenstates calculated at the Γ point. The full band structure along the Brillouin zone is presented in Figure 4.7. The

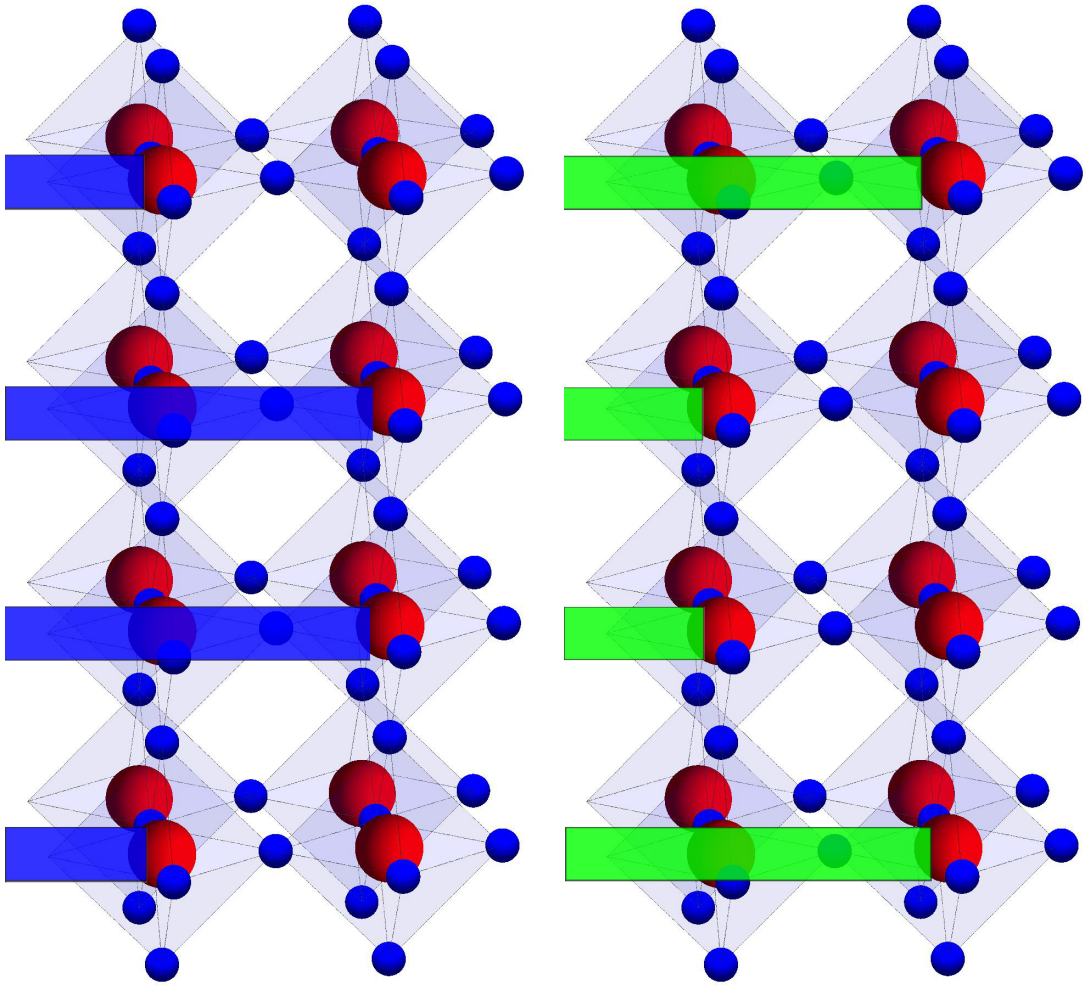

(a) Titanium-sites character of the electronic states at the bottom of the conduction band (I).

(b) Titanium-sites character of the electronic states at the bottom of the conduction band (II).

Figure 4.6: There are a total of eight degenerate states at the bottom of the conduction part. Four of them with the profile shown in Figure 4.4 and the other half with the profile shown in Figure 4.5.

valence part has a strong p-character and the big majority of the contribution is coming from the Oxygen atoms. 2.96 eV separates the top of the valence band and

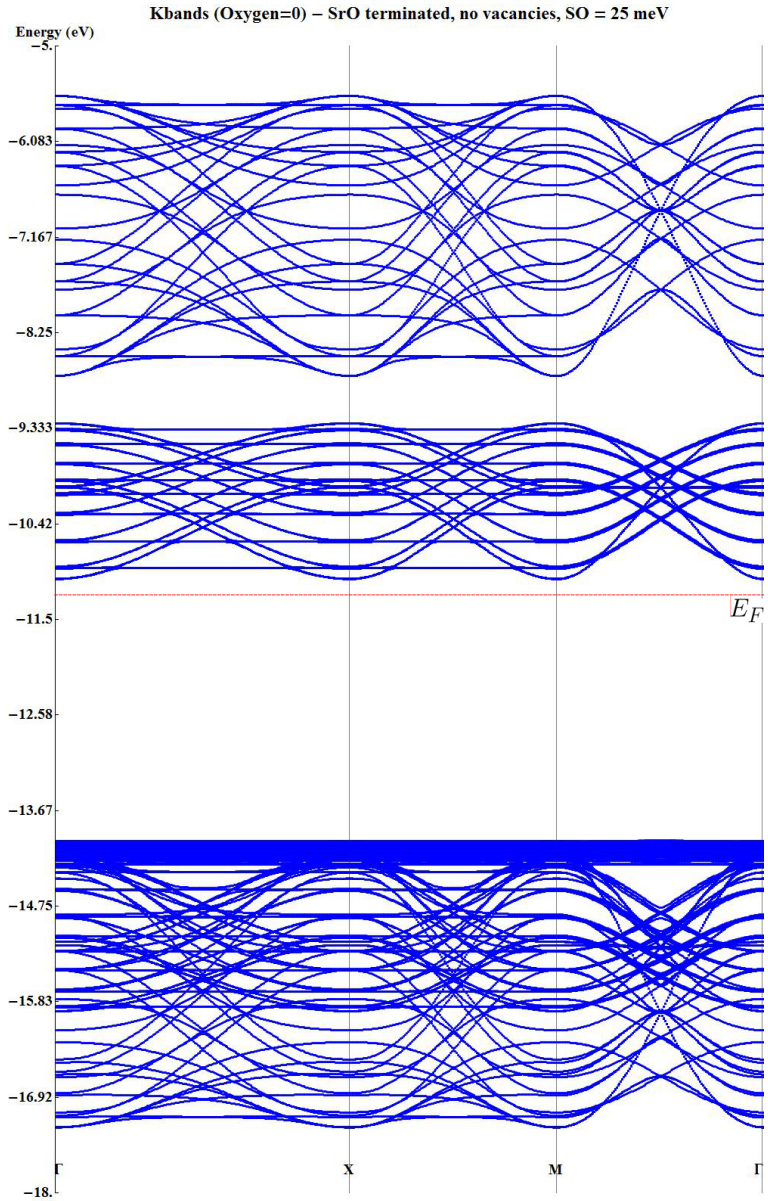

Figure 4.7: Band structure of the pure $2 \times 2 \times 4$ cluster.

the bottom of the conduction band. The conduction band has two parts due to the splitting of the e_g and t_{2g} orbitals in the perovskite structure. In the absence of Oxygen vacancies, the Fermi level is located above the valence bands. Thus, a

large amount of energy is required to promote on electron from the valence to the conduction part, and this is why $SrTiO_3$ is a good insulator. This band structure will suffer some changes when we introduce Oxygen vacancies, as we will see in the coming sections.

Summary

- The electronic structure of the SrO-terminated cluster is that of a common insulator. The valence and conduction states are clearly separated by a band gap.
- The valence states are mainly oxygen-p states. The conduction states have strong Titanium d character.
- The orbital character of the bottom of the conduction band is d_{xy}.
- We will consider the case of the pure TiO_2 terminated cluster in section 4.4.

4.2 SrO-termination. One apical vacancy

The simplest case to analyze is the one where one of the Oxygen atoms of the top SrO layer is removed (green site in Figure 4.8).

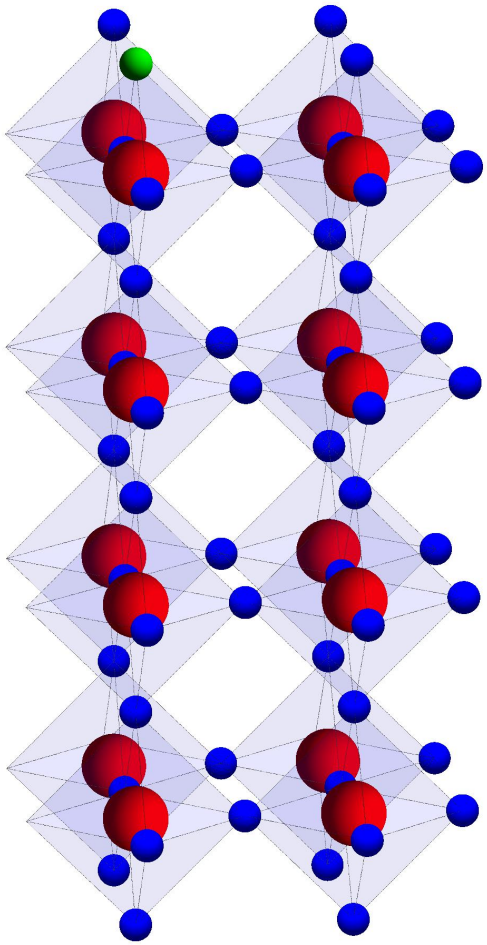

Figure 4.8: The cluster with one Oxygen vacancy on the top SrO layer.

As it was stated at the beginning of this chapter, the on-site energy of site 20 (site of the vacancy, see Figure 4.2) will be smoothly turned to zero and all the hopping amplitudes connecting this site with its neighbors will also be removed, leaving this vacuum-site isolated from the rest of the supercell. This vacuum-site will create new electronic states at 0 eV, quite far from the top of the conduction part. Since these states are completely orthogonal to the rest of the states, they will never be filled with electrons and they do not affect the electronic structure of the system.

The Titanium atom right below the Oxygen vacancy will be pulled down in the z-direction as an adaptation to the new local crystal field.

The change in the crystal field surrounding the Titanium atom below the vacancy lifts the degeneracy of the t_{2g} and e_g orbitals of this particular atom. That is, the on-site energy of the d_{z^2} will be lowered now that there is not a p_z orbital above it to couple with. Analogously, and for the same reason, there will be a slight change in the on-site energies of the d_{xz} and d_{yz} orbitals (these are the only two that remain degenerate in energy).

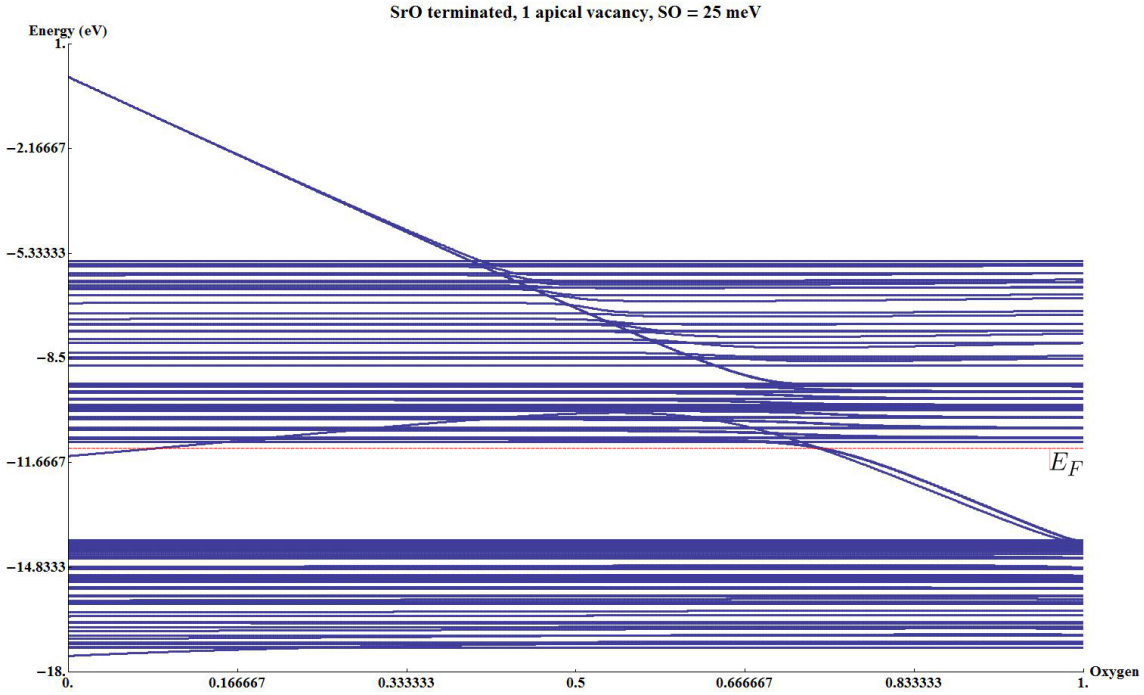

Figure 4.9: Electronic states at the Γ point when one Oxygen atom is removed. On the right, the electronic states when the Oxygen atom has not been removed. On the left, the electronic states when the Oxygen atom has been completely removed and the neighboring atoms have adapted to the new local crystal field.

Figure 4.9 shows the transition of the electronic states when the Oxygen atom is removed. On the right side of the plot one can find the energy states of the supercell at the Γ point when there is still an Oxygen in place and the system has not been perturbed (these states are identical to the ones found in Figure 4.3). On the left side one can find the new electronic states once the Oxygen atom has been fully removed. In the middle, the smooth transition between the two physical situations.

There are several differences between both sides of the plot, but there are two features that are critical:

1. There are six new degenerate states at 0 eV. These states emerge in the case of an atomic configuration where one (or more) Oxygen atom is missing. These states are completely decoupled from the rest of the system because the 'interatomic' matrix elements connecting this site with the rest of the cluster are zero. Moreover, the fact that these states are far from the top of the conduction part prevents any electron from getting there when the system is

doped.

2. There are two new in-gap states around 0.42 eV below the bottom of the conduction band.

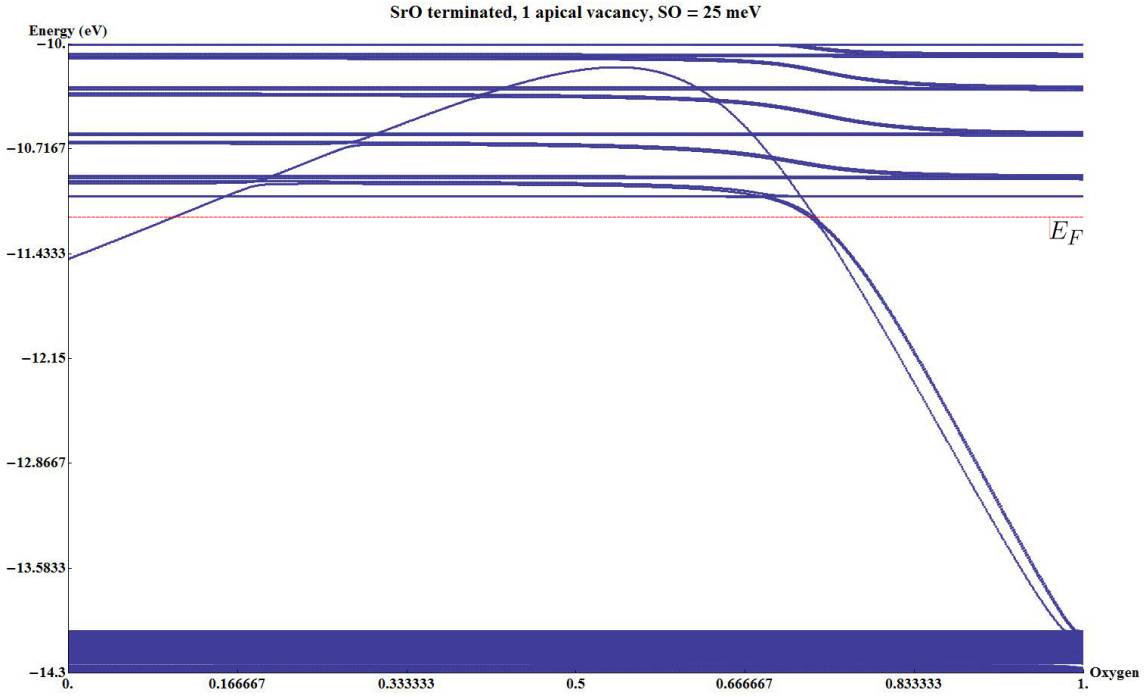

Figure 4.10: Zoom of Fig. 4.9.

In Figure 4.10 we can clearly see the new in-gap state coming from the valence part, and several new electronic states that are created above the bottom of the conduction band.

It is important that we understand the orbital and site character of the new states found in the gap and the other new states that appear in the vicinity of the bottom of the conduction part.

The orbital and site character of the two new degenerate in-gap states is shown in Figure 4.11. They are mostly a mixing of d_{z^2}-p_z orbitals coming from atoms 4 and 17. Atom 4 is the Titanium atom right below the vacancy (see Fig. 4.2) and atom 17 is the Oxygen atom right below the Titanium atom. This means that these states are quite localized in the vicinity of the vacancy introduced and that the neighboring atoms are affected much more than the other atoms in the slab. There is also a bit

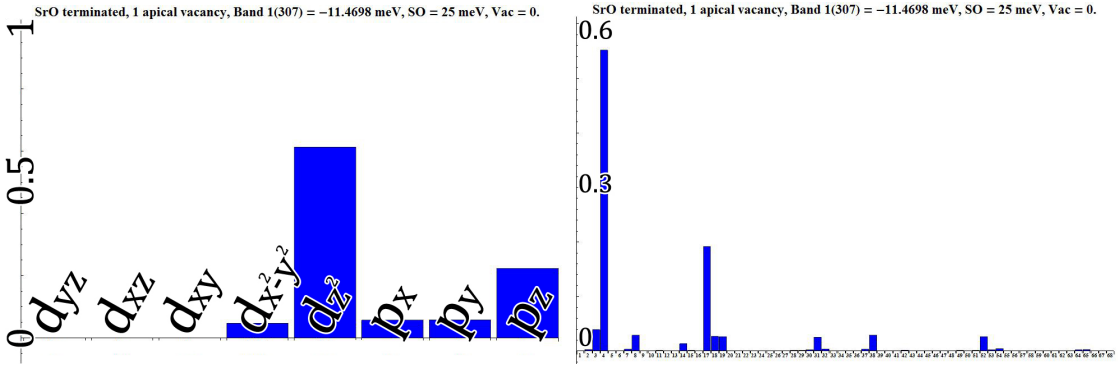

(a) Orbital (b) Sites

Figure 4.11: Orbital/site character of the two new electronic states found in the gap.

of $d_{x^2-y^2}$-$p_{x/y}$ mixing coming from the Titanium and Oxygen atoms in the vicinity of the vacancy, but it is minimal.

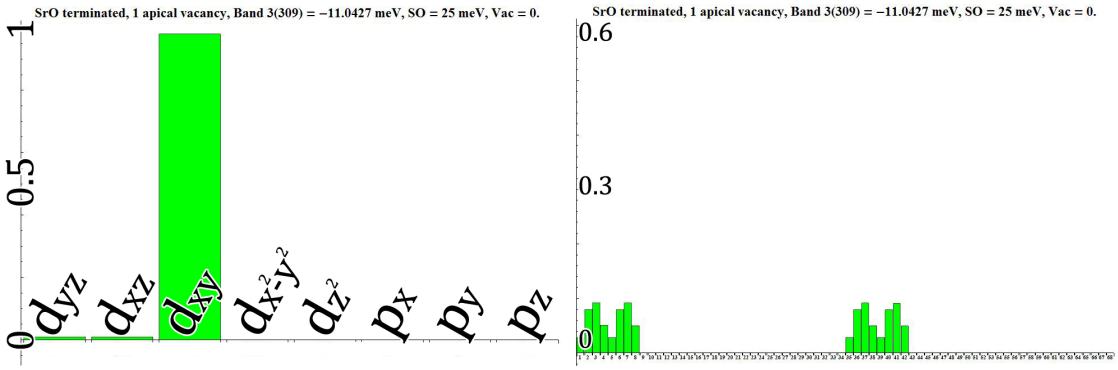

(a) Orbital (b) Sites

Figure 4.12: Orbital/site character of the electronic states at the bottom of the conduction band.

Above these two new in-gap states there is the bottom of the conduction band. The orbital and site character of the first degenerate states in the conduction band is shown in Figure 4.12. It can be clearly seen that it is an almost pure d_{xy} state, similar to what was found in the cluster with no vacancies. Figure 4.12b shows that the Titanium atoms in the middle of the cluster contribute more than the Titanium atoms situated close to the surface, but the contribution is not completely symmetric.

That is, the Titanium atoms that are closer to the vacancy contribute more than the atoms that are further. This s a bit different from what was found in the cluster with no vacancies.

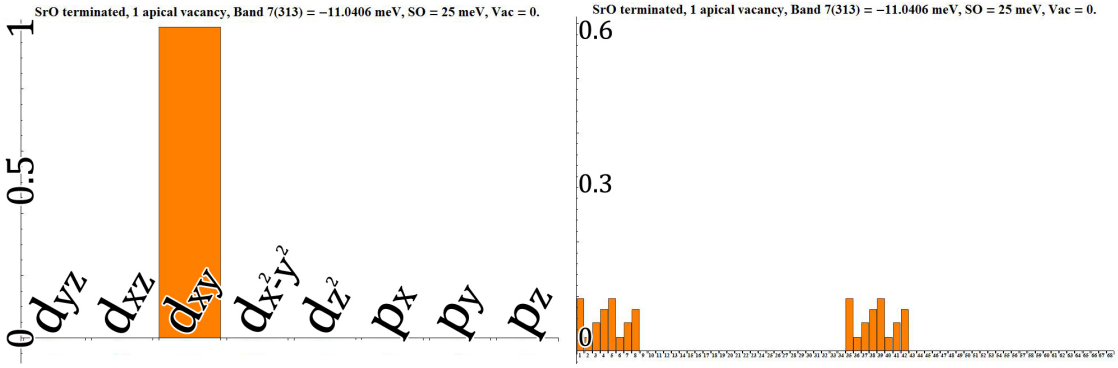

(a) Orbital (b) Sites

Figure 4.13: Orbital/site character of the lowest new electronic states above the bottom of the conduction band.

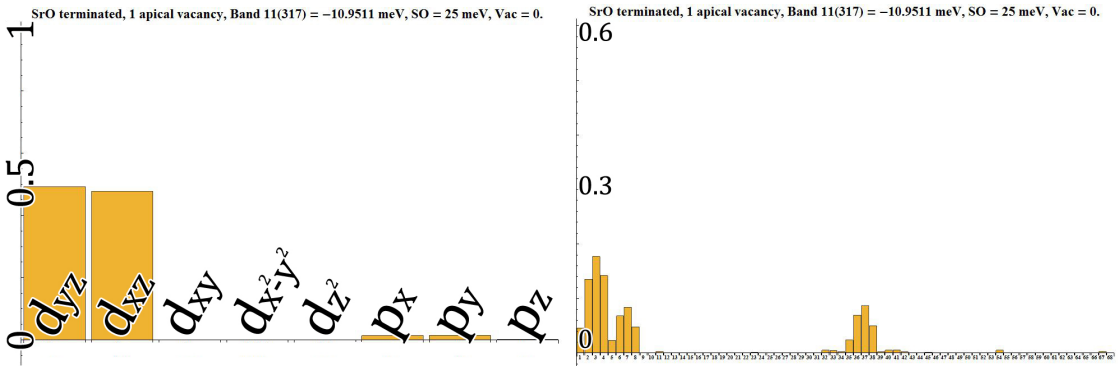

(a) Orbital (b) Sites

Figure 4.14: Orbital/site character of the next new electronic states above the bottom of the conduction band.

Several new states appear in the conduction part. Figure 4.13 shows the orbital/site character of the lowest new degenerate states. They are pure d_{xy} states mainly localized on the edges of the cell. Figure 4.14 shows the character of one of the degenerate new states found above the previous d_{xy} states. It is a mixture of d_{xz} and d_{yz} orbitals localized mainly around the Titanium number 3 and around the other

Titanium atoms belonging to the column of the Oxygen vacancy. Titanium atoms on the adjacent columns also contribute a bit. The contribution coming from the diagonally opposed column is negligible.

Special attention has to be paid to the symmetry of the system. We mentioned in the beginning of the chapter that the cluster was periodic in the x and y directions and that, in the absence of distorsions, the system is completely symmetric in the x-y plane. This symmetry remains untouched when we introduce one apical vacancy in the top SrO layer. This feature can be read off from the histograms, where the weight of the p_x and p_y orbitals is the same (as well as the d_{xz} and d_{yz}). Also, the weight of Titanium/Oxygen atoms in the x axis is the same as the atoms found when the system is rotated by 90°. This analysis seems to be false when we look at the last set of histograms (Figure 4.14). The histograms show a slight difference between the d_{xz} and the d_{yz} orbitals as well as a difference between the four columns of the cell. This is because we showed the orbital/site character of only one of the degenerate states in the conduction band. A closer look to the histograms of the other degenerate states reveals that all the histograms can be paired such that in the end a perfect xy symmetry is recovered.

Once again, the energy states shown in Figure 4.9 are calculated at the Γ point, but we can calculate the energy states of the system when the Oxygen has been completely removed at different points in the Brillouin zone, as shown in Figure 4.15. The main feature in this structure is the appearance of two new degenerate bands between the valence and the conduction part (and their counterparts below the valence bands). The orbital contribution of these two states can be studied at any point along Figure 4.9 (in the process of removing the Oxygen atom). What we see is that initially there is a big contribution coming from the Oxygen to be removed, so the orbital character is mainly p. There is a small contribution coming from the d orbitals of the Titanium below the (future) vacancy and from other surrounding Oxygen atoms. As soon as we *start removing* the Oxygen atom (diminishing the interatomic hopping amplitudes, changing the on-site energies of some particular orbitals and *relaxing* the structure) the contribution of the Oxygen atom diminishes and the Titanium atom below begins to contribute more to this state. This is why in Figure 4.9 we see a state from the valence band taking off towards the conduction part. The contribution to this state coming from the different atomic orbitals suffers some changes along the process of removing the Oxygen atom. In the end, we recover Figure 4.11. The orbital and site character of these states does not strongly depend on k. Similar orbital contributions are obtained when the new states are evaluated at other points of the Brillouin zone. The Fermi level is located between the new

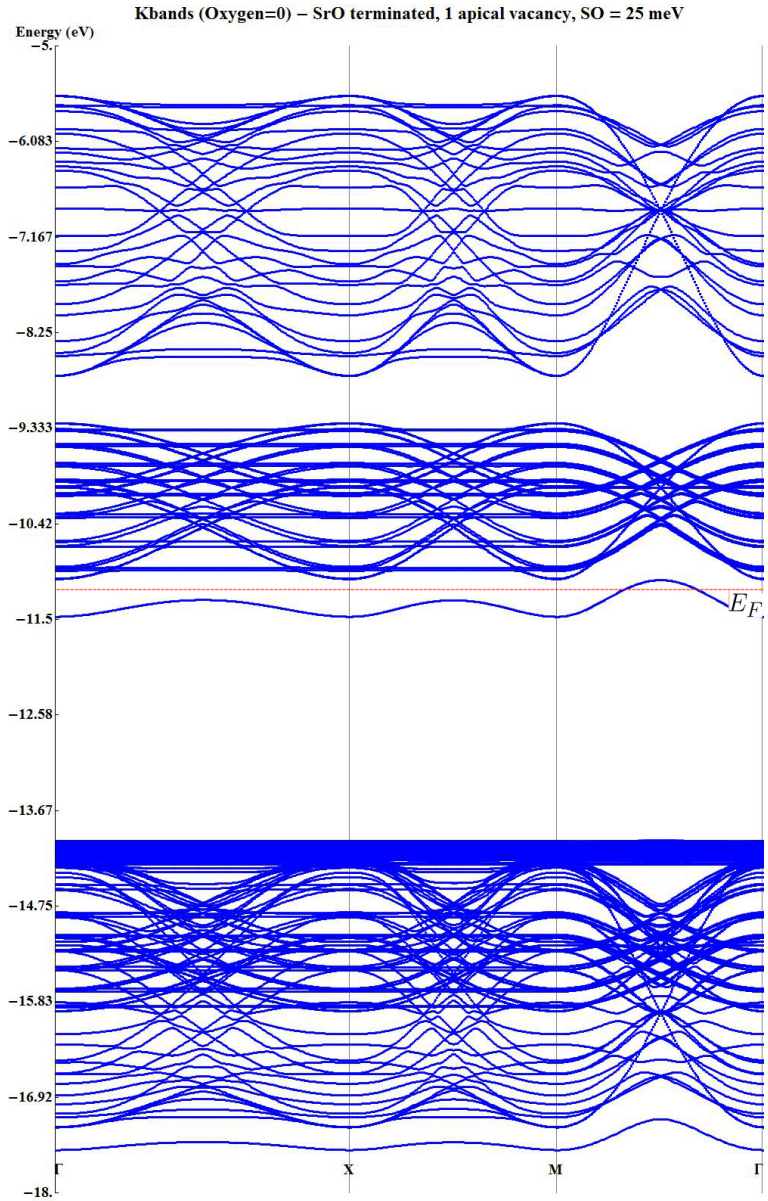

Figure 4.15: Band structure of the $2 \times 2 \times 4$ cluster with one apical Oxygen vacancy.

in-gap states (which are filled with electrons) and the conduction part.

Summary

- New features appear in the band structure when one apical vacancy is introduced on the SrO surface.
- Two degenerate states appear in the gap close to the bottom of the conduction part. These are states localized around the Titanium below the vacancy and their orbital character is mainly d_{z^2}.
- The bottom of the conduction band remains unchanged, although its localization within the slab is slightly different due to the symmetry breaking in the z direction.
- Other new states appear in the conduction band. These are t_{2g} states.
- Some of the new conduction states are d_{xy} states. Others are a combination of $d_{xz} - d_{yz}$ states.

4.3 SrO-termination. Two vertical vacancies

There are other positions where we can introduce a single vacancy. We show results for a single vacancy introduced in the first TiO_2-plane in *appendix C*. In this section we will study the electronic structure of the cluster when we introduce two Oxygen vacancies vertically aligned as shown in Figure 4.16.

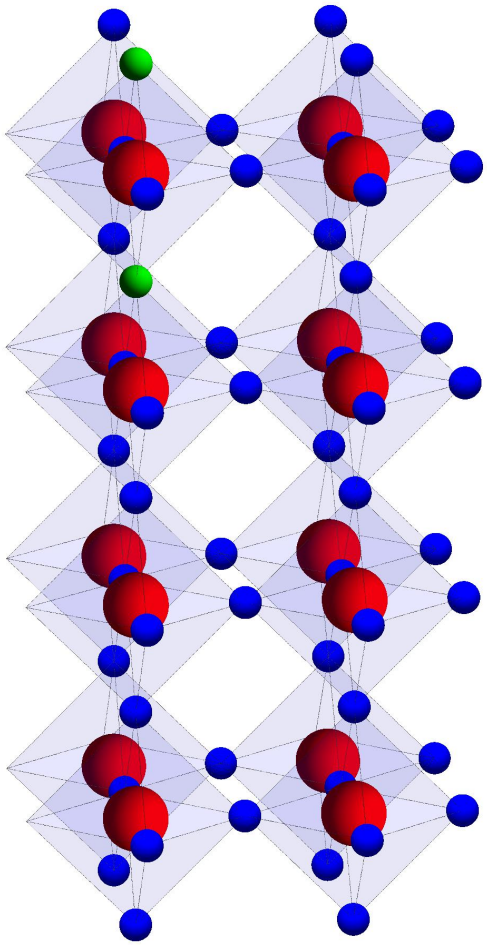

Figure 4.16: The cluster with two Oxygen vacancies vertically aligned

Again, the on-site energy of sites 17 and 20 (sites where the Oxygen atoms are removed, see Figure 4.2) will be smoothly turned to zero and all the hopping amplitudes connecting these sites with their neighboring atoms will also be removed, leaving these vacuum-sites isolated from the rest of the supercell. Once again, these vacuum-sites will create new electronic states at 0 eV, completely orthogonal to the rest of the states, that will never be filled with electrons and that do not affect the electronic structure of the system.

This time the Titanium atom (4) right below the first Oxygen vacancy (20) will not be pulled down in the z-direction because the local crystal field at site 4 is symmetric in this direction. However, the Titanium (3) below the second vacancy (17) will adapt to the new non-symmetric local crystal field and will be pulled down in the z-direction.

The change in the crystal field surrounding the Titanium atom below the second vacancy lifts the degeneracy of the t_{2g} and e_g orbitals of this particular atom. That is, the on-site energy of the d_{z^2} will be

lowered now that there is not a p_z orbital above it to couple with. Analogously, and for the same reason, there will be a slight change in the on-site energies of the d_{xz} and d_{yz} orbitals (these are the only two that remain degenerate in energy).

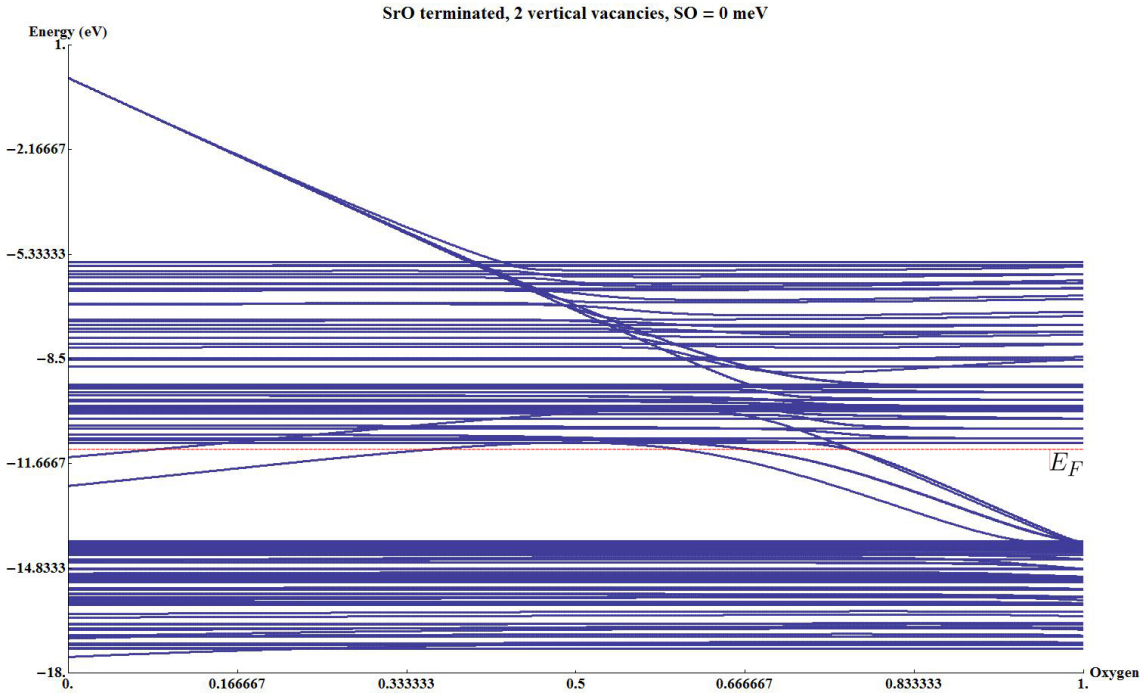

Figure 4.17: Electronic states at the Γ point when two Oxygen atoms are removed. On the right, the electronic states when the Oxygen atoms have not been removed. On the left, the electronic states when the Oxygen atoms have been completely removed and the neighboring atoms have adapted to the new local crystal field.

Figures 4.17 and 4.18 show the energy states calculated at the Γ point. Again we see that the right side of the picture is the same as Figure 4.3 because the Oxygen atoms have not been removed yet. However, the left side of the picture shows the energy states when both Oxygen atoms have been completely removed. We can clearly see the appearance of new states in the gap, similar to what was found in the previous section.

A closer look reveals that, apart from the in-gap states, there are also new states formed above the bottom of the conduction band.

The orbital and site character of the two lowest new degenerate in-gap states is shown in Figure 4.19. They are mostly a mixing of d_{z^2}-p_z and $d_{x^2-y^2}$-$p_{x/y}$ orbitals

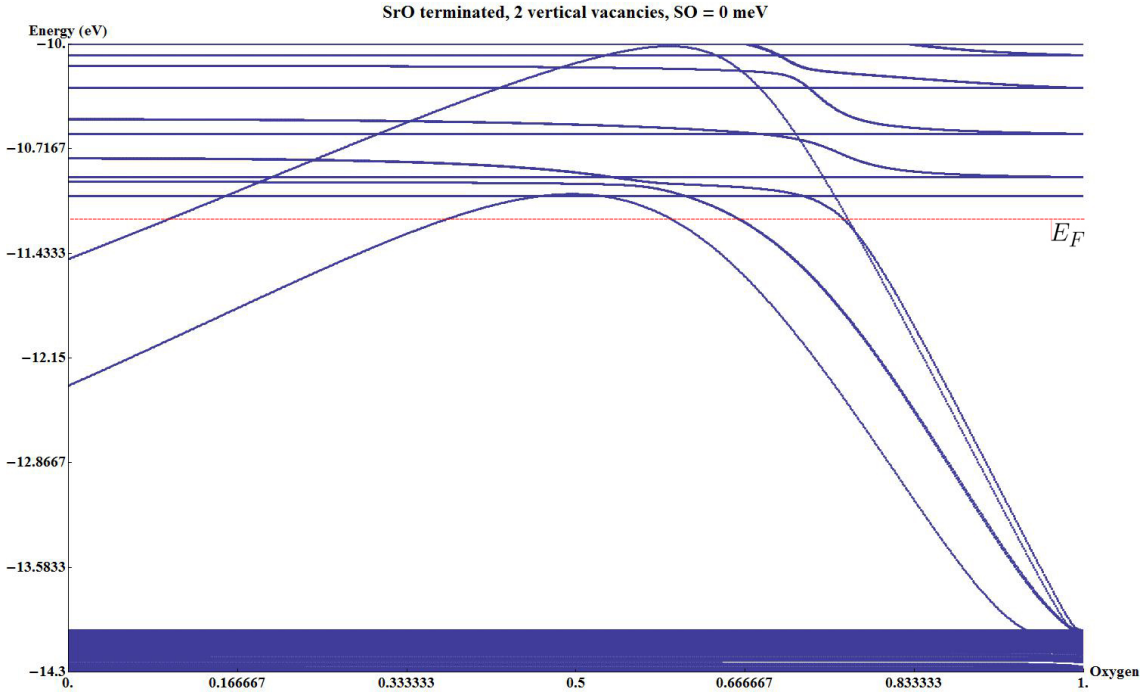

Figure 4.18: Zoom of Fig. 4.17.

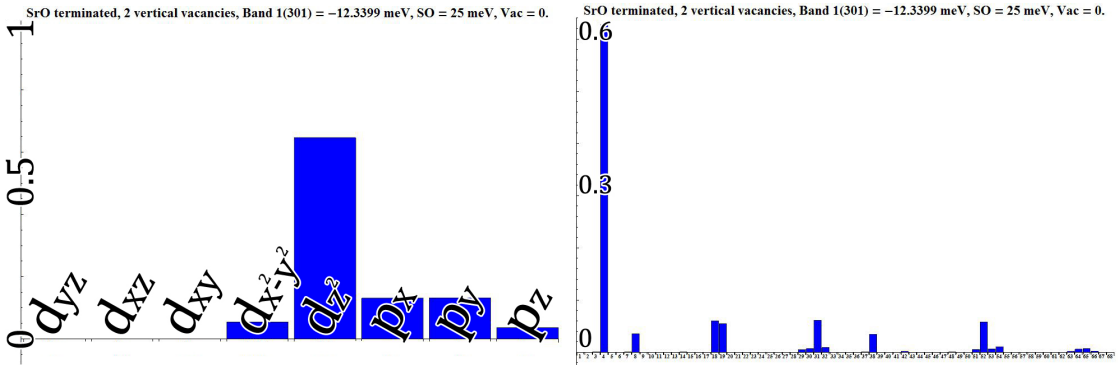

(a) Orbital (b) Sites

Figure 4.19: Orbital/site character of the first in-gap state.

coming from atom 4 and its neighbors. That is the Titanium atom between the two vacancies and the surrounding Oxygen atoms. This means that these states are quite localized in the vicinity of the vacancies introduced and that the neighboring atoms are affected much more than the other atoms in the slab.

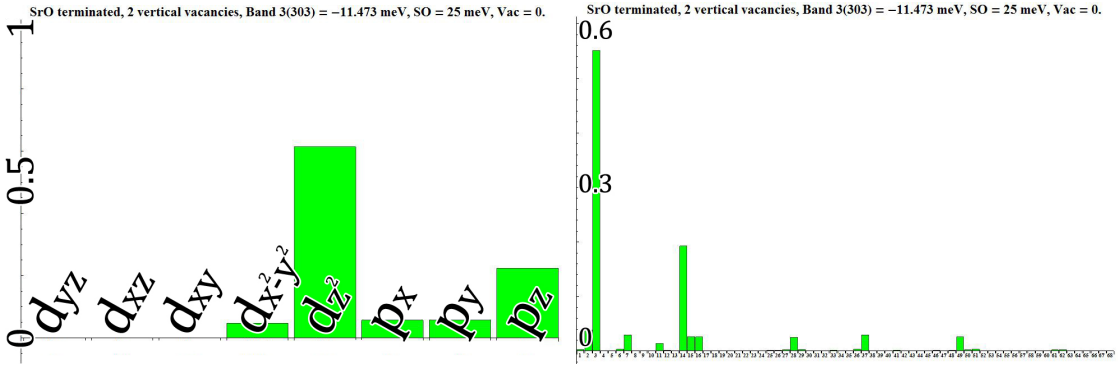

(a) Orbital (b) Sites

Figure 4.20: Orbital/site character of the second in-gap state.

The orbital and site character of the next two new degenerate in-gap states is shown in Figure 4.20. This time there is more contribution coming from the d_{z^2}-p_z orbitals of atoms 4 and 14, that is, the Titanium atom below the second vacancy and the Oxygen atom right below. There is also a bit of $d_{x^2-y^2}$-$p_{x/y}$ mixing coming from the Titanium and Oxygen atoms in the vicinity of the vacancies, but it is minimal.

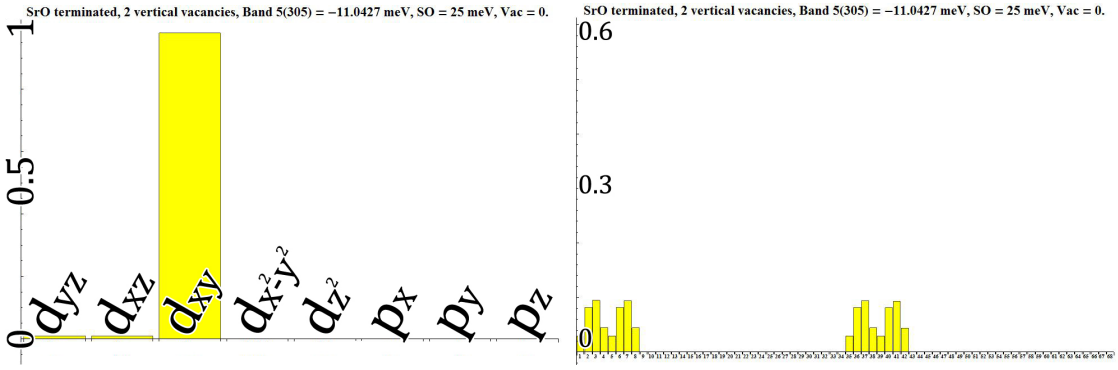

(a) Orbital (b) Sites

Figure 4.21: Orbital/site character of the states found at the bottom of the conduction band.

Above these four new in-gap states there is the bottom of the conduction band. The orbital and site character of the first degenerate states in the conduction band is show in Figure 4.21. It can be clearly seen that it is an almost pure d_{xy}, similar to what was found in the cluster with no vacancies or with a single vacancy. Figure

4.21b shows that the Titanium atoms in the middle of the cluster contribute more than the Titanium atoms situated close to the surface, but the contribution is not completely symmetric.

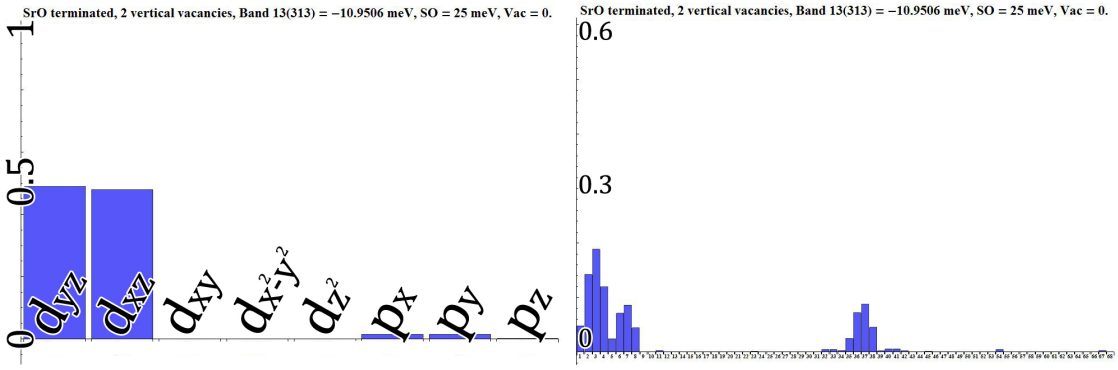

(a) Orbital (b) Sites

Figure 4.22: Orbital/site character of the first new conduction state.

Figure 4.22 shows the character of the lowest new conduction state. This state is very similar to the one found in the single-vacancy case (see Fig. 4.22). It is a mixture of d_{xz} and d_{yz} orbitals localized mainly around the Titanium number 3 and around the other Titanium atoms that belong to the same column (column of the vacancies).

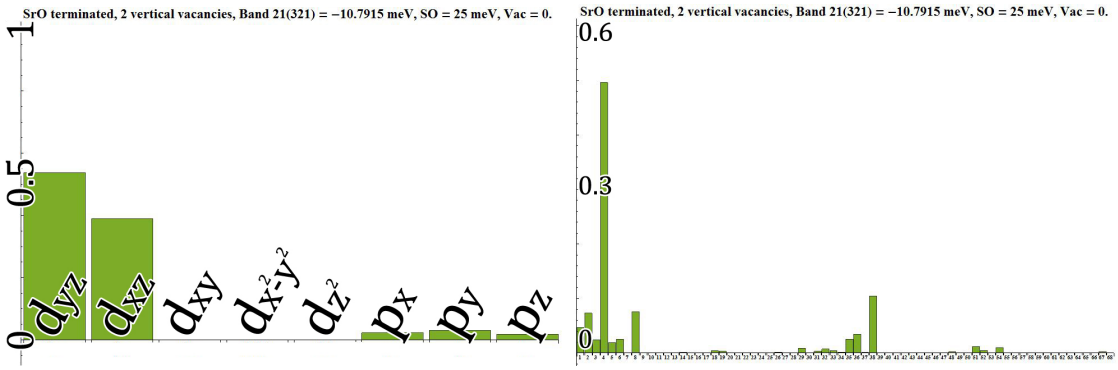

(a) Orbital (b) Sites

Figure 4.23: Orbital/site character of the second new conduction state.

Higher new conduction states have the character shown in Figure 4.23. We encounter again that the d_{xz}-d_{yz} orbitals are contributing the most. The main difference is that

now these states are localized around the Titanium atom between the two vacancies (atom number 4).

Again, this particular cluster with two vacancies along the z axis is symmetric in the x-y plane, something that can be clearly seen in the histograms. The last two sets do not show this symmetry because they only show the properties of one of the degenerate states created. The histograms of the other degenerate states are the xy-mirrors of the histograms shown.

Once again, the energy states show in Figure 4.17 are calculated at the Γ point, but we can calculate the energy states of the system when the Oxygen atoms have been completely removed at different points in the Brillouin zone, as shown in Figure 4.24. This time we see the appearance of two pairs of degenerate bands in the gap separating the valence and conduction parts (corresponding to the new in-gap states shown in Figure 4.17). Just like in the previous case, these new bands rise from the valence band, they do not drop from the conduction part, even though they both show strong d-character. This is because the p-character shrinks in the process of *removing the Oxygen atom*. And again, the histograms shown in Figures 4.19 and 4.20 calculated at the Γ point can be reproduced at any other point in the Brillouin zone. These new bands are filled, such that the Fermi energy can be located above the highest in-gap state, below the conduction part.

Summary

- Several new states appear both in the gap and within the conduction part when two apical vacancies are created.
- Two distinct pairs of degenerate states appear in the gap.
- The lowest pair of in-gap states is localized around the Titanium between the two vacancies. The orbital character is mainly d_{z^2}.
- The second pair has also strong d_{z^2} character. It is localized around the Titanium atom below the second vacancy and the Oxygen atom below.
- The bottom of the conduction band remains unchanged (slightly different localization).
- Other new states appear in the conduction band. These are t_{2g} states, mainly a combination of $d_{xz} - d_{yz}$ states.

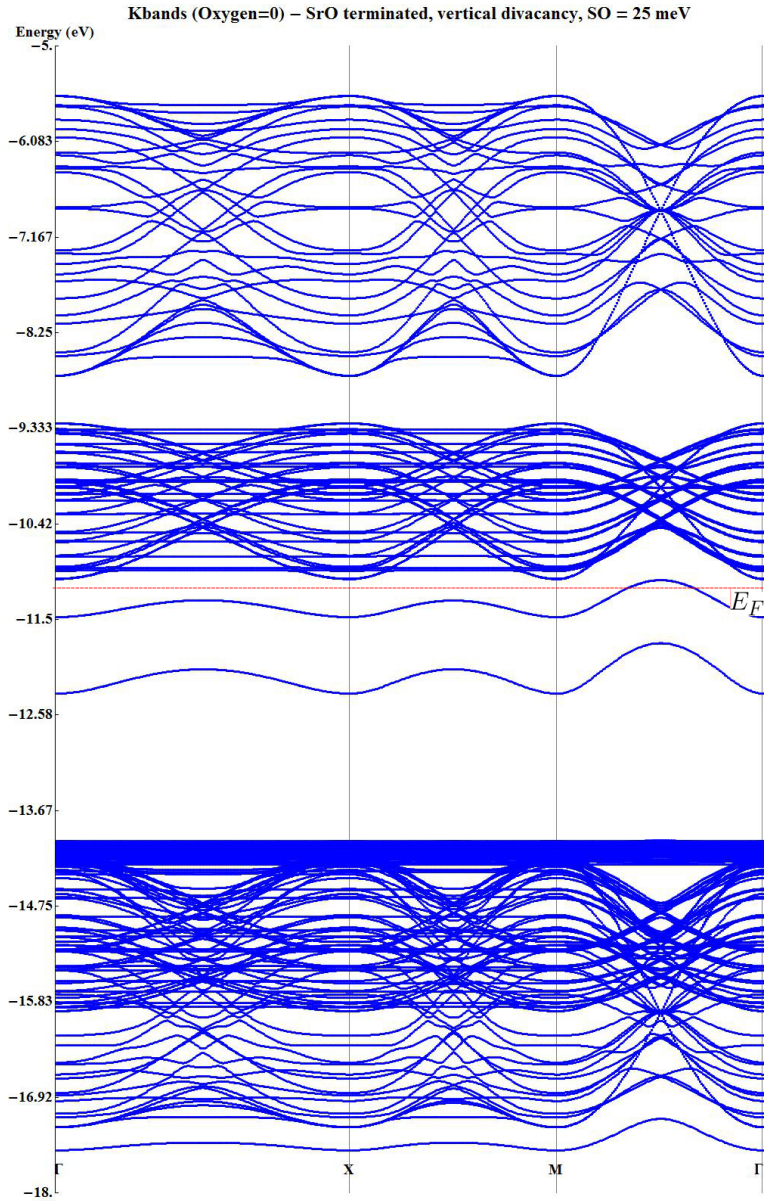

Figure 4.24: Band structure of the cluster with two vacancies. Two new in-gap bands appear, as well as new conduction states.

4.4 TiO_2-termination. No vacancies.

We have pointed out that the termination of the surface plays an important role in the band structure and electronic properties of this material. The SrO termination preserves the octahedral Oxygen environment of Titanium atoms. In the case of the TiO_2 termination, an entire surface of Oxygen atoms is removed, which is a large perturbation. Presumably a physical surface is a mixture of both types of terminations. Here I will show some of the properties of the electronic states found when we consider the TiO_2-termination before we introduce more Oxygen vacancies. In *appendix C* I will include different cases with single and double vacancies and we will compare the differences in the electronic structure.

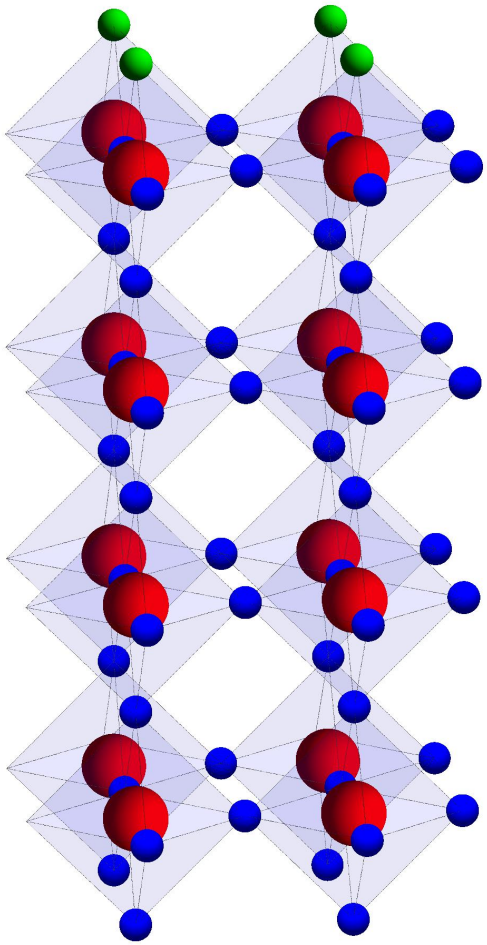

Figure 4.25: Four Oxygen vacancies need to be introduced in order to study the TiO_2 surface.

As we mentioned before, a particular feature of the TiO_2-terminated cluster is that it already has four vacancies (for the actual structure, we also remove Strontium atoms, which implies that, overall, one does not introduce charges in the system, whereas a normal vacancy would). Namely, the top four Oxygen atoms that formed the top SrO-layer have been removed. This is a significant perturbation from the standpoint of the chemical structure. It is unclear if the system does not reconstruct or strains. Thus, the TiO_2-terminated cluster is analogous to the SrO-terminated cluster in the presence of four apical Oxygen vacancies.

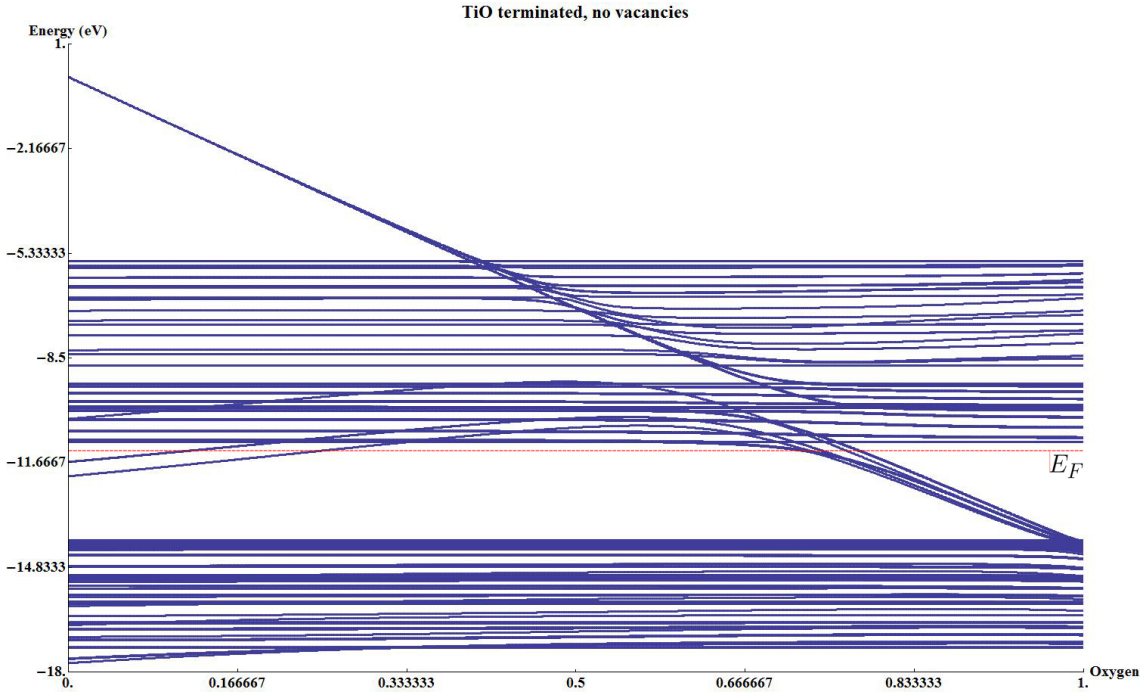

Figure 4.26: Electronic states at the Γ point when the top SrO layer is removed. On the right, the electronic states of the SrO -terminated cluster without vacancies. On the left, the electronic states when it is TiO_2-terminated.

Figures 4.26 and 4.27 show the electronic states at the Γ point before and after removing the top layer of Oxygen atoms. It is interesting to note that several states appear in the valence-conduction gap and also within the conduction part. This is in contradiction to what is found experimentally and to what DFT calculations show. These in-gap states should not appear for any kind of termination. There are several reasons why this is happening. One of them is the way we implement the crystal field. The on-site energies of the atomic orbitals depend on the relative position of the neighboring atoms. Removing a full layer of Oxygen atoms dramatically changes de crystal field felt by the Titanium atoms below due to relaxation effects. The numerical calculations need to be tuned to match this crystal field to what is shown in the literature. In any case, it is important to note that this calculation of the electronic structure without vacancies will be used as a benchmark in order to study the impact of Oxygen vacancies in the cluster. Below I will show the orbital and site character of all these states. These states will be found (in addition to others) when we include other vacancies, so it is important to *rule them out* when evaluating other configurations.

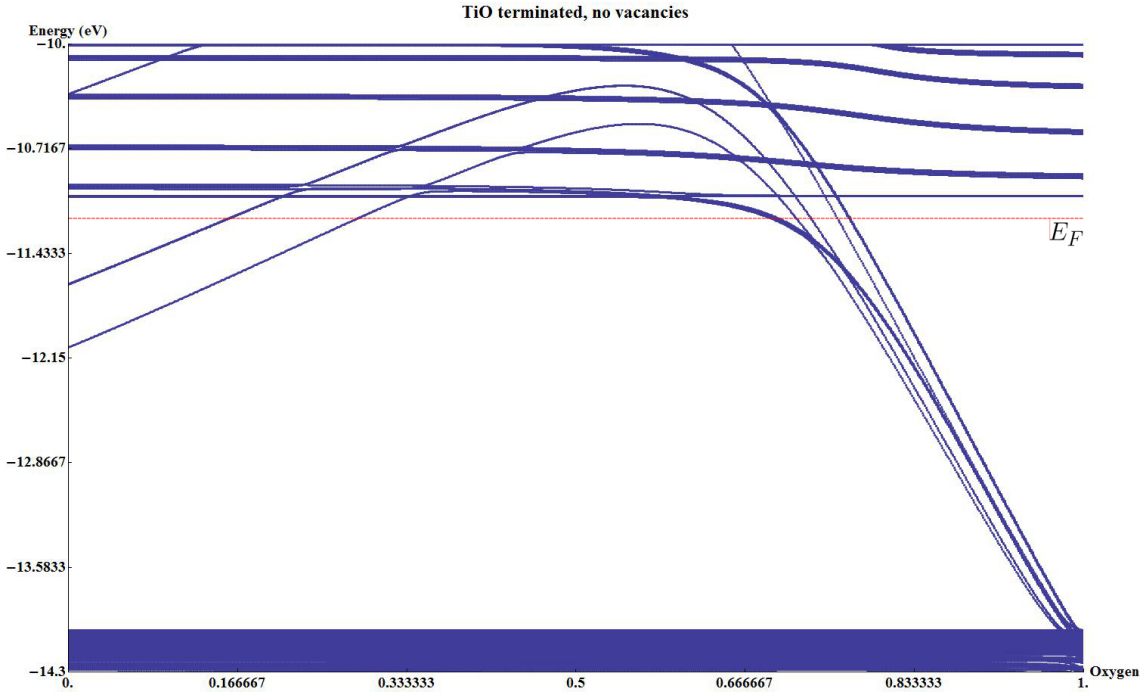

Figure 4.27: Electronic states at the Γ point when one Oxygen atom is removed. On the right, the electronic states when the Oxygen atom has not been removed. On the left, the electronic states when the Oxygen atom has been completely removed and the neighboring atoms have adapted to the new local crystal field.

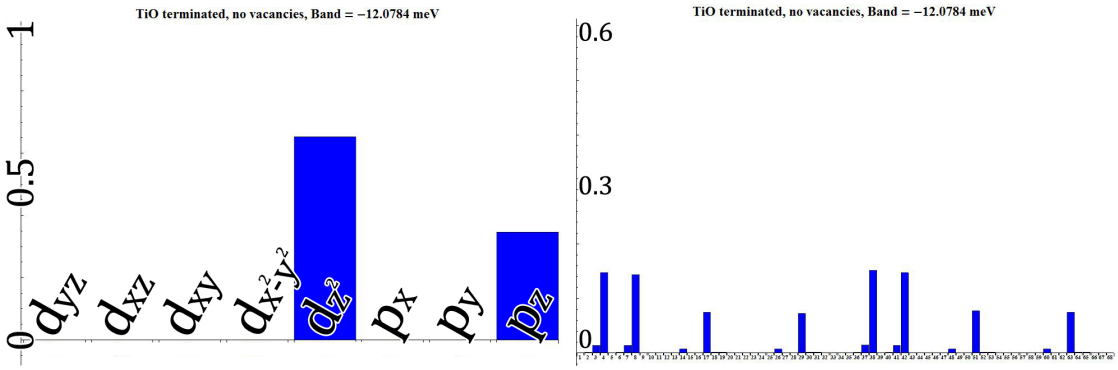

(a) Orbital (b) Sites

Figure 4.28: Orbital/site character of the first pair of degenerate in-gap states that appears when we remove the top SrO layer.

First we encounter a pair of degenerate states with d_{z^2}-p_z character localized around the Titanium atoms in the top layer and the Oxygen atoms below (Fig. 4.28). This histogram is similar to Figure 4.11b, where one apical vacancy was introduced in the top SrO-layer. We obtain similar states because we are doing something similar. We are introducing four similar vacancies in the top SrO-layer.

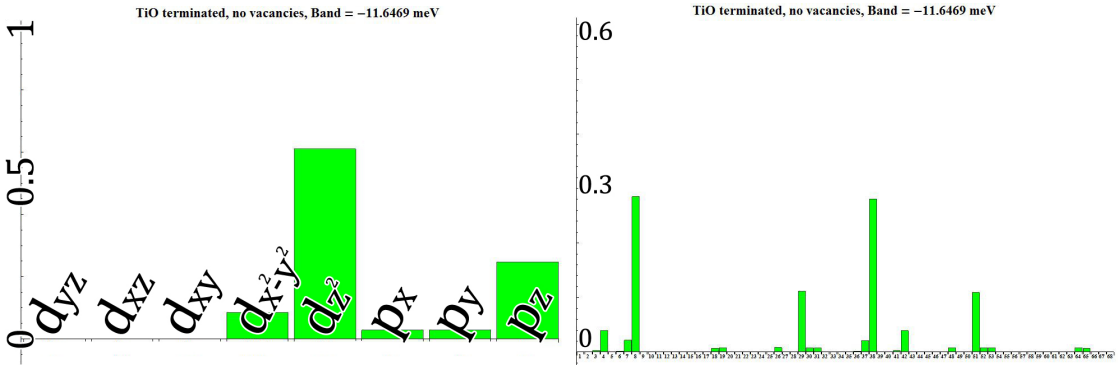

(a) Orbital (b) Sites

Figure 4.29: Orbital/site character of the second pair of in-gap states.

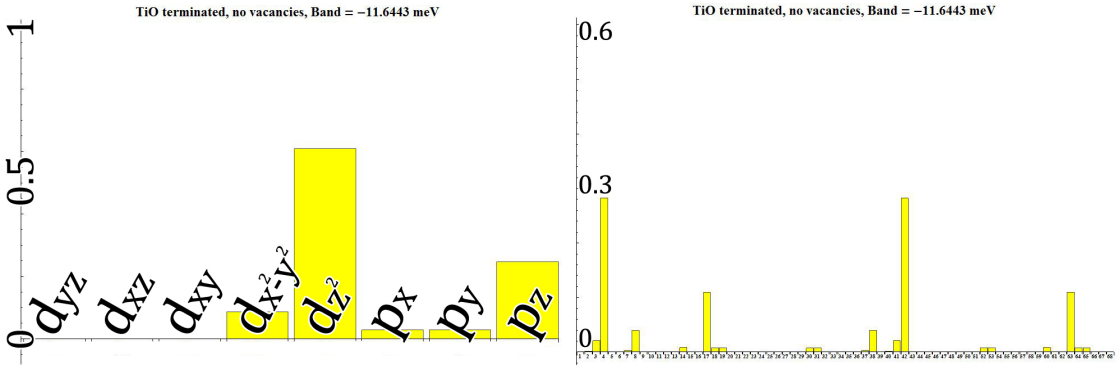

(a) Orbital (b) Sites

Figure 4.30: Orbital/site character of the third pair of in-gap states.

Next we find four degenerate states with similar characteristics. Figures 4.29 and 4.30 shows the histograms for one of these four states. The orbital character is the same, but the site-contribution is slightly different. In the first case, the state is localized around two of the top Titanium atoms (numbers 8 and 38). in the second case, the states are localized around Titanium atoms 4 and 42. So in the end the

full xy symmetry is recovered. There is a fourth pair of states that is created when we study the TiO_2-termination, but it falls higher in the conduction band.

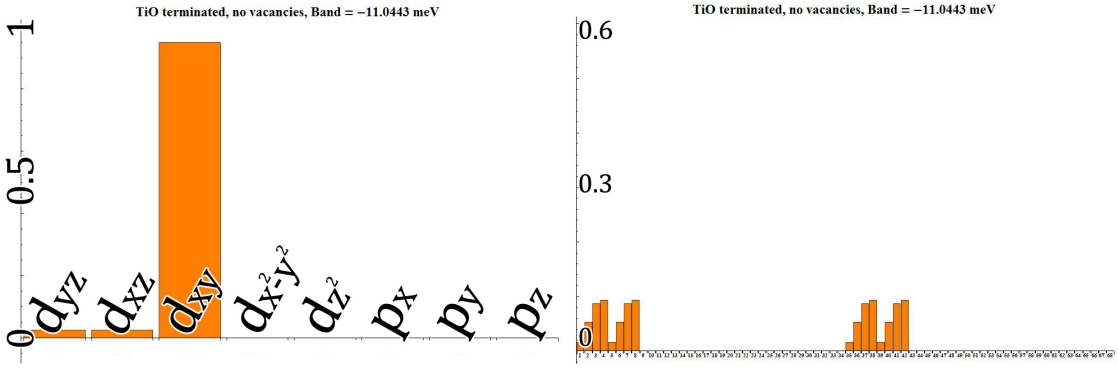

(a) Orbital (b) Sites

Figure 4.31: Orbital/site character of the bottom of the conduction band.

Finally we show the orbital character of the bottom of the conduction band. It has the usual d_{xy} character, this time localized close to the TiO_2 surface.

In Figure 4.32 we show the band structure along the Brillouin zone. We can see that the momentum-dependence of the in-gap states found when we chop the top SrO layer is different than that of the in-gap states found in the previous sections. This time, the states are part of the conduction band. As we mentioned before, these states should fall within the conduction part and they are not *truly* in-gap states. The crystal field of the cluster needs to be tuned so that these results match DFT calculations and experimental data.

Summary

- A TiO_2-terminated surface is a big perturbation to the cluster. The top SrO surface needs to be removed.
- In the absence of Oxygen vacancies, we recover the insulating band structure with a clear differentiation between the valence and conduction parts.
- The bottom of the conduction part is mainly d_{xy}.

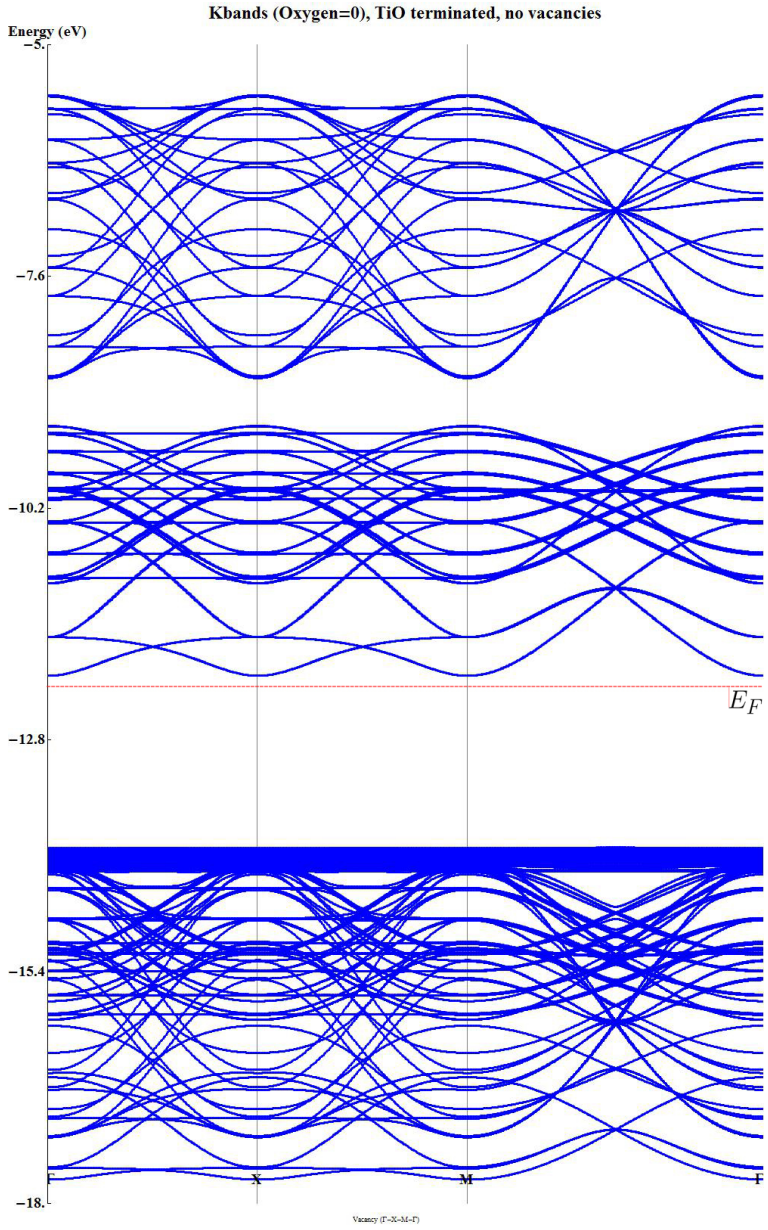

Figure 4.32: Energy bands of the TiO_2 terminated cluster in the absence of Oxygen vacancies.

4.5 TiO_2-termination. Two vertical vacancies.

In the previous section we showed the electronic properties of the TiO_2-terminated cluster in the absence of Oxygen vacancies. In this section we will introduce two apical vacancies vertically aligned in the lowest SrO subsurfaces. We will see that new in-gap states appear in addition to the ones found without defects. We will show the properties of these new states and we will see the differences in the band structure.

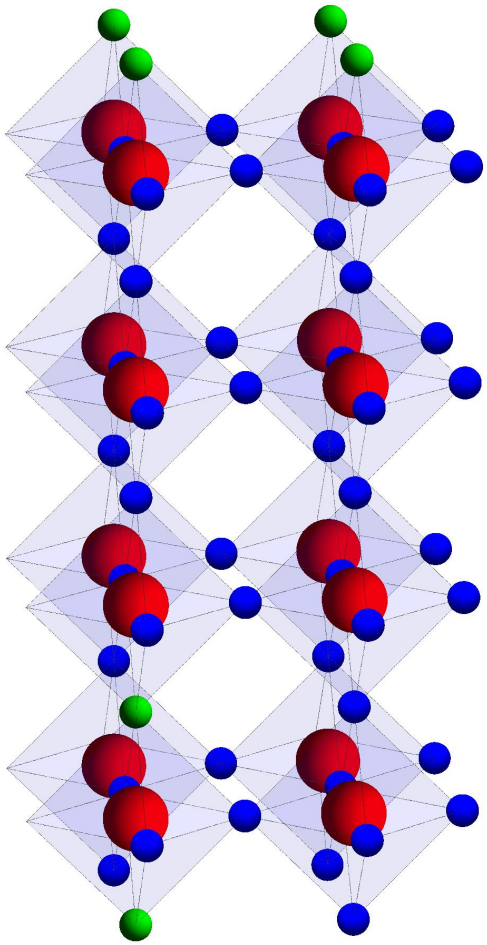

Figure 4.33: The TiO_2-terminated cluster with two Oxygen vacancies in the bottom SrO subsurfaces.

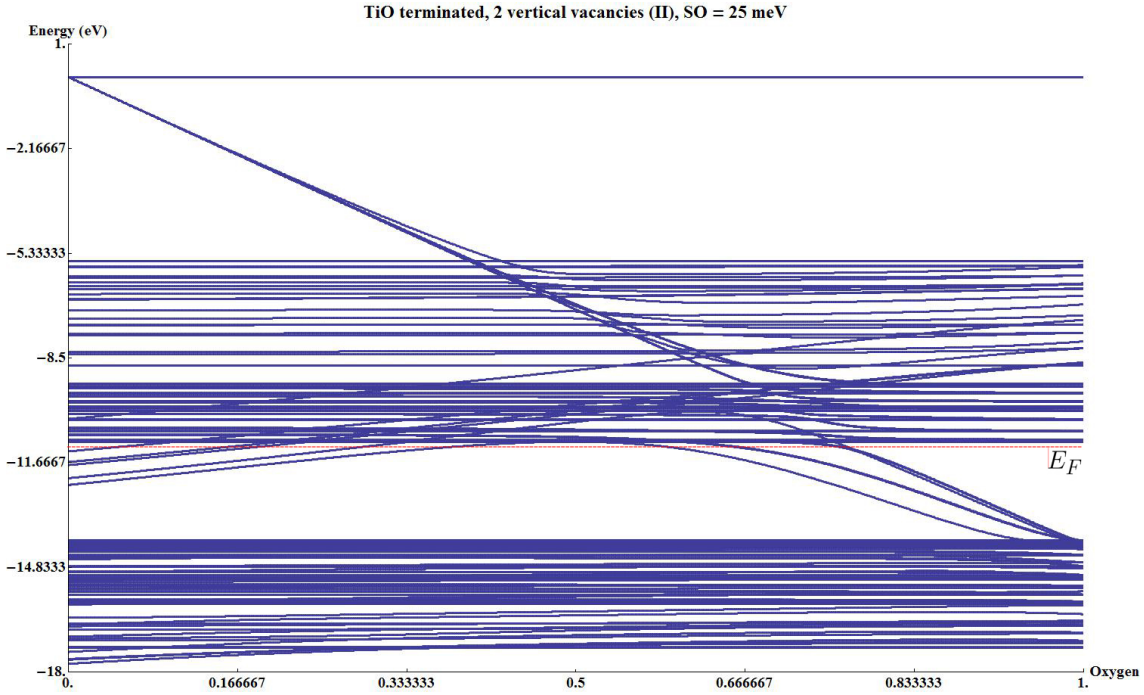

Figure 4.34: Electronic states at the Γ point when two Oxygen atoms vertically aligned are removed. On the right, the electronic states when the Oxygen atoms have not been removed. On the left, the electronic states when the Oxygen atoms have been completely removed and the neighboring atoms have adapted to the new local crystal field.

Figures 4.34 and 4.35 show the new electronic states that appear when we remove the two Oxygen vacancies in the SrO subsurfaces (in addition to the top Oxygen atoms to create the TiO_2 termination). We can clearly see that several in-gap states appear. Some of them are the same as those we found in the previous section. But others are new. It is important that we understand the properties of the new in-gap states.

The lowest new in-gap state is a d_{z^2} state localized around the Titanium atom between the two vacancies (Fig. 4.36). This state is similar to the one we found when we introduced two apical vacancies in the SrO-terminated cluster.

The next three pairs of states (Figures 4.37, 4.38 and 4.39) show the states that we already found in the absence of vacancies. These are the states that need to be tuned with the crystal field so that they rise to the conduction band, as DFT calculations and experiments show. Thus, these six states are not new in-gap states.

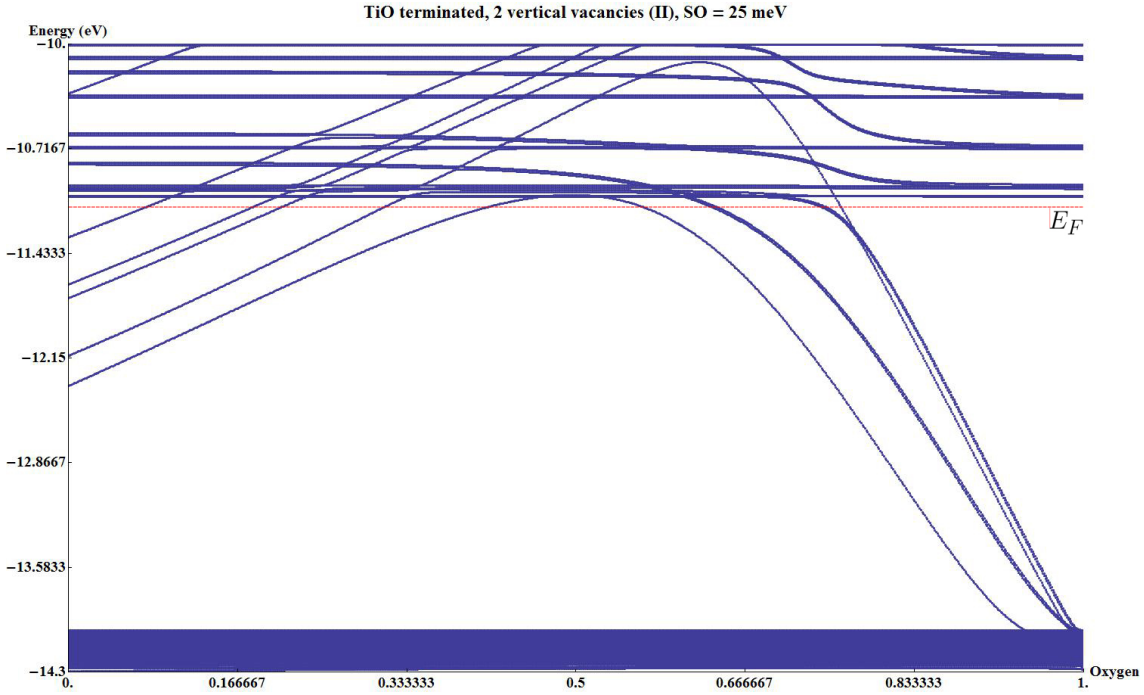

Figure 4.35: Electronic states at the Γ point when one Oxygen atom is removed. On the right, the electronic states when the Oxygen atom has not been removed. On the left, the electronic states when the Oxygen atom has been completely removed and the neighboring atoms have adapted to the new local crystal field.

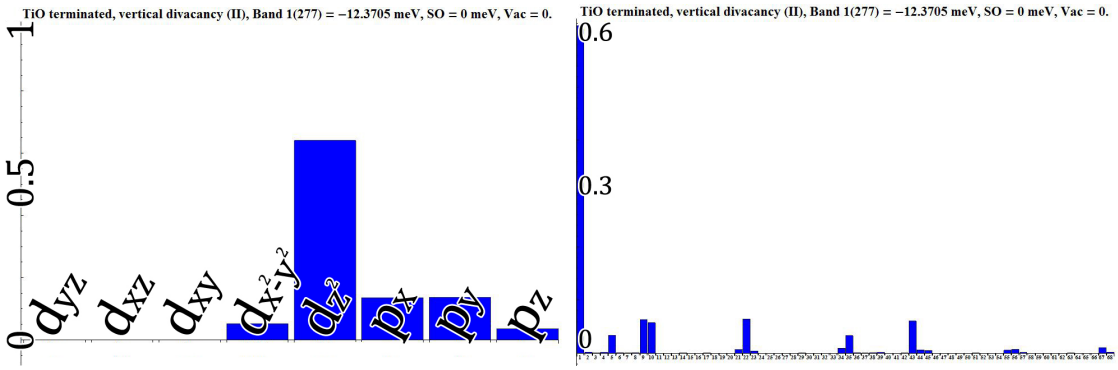

(a) Orbital (b) Sites

Figure 4.36: Orbital/site character of the first in-gap states. This state is generated by the vertical vacancies on the bottom of the slab.

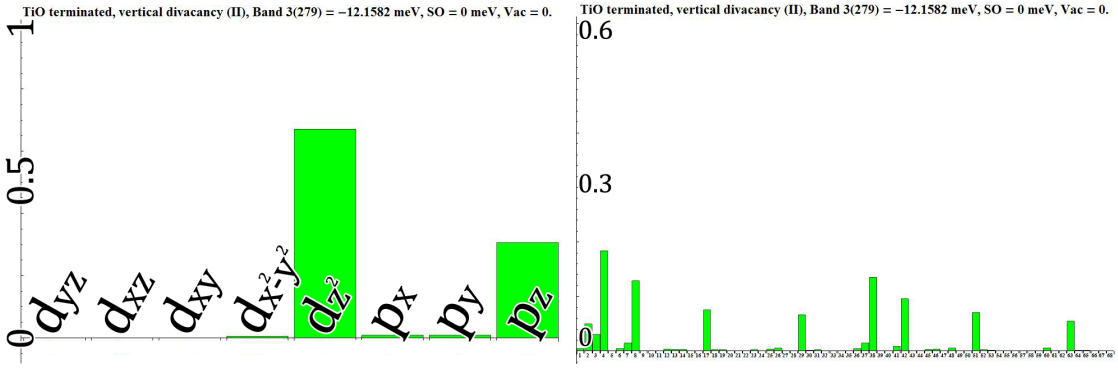

(a) Orbital (b) Sites

Figure 4.37: Orbital/site character of the second pair of in-gap states. This state was already present without the two vacancies (see previous section) and it is generated by the top TiO_2 surface.

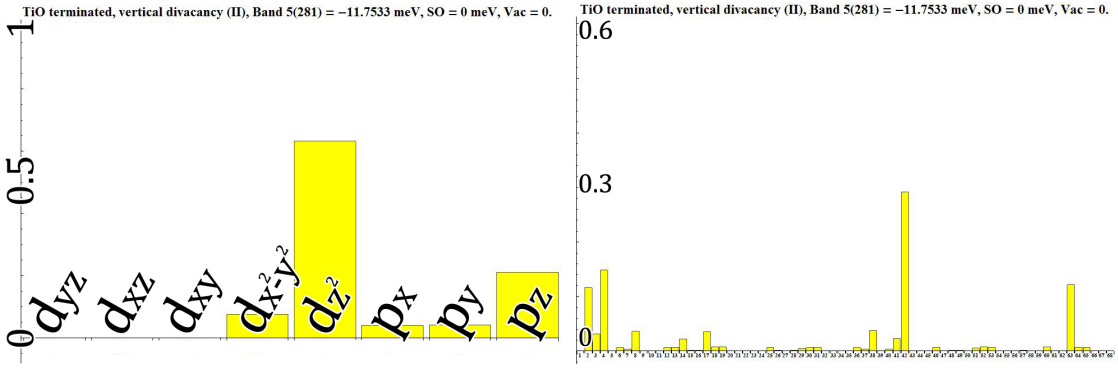

(a) Orbital (b) Sites

Figure 4.38: Orbital/site character of the third pair of in-gap states (generated by the top TiO_2 surface).

Figure 4.40 shows the second in-gap state that we would encounter due to the presence of the two Oxygen vacancies. As expected, it is a d_{z^2}-p_z state localized around the Titanium above the second vacancy and the neighboring Oxygen atom in the z axis. These results are very similar to those found when two vacancies vertically aligned were introduced in the SrO-terminated cluster.

Finally, we encounter the usual d_{xy} state at the bottom of the conduction band (Fig. 4.41).

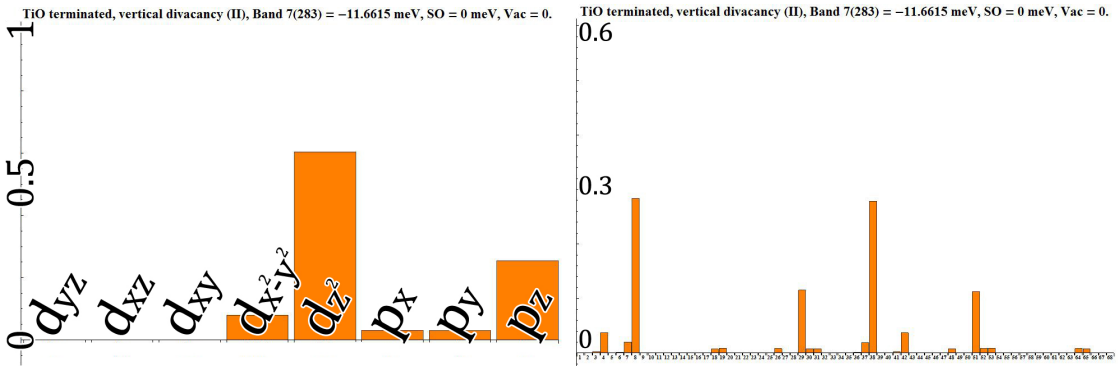

(a) Orbital (b) Sites

Figure 4.39: Orbital/site character of the fourth pair in-gap states (generated by the top TiO_2 surface).

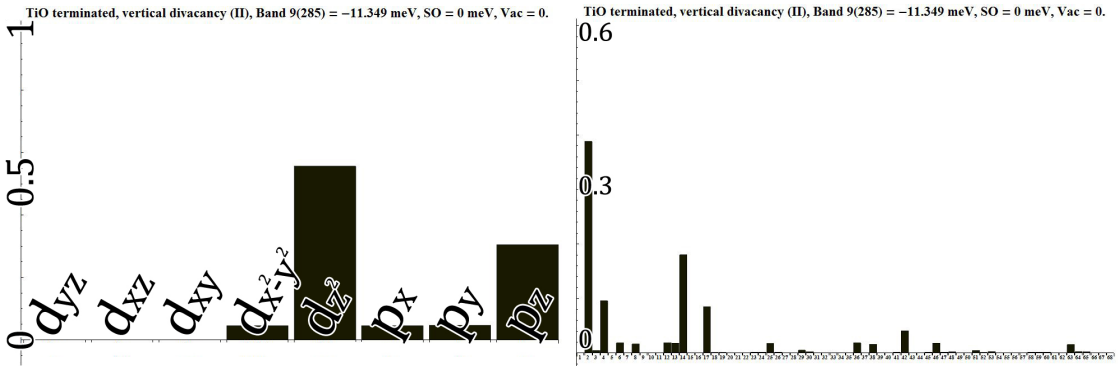

(a) Orbital (b) Sites

Figure 4.40: Orbital/site character of the fifth and last pair in-gap states. It is generated by the two vacancies vertically aligned.

When we plot the energy spectrum of this system along the Brillouin zone we can clearly see that there are two types of in-gap bands (Fig. 4.42). One type belongs to the conduction band, and these new bands are created by the four Oxygen vacancies that we need to implement in order to create a TiO_2 termination. The other type of bands are *truly* in-gap bands generated by the two vacancies introduced at the bottom of the slab.

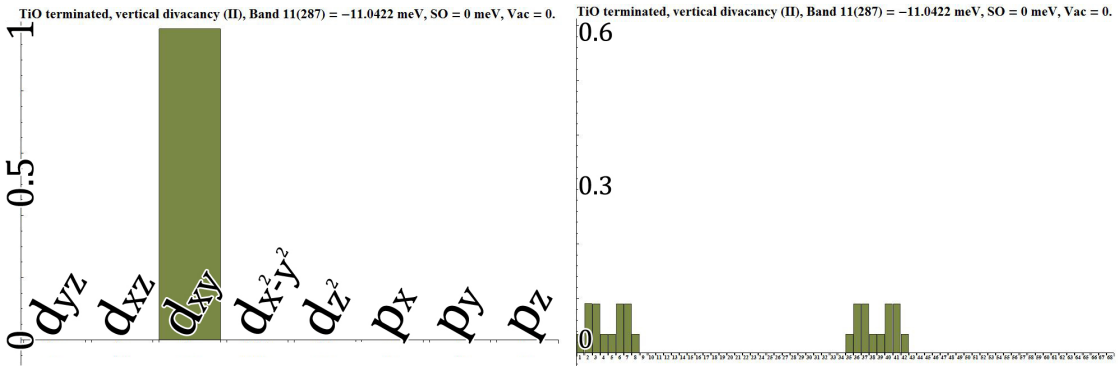

(a) Orbital (b) Sites

Figure 4.41: Orbital/site character of the bottom of the conduction band.

Summary

- Several new states appear when we include two vertical vacancies on the bottom of the cluster.
- We recover the same in-gap states/bands that we found in the TiO_2-terminated cluster in the absence of vacancies.
- We find two new pairs of states similar to the ones we found in the SrO-terminated cluster when two vacancies were vertically aligned.
- The bottom of the conduction band does not suffer major changes.

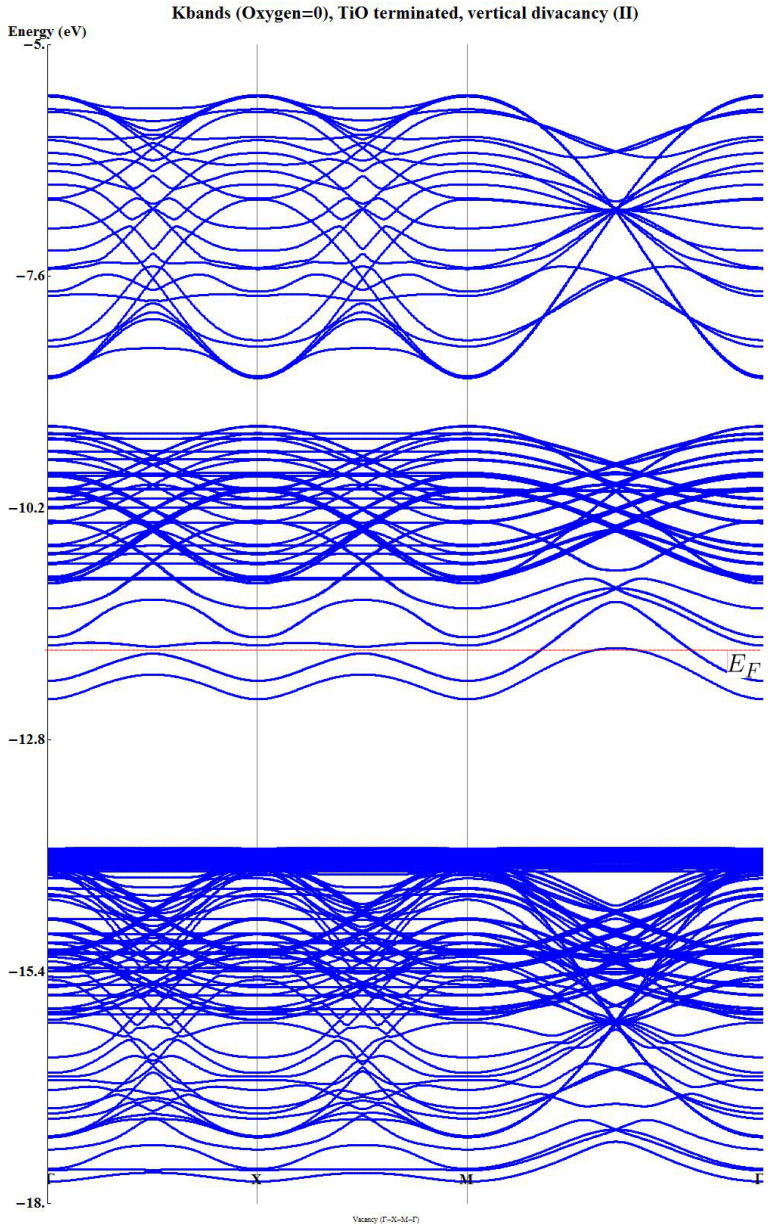

Figure 4.42: Energy bands of the TiO_2-terminated cluster with two vacancies vertically aligned. We can see some in-gap states that are generated by the presence of the two vacancies. The in-gap states generated by the *removal* of the top SrO layer are part of the conduction band.

5 Comparison with DFT

Our calculations need to be tuned so that our results are consistent with DTF calculations and experimental observations. Particularly we will compare our results with those found by Roser Valentí *et al.* [65, 66, 80].

Single vacancies

When we introduce one Oxygen vacancy in the cluster we find a new in-gap state in the band structure. Similar calculations [66, 65, 80] done in a stoichiometric 2x2x6 relaxed slab[3]suggest that this new state should be in the conduction part.

	Our calculations	DFT
One vacancy	One in-gap state is found. The orbital character of this in-gap state is d_{z^2}-p_z if the vacancy is on a SrO plane and $d_{x^2-y^2}$-$p_{x/y}$ if it is on a TiO_2 plane. The bottom of the conduction band has d_{xy} character.	No in-gap state is found. The energy of the electronic structure is lower when the vacancy is in the TiO_2 plane.
Fermi level	The electrons released by the Oxygen atom go to the in-gap state. Thus, the Fermi level is above this state and the conduction band has no electrons.	The Fermi level is in the conduction band. For the same oxygen-vacancy doping, TiO_2 terminated slabs lead to the occupation of more Ti d_{xy} bands than the SrO terminated slabs.

Table 2: Some differences between our calculations and DFT when one single vacancy is introduced in the slab.

[3]Structure relaxations were done by considering the Born-Oppenheimer procedure as implemented in the Vienna *ab initio* simulation package (VASP). The wave functions were represented using the projector augmented wave (PAW) method and they considered the LDA+U functional with $U = 5\ eV$ and $J = 0.64\ eV$ for the Ti $3d$ states in all the relaxations. The Brillouin zone was sampled with a k-mesh of (442) for the 2x2x4 slab. Based on the optimized structure, the electronic properties were calculated using the all-electron full potential local orbital (FPLO) method and they employed both the generalized gradient approximation (GGA)as well as the GGA+U approximation as exchange-correlation functionals within DFT

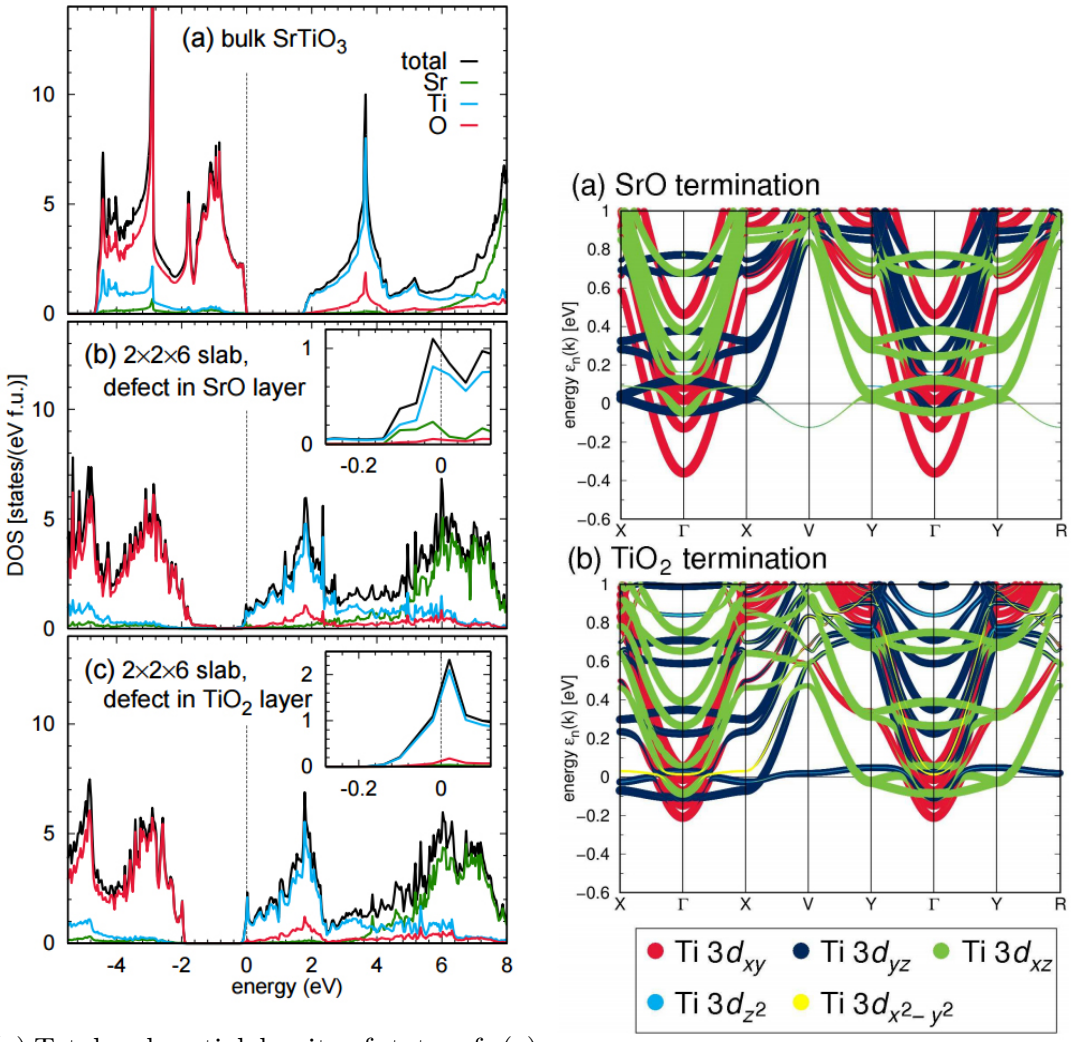

(a) Total and partial density of states of: (a) bulk STO; (b) 2x2x6 SrO-terminated slab with one vacancy in the top SrO layer; (c) 2x2x6 TiO_2-terminated slab with one vacancy in the top TiO_2 layer.

(b) Orbital character of the band structure of the 2x2x6 cluster with oxygen vacancy. (a) SrO termination; (b) TiO2 termination.

Figure 5.1: No in-gap states are found when one Oxygen vacancy is introduced [66].

Figure 5.1b shows the band structure of STO with one single vacancy. We can clearly see that there is no in-gap state. The fact that they do not seem to see an in-gap

state suggests that the vacancy is fully ionized. In the bulk (see Fig. 1.5) we see a *small* number of bands on the bottom of the conduction part. The perfect perovskite symmetry of the bulk is broken when we study slabs because The Titanium (and Oxygen) atoms are not equivalent any more. This is why we can see in Figures 5.1b and 4.7 how the electronic structure splits into a ladder of subbands.

In summary, we find that the main difference between our calculations and DFT is the existence of a new in-gap state. The energy of this state is very important and it affects the electronic properties of the structure. If it is below the conduction part, then there are no conducting electrons in the band structure, they are localized around the Titanium atoms neighboring the vacancy. If, as DFT suggests, this state merges into the conduction band, then we would find that the bottom of the conduction band is partically filled with electrons.

Double vacancies

In our calculations we seem to find a new pair of (degenerate) in-gap states for each Oxygen vacancy introduced in the cluster. Thus, when we include two vacancies we found two pairs of in-gap states. The orbital character of this states depends on the position of the vacancies. DFT calculations suggest that only one state can be found in-gap when two vacancies are present.

In [66, 65, 80] they study different configurations for two Oxygen vacancies within a 3x3x4 STO slab. Apparently, some of the energetically most favorable configurations are:

- Two vacancies aligned in the top TiO_2 plane (see page 138).
- Two vacancies non-aligned in the first TiO_2 plane (page 119).
- Two vertically aligned vacancies in the first two SrO planes (page 61).

One of the observations that we made is that when we introduce a vacancy in the SrO layer, we find new localized d_{z^2}-p_z states, whereas if the vacancy is in the TiO_2 layer these localized states are $d_{x^2-y^2}$-$p_{x/y}$. These observations are in agreement with DFT. However, LDA+U calculations suggest that when only one vacancy is present, the two electrons only contribute to the conduction band and no localized-in-gap states are found (Figure 5.1). As I mentioned before, we seem to find a new pair of (degenerate) in-gap states for each Oxygen vacancy introduced in the cluster. Figure 5.2 shows the density of states (and orbital distribution) when two vacancies

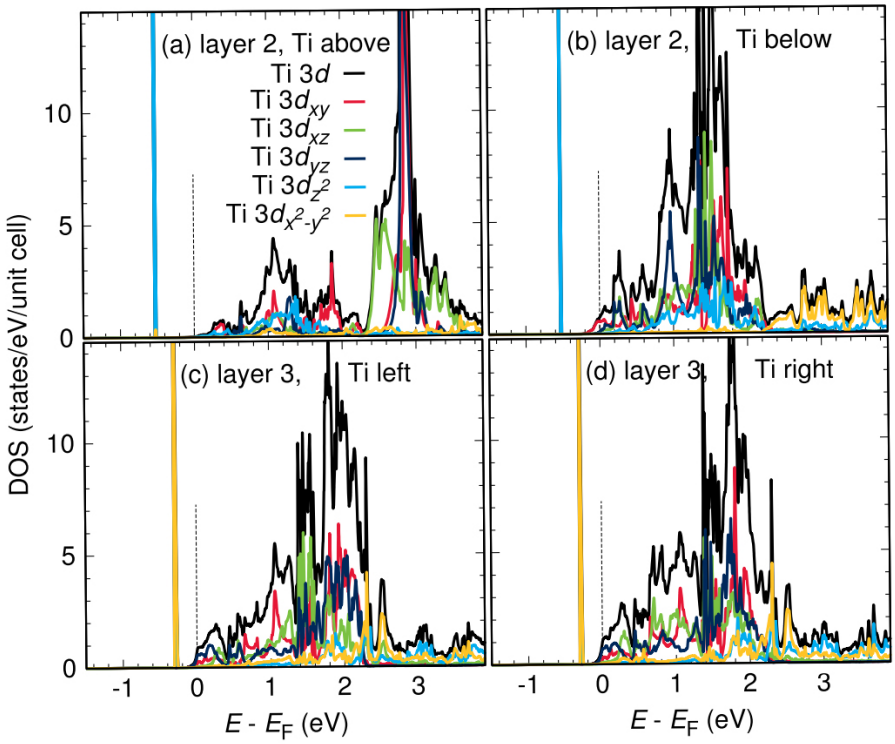

Figure 5.2: Partial densities of states for Titanium ions neighboring Oxygen vacancies. (a) and (b) vacancy is in the SrO plane. (c) and (d) in the TiO_2 plane [65].

are introduced ((a) and (b) vertically aligned, (c) and (d) horizontally aligned). It seems that only one pair of degenerate states is found (with the appropriate orbital distribution). DFT calculations suggest that in-gap states can be observed only if we cluster two (or more) vacancies in the cell. The reason for this disagreement might be that our new in-gap states are very low in energy.

Cyril Martins found similar results. He considered a TiO_2-terminated relaxed structure and performed DFT calculations using a GGA+U functional ($U = 5$, $J = 0.64$ eV). Figure 5.3 shows that for a divacancy column two new bands appear. Only one of them is in the gap, the second is above the bottom of the conduction band. Also, the fact that it is TiO_2-terminated does not provide extra in-gap bands. However, our study of the orbital and site character of the new states is consistent with these DFT calculations, and we have a better understanding of the origin of the new states generated by the Oxygen vacancies.

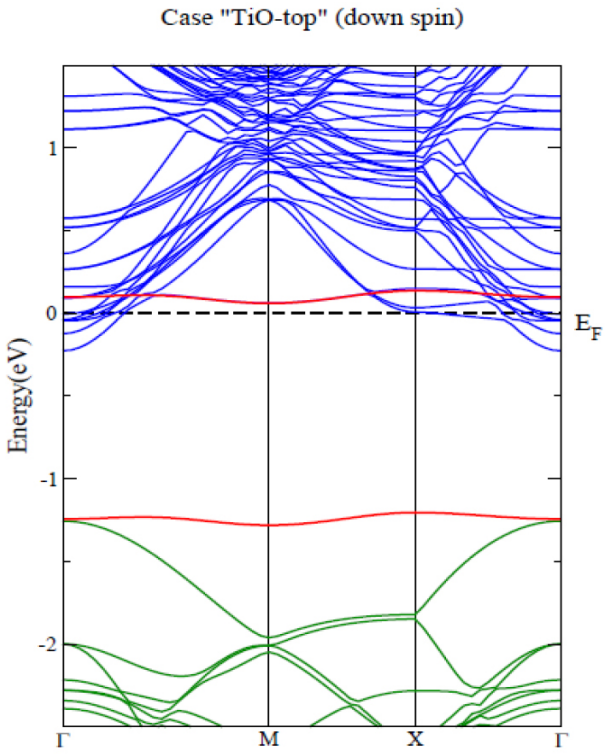

Figure 5.3: DFT calculations of a TiO_2-terminated 2x2x4 slab with an oxygen di-vacancy column. In red, Ti-d_{z^2} states. In blue Ti-t_{2g} states. In green O-p states.

Spin textures and magnetism

A particular phenomenon that can be observed in the surface of STO is the coexistence of superconductivity and magnetism. This coexistence could be explained by the presence of Oxygen vacancies. When we include configurations of two vacancies, we find an in-gap state (around 1 eV below the conduction part) that seems to give rise to localized magnetism. There are also other t_{2g} conduction states caused by the di-vacancy that appear to contribute to the (Rashba) spin texture. In Figure 5.2 we can appreciate a peak in the density of states below the Fermi energy. This might promote a magnetic stability, if, as Stoner criterion states, $Un(EF) = 1$ where $n(EF)$ is the number of electrons at the Fermi level. Essentially, the in-gap states (of e_g character) can be occupied by 0, 1 or 2 electrons. Magnetism would arise in the presence of a single electron. This is not the case with zero or two electrons unless

there are several e_g orbitals available to place the second electron. Due to Coulomb repulsion, the second electron could also be promoted to the conduction band (t_{2g} state), and it is this kind of itinerant carriers the responsible for producing Rashba spin-textures near the surface of $SrTiO_3$.

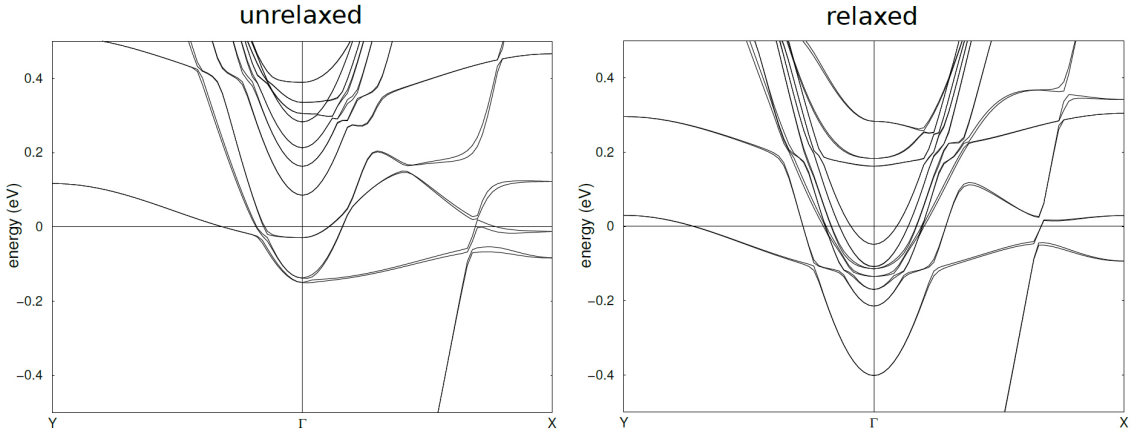

Figure 5.4: Nonmagnetic GGA+SO bandstructure for the unrelaxed (left) and relaxed (right) 1x1x6 slab.

Figure 5.4 shows the band structure of a 1x1x6 slab. When the slab is unrelaxed, the conduction electrons are very confined to the surface (around the Titanium atoms neighboring the Oxygen vacancies). When the slab is relaxed it suffers strong reconstruction and the electrons are redistributed over the whole slab. In this case, a few partially occupied d_{xy} bands can be observed at the Fermi surface.

Relativistic FPLO calculations of the 1x1x6 relaxed slab reveal the spin texture at the $k_z = 0$ Fermi surface, as shown in Figure 5.5. It seems that the bands split a few meV in the nonmagnetic case. The spins are almost fully polarized parallel to the $k_z = 0$ surface, pointing in opposite directions to each other in the split bands. It is because inversion symmetry at the surface of $SrTiO_3$ has been broken that we can see the manifestation of the relativistic Rashba effect. Conversely, when a magnetic moment along **z** is included, the Rashba winding is still present but weaker compared to the nonmagnetic case. The in-plane spin component is now rather small and the splitting of the bands is much larger. Despite the revealing results of these calculations, one has to be aware that they might be over amplified due to the fact that periodicity in the planar direction leads to configurations with $1D$ rows of vacancies. This is a very high density of vacancies per unit cell. The density of states in the presence of $1D$ rows of vacancies diverges at the edges of the

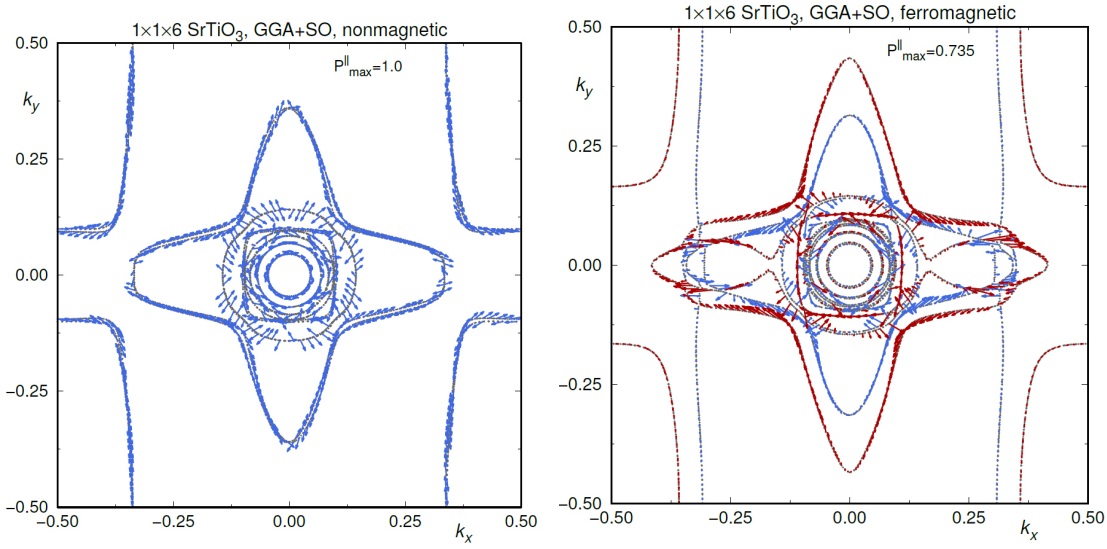

(a) Nonmagnetic. (b) Ferromagnetic $\mathbf{m} \parallel \mathbf{z}$.

Figure 5.5: Spin-texture in GGA+SO for the relaxed slab.

Brillouin zone, such that Stoner criterion is fulfilled even for very small U. This is the reason why itinerant magnetism is exaggerated. Analogous calculations[4]have been done on bigger slabs [80]. Figures 5.6(a)-(c) show the electronic structure and the spin textures of a 2x2x4 slab with one single vacancy. Figures 5.6(d)-(f) show the case where two Oxygen vacancies are introduced in the TiO surface of a 3x3x4 slab. Again, since the vacancies break of inversion symmetry at the surface of $SrTiO_3$, they find clear signatures of the relativistic Rashba effect.

[4]Generalized-gradient approximation (GGA) in the Dudarev GGA+U scheme for the relaxations and electronic structure. Analysis using the all-electron full-potential local orbital (FPLO) method and GGA+U functional. Checks were also performed with the all-electron full-potential linearized augmented plane wave method as implemented in Wien2k. Spin textures for the various slabs were obtained from full relativistic calculations in FPLO (GGA+SO+U) with a newly implemented subroutine. (a) and (d) are based on nonmagnetic GGA+SO+U calculations with $U = 5\ eV$, and (b), (c), (e), (f) are obtained from ferromagnetic GGA+SO+U calculations with $\mathbf{m} \parallel \mathbf{z}$. Reciprocal space units are 0.402 $\mathring{A}^{-}1$ for (a) and (c), 0.268 $\mathring{A}^{-}1$ for (d) and (f).

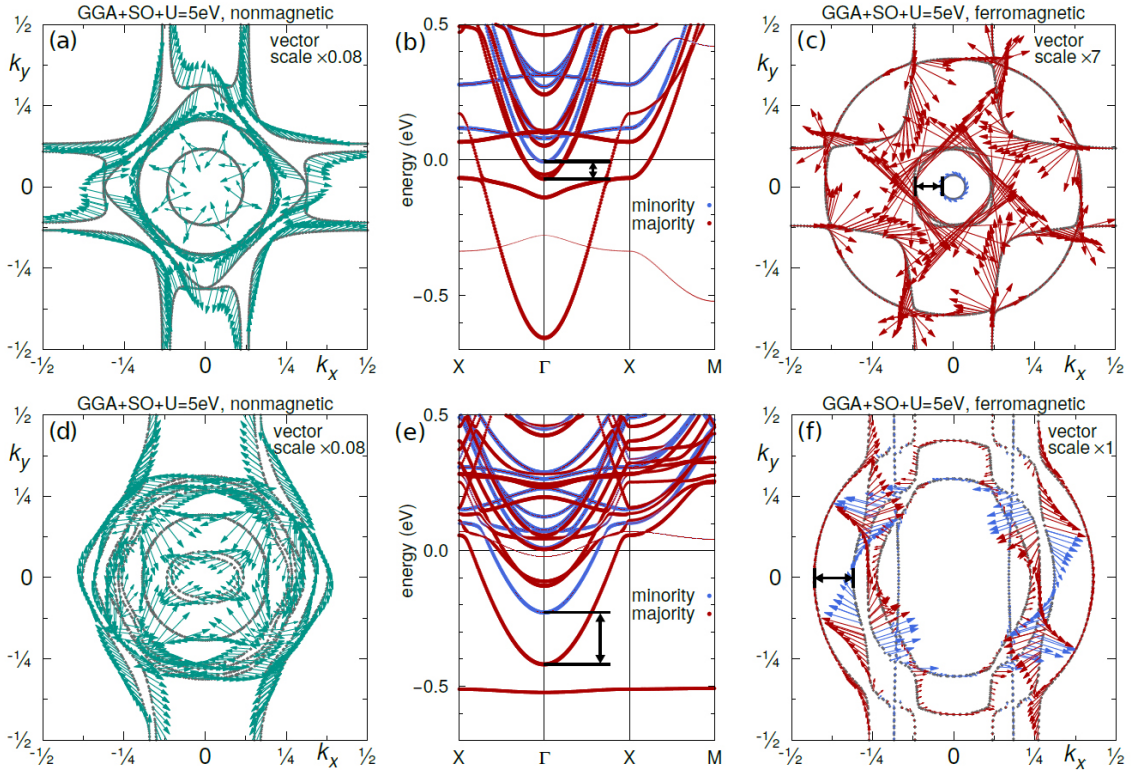

Figure 5.6: (a)-(c) Spin-textures and spin-polarized bandstructures for a relaxed 2x2x4 slab with one Oxygen vacancy. (d)-(f) -for a relaxed 3x3x4 slab with an Oxygen divacancy in the surface TiO2 layer.

In-gap states and number of vacancies

In the previous chapter we showed some of the results that we obtain when we introduce one or two vacancies in the 2x2x4 cluster. In general, we found that the number of in-gap states is proportional to the number of Oxygen vacancies present. There are no in-gap states if we do not remove any Oxygen atom. When we intrroduce a single vacancy, we find a pair of degenerate in-gap states appearing below the conduction band. For two vacancies, we find two pairs of degenerate states.

Figure 5.7 shows the band structure of the 2x2x4 slab using DFT. When a single vacancy is introduced, a new in-gap state of e_g character is formed below the Fermi level. Most of the charge originated by this vacancy is shared by the d_{xy} orbitals of the Titanium atoms in the surface. For two vacancies, another in-gap state appears.

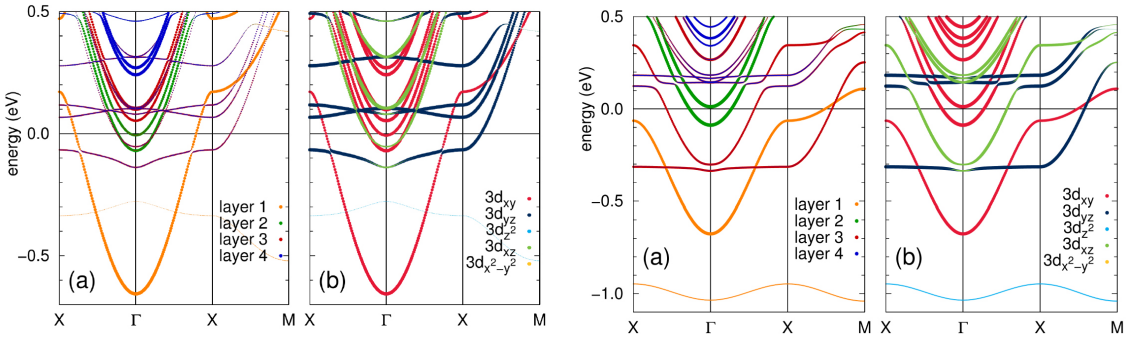

(a) One single Oxygen vacancy. (b) Two Oxygen vacancies at the surface.

Figure 5.7: Ferromagnetic GGA+SO+U Ti 3*d* bandstructure for the relaxed 2x2x4 slab with Oxygen vacancies with a $\mathbf{m} \parallel \mathbf{z}$ setup. (a) Layer resolved. (b) Orbitally resolved. Note that the thickness of lines is proportional to the strength of the 3*d* character on the bands.

We conclude that there is an agreement between the tight-binding calculations and DFT regarding the appearance of in-gap states as a function of number of vacancies. There is also a perfect agreement about their orbital character. However, there is still a disagreement regarding the exact energies of these in-gap states with respect to the conduction band. Particularly, tight binding calculations need to be tuned better to check wether the new states appear in-gap or *within* the conduction band, as DFT suggests.

6 Conclusions

In this thesis we have studied the electronic properties of the surface of Strontium Titanate. $SrTiO_3$ flat surfaces can be used for a vast range of applications, making this material very attractive for technical applications, and it is important to understand its properties.

This work can be divided into two parts. in the first part we studied the (111) bilayer of this material and investigate the existence of topological states (chapter 2). The second part focuses on the examination of the electronic structure of the (001) surface of $SrTiO_3$ and the role that Oxygen vacancies play (chapters 3 and 4).

In chapter 2 we analyzed the (111) bilayer of transition metal oxides (TMOs) and we found that interesting properties arose when we limit the system in size. Namely, several states appear that are localized on the edge of the system (at least in some parts of the Brillouin zone) and their parity is not the same everywhere. This is a hint that topological states will arise. A topological metallic state can be created both in $SrTiO_3$ and $KTaO_3$ (111) through doping, to bring the Fermi level to the M points, but the relevant energies make it easier in the case of $KTaO_3$.

The second backbone of this work is the study of the properties of the electronic structure for different terminations and Oxygen vacancies of $SrTiO_3$. In general, we know that there is a gap separating the top of the valence band ($2p$ Oxygen states) and the bottom of the conduction band ($3d$ Titanium states), and that the Fermi level is within the gap. One or more Oxygen vacancies would dope the system with extra electrons (each Oxygen vacancy providing two electrons). These electrons would then occupy the Ti 3d states at the bottom of the conduction band.

First let us compare one of the two terminations when we remove one Oxygen atom, the SrO terminated surface. A surface Oxygen would be one of the apical Oxygen atoms in the SrO layer, as shown in Figure 4.8. The removal of this atom affects mainly the Titanium atom below the vacancy, and the occupied Ti $3d$ orbital shows strong d_{z^2}character. In this case the local symmetry around the Oxygen vacancy has fourfold rotation on the top SrO layer. In principle one might think that, since the e_g states are higher in energy compare with the t_{2g} triplet in the perovskite structure, then the extra electron(s) introduced into the system would occupy the t_{2g} states of the Ti atom. However, as we showed in previous chapters, this is not actually the case. The reason is that when we remove the apical Oxygen of the first (001) SrO

layer, then we remove the rather strong $pd\sigma$ hybridization between the p_z-d_{z^2}orbitals, pulling the $3d_{z^2}$ state back into the gap.

We will now turn to the TiO_2 terminated surface. Lets consider that the Oxygen to be removed is one between two Titanium atoms, as shown in Figure 6.37. This time the local symmetry around the vacancy has twofold rotation on the TiO_2 plane that has the vacancy. Before removing the Oxygen atom, the degenerate d_{yz} and d_{xz} states are lower in energy compared to the d_{xy} states because there is an Oxygen atom missing in the z-direction (i.e., the SrO layer that does not exist anymore). If we now decide to remove the Oxygen atom between two Titanium atoms (in the x axis), then the d_{xz} and $d_{x^2-y^2}$ are further pulled down in energy due to the loss of $pd\pi$ and $pd\sigma$ hybridizations, respectively.

We find that Oxygen vacancies create both in-gap states and new conduction states. Usually the in-gap states have e_g character and are localized around the position of the vacancy. The conduction states are mostly t_{2g} states that are also in the vicinity of the vacancy.

To conclude this work, I will make some comments regarding the $LaAlO_3/SrTiO_3$ interface. As stated in the introduction of this thesis, $SrTiO_3$ has two possible terminations in the (001) direction. If we look at the $LaAlO_3/SrTiO_3$ interface, this means that if the termination of the $SrTiO_3$ crystal is a TiO_2 plane, then $LaAlO_3$ will continue with a LaO plane. Conversely, it will continue with a AlO_2 plane when $SrTiO_3$ terminates with a SrO plane. We know that both TiO_2 and SrO are neutral, meanwhile AlO_2 and LaO are negatively and positively charged, respectively. This means that the alternance of a neutral and a charged plane will induce a dipole in the interface, producing an electric potential that diverges with thickness. This is known as the polar catastrophe.

The polar catastrophe can be avoided. The divergence of the electric potential can be removed if half an electron (per unit cell) is added to the TiO layer in the interface (obtaining a conducting n-doped interface). If the interface is AlO_2/SrO, then we need to introduce Oxygen vacancies on the SrO layer (leading to an insulating p-doped interface with some atomic reconstruction).

Several experiments and DFT calculations reveal the coexistence of ferromagnetism and superconductivity at the LAO/STO interface. It has been demonstrated that the ferromagnetic property of the 2DEG comes from the existence of Oxygen vacancies in the LAO or STO layers [30].

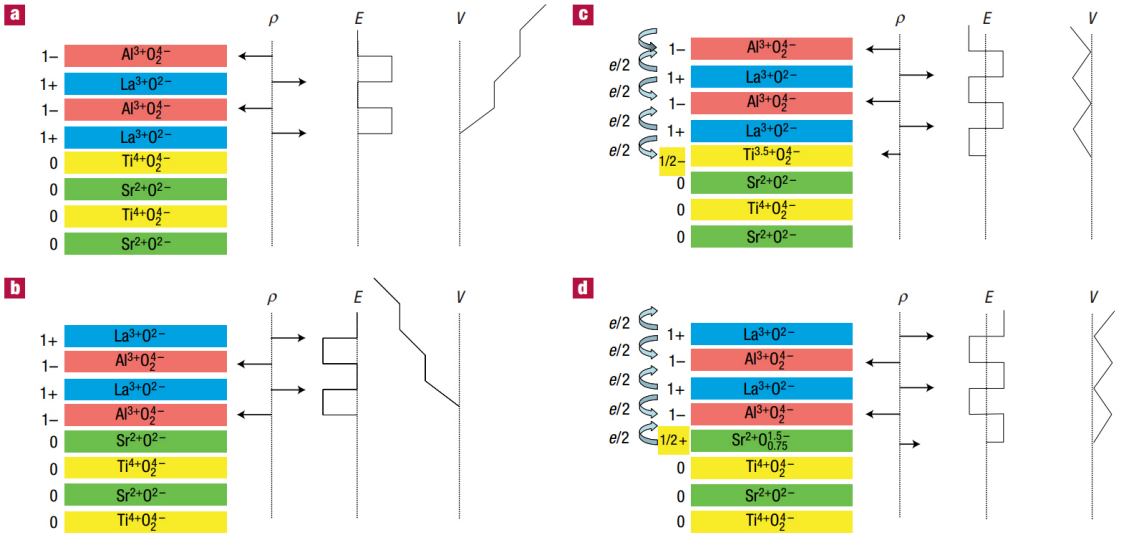

Figure 6.1: Image taken from [56]. The polar catastrophe illustrated for atomically abrupt (001) interfaces between $LaAlO_3$ and $SrTiO_3$. a) If the interface plane is $AlO_2/LaO/TiO_2$, this produces a non-negative electric eld (E), leading in turn to an electric potential (V) that diverges with thickness. b) If the interface is instead placed at the $AlO_2/SrO/TiO_2$ plane, the potential diverges negatively. c) The divergence catastrophe at the $AlO_2/LaO/TiO_2$ interface can be avoided if half an electron is added to the last TiO layer. d) The divergence for the $AlO_2/SrO/TiO_2$ interface can also be avoided by removing half an electron from the SrO plane in the form of Oxygen vacancies.

6.1 Further work

The results shown in this work have been calculated using the $2 \times 2 \times 4$ cell without distortions. We are aware that both ferroelectric and antiferrodistortive distortions modify the band structure and properties of the electronic states. Even though we have some data showing this phenomenon, this study is preliminary, and a more exhaustive research is needed in order to fully understand how important these distortions are and how critical is their impact on the electronic properties of the $SrTiO_3$ surface.

Even though the nature of the in-gap and conduction states is clear, we need to review our model of the crystal field and our numerical parameters so that we can recreate better experimental and DFT results. It looks like the single band found in

the presence of one single vacancy should fall within the conduction band instead of the top of the gap. Also, all the states that appear due to the *removal* of the top SrO layer should fall within the conduction part as well. We should only see in-gap states when two (or more) vacancies are introduced in the system. At least this is what DFT calculations show.

A complete study on the magnetic properties and spin textures (Rashba) of this system is also missing. There are already several DFT studies that report the existence of bound states below the conduction band and of magnetism when one or more Oxygen vacancies are introduced in the $SrTiO_3$ structure. These phenomena can be studied if we include local correlation effects in our model.

Appendix

A- Slater-Koster interactions

The Slater-Koster rules can be used to calculate the *hopping amplitude* when an electron located in a particular orbital jumps to another orbital located at a different position. Particularly, we are interested in the interaction between $2p$ and $3d$ orbitals (see chapter 1.2) [8].

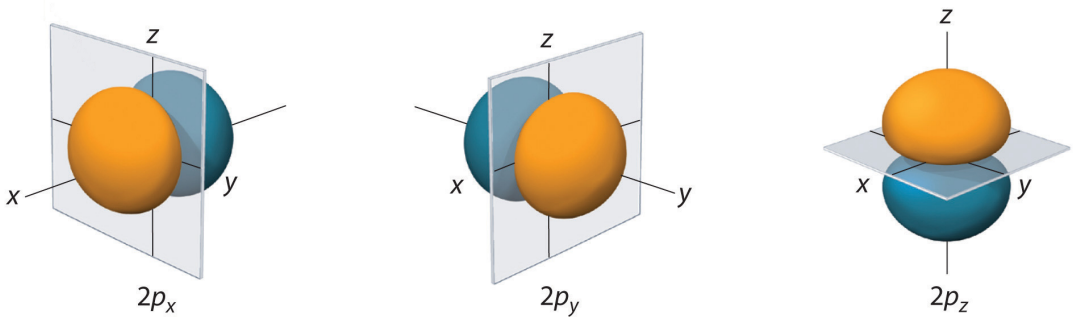

Figure 6.2: Spatial representation of the three $2p$ orbitals.

It is important to determine all the interatomic matrix elements between $2p$ and $3d$ orbitals. We will assume that the electron jumps from orbital orb_a located at position $\vec{v}_a$ to another orbital orb_b located at position $\vec{v}_b$. In this case the matrix element would be proportional to the following integral:

$$t_{ab} \sim \int_{vol.} \Psi_a^{\dagger}(\mathbf{r} - \mathbf{v}_a) H \Psi_b(\mathbf{r} - \mathbf{v}_b) dv \tag{2}$$

Computing this integral is not an easy task. In order to simplify things we will assume that the first orbital is at the origin of coordinates and that the second orbital is somewhere on one of the conventional x-y-z axis. The Hamiltonian can be replaced by a potential that is then symmetric in the directions orthogonal to such axis. We will not compute the full integral, we will just evaluate whether it is zero or has another value. The mathematical form of the $2p$ and $3d$ orbitals is given in Table 5. An easy way to evaluate integral (2) is to remove the radial part of the

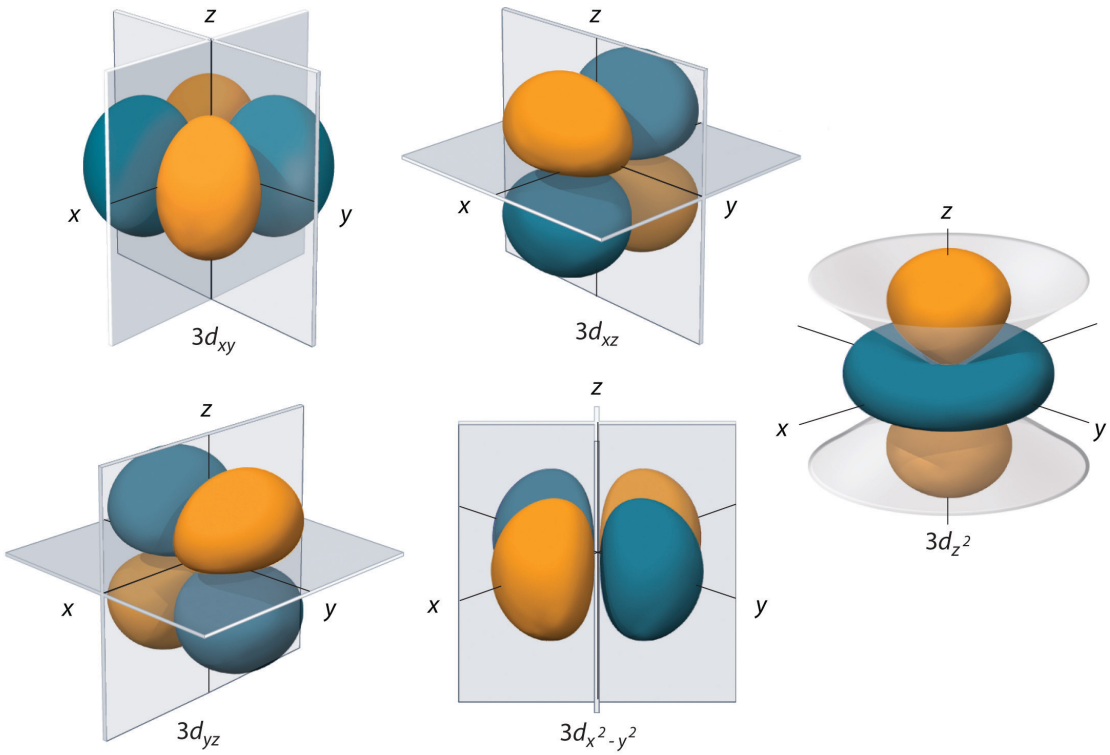

Figure 6.3: Spatial representation of the five $3d$ orbitals.

wave equations and to pull out the constants. Thus, the wave functions that we will use to compute the integral can be found in Table 3.

$2p$ orbitals	$3d$ orbitals
$\Psi_{p_x} = x$	$\Psi_{d_{xy}} = xy$
$\Psi_{p_y} = y$	$\Psi_{d_{xz}} = xz$
$\Psi_{p_z} = z$	$\Psi_{d_{yz}} = yz$
	$\Psi_{d_{x^2-y^2}} = \frac{x^2-y^2}{2}$
	$\Psi_{d_{z^2}} = \frac{2z^2-x^2-y^2}{2\sqrt{3}}$

Table 3: Simplified orbital equations of the $2p$ and $3d$ orbitals

p-p interactions

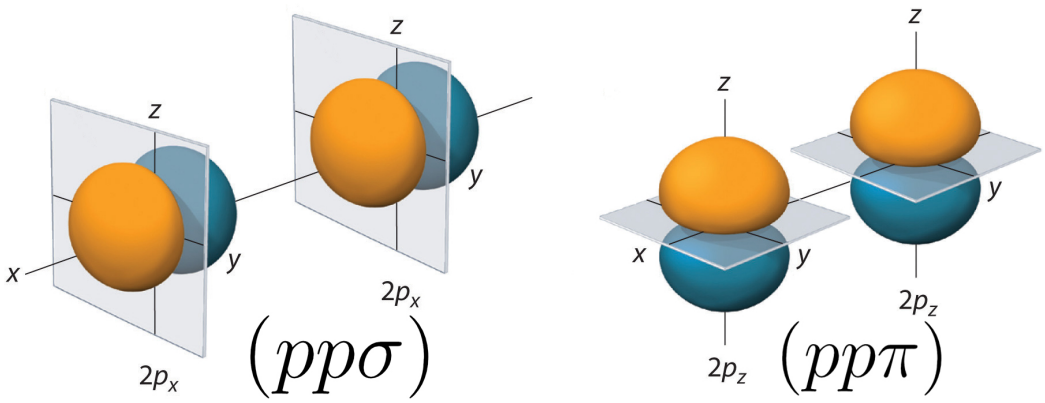

(a) (b)

Figure 6.4: Any interaction between two p orbitals can be expressed as a linear combination of these two simplified interactions.

We will consider that the two p-orbitals are aligned in the x axis. Figure 6.4 illustrates the two possible configurations where the integral (2) does not vanish with two $2p$ orbitals. It is easy to see that any configuration that involves two different p orbitals would vanish because of the odd parity of the product $\Psi_a^\dagger \Psi_b$. The integral for the p_x-p_x case would have the form $\int_{vol.} x^2 V(x) dv$ that, in principle, is non-zero. We will define this integral as $pp\sigma$, a constant. Similarly, the p_y-p_y and p_z-p_z cases would lead to $\int_{vol.} y^2 V(x) dv$ and $\int_{vol.} z^2 V(x) dv$, respectively. These integrals have the same value because of the y-z symmetry when the two orbitals are aligned in the x axis. We define the value of these two integrals as $pp\pi$.

Thus, we only need two constants ($pp\sigma$ and $pp\pi$) to calculate any possible interaction between two arbitrary p-orbitals. If the orbitals are not aligned along the x axis (which is usually the case), we can always consider a new coordinate system where the new x' axis is the line connecting both orbitals (see *Transformation of coordinates* at the end of the section), then rewrite the *old* orbitals as a linear combination of the p orbitals in the *new* coordinate system and then calculate the interaction amplitude between these *new* orbitals aligned in the x' axis.

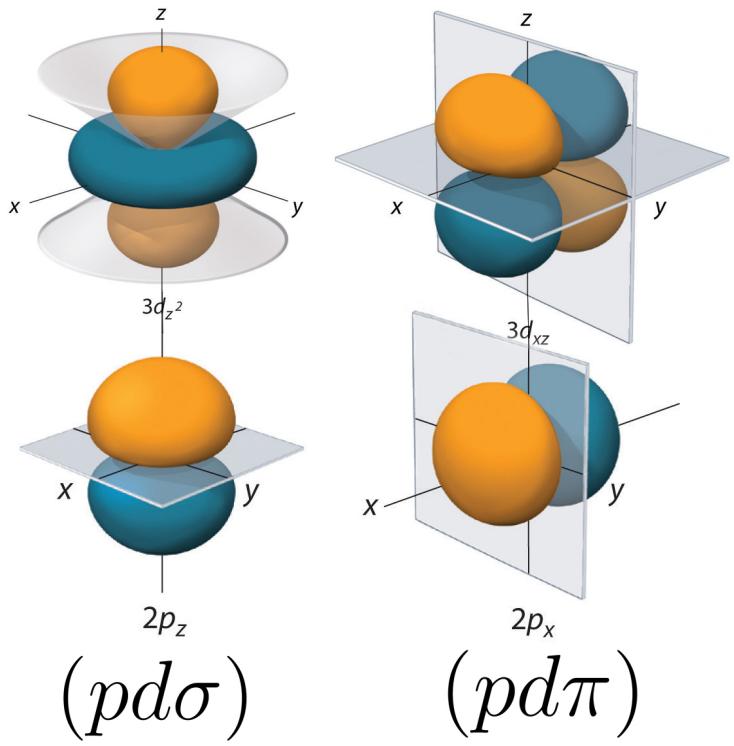

(a) (b)

Figure 6.5: Any interaction between a p orbital and a d orbital can be expressed as a linear combination of these two simplified interactions.

p-d interactions

This time, for convenience, we consider the two orbitals aligned along the z axis. Figure 6.5 illustrates two possible configurations where the integral (2) does not vanish with one $2p$ orbital and one $3d$ orbital. For convenience, we define the integral for the p_z-d_{z^2} case as a constant named $pd\sigma$. This integral would have the form $\int_{vol.} z(2z^2 - x^2 - y^2)V(z)dv$ that, in principle, is non-zero. We also define the integral involving the p_x-d_{xz} orbitals as a constant named $pd\pi$, having the form $\int_{vol.} zx^2V(z)dv$.

It is easy to see that the integral becomes zero if the interaction is between a p_x orbital and a $d_{z^2}/d_{x^2-y^2}$ (odd parity in the x direction) or between p_x and d_{xy}/d_{yz} (odd parity in the y direction). Since the two orbitals are aligned in the z-direction, the same results apply when we consider interactions involving the p_y orbital.

It is also easy to see that the integral becomes zero when p_z interacts with $d_{xy}/d_{xz}/d_{yz}$ due to the odd parity in the x and/or y directions. The only integral that needs to be analyzed is the one involving p_z and $d_{x^2-y^2}$. This integral, $\int_{vol.} z(x^2-y^2)V(z)dv$, is also zero because, even though is it even in the x-y directions, the integral taken along the x direction cancels the one taken along the y direction due to the symmetry of the $d_{x^2-y^2}$ orbital.

Thus, we only need two constants ($pd\sigma$ and $pd\pi$) to calculate any possible interaction between two arbitrary p and d-orbitals. Again, if the orbitals are not aligned along the z axis, we can always consider a new coordinate system where the new z' axis is the line connecting both orbitals, then we can rewrite the *old* orbitals as a linear combination of the p and d orbitals in the *new* coordinate system and then calculate the interaction amplitude between these *new* orbitals aligned in the z' axis.

d-d interactions

Let us consider again that the two $3d$ orbitals are aligned along the z direction. It is easy to see that the interaction of two different t_{2g} orbitals would cancel the integral (2) due to the odd parity of either x or y or both. If we combine two d_{xy} orbitals then (2) would become $\int_{vol.} x^2y^2V(z)dv$, and we can define the value of this integral as $dd\delta$. A combination of two d_{yz} orbitals would give $\int_{vol.} y^2z^2V(z)dv$. The value of this integral is different because the potential depends on the z coordinate. The value of this integral is defined as $dd\pi$. We obtain a similar result when we combine two d_{xz} orbitals. Integral (2) becomes zero when we mix a t_{2g} with an e_g because it will become odd in either x or y. Thus, we only need to investigate interactions between two e_g orbitals. If we combine two d_{z^2} orbitals (2) becomes proportional to $\int_{vol.}(2z^2-x^2-y^2)^2V(z)dv$ and it does not vanish. We define the value of this integral as $dd\sigma$. The interaction between d_{z^2} and $d_{x^2-y^2}$ is zero because the integral taken in the x direction would cancel the one taken in the y direction. We only need to investigate the interaction between two $d_{x^2-y^2}$ orbitals. This interaction is analogous the interaction between two d_{xy} orbitals and we obtain again $dd\delta$.

Transformation of coordinates

We have seen that the interaction between any two orbitals aligned along the x or the z axis can be expressed as a linear combination of other interactions that we

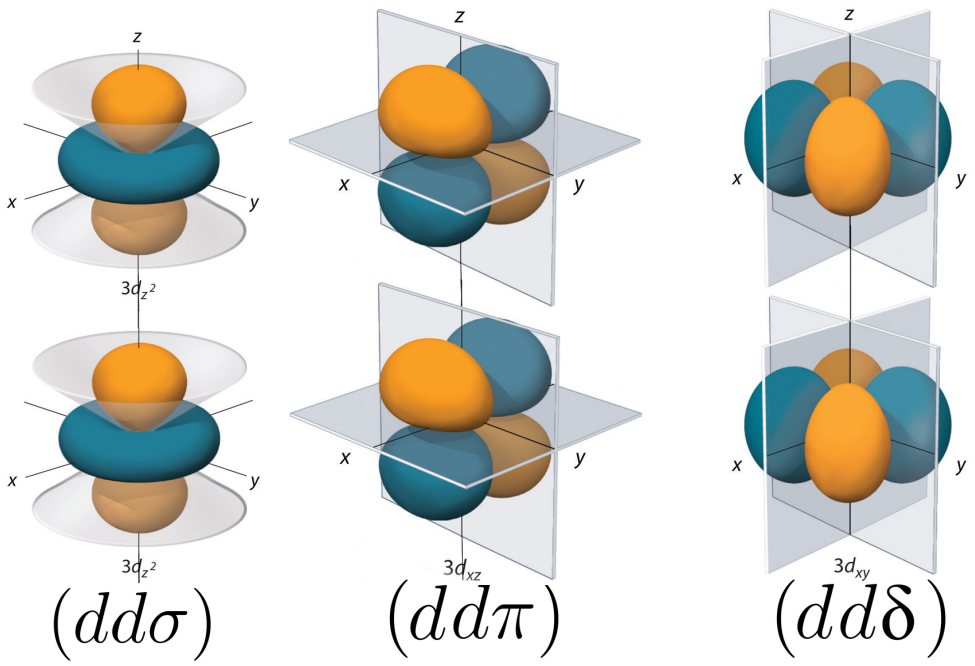

(a) (b) (c)

Figure 6.6: Any interaction between two d orbitals can be expressed as a linear combination of these three simplified interactions.

already know. Thus, the general idea to calculate the interaction of any two orbitals whose relative position is arbitrary is the following:

- We want to calculate the interaction amplitude between two orbitals located at arbitrary positions.
- We consider that the first orbital is located at the origin of coordinates. The second orbital is located at an arbitrary position defined by the cosines of the angles formed by the line connecting both orbitals and the (x, y, z) axis, respectively. That is, a position defined by the three numbers $(l = cos(\theta_x), m = ccos(\theta_y), n = cos(\theta_z))$.
- We define a new coordinate system where both orbitals are aligned along a particular axis (usually the new x' or z' axis).
- We rewrite the orbitals in the new coordinate system doing a transformation of coordinates. Thus, any particular orbital can be expressed as a linear com-

bination of the orbitals in the new coordinate system.

- We express the interaction between the two linear combinations of orbitals as a sum of interactions between single orbitals aligned in a particular axis.
- We use the constants defined in this chapter in order to calculate th interaction term.

If we follow the previous steps, we can calculate the interaction between any two orbitals as a function of l, m and n. Table 4 shows the interaction amplitudes for all the possible pairs of orbitals.

Table 4: Interaction amplitudes for different pair of orbitals

$p_x - p_x$	$(1-l^2)(pp\pi) + l^2(pp\sigma)$
$p_x - p_y$	$-lm(pp\pi) + lm(pp\sigma)$
$p_x - p_z$	$-ln(pp\pi) + ln(pp\sigma)$
$p_y - p_y$	$(1-m^2)(pp\pi) + m^2(pp\sigma)$
$p_y - p_z$	$-mn(pp\pi) + mn(pp\sigma)$
$p_z - p_z$	$(l^2+m^2)(pp\pi) + (1-l^2-m^2)(pp\sigma)$
$d_{xy} - p_x$	$m(1-2l^2)(pd\pi) + \sqrt{3}l^2m(pd\sigma)$
$d_{xz} - p_x$	$n(1-2l^2)(pd\pi) + \sqrt{3}l^2n(pd\sigma)$
$d_{yz} - p_x$	$-2lmn(pd\pi) + \sqrt{3}lmn(pd\sigma)$
$d_{x^2-y^2} - p_x$	$(1-l^3+lm^2)(pd\pi) + \frac{\sqrt{3}}{2}l(l^2-m^2)(pd\sigma)$
$d_{z^2} - p_x$	$\sqrt{3}n(l^2+m^2)(pd\pi) - \frac{l}{2}(-2+3l^2+3m^2)(pd\sigma)$
$d_{xy} - p_y$	$l(1-2m^2)(pd\pi) + \sqrt{3}lm^2(pd\sigma)$
$d_{xz} - p_y$	$-2lmn(pd\pi) + \sqrt{3}lmn(pd\sigma)$
$d_{yz} - p_y$	$n(1-2m^2)(pd\pi) + \sqrt{3}m^2n(pd\sigma)$
$d_{x^2-y^2} - p_y$	$m(1-l^2+m^2)(pd\pi) + \frac{\sqrt{3}}{2}m(l^2-m^2)(pd\sigma)$
$d_{z^2} - p_y$	$\sqrt{3}m(-1+l^2+m^2)(pd\pi) - \frac{m}{2}(-2+3l^2+3m^2)(pd\sigma)$
$d_{xy} - p_z$	$-2lmn(pd\pi) + \sqrt{3}lmn(pd\sigma)$
$d_{xz} - p_z$	$l(-1+2l^2+2m^2)(pd\pi) - \sqrt{3}l(-1+l^2+m^2)(pd\sigma)$
$d_{yz} - p_z$	$m(-1+2l^2+2m^2)(pd\pi) - \sqrt{3}m(-1+l^2+m^2)(pd\sigma)$
$d_{x^2-y^2} - p_z$	$n(-l^2+m^2)(pd\pi) + \frac{\sqrt{3}}{2}n(l^2-m^2)(pd\sigma)$
$d_{z^2} - p_z$	$\sqrt{3}n(l^2+m^2)(pd\pi) - \frac{n}{2}(-2+3l^2+3m^2)(pd\sigma)$

Further explanations on how to compute this table can be found in *J. C. Slater and G. F. Koster. Simplified LCAO Method for the Periodic Potential Problem* [4].

B- Atomic orbitals and spin-orbit coupling

A free electron with spin $\vec{s}$ and momentum $\vec{k}$ that moves under the influence of an electric field along the z direction can be described with the Rashba Hamiltonian:

$$H_R \sim (\hat{z} \times \hbar\vec{k})\vec{s} \tag{3}$$

The Rashba interaction terms are the ones responsible for the lifting of the spin-degeneracy in two-dimensional electron systems. The microscopic origin of this effect is the spin-orbit coupling. This effect can be described as

$$H_{SOC} \sim (\vec{\nabla}V \times \vec{p})\vec{s} \tag{4}$$

where V is the crystal potential and $\vec{p}$ is the momentum of the electron. It is quite easy to see that one recovers the Rashba Hamiltonian making use of the fact that an electric field can be expressed is terms of the gradient of a potential. This expression can be simplified a bit when the potential is spherically symmetric (usually it is the nucleus of the atom the one that contributes most to the potential gradient). In this case the spin-orbit coupling Hamiltonian reads

$$H_{SOC} \sim \frac{1}{r}\frac{dV(r)}{dr}\mathbf{L} \cdot \mathbf{s} \tag{5}$$

Equation (5) describes the coupling of the angular momentum of an electron and its spin. We can consider the potential contribution to be constant in the vicinity of a particular atom. We can also make use of the ladder operators: $L_x = \frac{L_+ + L_-}{2}$ $L_y = \frac{L_+ - L_-}{2i}$ $S_x = \frac{S_+ + S_-}{2}$ $S_y = \frac{S_+ - S_-}{2i}$ so that the final form of the Hamiltonian becomes

$$H_{SOC} = \lambda\mathbf{L} \cdot \mathbf{S} = \lambda(L_x S_x + L_y S_y + L_z S_z) = \frac{\lambda}{2}(L_+ S_- + L_- S_+ + 2L_z S_z) \tag{6}$$

where λ is the spin-orbit coupling constant.

In chapter 1.2 it was mentioned that the electron configurations of Titanium and Oxygen are [Ar] $3d^2$ $4s^2$ and [He] $2s^2$ $2p^4$, respectively. The electrons of the outer shells belong then to $3d$ and $2p$ orbitals. Thus, we need to know the mathematical description of these orbitals in order to calculate the spin-orbit Hamiltonian. The

equation of the $2p$ and $3d$ atomic orbitals are given in Table 5, as a function of the spatial coordinates.

$2p$ orbitals	$3d$ orbitals
$\Psi_{p_x} = R_{2p}\sqrt{\frac{3}{4\pi}}\frac{x}{r}$	$\Psi_{d_{xy}} = R_{3d}\sqrt{\frac{60}{16\pi}}\frac{xy}{r^2}$
$\Psi_{p_y} = R_{2p}\sqrt{\frac{3}{4\pi}}\frac{y}{r}$	$\Psi_{d_{xz}} = R_{3d}\sqrt{\frac{60}{16\pi}}\frac{xz}{r^2}$
$\Psi_{p_z} = R_{2p}\sqrt{\frac{3}{4\pi}}\frac{z}{r}$	$\Psi_{d_{yz}} = R_{3d}\sqrt{\frac{60}{16\pi}}\frac{yz}{r^2}$
	$\Psi_{d_{x^2-y^2}} = R_{3d}\sqrt{\frac{15}{16\pi}}\frac{x^2-y^2}{r^2}$
	$\Psi_{d_{z^2}} = R_{3d}\sqrt{\frac{5}{16\pi}}\frac{2z^2-x^2-y^2}{r^2}$
$R_{2p} = \frac{1}{2\sqrt{6}}\rho Z^{3/2}e^{-\rho/2}$	$R_{3d} = \frac{1}{9\sqrt{30}}\rho^2 Z^{3/2}e^{-\rho/2}$

Table 5: Orbital equations of the $2p$ and $3d$ orbitals. r is the radius expressed in atomic units, Z is effective nuclear charge for a particular orbital in that atom and $\rho = \frac{2Zr}{n}$ where n is the principal quantum number (2 for the $2p$ orbitals and 3 for the $3d$ orbitals).

The evaluation of the Hamiltonian using the orbital equations of Table 5 is nontrivial. It is much easier to express these equations as functions of the spherical harmonics and a radial term. We show this dependence in Table 6 (we do not include the radial term because it is not affected by the spin-orbit Hamiltonian).

$2p$ orbitals	$3d$ orbitals
$\Psi_{p_x} = \frac{1}{i\sqrt{2}}(Y_1^1 + Y_1^{-1})$	$\Psi_{d_{xy}} = \frac{-i}{\sqrt{2}}(Y_2^2 - Y_2^{-2})$
$\Psi_{p_y} = \frac{1}{\sqrt{2}}(Y_1^1 - Y_1^{-1})$	$\Psi_{d_{xz}} = \frac{-1}{\sqrt{2}}(Y_2^1 - Y_2^{-1})$
$\Psi_{p_z} = Y_1^0$	$\Psi_{d_{yz}} = \frac{i}{\sqrt{2}}(Y_2^1 + Y_2^{-1})$
	$\Psi_{d_{x^2-y^2}} = \frac{1}{\sqrt{2}}(Y_2^2 + Y_2^{-2})$
	$\Psi_{d_{z^2}} = Y_2^0$

Table 6: Orbital equations of the $2p$ and $3d$ orbitals. r is the radius expressed in atomic units, Z is effective nuclear charge for a particular orbital in that atom and $\rho = \frac{2Zr}{n}$ where n is the principal quantum number (2 for the $2p$ orbitals and 3 for the $3d$ orbitals).

Finally, using the description of the atomic orbitals given in Table 6, the Hamiltonian (5) and the fact that

$$L_+ Y_l^m = \sqrt{l(l+1) - m^2 - m} Y_l^{m+1}$$
$$L_- Y_l^m = \sqrt{l(l+1) - m^2 + m} Y_l^{m-1}$$
$$L_z Y_l^m = m Y_l^m$$

$$S_+ Y^\uparrow = 0$$
$$S_+ Y^\downarrow = Y^\uparrow$$
$$S_- Y^\uparrow = Y^\downarrow$$
$$S_- Y^\downarrow = 0$$
$$S_z Y^\uparrow = \frac{1}{2} Y^\uparrow$$
$$S_z Y^\downarrow = \frac{-1}{2} Y^\downarrow$$

we can already compute the spin-orbit Hamiltonian for both the p and d atomic orbitals:

$$H_{SOC,2p} = \frac{\lambda}{2} \begin{pmatrix} 0 & i & 0 & 0 & 0 & -1 \\ -i & 0 & 0 & 0 & 0 & -i \\ 0 & 0 & 0 & -1 & -i & 0 \\ 0 & 0 & -1 & 0 & -i & 0 \\ 0 & 0 & i & i & 0 & 0 \\ -1 & i & 0 & 0 & 0 & 0 \end{pmatrix}$$

where the basis of $H_{SOC,2p}$ is $(p_{x,\uparrow}, p_{x,\downarrow}, p_{y,\uparrow}, p_{y,\downarrow}, p_{y,\uparrow}, p_{y,\downarrow})$.

$$H_{SOC,3d} = \frac{\lambda}{2}\begin{pmatrix} 0 & -i & 0 & 0 & 0 & 0 & 0 & -1 & i & i\sqrt{3} \\ i & 0 & 0 & 0 & 0 & 0 & 0 & -i & -1 & i\sqrt{3} \\ 0 & 0 & 0 & -2i & 0 & 1 & i & 0 & 0 & 0 \\ 0 & 0 & 0 & 0 & 0 & -i\sqrt{3} & -\sqrt{3} & 0 & 0 & 0 \\ 0 & 0 & 1 & i & i\sqrt{3} & 0 & i & 0 & 0 & 0 \\ 0 & 0 & -i & 1 & -\sqrt{3} & -i & 0 & 0 & 0 & 0 \\ -1 & i & 0 & 0 & 0 & 0 & 0 & 0 & 2i & 0 \\ -i & -1 & 0 & 0 & 0 & 0 & 0 & -2i & 0 & 0 \\ -i\sqrt{3} & \sqrt{3} & 0 & 0 & 0 & 0 & 0 & 0 & 0 & 0 \end{pmatrix}$$

where the basis of $H_{SOC,3d}$ is $(d_{yz,\uparrow}, d_{yz,\downarrow}, d_{xz,\uparrow}, d_{xz,\downarrow}, d_{xy,\uparrow}, d_{xy,\downarrow}, d_{x^2-y^2,\uparrow}, d_{x^2-y^2,\downarrow}, d_{z^2,\uparrow}, d_{z^2,\downarrow})$.

C- Other configurations of Oxygen vacancies in the (001) surface of $SrTiO_3$

This appendix is a continuation of chapter 4. We will describe the electronic structure of the cluster for different positions of the Oxygen vacancies and for different terminations of the surface.

In the end, we include a table with the main features.

SrO-terminated. Two non-aligned vacancies

After removing one of the apical Oxygen atoms, we can also remove one of the neighboring Oxygen atoms in the first TiO_2 layer. This particular position of the Oxygen divacancy is interesting because the Hamiltonian has to be particularly tuned. We consider that the total impact of the two vacancies in the cluster is the linear sum of the impact of each vacancy separately. This means the following:

1) The vacancy on the top SrO layer will only affect the Titanium atom right below. This particular atom will suffer the same changes than that of section 4.2. It will be pulled down in the z-direction as an adaptation to the new local crystal field. The on-site energy of the d_{z^2} will be lowered now that there is not a p_z orbital above it to couple with. There will also be a slight change in the on-site energies of the d_{xz} and d_{yz} orbitals.

2) The vacancy on the first TiO_2 layer will affect the two adjacent Titanium atoms. These atoms will be displaced in the x-direction away from the vacancy. The self energies of their $d_{x^2-y^2}$ and $d_{xy/xz}$ orbitals will be lowered as well.

Moreover, this and other of the studied configurations are of particular interest from an energetic point of view [65].

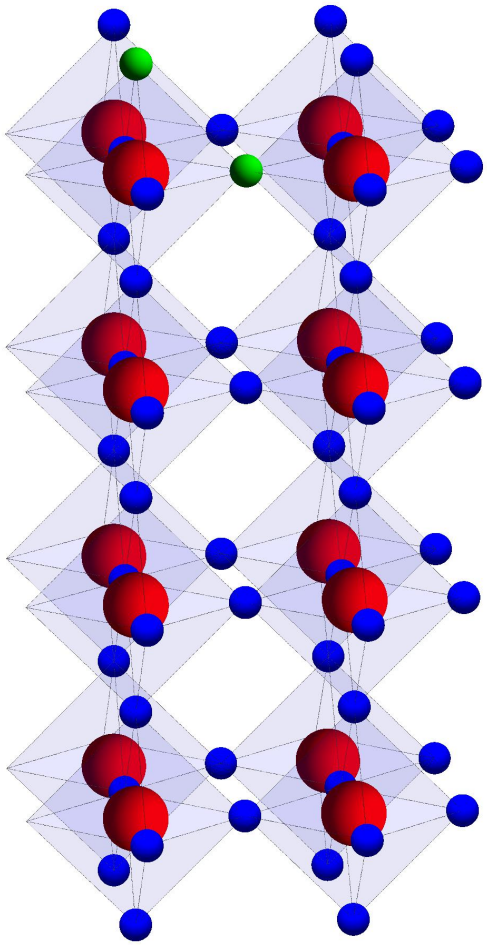

Figure 6.7: One vacancy in on the top SrO plane. The second vacancy is located in the first TiO_2 layer.

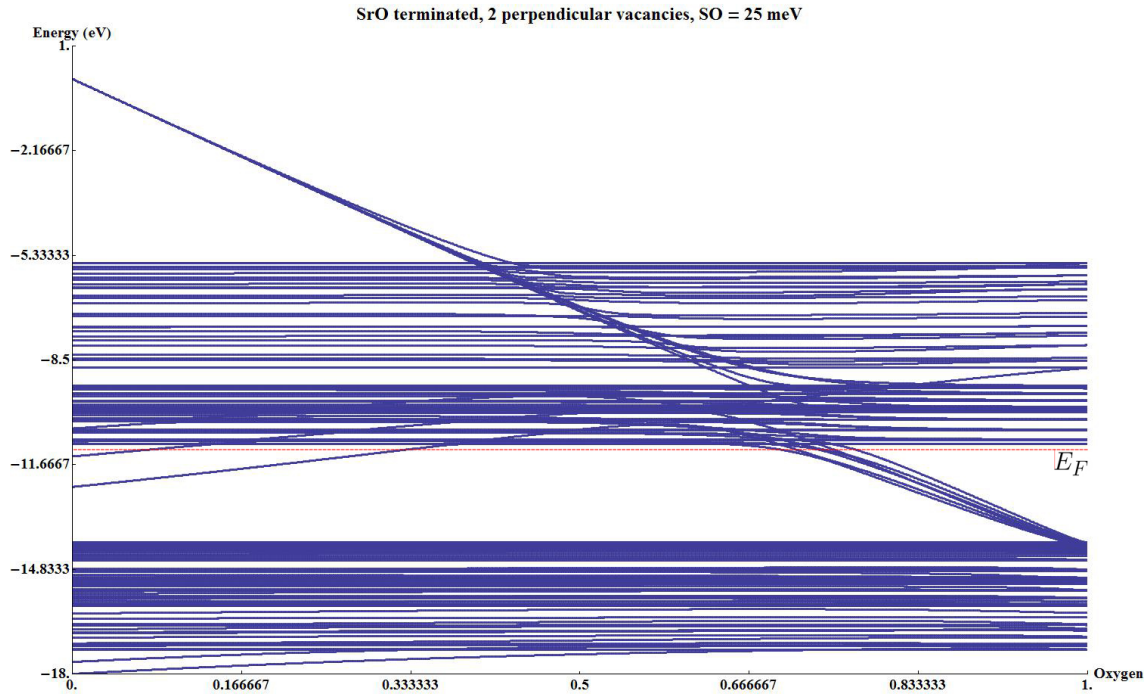

Figure 6.8: Electronic states at the Γ point when two Oxygen atoms are removed. On the right, the electronic states when the Oxygen atoms have not been removed. On the left, the electronic states when the Oxygen atoms have been completely removed and the neighboring atoms have adapted to the new local crystal field.

Figure 6.8 shows the transition of the electronic states when the Oxygen atoms are removed. Once again, the left side of the plot one shows the energy states of the supercell at the Γ point when the two Oxygen atoms are still part of the cluster and the system has not been perturbed. On the left side we can find the new electronic states once the Oxygen atoms have been fully removed. In the middle, the smooth transition between the two physical situations. We can clearly see the appearance of two pairs of degenerate states in the gap below the conduction band.

A closer look reveals the appearance of both in-gap states and new conduction states.

The orbital character of the lowest in-gap state is shown in Figure 6.10. One can see a strong coupling of the $d_{x^2-y^2}$-p_y orbitals coming from the two Titanium atoms affected by the vacancies and the neighboring atoms in the y-direction. There is also some coupling of the d_{z^2}-p_z orbitals between the Titanium below the apical vacancy and the Oxygen atom below. Of course the main contribution is coming from atom

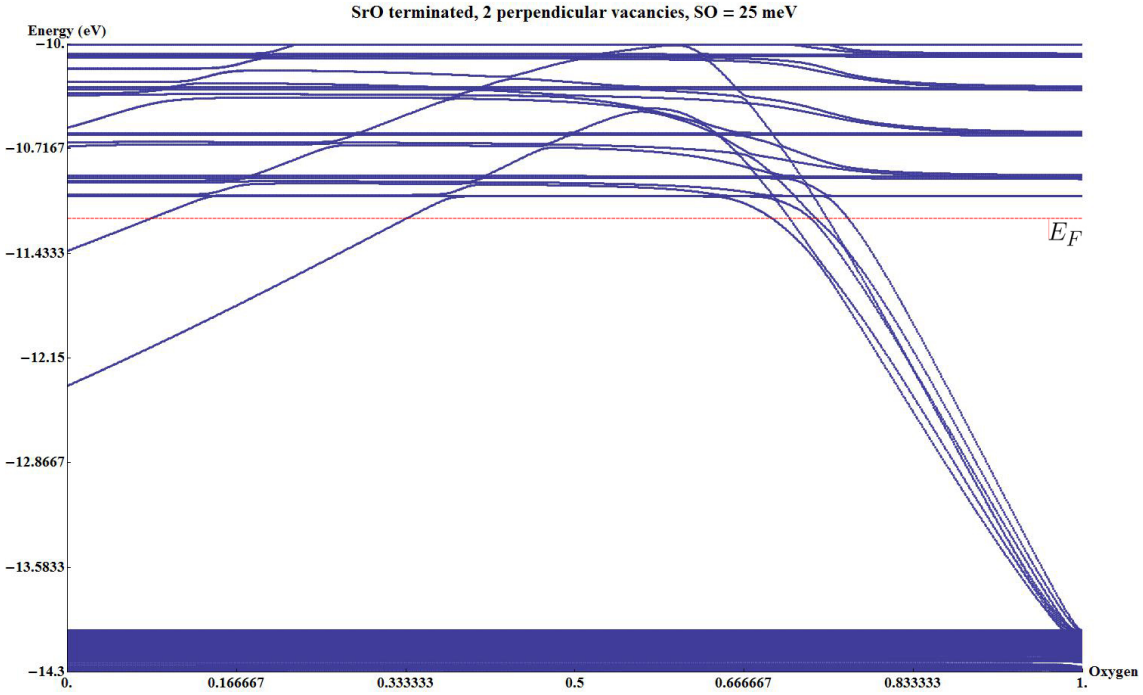

Figure 6.9: Zoom of Fig. 6.8.

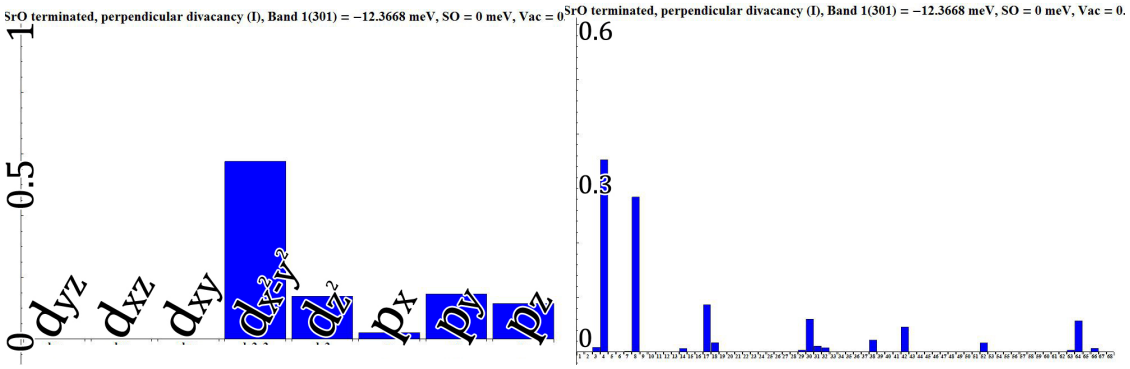

(a) Orbital (b) Sites

Figure 6.10: Orbital/site character of the first pair of in-gap states.

4, the Titanium affected by both vacancies. And the absence of p_x character of this state is due the removal of the Oxygen atom connecting the two Titanium atoms in the y-direction.

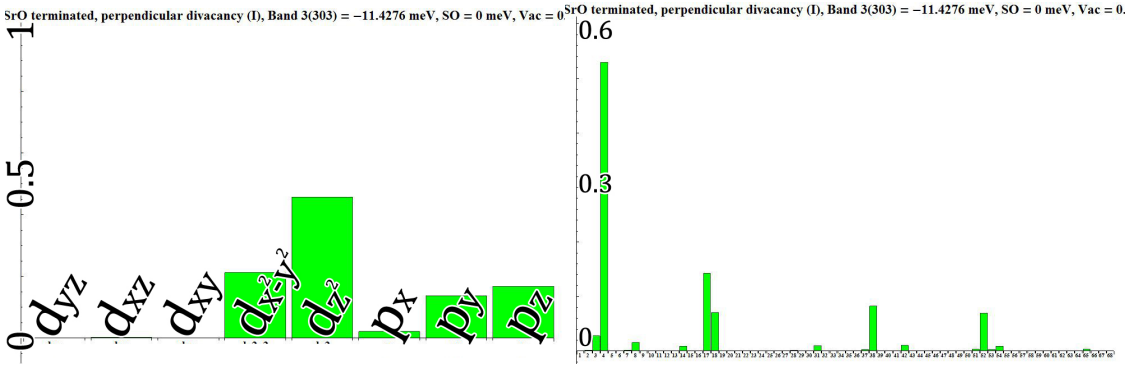

(a) Orbital (b) Sites

Figure 6.11: Orbital/site character of the second pair of in-gap states.

The orbital character the second in-gap state is shown in Figure 6.11. This time the dominant orbitals are d_{z^2}-p_z coming from the Titanium atom most affected by both vacancies and the Oxygen atom below. The contribution of the $d_{x^2-y^2}$-p_y orbitals coming from the two Titanium atoms surrounding the vacancy in the TiO_2 plane is also present. Again we see the absence of the p_x orbital. This is because we decided to create the Oxygen vacancy between two Titanium atoms in the y axis breaking the x-y symmetry of the system.

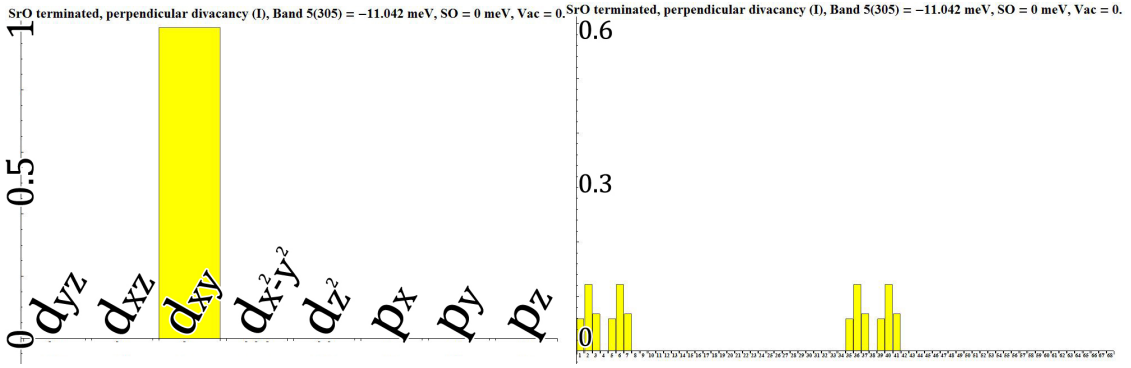

(a) Orbital (b) Sites

Figure 6.12: Orbital/site character of the states found at the bottom of the conduction band.

Finally, we show in Figure 6.12 again the d_{xy}-character of the bottom of the conduction band.

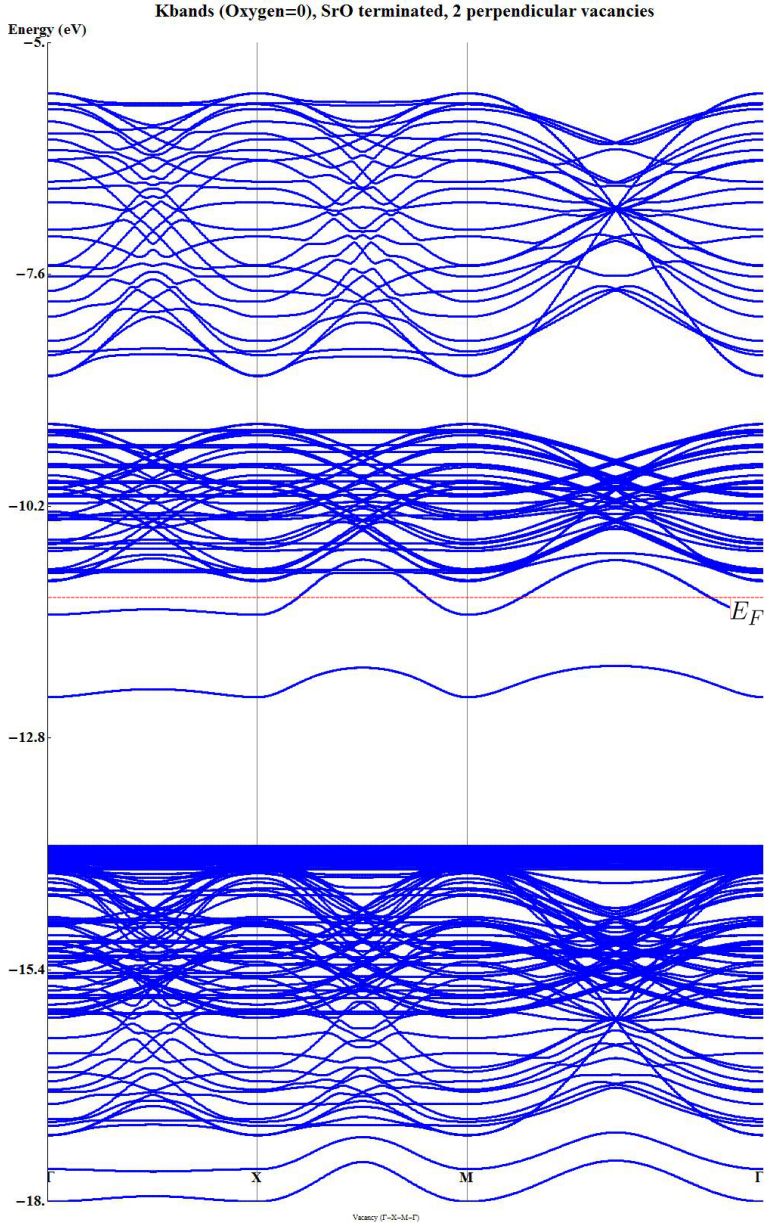

Figure 6.13: Band structure. We can clearly see the two in-gap states generated by the vacancies.

The full band structure of this configuration is shown in Figure 6.13. We can clearly see the two in-gap states that are generated by the two oxygen vacancies. These

results have some similarities with the ones we found when the two vacancies were vertically aligned. The main difference here is the orbital/site contribution of one of the new bands.

At the end of this appendix we include a table showing the main features of these configurations.

SrO-terminated. One vacancy in the first TiO_2 layer.

Previously we showed the electronic properties of the cluster when one single vacancy is introduced in the top SrO plane. It is also interesting to study the case where one single vacancy is introduced in the first TiO_2 plane.

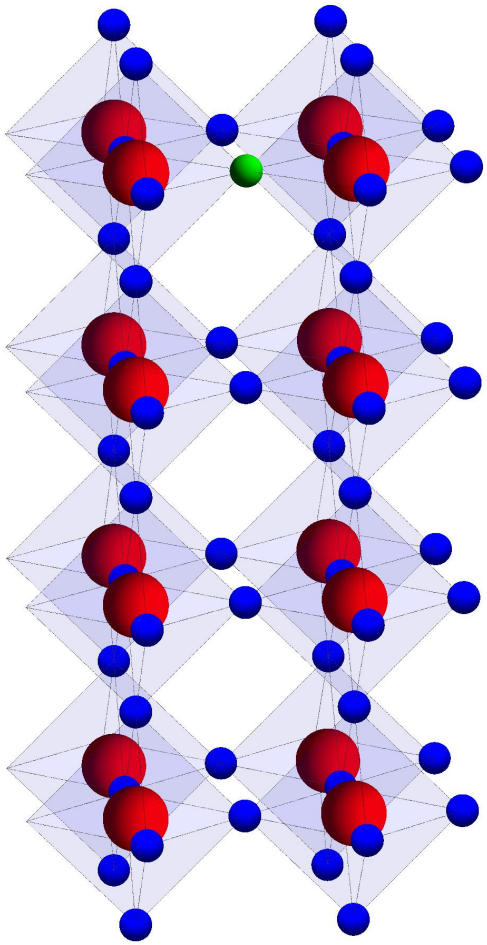

Figure 6.14: The 2x2x4 cluster with one vacancy in the top TiO_2 layer.

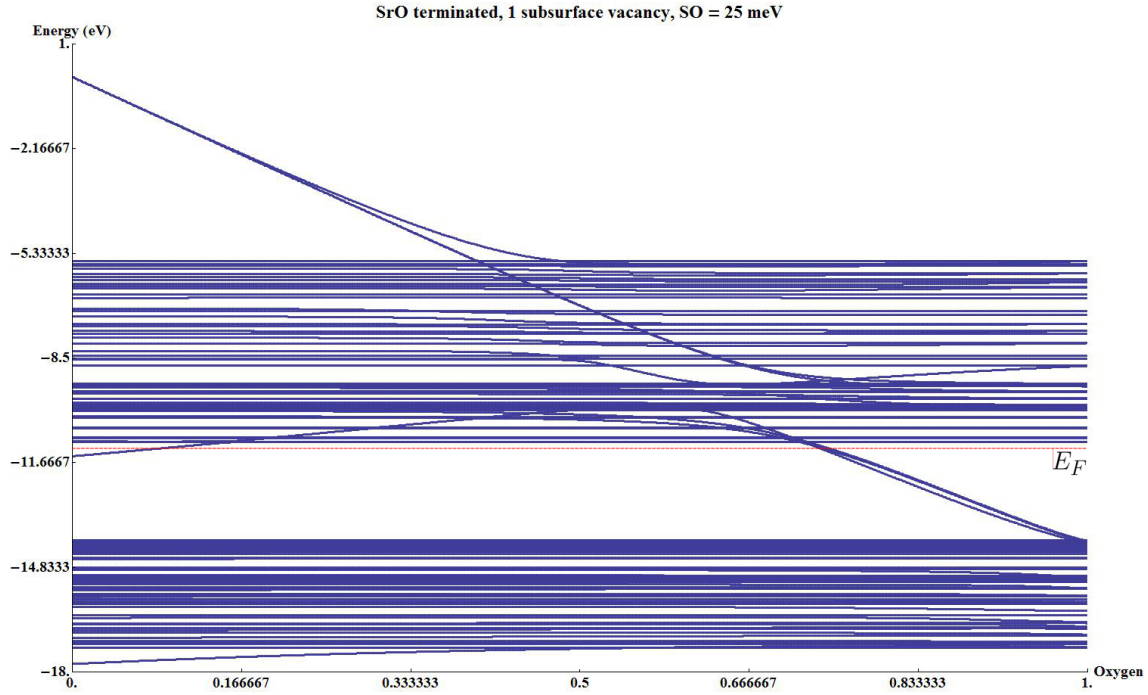

Figure 6.15: Electronic states at the Γ point when one Oxygen atom is removed. On the right, the electronic states when the Oxygen atom has not been removed. On the left, the electronic states when the Oxygen atom has been completely removed and the neighboring atoms have adapted to the new local crystal field.

Figure 6.15 shows the transition of the electronic states when the Oxygen atom in removed. Once again, the left side of the plot one shows the energy states of the supercell at the Γ point when the Oxygen atom is still part of the cluster and the system has not been perturbed. On the left side we can find the new electronic states once the Oxygen atom has been fully removed. In the middle, the smooth transition between the two physical situations. We can clearly see the appearance of a new in-gap state below the conduction band.

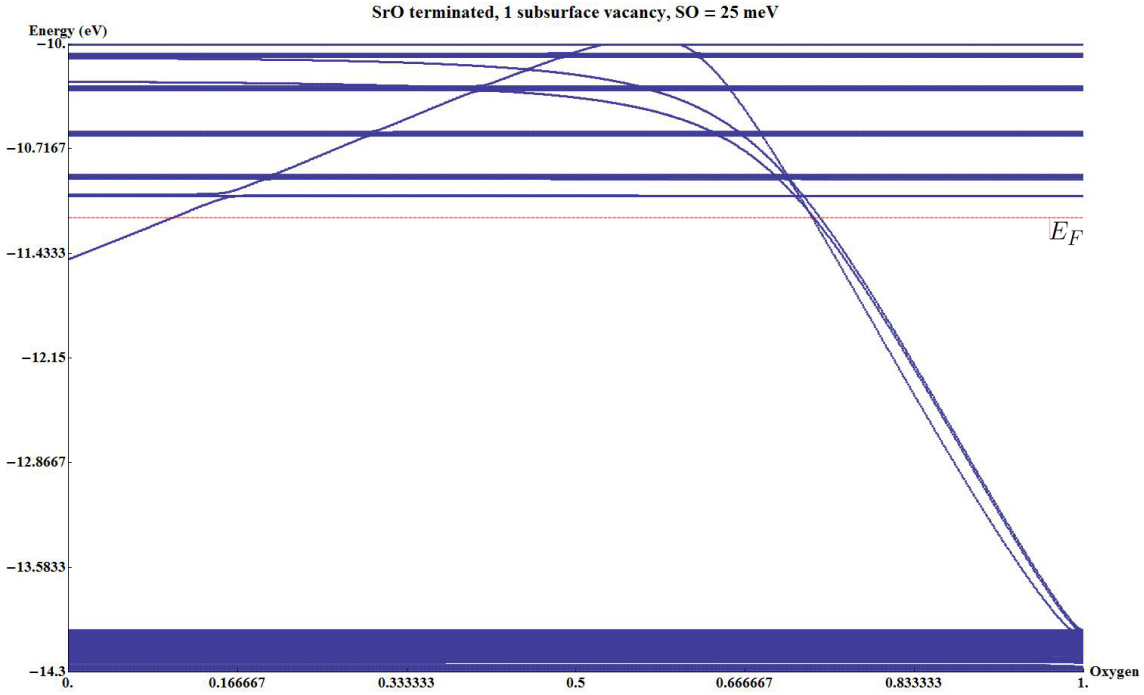

Figure 6.16: Zoom of Fig. 6.15.

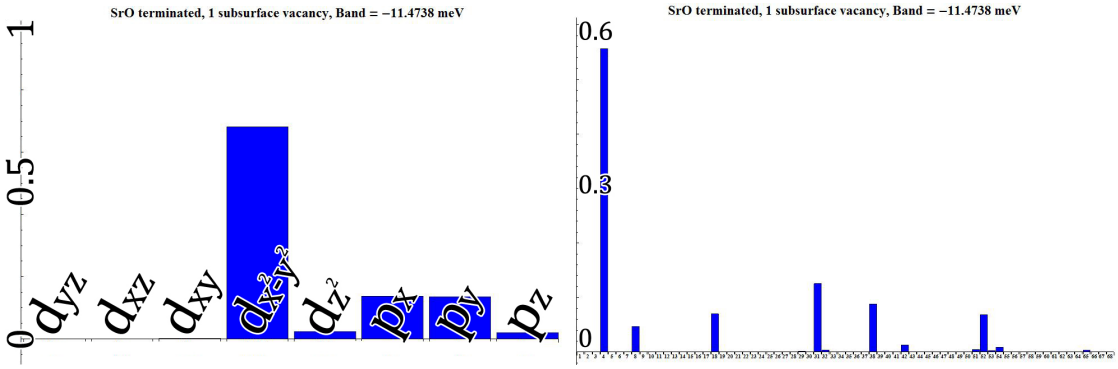

(a) Orbital (b) Sites

Figure 6.17: The pair of gap states has $d_{x^2-y^2}$-p_x/p_y character. These states are located around the two Titanium atoms surrounding the vacancy. This pair of degenerate states is similar to one of the pairs that we found in the previous configuration.

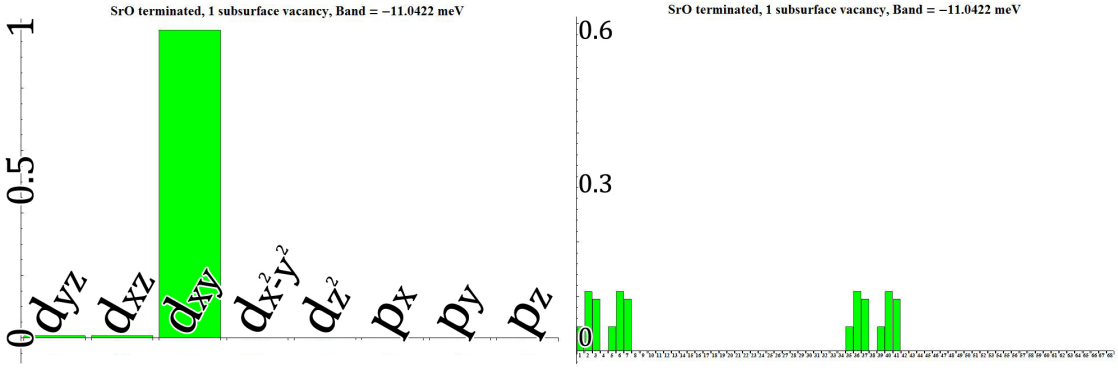

(a) Orbital (b) Sites

Figure 6.18: The bottom of the conduction band has the usual d_{xy} character.

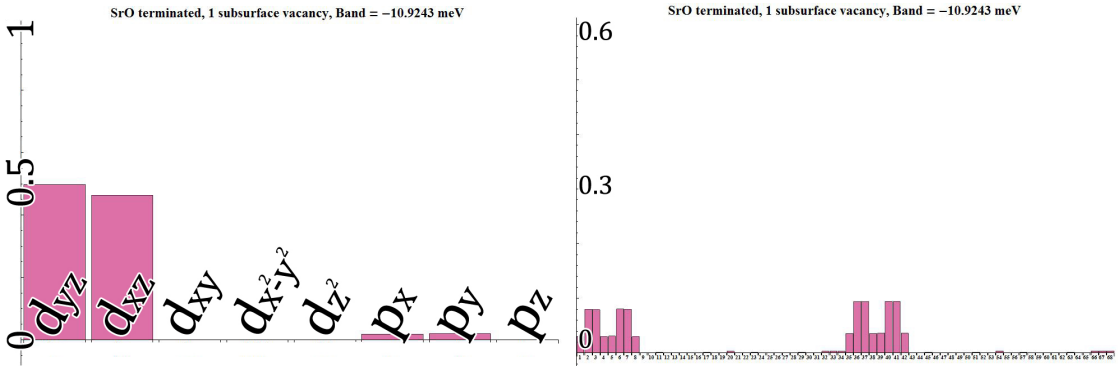

(a) Orbital (b) Sites

Figure 6.19: Other new states are found within the conduction part. These states have the usual t_{2g} character similar to the ones we found in previous configurations.

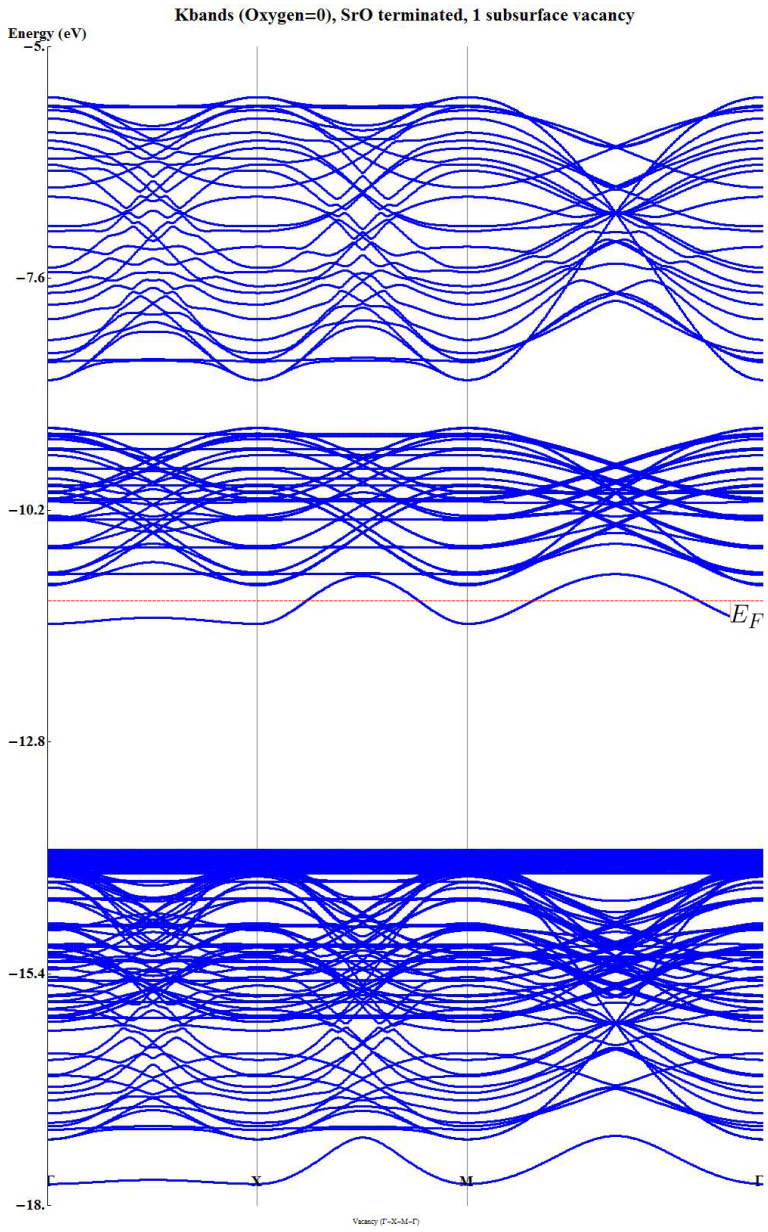

Figure 6.20: The full band structure reveals the in-gap band created by the vacancy. The $d_{x^2-y^2}$-p_y character remains the same along the Brillouin zone.

SrO-terminated. Two non-aligned vacancies in the first TiO_2 layer.

Another interesting configuration arises when two vacancies are introduced in the same TiO_2 plane. They can be either aligned in one direction or they can form 90° with their neighboring Titanium atom. We will study both configurations in this section and the next.

Particularly, we will see that one single vacancy creates an in-gap state below the conduction bands. DFT calculations do not show this state. This probably means that this state should be higher in energy, and it should be part of the conduction band. In general we found a pair of degenerate in-gap states for each Oxygen vacancy that we introduce in the cluster. DFT calculations usually show in-gap states whenever we introduce two or more vacancies.

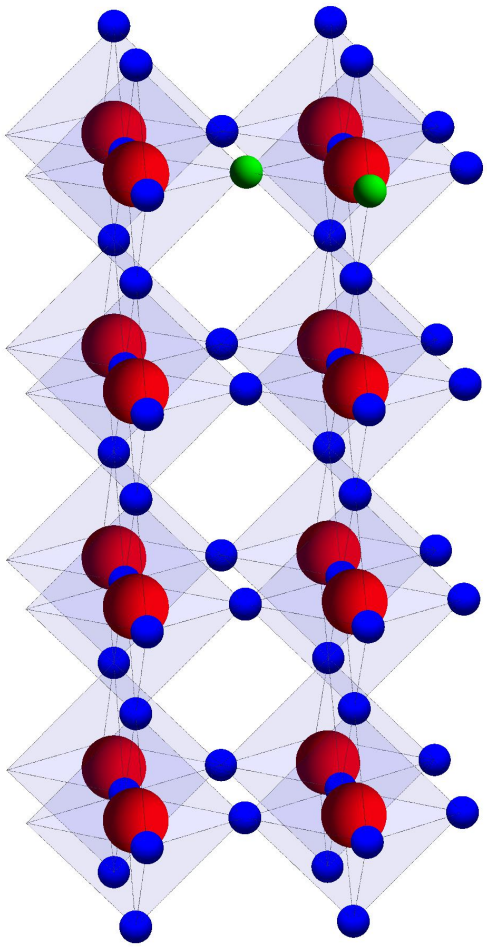

Figure 6.21: Cluster with two vacancies in the top TiO_2 plane.

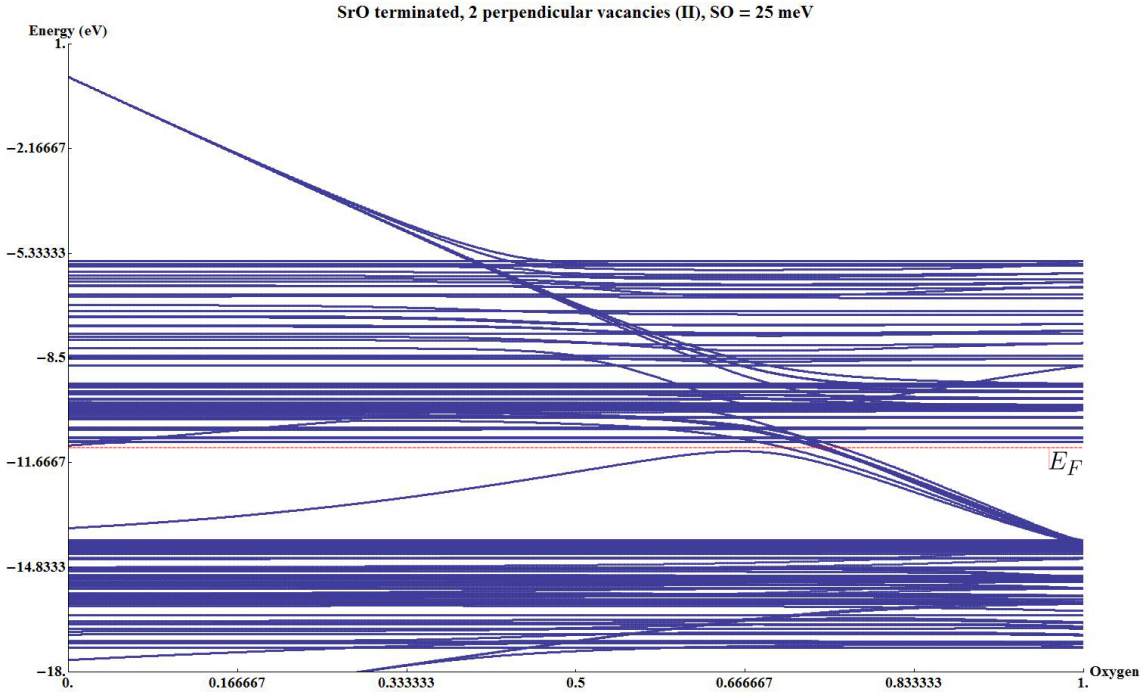

Figure 6.22: Electronic states at the Γ point when the vacancies are introduced.

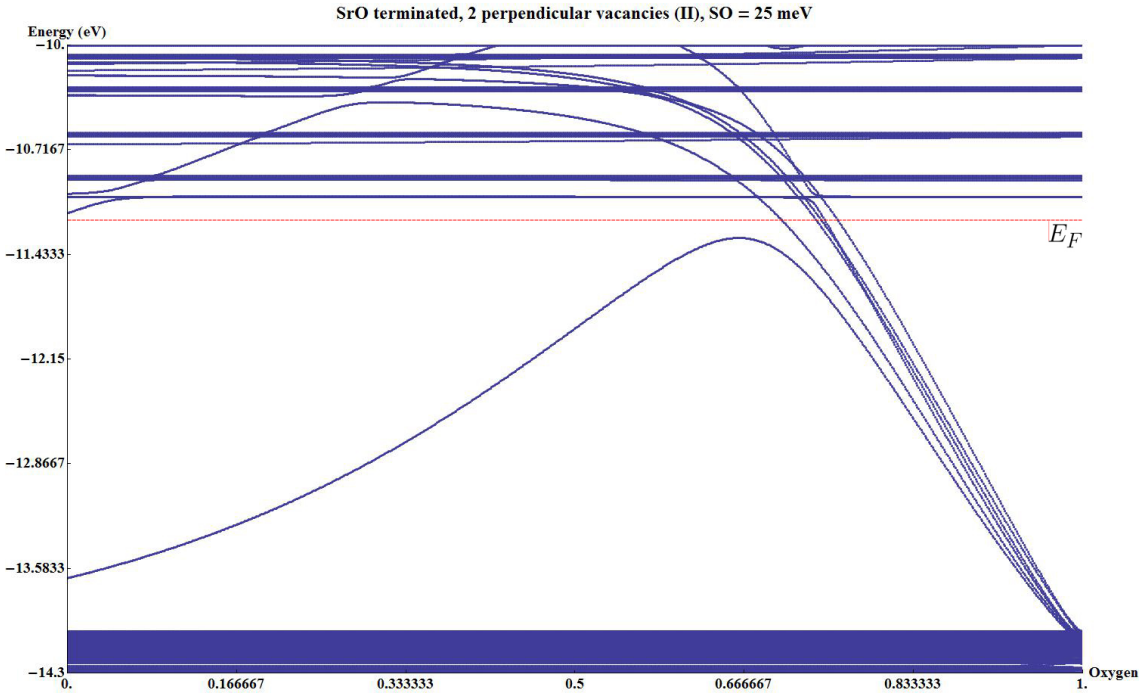

Figure 6.23: Zoom of Fig. 6.22.

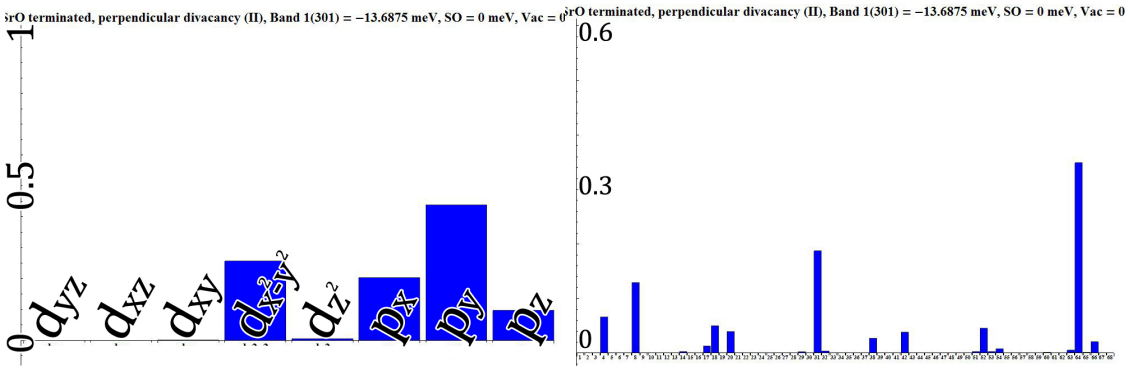

(a) Orbital (b) Sites

Figure 6.24: The first pair of in-gap states has strong $d_{x^2-y^2}$-$p_{x/y}$ character and it is located in the vicinity of the vacancies.

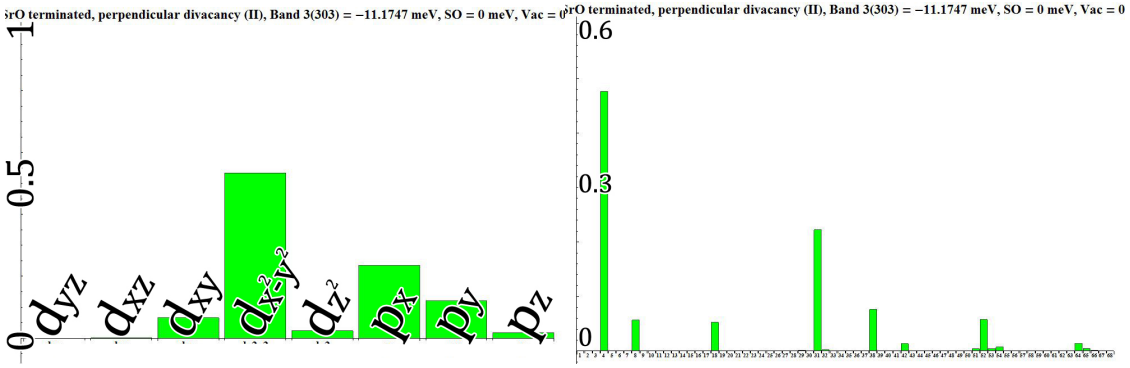

(a) Orbital (b) Sites

Figure 6.25: The second pair of in-gap states has similar orbital character and it is also located in the vicinity of the vacancies. This time the d contribution coming from the Titanium atoms is stronger, and this is why this states are higher in energy.

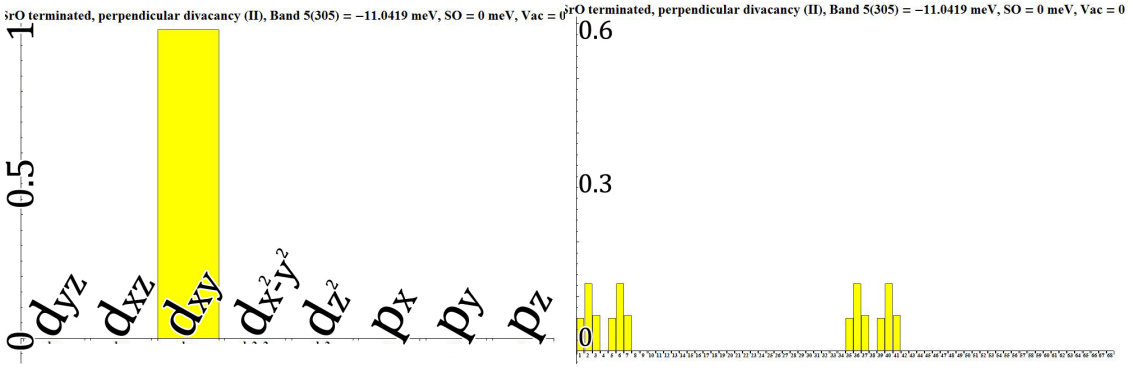

(a) Orbital (b) Sites

Figure 6.26: The bottom of the conduction band has the usual d_{xy} character.

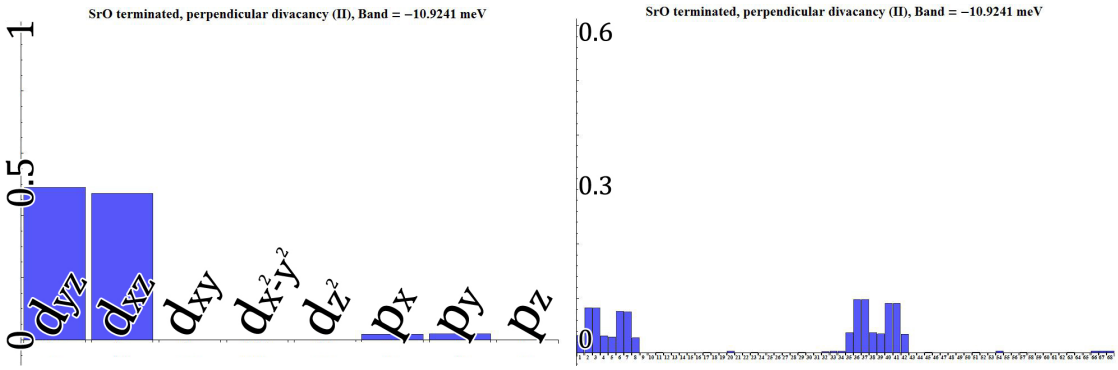

(a) Orbital (b) Sites

Figure 6.27: Other new conduction states are created due to the presence of the vacancies. These states have the usual t_{2g} character.

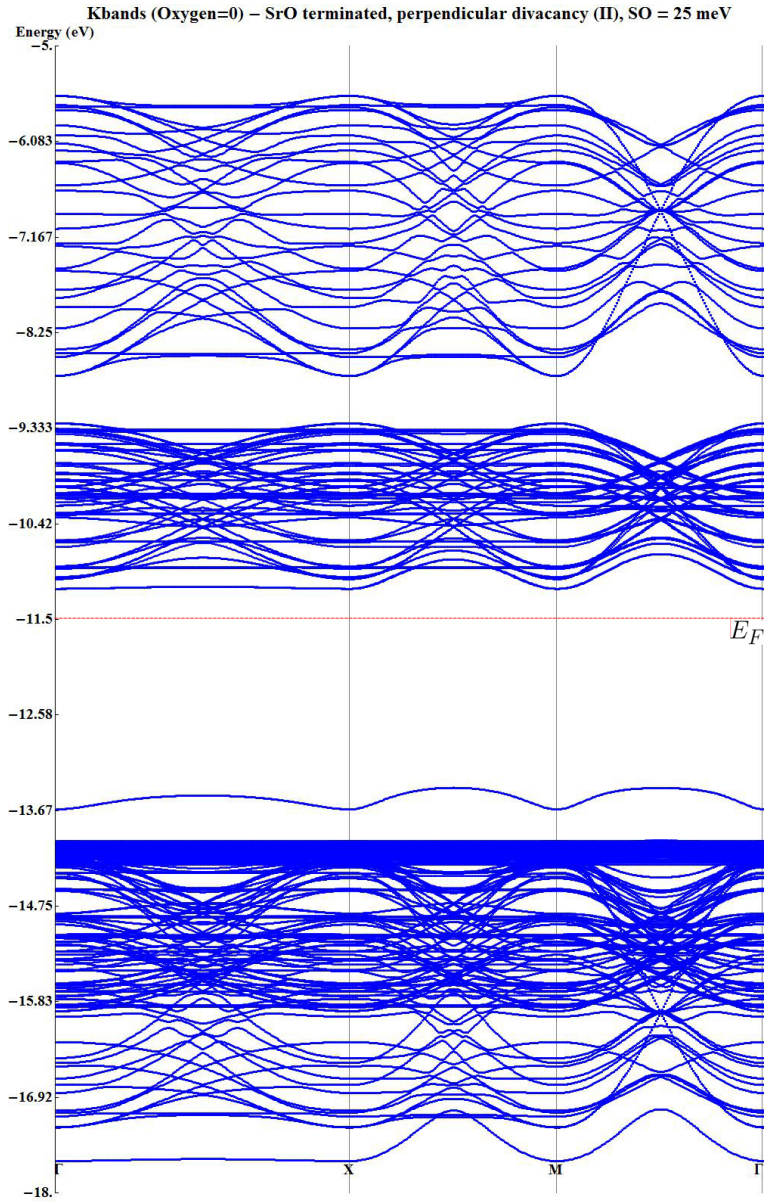

Figure 6.28: the band structure shows the bands generated by the Oxygen vacancies. It is particularly interesting that the first band is now much closer to the valence part and the second band is right below the conduction bands.

SrO-terminated. Two aligned vacancies in the first TiO_2 layer.

Here we show the second configuration when two vacancies are introduced in the same TiO_2 plane. This time the vacancies are aligned in the y direction

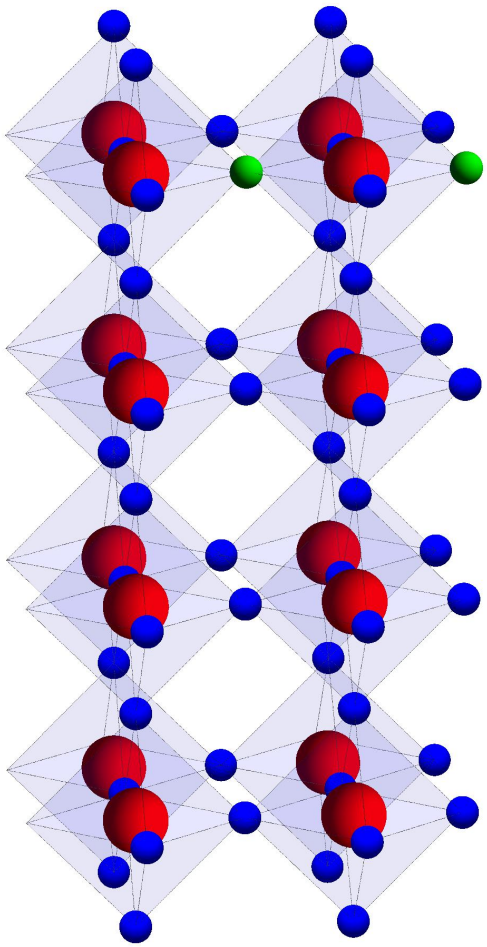

Figure 6.29: Two aligned vacancies in the top TiO_2 layer.

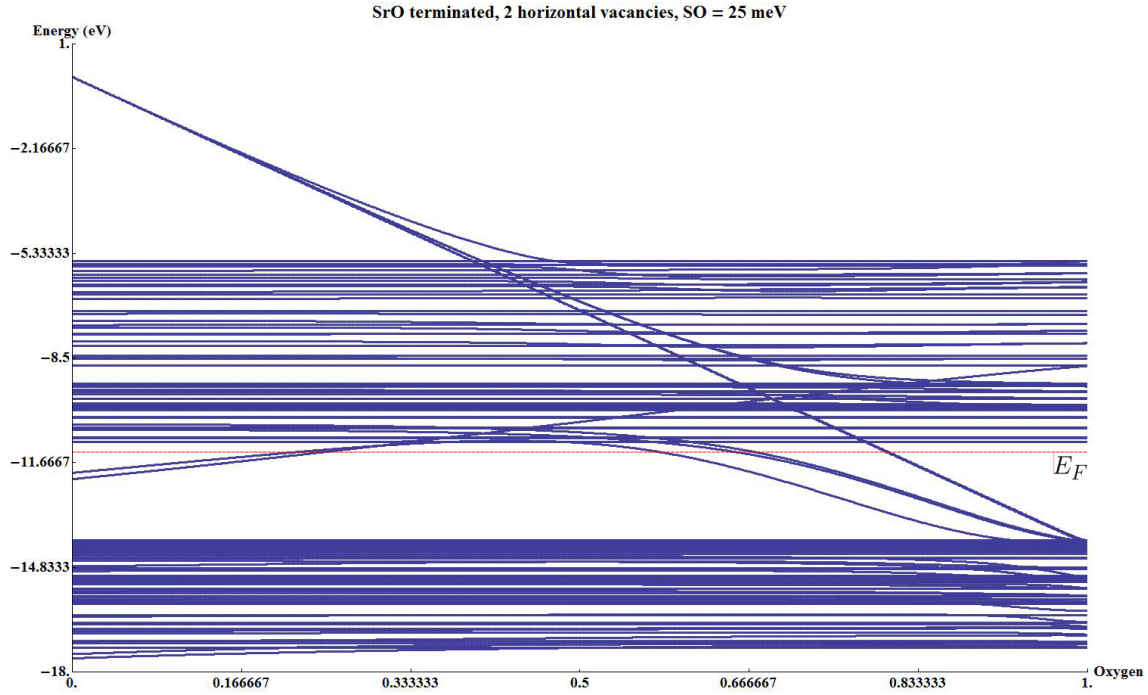

Figure 6.30: Electronic states at the Γ point when two Oxygen vacancies are introduced in the top TiO_2 layer.

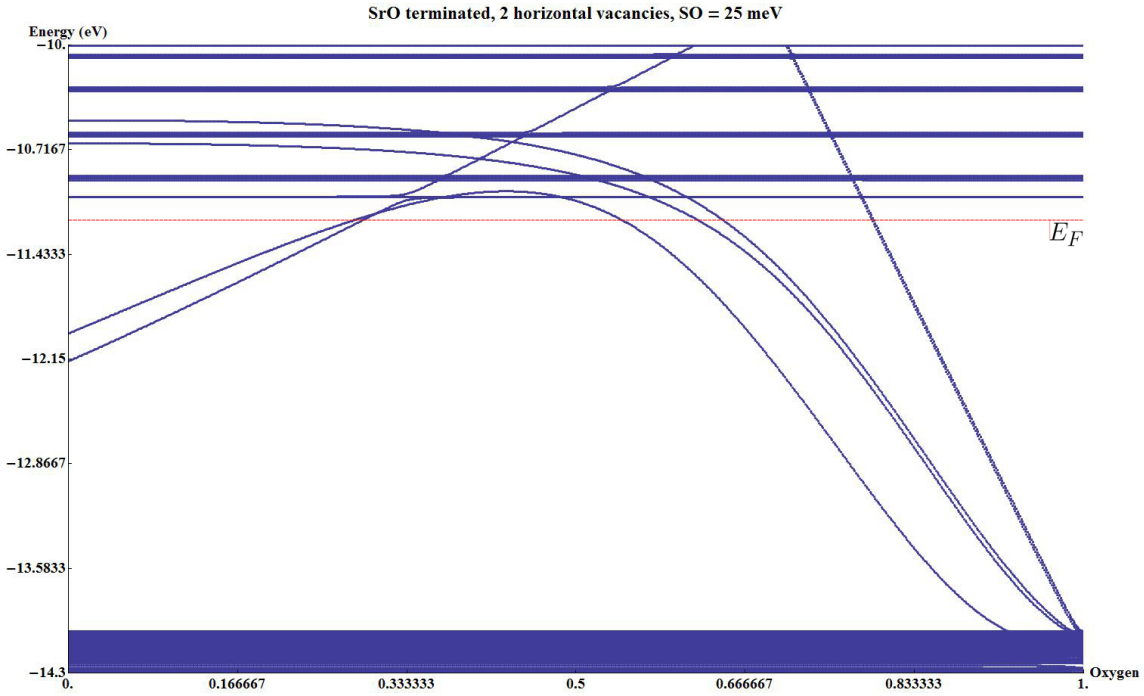

Figure 6.31: Zoom of Fig. 6.30.

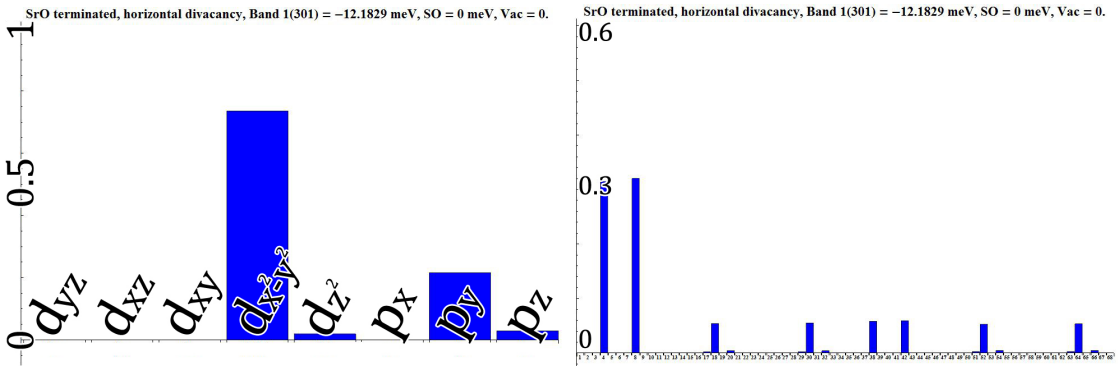

(a) Orbital (b) Sites

Figure 6.32: The first pair of in-gap states has strong $d_{x^2-y^2}$-p_y character coming from the Titanium atoms close to the vacancies in the y direction.

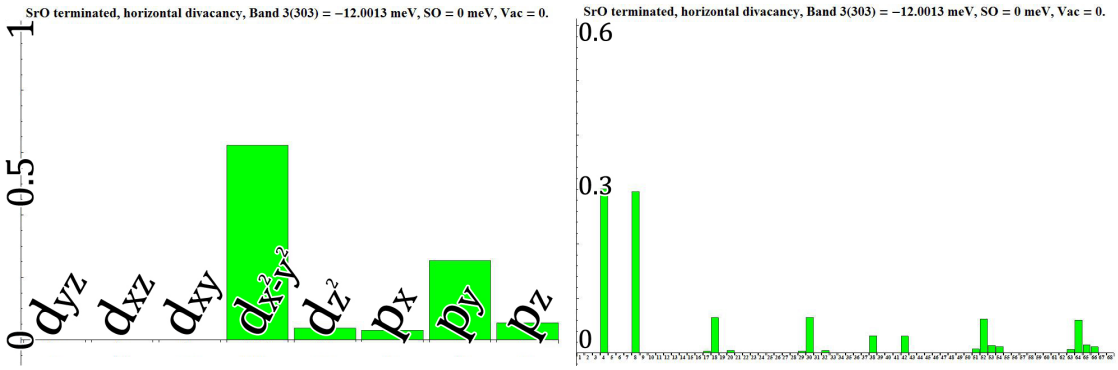

(a) Orbital (b) Sites

Figure 6.33: The second pair of states is very similar. It also shows the strong $d_{x^2-y^2}$-p_y character and they also come from the Titanium atoms close to the vacancies in the y direction. This results can be understood knowing that these vacancies break the xy symmetry of the cluster and that the $d_{x^2-y^2}$ is energetically favored by these vacancies.

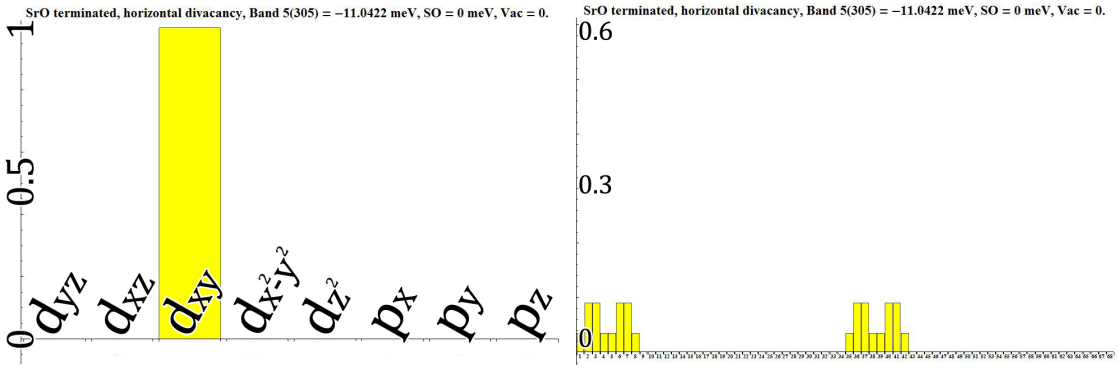

(a) Orbital (b) Sites

Figure 6.34: The d_{xy} character of the bottom of the conduction band remains unchanged.

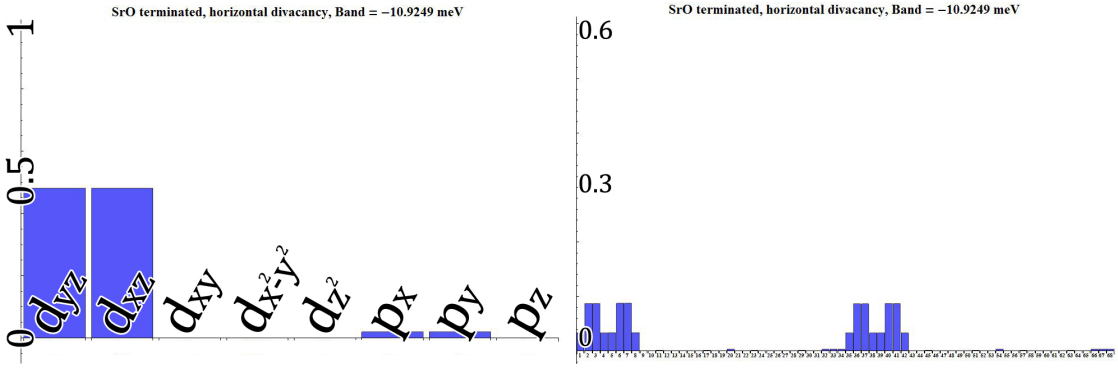

(a) Orbital (b) Sites

Figure 6.35: These vacancies also generate new conduction states. These states have the usual t_{2g} character, similar to what we found in previous cases.

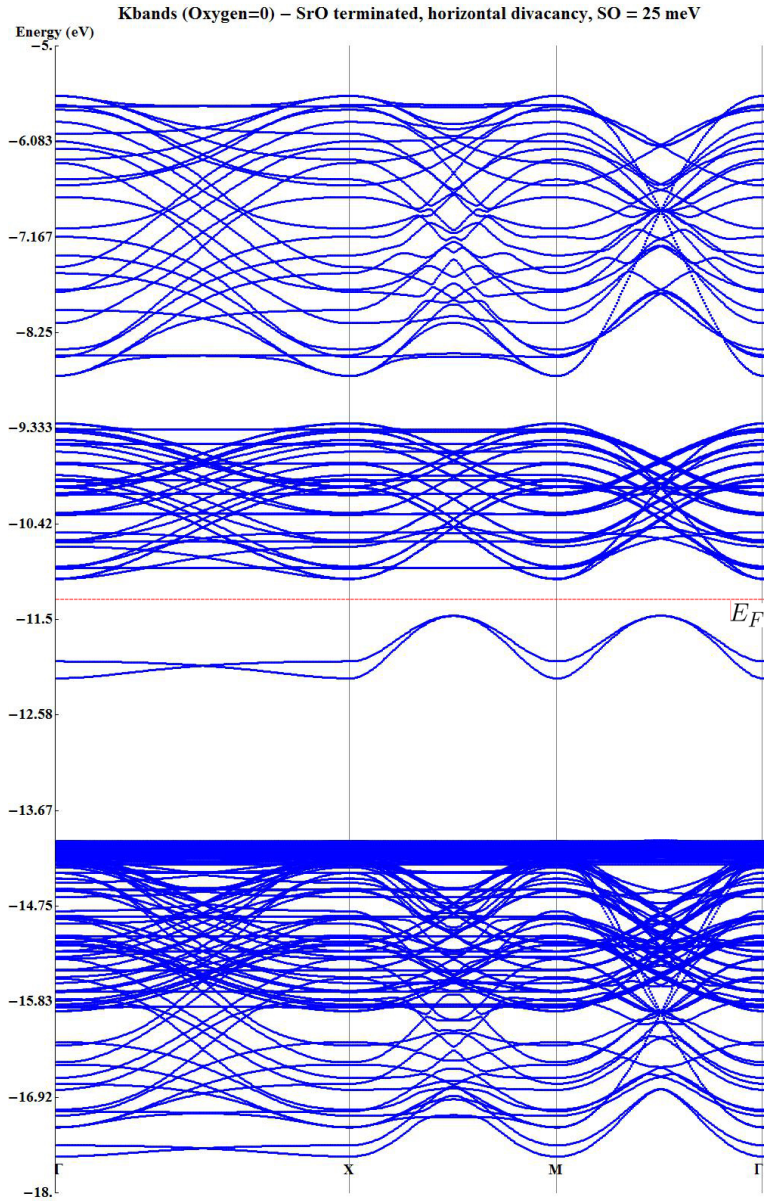

Figure 6.36: The band structure shows the two pairs of in-gap bands generated by the removal ot he two Oxygen atoms in the top TiO_2 layer.

TiO_2-terminated. One vacancy in the top surface.

We will study now the electronic properties of the TiO_2-terminated cluster with one Oxygen vacancy in the surface (that is, the TiO_2 layer).

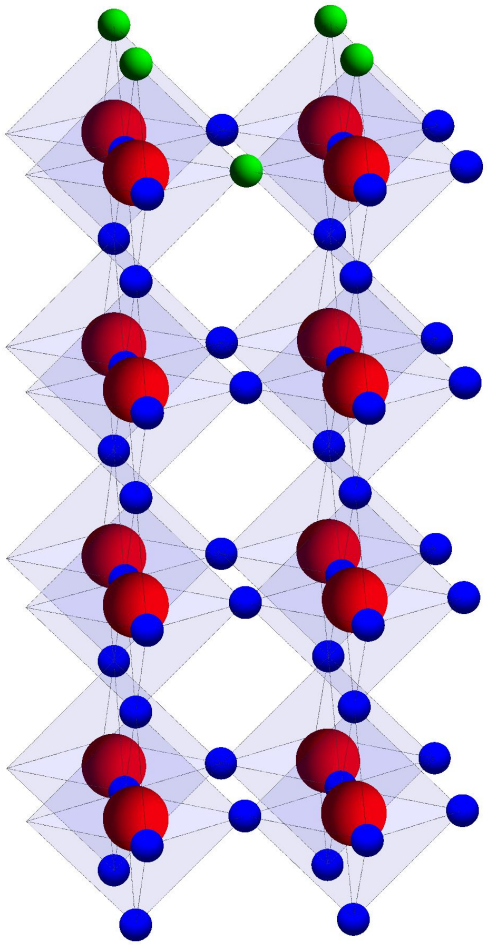

Figure 6.37: The TiO_2-terminated cluster with one extra vacancy.

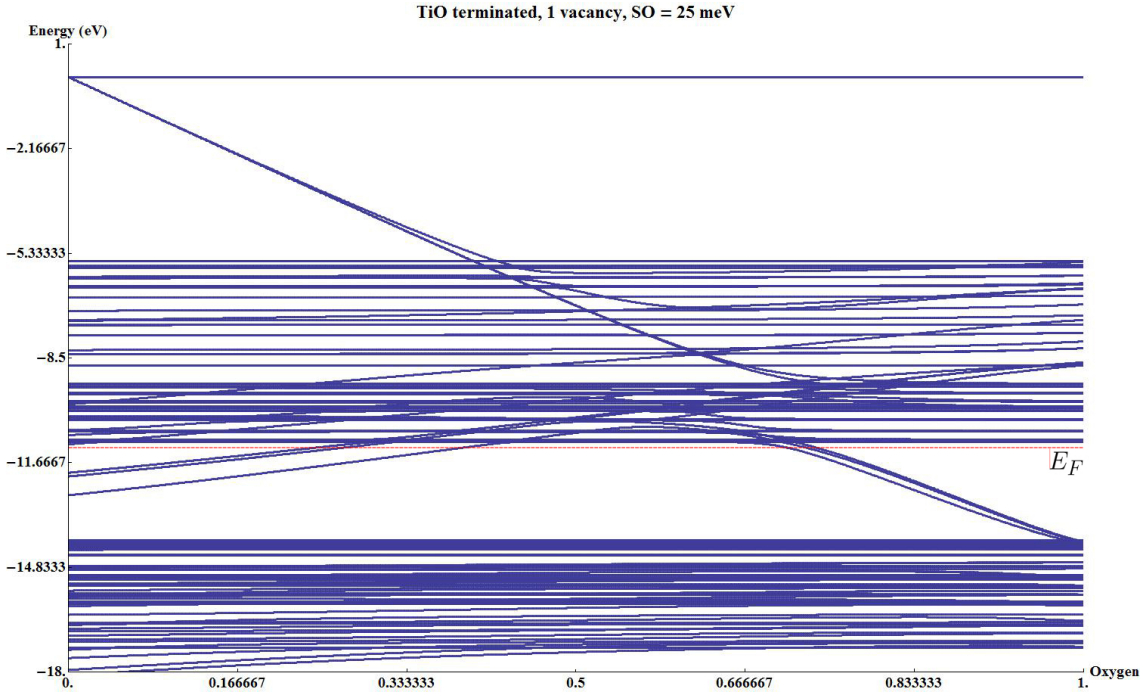

Figure 6.38: Electronic states at the Γ point when one Oxygen atom is removed.

Several in-gap states are found. Many of these states are generated by the Oxygen atoms that have been removed in the top SrO layer so that we get the TiO_2 termination. Other states are generated by the vacancy in the top TiO_2 layer.

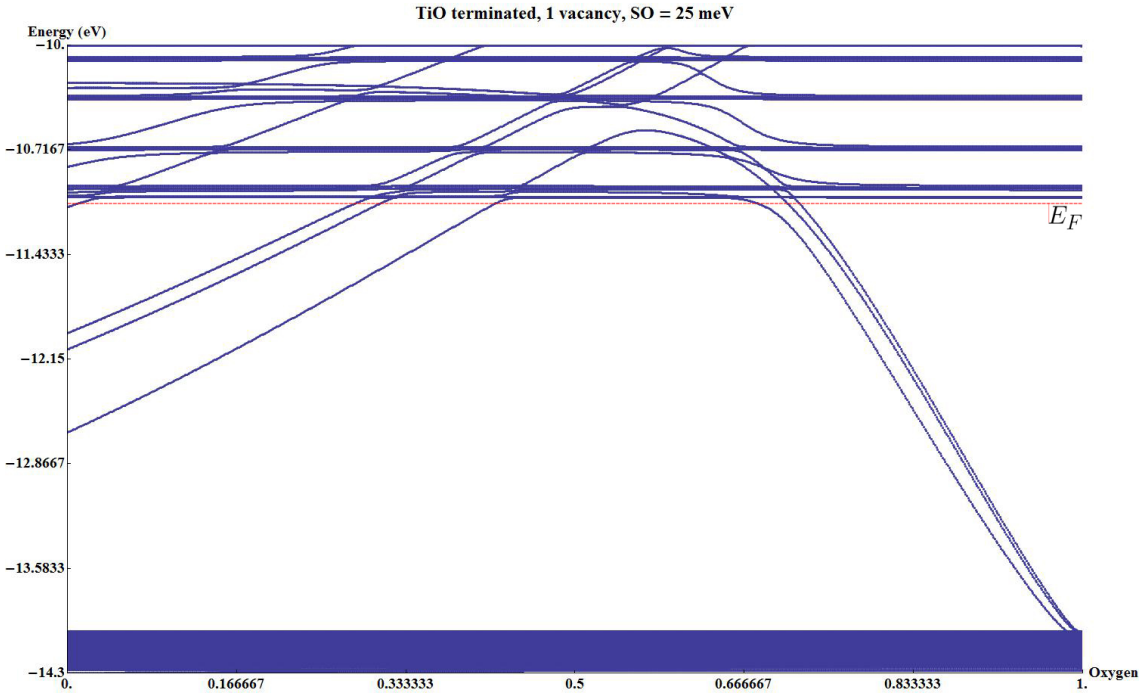

Figure 6.39: Zoom of Fig. 6.38.

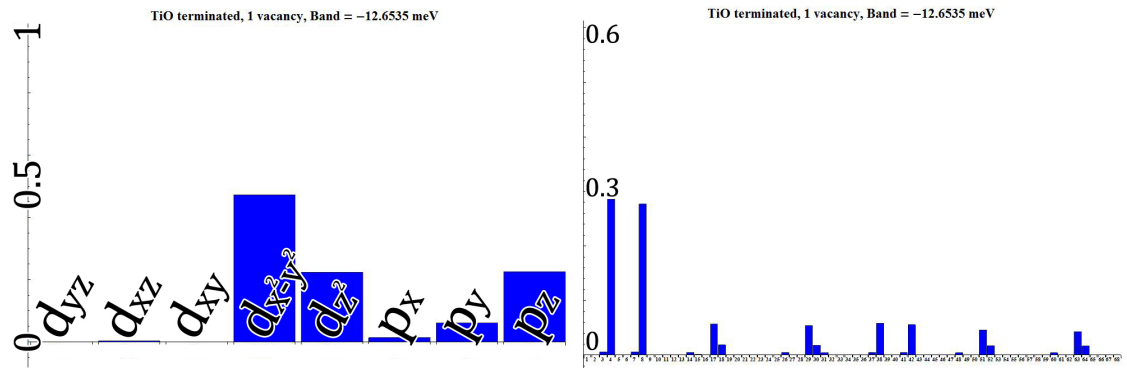

(a) Orbital (b) Sites

Figure 6.40: This pair of states has strong *eg* character and it is located around the Titanium atoms close to the vacancy.

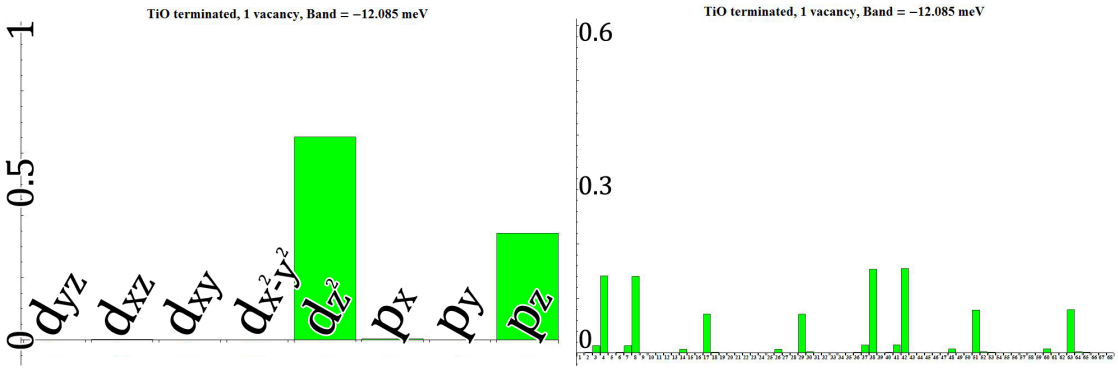

(a) Orbital (b) Sites

Figure 6.41: The second pair of states is attributed to the TiO_2 termination. These states are always found when we consider this termination. Usually these states should fall within the conduction band.

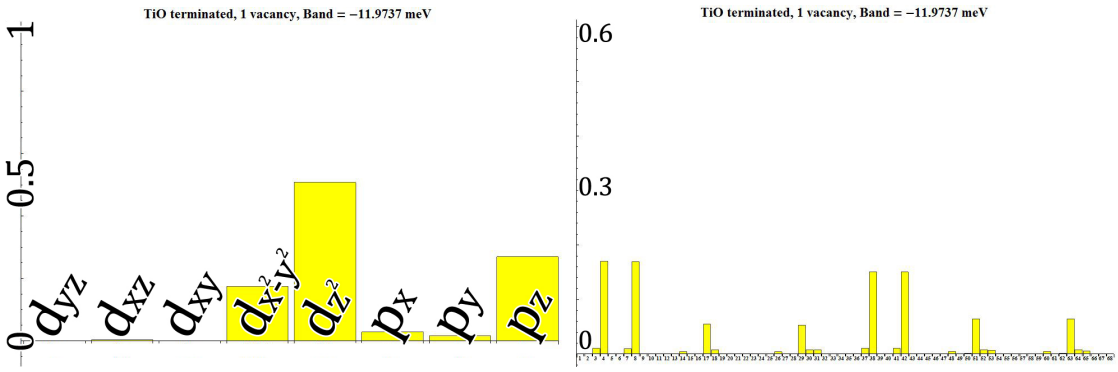

(a) Orbital (b) Sites

Figure 6.42: The third pair of states is also a consequence of the surface termination. It is located in the top surface.

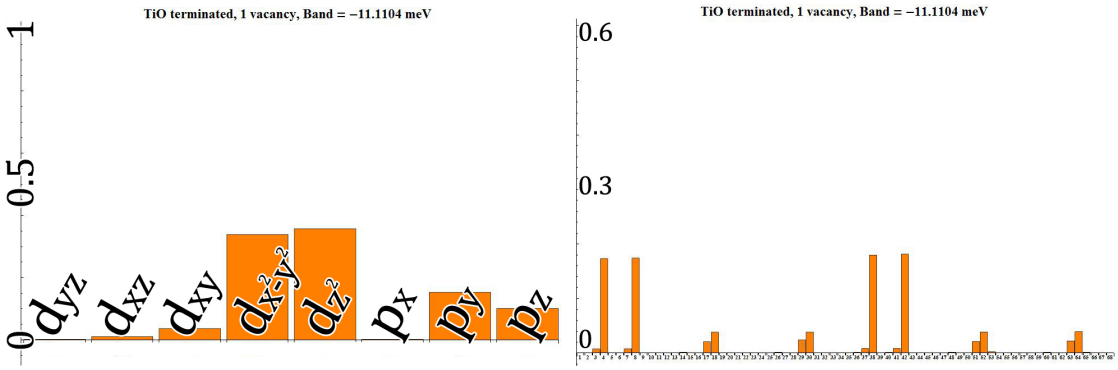

(a) Orbital (b) Sites

Figure 6.43: Similar d_{z^2}-$d_{x^2-y^2}$ character is found in the fourth pair of states. Only the first pair is generated by the Oxygen vacancy. The rest of the states are generated by the removal of the top SrO surface.

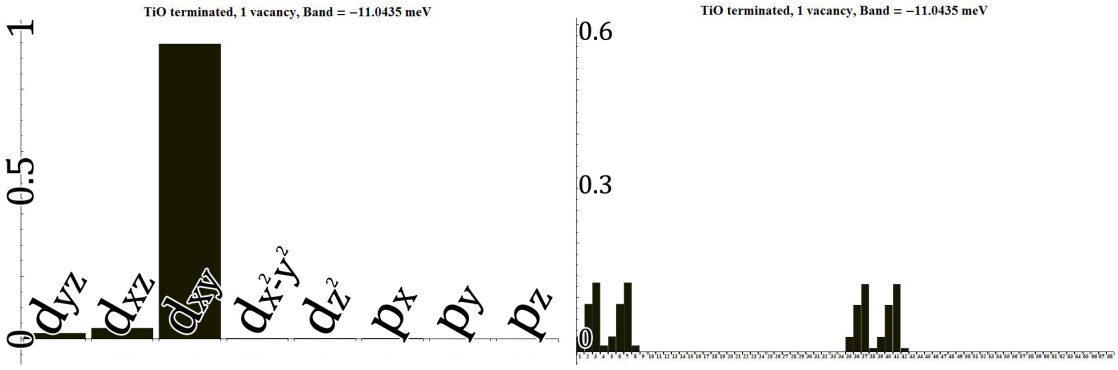

(a) Orbital (b) Sites

Figure 6.44: The bottom of the conduction band has the usual d_{xy} character, this time located mostly around the second TiO_2 layer.

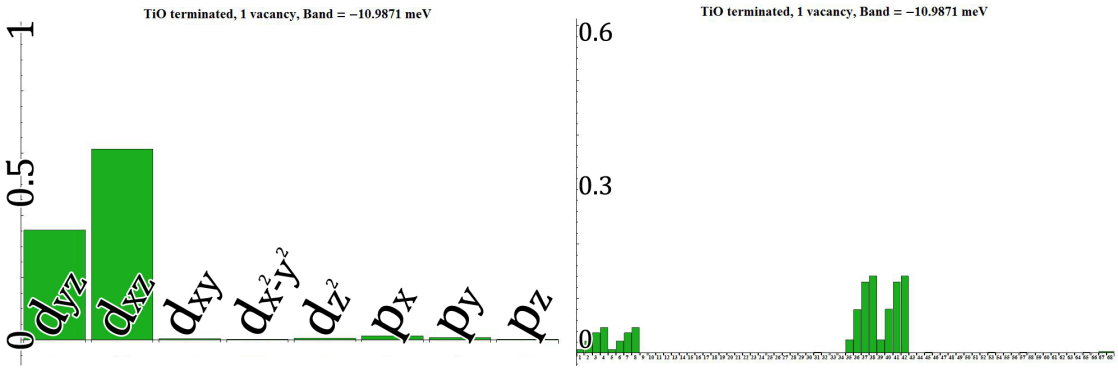

(a) Orbital (b) Sites

Figure 6.45: Other conduction states are generated. These states have the usual d_{xz}-d_{yz} character.

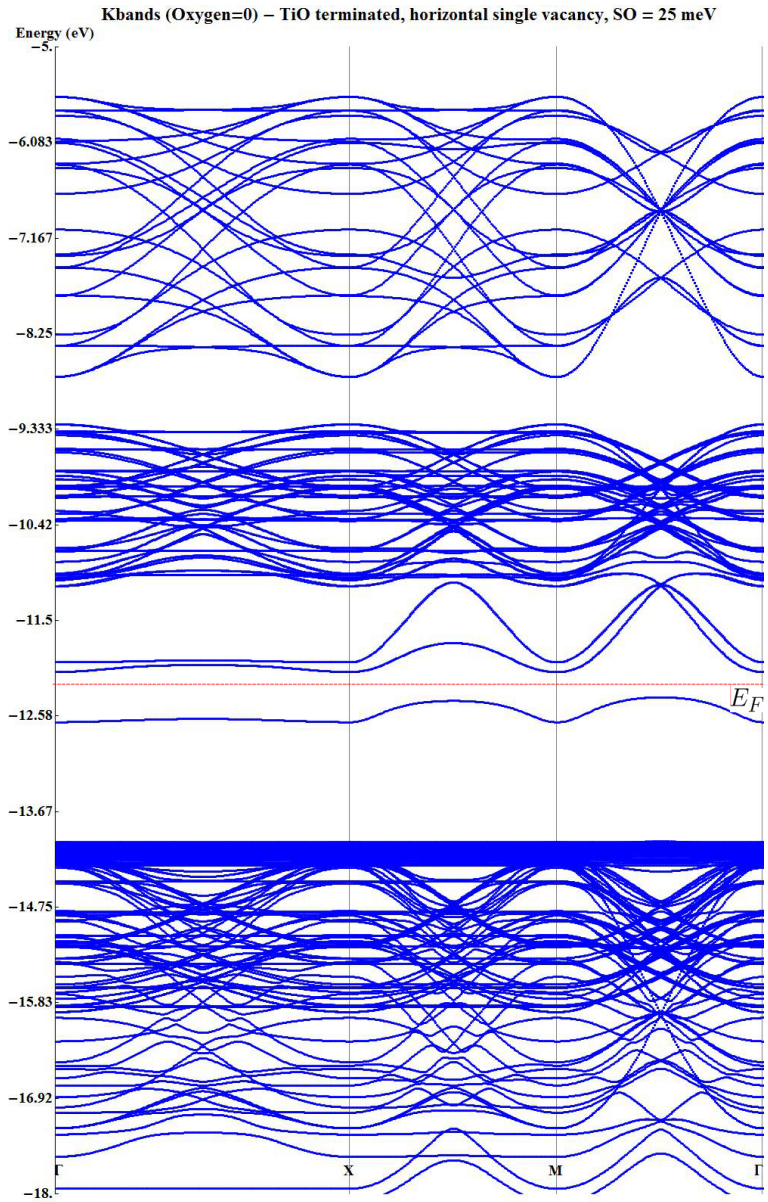

Figure 6.46: The complete band structure reveals what we have commented in the previous images. Only one band remains in the gap. This band is generated by the vacancy (they are actually two degenerate bands). The other bands belong to the conduction part. They should be higher in energy. We find them *in the gap* due to a simplification of the crystal field.

TiO_2-terminated. Two aligned vacancies in the first TiO_2 layer.

In this section we will study the configuration where two Oxygen vacancies are aligned in the y-direction in the top TiO_2-surface.

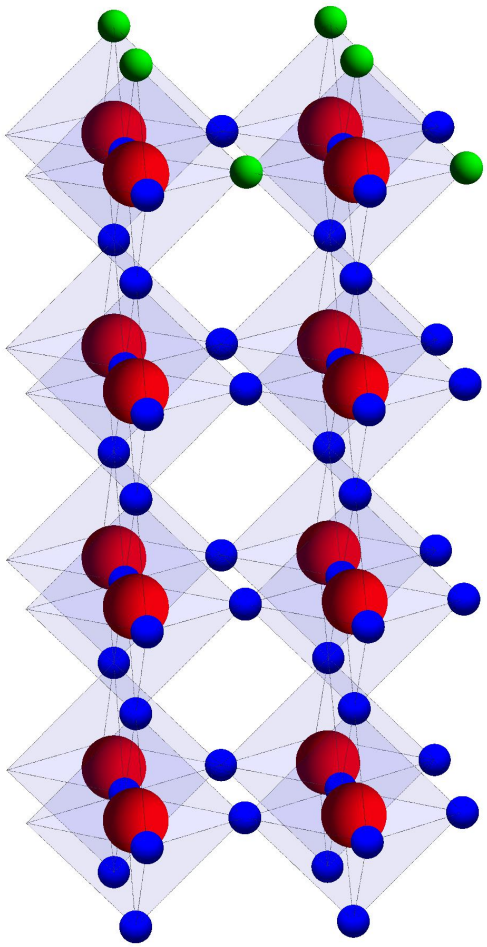

Figure 6.47: Cluster with two oxygen vacancies in the top TiO_2 surface.

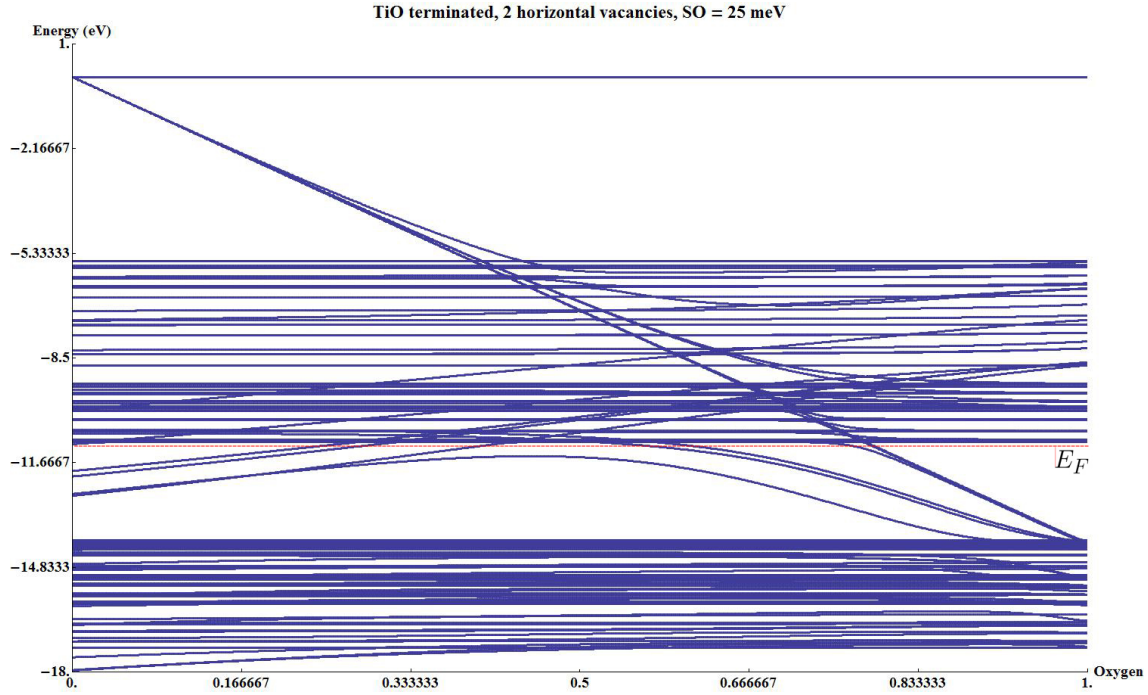

Figure 6.48: Electronic states at the Γ point when both Oxygen atoms are removed.

We find again several in-gap states and new conduction states. Some of these states are generated by the two vacancies introduced, but others are a consequence of the surface termination.

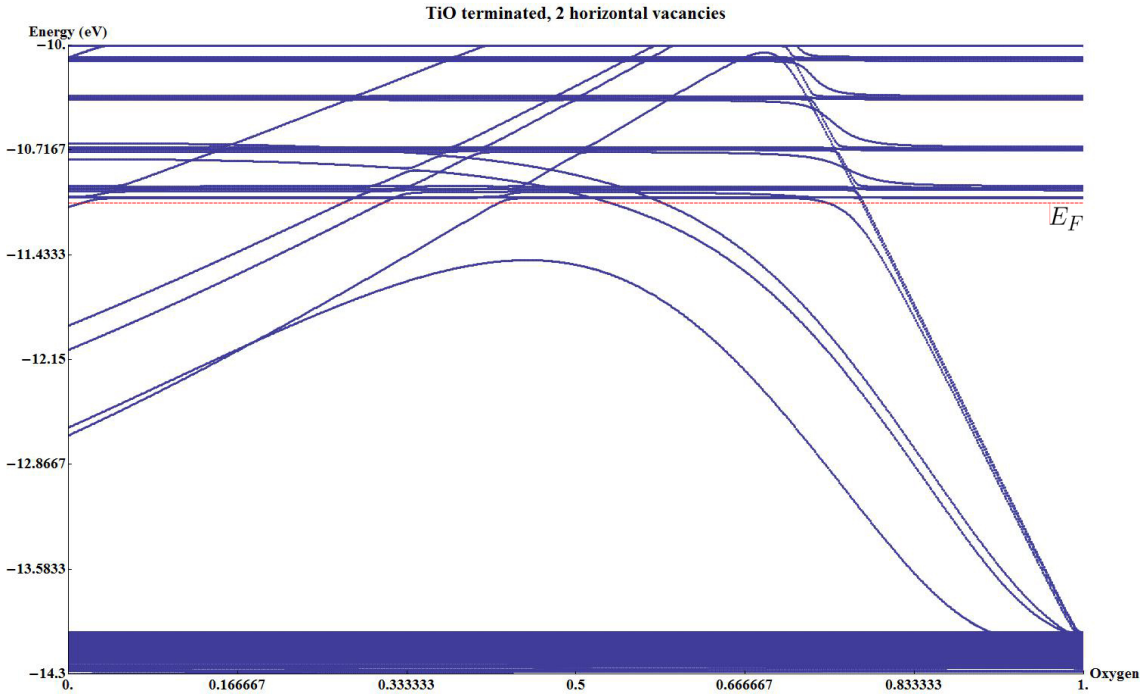

Figure 6.49: Zoom of Fig. 6.48.

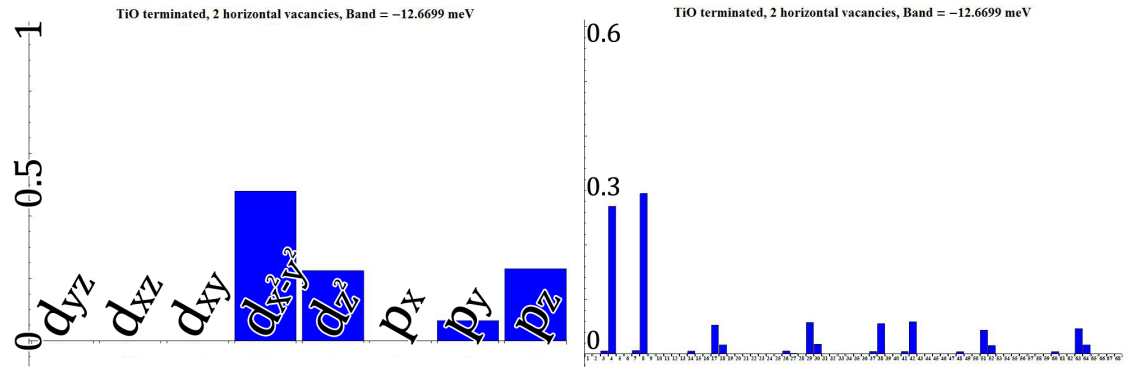

(a) Orbital (b) Sites

Figure 6.50: The first in-gap states have strong d_{z^2}-$d_{x^2-y^2}$ character and are located around the two Titanium atoms surrounding the vacancies. These degenerate states are actually generated by the two Oxygen vacancies.

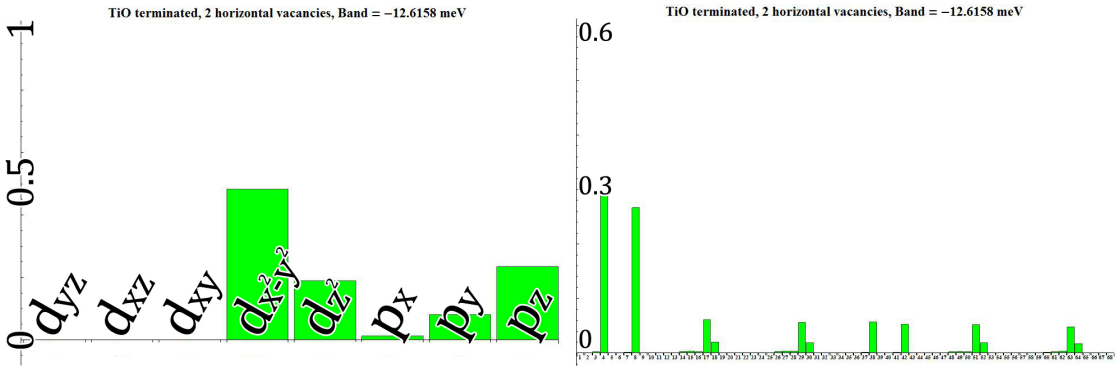

(a) Orbital (b) Sites

Figure 6.51: The second pair of in-gap states also has strong d_{z^2}-$d_{x^2-y^2}$ character and it is also located around the two Titanium atoms surrounding the vacancies.

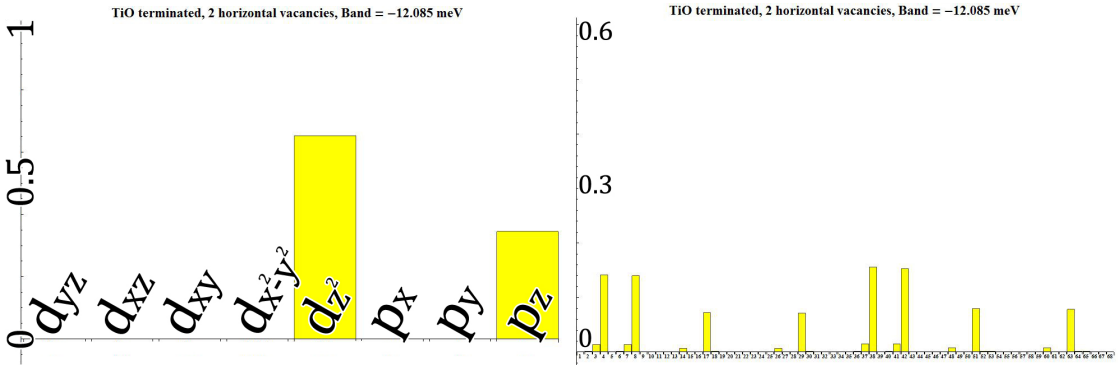

(a) Orbital (b) Sites

Figure 6.52: The third pair of states have the d_{z^2} character characteristic of apical vacancies. These states are generated by the removal of the top SrO layer. This histogram is also representative of the fourth and fifth pairs of states found in the gap. All these states should be within the conduction band because they are not generated by the vacancies.

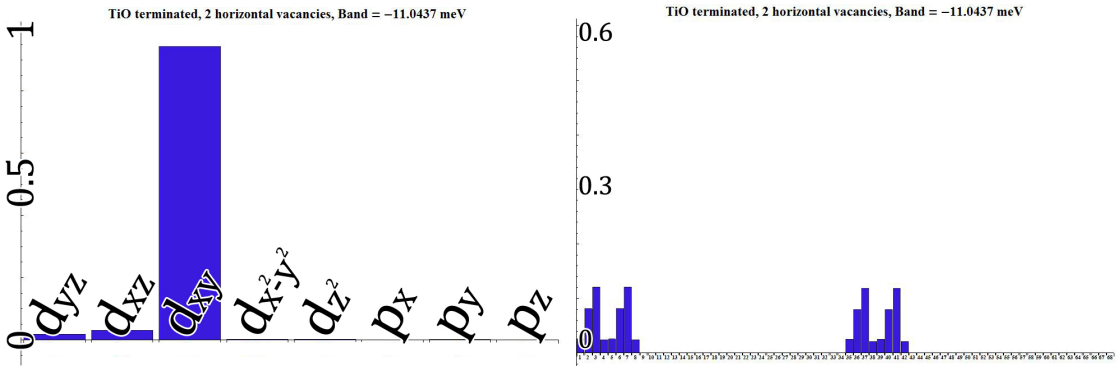

(a) Orbital (b) Sites

Figure 6.53: The bottom of the conduction band has the usual d_{xy} character.

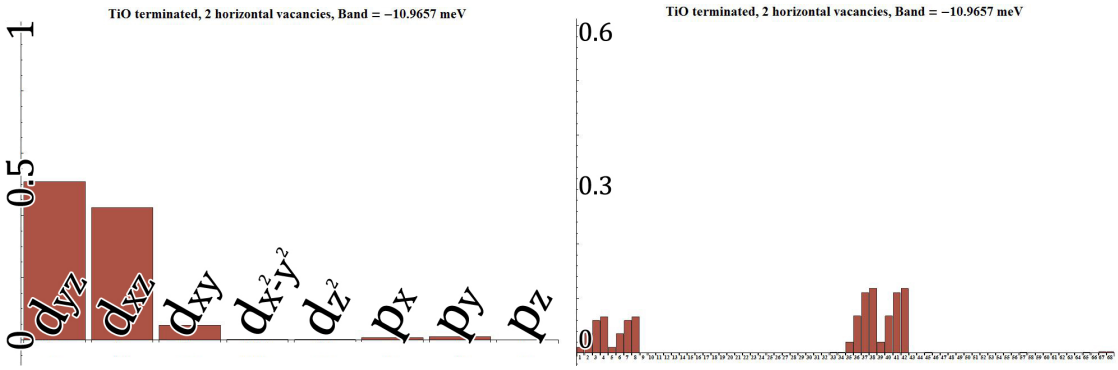

(a) Orbital (b) Sites

Figure 6.54: Other conduction states are generated. They have the t_{2g} character that we have seen in previous configurations.

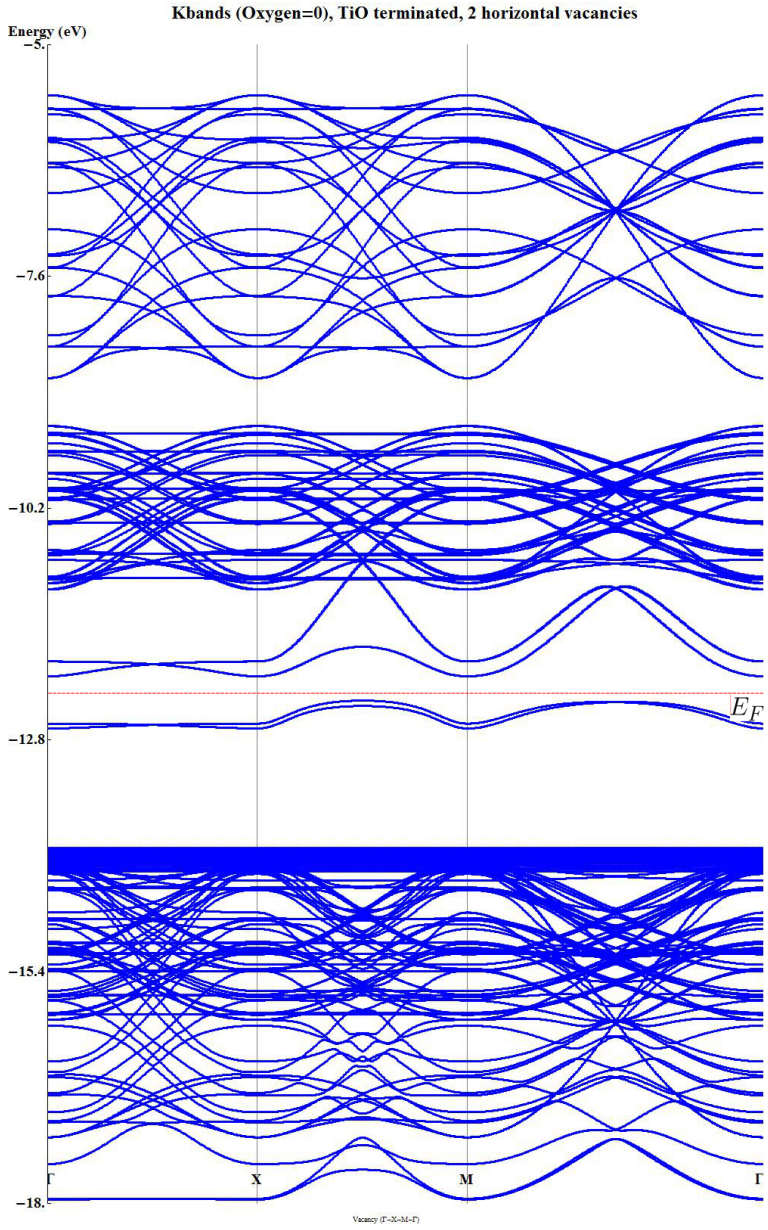

Figure 6.55: The band structure reveals that, indeed, only some of the in-gap states are actually in-gap states generated by the vacancies. The other bands are conduction bands that are too low in energy. These results are similar to the ones we found in the previous section.

TiO_2-terminated. Two apical vacancies.

The final configuration that we will show in this work is the case where we introduce two sub-surface apical vacancies below the top TiO_2 surface.

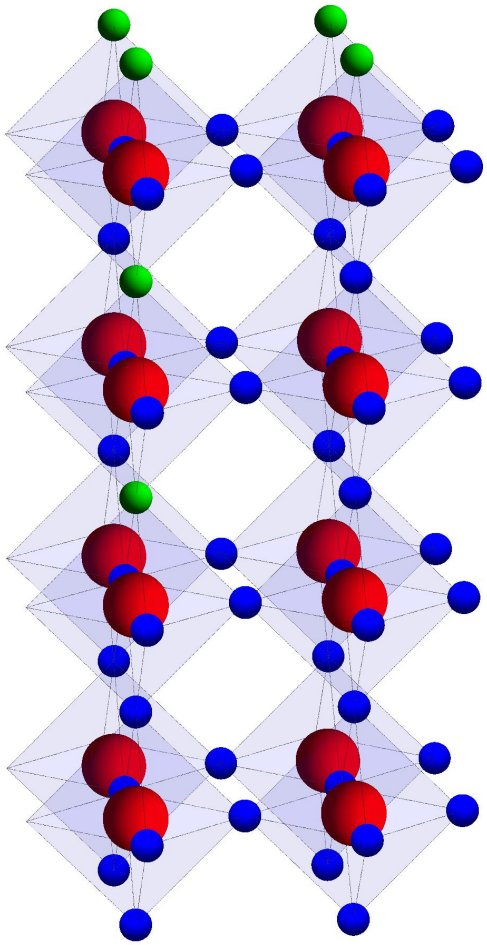

Figure 6.56: Two vertically aligned Oxygen vacancies below the TiO_2 surface.

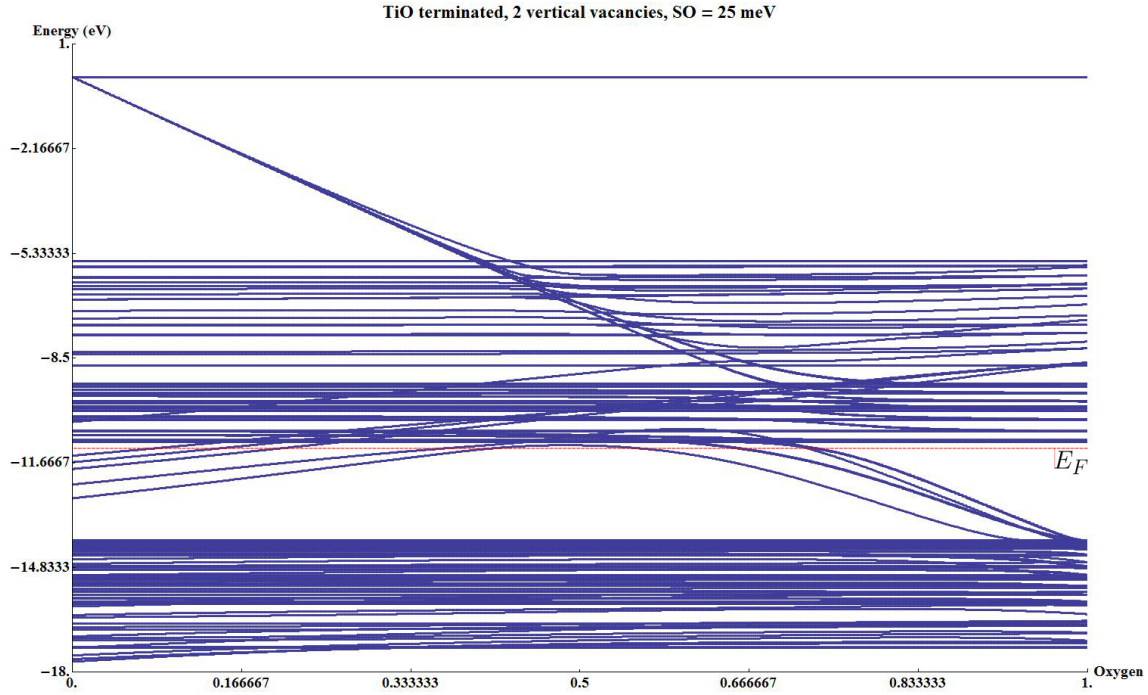

Figure 6.57: Electronic states at the Γ point when two Oxygen atoms are removed.

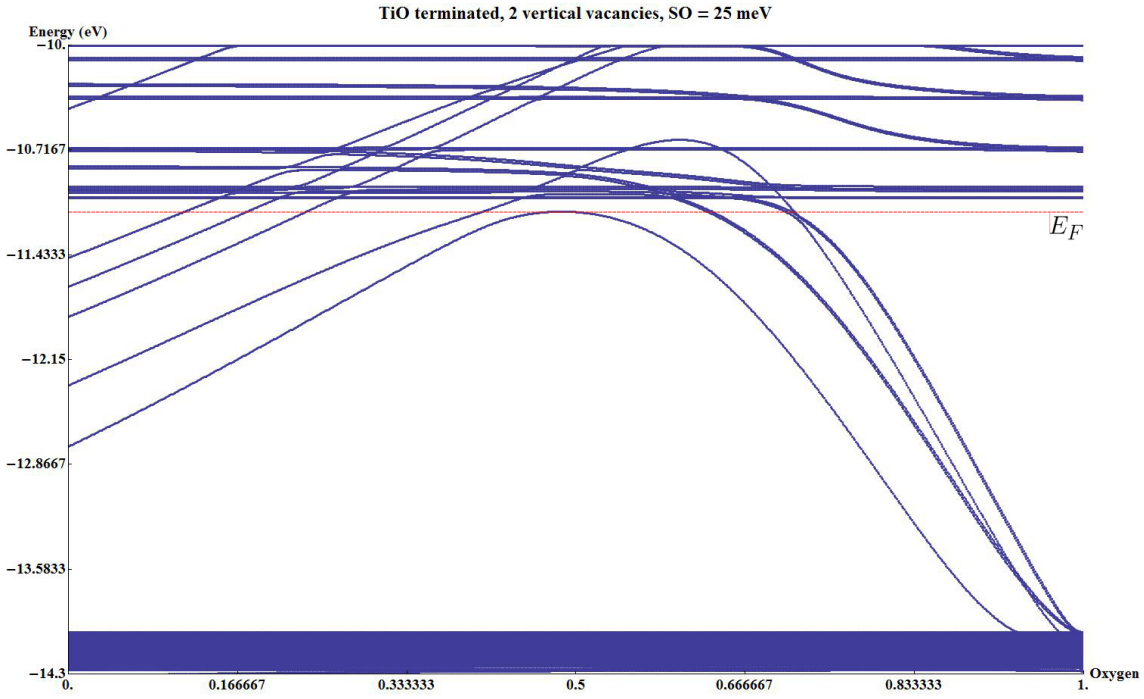

Figure 6.58: Zoom of Fig. 6.57.

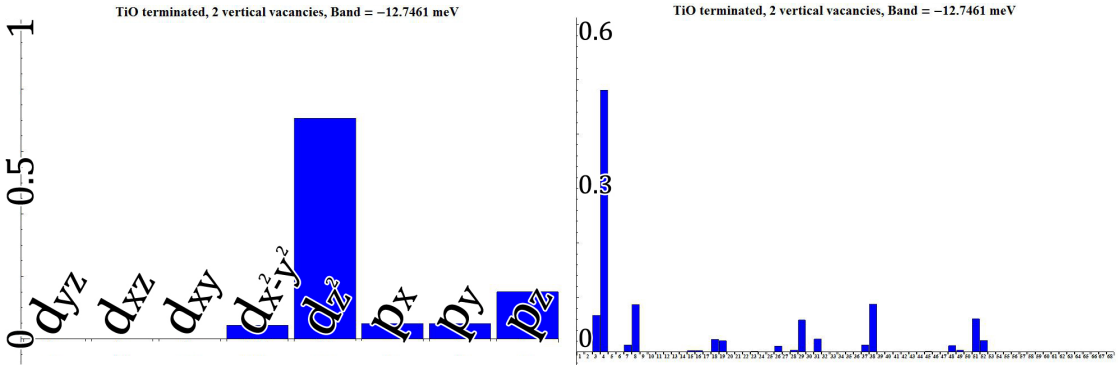

(a) Orbital (b) Sites

Figure 6.59: The first pair of in-gap states has strong d_{z^2}-p_z character and it is located around Titanium atom number 4. This state is generated because we have removed the two Oxygen atoms above and below this Titanium atom.

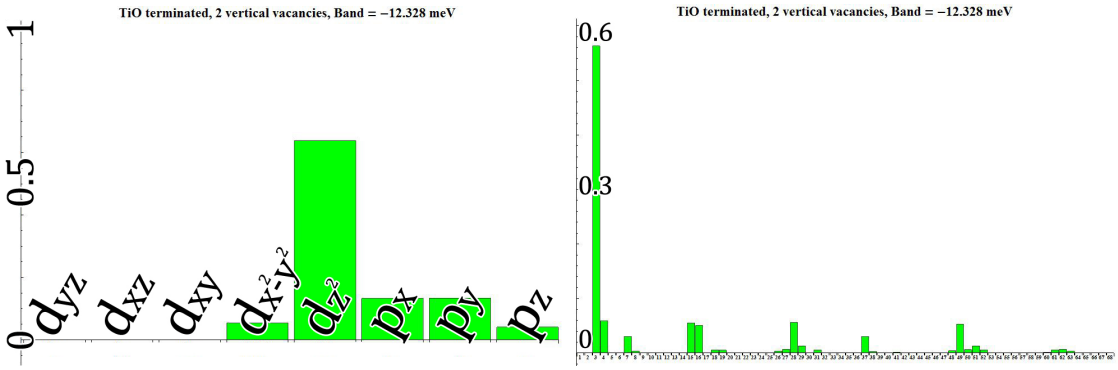

(a) Orbital (b) Sites

Figure 6.60: The second pair of in-gap states also has strong d_{z^2}-p_z character and it is located around Titanium atom number 3. This is the Titanium between the two apical vacancies. This state is very similar to the one we found when two apical vacancies were introduced in the SrO-terminated cluster.

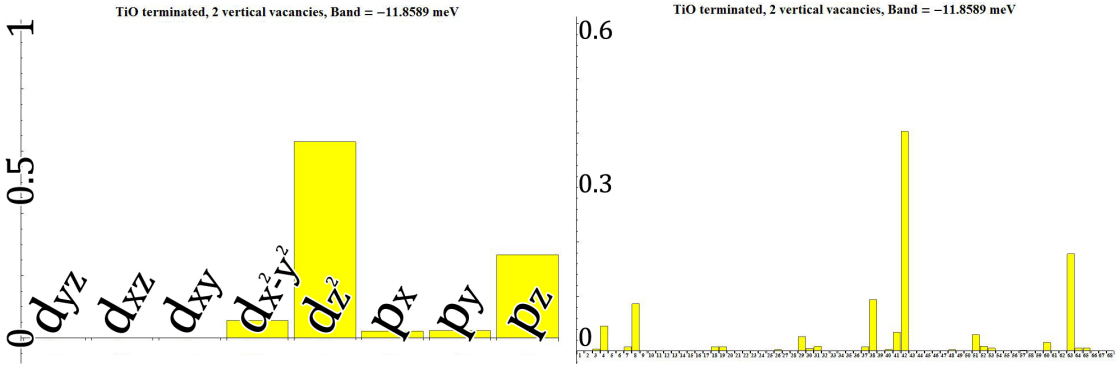

(a) Orbital (b) Sites

Figure 6.61: the next three pairs of states have the d_{z^2} character located in the first TiO_2 layer that corresponds to the vacancies introduced to remove the SrO layer. These states belong to the conduction band in theory.

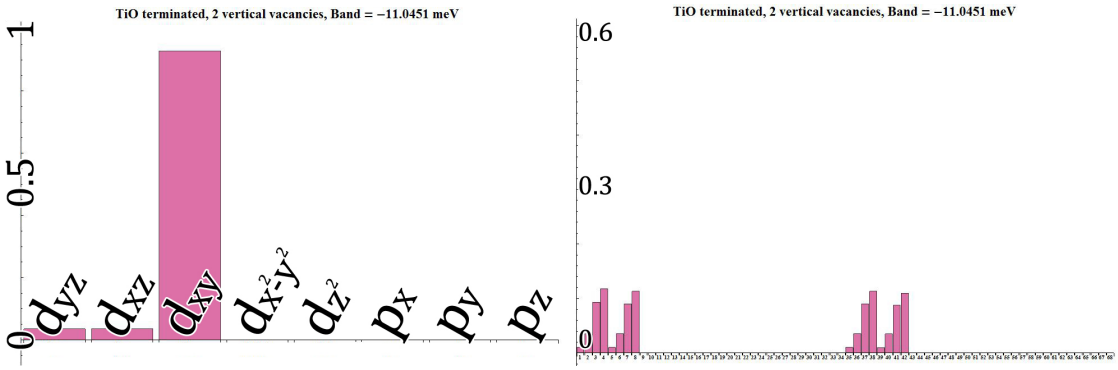

(a) Orbital (b) Sites

Figure 6.62: The bottom of the conduction band remains d_{xy}.

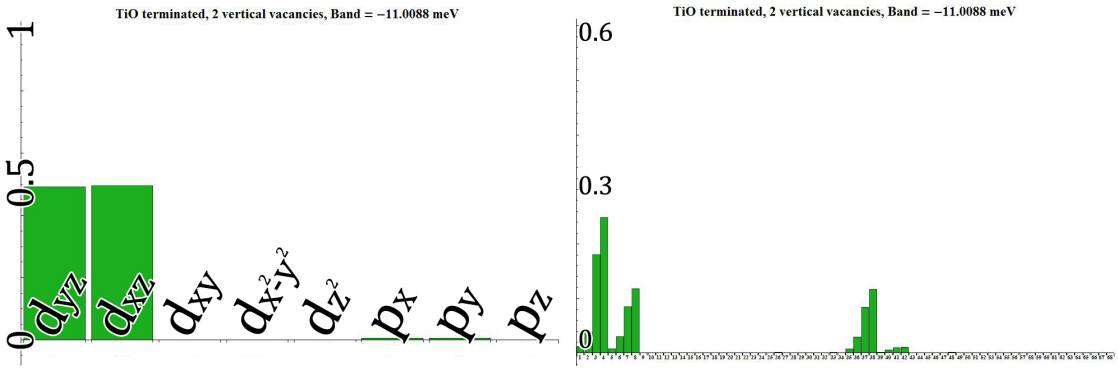

(a) Orbital (b) Sites

Figure 6.63: Other conduction t_{2g} states are generated by the vacancies. These states are similar to the ones we found in previous configurations.

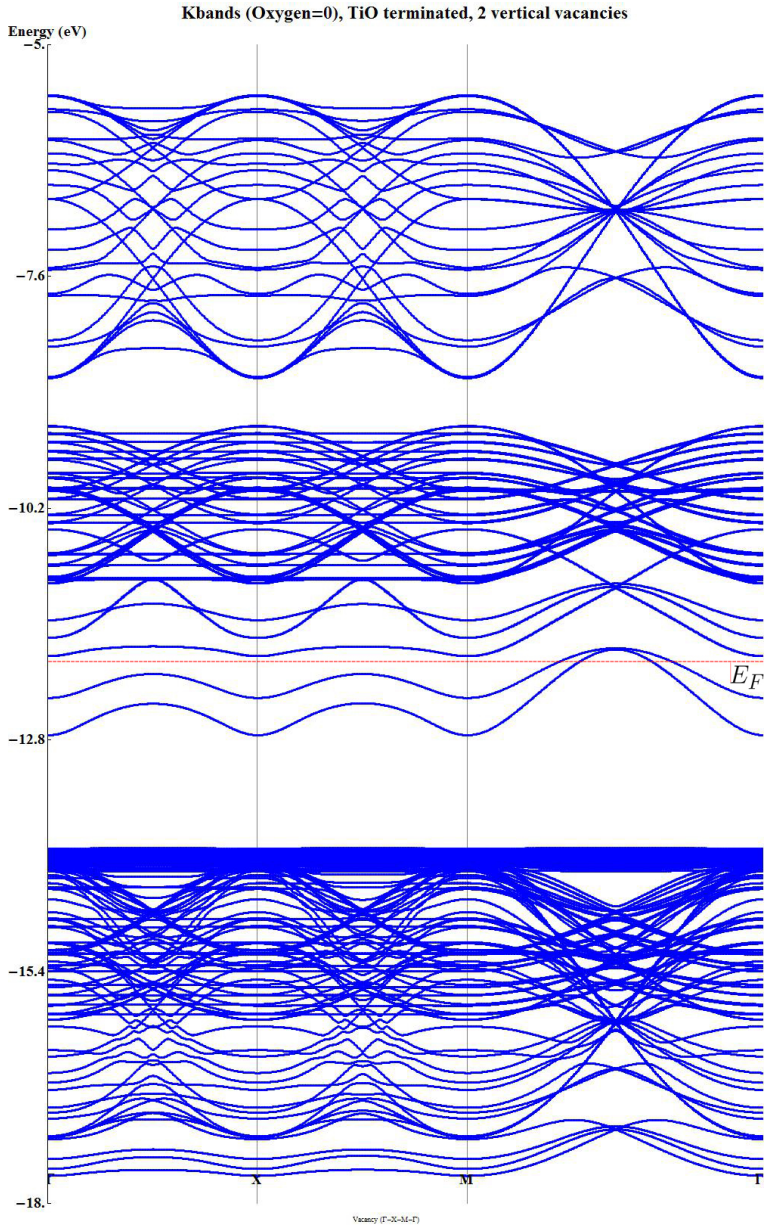

Figure 6.64: We can again see that the highest in-gap bands are actually part of the conduction states. These bands should be higher in energy. Only the bands generated by the apical vacancies remain in the gap.

Configuration	SrO termination	TiO_2 termination
No vacancies	Insulator. Valence and conduction bands separated by a gap.	Similar valence-conduction bands. Several states appear in-gap. These states actually belong to the conduction part, they should be higher in energy.
One vacancy in the SrO surface	Appearance of two degenerate in-gap d_{z^2} states and several conduction t_{2g} states.	-
One vacancy in the first TiO_2 layer	Two degenerate states appear in the gap. They have strong $d_{x^2-y^2}$ character and they are localized around the Titanium atoms surrounding the vacancy.	Similar degenerate $d_{x^2-y^2}$ appear in the gap localized around the Titanium atoms close to the vacancy.
Two vacancies vertically aligned	Two in-gap states are found. Both have strong d_{z^2} character and are located around the Titanium atoms close to the vacancy.	Similar pair of (degenerate) d_{z^2} bands appear in the gap. These states are localized around the Titanium atoms surrounded by the vacancies.
Two vacancies in the TiO_2 plane	Two pairs of degenerate states appear in the gap. They have strong $d_{x^2-y^2}$ character and they are localized around the Titanium atoms close to the vacancy.	Two pairs of degenerate $d_{x^2-y^2}$ states appear in the gap.

Table 7: Some properties of the electronic states in the 2x2x4 cluster for some configurations of Oxygen vacancies.

There are some features that seem to be universal:

- Each vacancy creates a pair of degenerate states in the gap.
- If the vacancy is created in the SrO layers, these states will show d_{z^2} character.
- If the vacancy is created in the TiO_2 layers, these states will show $d_{x^2-y^2}$ character.
- TiO_2-terminated clusters show *extra* states in the gap that should be within the conduction band.

References

1 Neil W. Ashcroft and N. David Mermin. Solid state Physics. *Saunders College, 1976. ISBN: 0030839939.*

2 Roland Winkler. Spin-orbit coupling effects in two-dimensional electron and hole systems (chapters 1-3). *Springer Tracts in Modern Physics. Volume 191 2003. ISBN: 978-3-540-01187-3.*

3 Charles Kittel. Introduction to Solid State Physics. *Wiley, 1995. ISBN: 047141526X.*

4 J. C. Slater and G. F. Koster. Simplified LCAO Method for the Periodic Potential Problem. *Physical Review. Volume 94, Number 6. June 15, 1954.*

5 S. Gariglio, M. Gabay, J. Mannhart, J.-M. Triscone. Interface Superconductivity. *Physica C Special Issue on Superconducting MaterialsGuest editors: J.E. Hirsch, M.B. Maple, F. Marsiglio, Vol 514, 189-198 (2015).*

6 P. Zubko, S. Gariglio, M. Gabay, P. Ghosez, J.-M. Triscone. Interface Physics in Complex Oxide Heterostructures. *Annu. Rev. Condens. Matter Phys. 2011.2:141-165.*

7 Claudine Chopin-Noguera. Physics and Chemistry at oxide Surfaces. *Cambridge Press. 1996. ISBN: 0 521 47214 8.*

8 Martin Silberberg. Principles of General Chemistry. *McGraw-Hill Education. 2010. ISBN: 0077274326.*

9 M. Gabay, S. Gariglio, J.-M. Triscone and A. F. Santander-Syro. 2-Dimensional oxide electronic gases: Interfaces and surfaces. *The European Physical Journal Special Topics. Volume 222, Issue 5, pp 1177-1183 (2013).*

10 N. Reyren, S. Thiel, A. D. Caviglia, L. Fitting Kourkoutis, G. Hammerl, C. Richter, C. W. Schneider, T. Kopp, A.-S. Rüetschi, D. Jaccard, M. Gabay, D. A. Muller, J.-M. Triscone, J. Mannhart. Superconducting interfaces between insulating oxides. *Science 317, 11961199 (2007).*

11 L. F. Mattheiss. Energy Bands for $KNiF_3$, $SrTiO_3$, $KMoO_3$ and $KTaO_3$. *Physical Review B. Volume 6, Number 12. 4718 (15 December 1972).*

12 L. F. Mattheiss. Effect of the 110K Phase Transition on the $SrTiO_3$ Conduction Bands. *Physical Review B. Volume 6, Number 12. 4740 (15 December*

1972).

13 G. Herranz, F. Snchez, N. Dix, M. Scigaj and J. Fontcuberta. High mobility conduction at (110) and (111) $LaAlO_3/SrTiO_3$ interfaces. *Scientific Reports, 2(110):758, (2012).*

14 N. C. Plumb, M. Salluzzo, E. Razzoli, M. Mansson, M. Falub, J. Krempasky, C.E. Matt, J. Chang, M. Schulte, J. Braun, H. Ebert, J. Minár, B. Delley, K.-J. Zhou, T. Schmitt, M. Shi, J. Mesot, L. Patthey and M. Radović. Mixed Dimensionality of Confined Conducting Electrons in the Surface Region of $SrTiO_3$. *PRL 113, 086801 (2014).*

15 T. C. Rödel, C. Bareille, F. Fortuna, F. Bertran, P. Le Fèvre, M. Gabay, O. Hijano Cubelos, M. J. Rozenberg, T. Maroutian, O. Lecoeur and A. F. Santander-Syro. Orientational tuning of the Fermi sea of confined electrons at the $SrTiO_3$ (110) and (111) surfaces. *Phys. Rev. Applied 1, 051002 (18 June 2014).*

16 S. Piskunov, E. Heifets, R. I. Eglitis and G. Borstel. Bulk properties and electronic structure of $SrTiO_3$, $BaTiO_3$, $PbTiO_3$ perovskites: an ab initio HF/DFT study. *Computational Materials Science 29 (2004) 165-178.*

17 Xinyue Fang. Phase Transitions in Strontium Titanate. *Term essays for Spring 2013. Course Physics 563: "Phase Transitions and the Renormalization Group". Department of Physics, University of Illinois at Urbana-Champaign.*

18 C. Bareille, T. Rödel, F. Fortuna, F. Bertran, M. Gabay, M. Bibes, A. Barthélémy, T. Maroutian, P. Lecoeur, J. Guevara, R. Weht, M. J. Rozenberg and A. F. Santander-Syro. Topological two-dimensional electron gas with honeycomb electronic structure at the (111) surface of $KTaO_3$. *Sci Rep. 2014; 4: 3586.*

19 C. Bareille, F. Fortuna, T. Rödel, F. Bertran, M. Gabay, O. Hijano Cubelos, A. Taleb-Ibrahimi, P. Le Fèvre, M. Bibes, A. Barthélémy, T. Maroutian, P. Lecoeur, M. J. Rozenberg and A. F. Santander-Syro. Two-Dimensional electron gas with six-fold symmetry at the (111) surface of $KTaO_3$. *Scientific Reports. 4:3586. DOI: 10.1038/srep03586. (2014).*

20 Guru Khalsa and A. H. MacDonald. Theory of the $SrTiO_3$ Surface State Two-Dimensional Electron Gas. *Phys. Rev. B 86, 125121 (17 September 2012).*

21 Matías Zilly. Electronic conduction in linear quantum systems: Coherent transport and the effects of decoherence. *PhD Dissertation. Department of Physics*

at the University of Duisburg-Essen, 2010.

22 P. R. Willmott, S. A. Pauli, R. Herger, C. M. Schleptz, D. Martoccia, B. D. Patterson, B. Delley, R. Clarke, D. Kumah, C. Cionca, and Y. Yacoby. Structural Basis for the Conducting Interface between $LaAlO_3$ and $SrTiO_3$. *Phys. Rev. Lett. 99, 155502 (2007).*

23 Zhicheng Zhong, Qinfang Zhang and Karsten Held. Quantum confinement in perovskite oxide heterostructures: tight binding instead of nearly free electron picture. *Phys. Rev. B 88, 125401 (3 September 2013).*

24 Miki Nagano, Ayaka Kodama, T. Shishidou and T. Oguchi. A first-principles study on the Rashba effect in surface systems. *J. Phys.: Condens. Matter 21 (2009) 064239. DOI: 10.1088/0953-8984/21/6/064239.*

25 A. F. Santander-Syro, F. Fortuna, C. Bareille, T. C. Rödel, G. Landolt, N. C. Plumb, J. H. Dil and M. Radović. Giant spin splitting of the two-dimensional electron gas at the surface of $SrTiO_3$. *Nature Materials. DOI: 10.1038/NMAT4107. (2014).*

26 A. F. Santander-Syro, O. Copie, T. Kondo, F. Fortuna, S. Pailhès, R. Weht, X. G. Qiu, F. Bertran, A. Nicolaou, A. Taleb-Ibrahimi, P. Le Fèvre, G. Herranz, M. Bibes, N. Reyren, Y. Apertet, P. Lecoeur, A. Barthélémy and M. J. Rozenberg. Two-dimensional electron gas with universal subbands at the surface of $SrTiO_3$. *Nature 469, 189193 (13 January 2011) doi:10.1038/nature09720.*

27 G. Bihlmayer, Yu. M. Koroteev, P. M. Echenique, E. V. Chulkov, S. Blügel. The Rashba-effect at metallic surfaces. *Surface Science 600 (2006) 3888-3891.*

28 Alejandro Lopez-Bezanilla, P. Ganesh and Peter B. Littlewood. Plentiful magnetic moments in Oxygen deficient $SrTiO_3$. *APL Mater. 3, 100701 (2015).*

29 N. Bickel, G. Schmidt, K. Heinz and K. Müller. Ferroelectric Relaxation of the $SrTiO_3$ (100) Surface. *PRL Volume 62, Number 17 (24 April 1989).*

30 Frank Lechermann, Lewin Boehnke, Daniel Grieger and Christoph Piefke. Electron correlation and magnetism at the $LaAlO_3/SrTiO_3$ interface: An DFT+DMFT investigation. *Phys. Rev. B 90, 085125.*

31 Zhiming Wang, Zhicheng Zhong, Xianfeng Hao, Stefan Gerhold, Bernhard Stöger, Michael Schmid, Jaime Sánchez-Barriga, Andrei Varykhalov, Cesare

Franchini, Karsten Held and Ulrike Diebold. Anisotropic two-dimensional electron gas at $SrTiO_3$ (110) protected by its native overlayer. *Proc Natl Acad Sci U S A. 2014 Mar 18; 111(11): 39333937. (2014).*

32 Prabir Pal, Pramod Kumar, Aswin V., Anjana Dogra and Amish G. Joshi. Chemical potential shift and gap-state formation in $SrTiO_{3-\delta}$ revealed by photoemission spectroscopy. *J. Appl. Phys. 116, 053704 (2014).*

33 K. van Benthem and C. Elsasser. Bulk electronic structure of $SrTiO_3$: Experiment and theory. *Journal of Applied Physics. Volume 90, number 12. 15-December-2001.*

34 Zhong Fang, Kiyoyuki Terakura. Spin and orbital polarizations around Oxygen vacancies on the (001) surfaces of $SrTiO_3$. *Surface Science 470 (2000) L75-L80.*

35 Guru Khalsa, Byounghak Lee and A. H. MacDonald. Theory of t_{2g} electron-gas Rashba interactions. *Phys. Rev. B 88, 041302(R). (2013).*

36 N. Pavlenko, T. Kopp, E. Y. Tsymbal, G. A. Sawatzky and J. Mannhart. Magnetic and superconducting phases at the $LaAlO_3/SrTiO_3$ interface: The role of interfacial Ti 3*d* electrons. *Physical Review B 85, 020407(R) (2012).*

37 A. Ohtomo and H. Y. Hwang. A high-mobility electron gas at the $LaAlO_3/SrTiO_3$ heterointerface. *Nature Vol 427. 29 January 2004.*

38 K. Yoshimatsu, K. Horiba, H. Kumigashira, T. Yoshida, A. Fujimori, M. Oshima. Metallic Quantum Well States in Artificial Structures of Strongly Correlated Oxide. *Science (15 July 2011). Vol. 333 no. 6040 pp. 319-322. DOI: 10.1126/science.1205771.*

39 Beena Kalisky, Eric M. Spanton, hilary Noad, John R. Kirtley, Katja C. Nowack, Christopher Bell, Hiroki K. Sato, Masayuki Hosoda, Yanwu Xie, Yasuyuki Hikita, Carsten Woltmann, Georg Pfanzelt, Rainer Jany, Cristoph Richter, Harold Y. Hwang, Jochen Mannhart and Kathryn A. Moler. Locally enhanced conductivity due to the tetragonal domain structure in the $LaAlO_3/SrTiO_3$ heterointerfaces. *Nature Materials. DOI: 10.1038/NMAT3753 (8 September 2013).*

40 Lu Li, C. Richter, J. Mannhart and R. C. Ashoori. Coexistence of magnetic order and two-dimensional superconductivity at $LaAlO_3/SrTiO_3$ interfaces. *Nature Physics. DOI: 10.1038/NPHYS2080 (4 September 2011).*

41 M. Huijben, G. Rijnders, D. H. A. Blank, S. Bals, S. V. Aert, J. Verbeeck, G. V. Tendeloo, A. Brinkman, and H. Hilgenkamp. Electronically coupled complementary interfaces between perovskite band insulators. *Nature Materials 5, 556 (2006).*

42 S. Thiel, G. Hammerl, A. Schmehl, C. W. Schneider, and J. Mannhart. Tunable quasi-two-dimensional electron gases in oxide heterostructures. *Science 313, 1942-1945 (2006).*

43 S. McKeown Walker, A. de la Torre, F. Y. Bruno, A. Tamai, T. K. Kim, M. Hoesch, M. Shi, M. S. Bahramy, P. D. C. King and F. Baumberger. Control of a two-dimensional electron gas on $SrTiO_3$ (111) by atomic Oxygen. *Phys. Rev. Lett., 113, 177601 (2014).*

44 Satoshi Okamoto, Wenguang Zhu, Yusuke Nomura, Ryotaro Arita, Di Xiao and naoto Nagaosa. Correlation effects in (111) bilayers of perovskite transition-metal oxides. *Phys. Rev. B 89, 195121. (2014)*

45 Markus König, Hartmut Buhmann, Laurens W. Molenkamp, Taylor Hughes, Chao-Xing Liu, Xiao-Liang Qi and Shou-Cheng Zhang. The Quantum Spin Hall Effect: Theory and Eperiment. *Journal of the Physical Society of Japan. Vol. 77, No 3 (March, 2008), 031007.*

46 Markus König, *et al.* Quantum Spin Hall Insulator State in $HgTe$ Quantum Wells. *Science 318, 766 (2007); DOI: 10.1126/science.1148047.*

47 Xiao-Liang Qi and Shou-Cheng Zhang. Topological insulators and superconductors. *Rev. Mod. Phys. 83, 1057. (2011).*

48 A. F. Santander-Syro, C. Bareille, F. Fortuna, O. Copie, M. Gabay, F. Bertran, A. Taleb-Ibrahimi, P. Le Fèvre, G. Herranz, N. Reyren, M. Bibes, A. Barthlmy, P. Lecoeur, J. Guevara, and M. J. Rozenberg. Orbital symmetry reconstruction and strong mass renormalization in the two-dimensional electron gas at the surface of $KTaO_3$. *Phys. Rev. B. 86, 121107(R) (2012).*

49 A. Janotti, D. Steiauf and C. G. Van de Walle. Strain effects on the electronic structure of $SrTiO_3$: Toward high electron mobilities. *Physical Review B 84, 201304(R) (2011).*

50 Ulrich Aschauer and Nicola A. Spaldin. Competition and cooperation between antiferrodistortive and ferroelectric instabilities in $SrTiO_3$. *J. Phys.: Condens. Matter 26 (2014) 122203.*

51 Hai-Yuan Cao, Shiyong Tan, Hongjun Xiang, D. L. Feng and Xin-Gao Gong. The interfacial effeccts on the spin density wave in $FeSe/SrTiO_3$ thin film. *Phys. Rev. B 89, 014501.*

52 Fedwa El-Mellouhi, Edward N. Brothers, Melissa J. Lucero, Ireneusz W. Bulik and Gustavo E. Scuseria. Structural Phase Transitions of the Metal Oxide Perovskites $SrTiO_3$, $LaAlO_3$ and $LaTiO_3$ Studied with a Screened Hybrid Functional. *Phys. Rev. B 87, 035107.*

53 Wanxiang Feng, Jun Wen, Jinjian Zhou, Di Xiao and Yugui Yao. Firt-principles calculation of topological invariants Z_2 within the FP-LAPW formalism. *Computer Physics Communications. Volume 183, Issue 9, September 2012, Pages 18491859.*

54 David J. Thouless. Topological Quantum Numbers in Nonrelativistic Physics. *World Scientific, 1998. ISBN: 9810229003.*

55 R. Bistritzer, G. Khalsa abd A. H. MacDonald. Electronic structure of doped d^0 perovskite semiconductors. *Physical Review B 83, 115114 (2011).*

56 R. Naoyuki Nakagawa, Harold Y. Hwang and David A. Muller. Why some interfaces cannot be sharp. *Nature Materials 5, 204 - 209 (2006).*

57 Markus König, Hartmut Buhmann, Laurens W. Molenkamp, Taylor Hughes, Chao-Xing Liu, Xiao-Liang Qi and Shou-Cheng Zhang. The Quantum Spin Hall Effect: Theory and Experiment. *Journal of the Physical Society of Japan. Vol.77, No. 3, (March, 2008), 031007.*

58 T. Thonhauser and David Vanderbilt. Insulator/Chern-insulator transition in the Haldane model. *Physical Review B 74, 235111 (2006).*

59 Di Xiao, Wenguang Zhu, Ying Ran, Naoto Nagaosa and Satoshi Okamoto. Interface engineering of quantum Hall effects in digital heterostructures of transition-metal oxides.
Nature Communications 2, Article number: 596 doi:10.1038/ncomms1602.

60 Liang Fu and C. L. Kane. Topological insulators with inversion symmetry. *Physical Review B 76, 045302 (2007).*

61 Jean-Noël Fuchs. Dirac fermions in graphene and analogues: magnetic field and topological properties. Chapters 1,3. *Habilitation à diriger des recherches (2013).*

62 Won-joon Son, Eunae Cho, Bora Lee, Jaichan Lee and Seungwu Han. Density and spatial distribution of charge carriers in the intrinsic n-type $LaAlO_3 - SrTiO_3$ interface. *Physical Review B 79, 245411 (2009).*

63 Nirmal Ganguli and Paul J. Kelly. Tuning ferromagnetism at interfaces between insulating perovskite oxides. *Phys. Rev. Lett. 113, 127201 .*

64 Marc Gabay and Jean-Marc Triscone. Hund rules with a twist. *Nature Physics, 9, 610 (2013).*

65 Harald O. Jeschke, Juan Shen and Roser Valentí. Localized versus itinerant states created by multiple Oxygen vacancies in $SrTiO_3$. *New J. Phys. 17 (2015) 023034.*

66 Juan Shen, Hunpyo Lee, Roser Valentí and Harald O. Jeschke. *Ab initio* study of the two-dimensional metallic state at the surface of $SrTiO_3$: importance of Oxygen vacancies. *Phys. Rev. B 86, 195119. (2012).*

67 Alexandre Fête. Magnetotransport experiments at the $LaAlO_3/SrTiO_3$ interface. *PhD thesis. Université de Genève. Section de Physique. Département de la matière condensée.*

68 Horst L. Stormer, Daniel C. Tsui, and Arthur C. Gossard. The fractional quantum Hall effect. *Rev. Mod. Phys. 71, S298. (1999).*

69 K. van Benthem and C. Elsasser. Bulk electronic structure of $SrTiO_3$: Experiment and theory. *Journal of Applied Physics. Volume 90. Number12. (15 December 2001).*

70 A. Hachemi, H. Hachemi, A. Ferhat-Hamida and L. Louail. Elasticity of $/SrTiO_3$ perovskite under high pressure in cubic, tetragonal and orthorhombic phases. *Phys. Scr. 82 (2010) 025602 (8pp)*

71 S. A. Hayward and E. K. H. Saljel. Cubic-tetragonal phase transition in $SrTiO_3$ revisited: Landau theory and transition mechanism. *Phase Transitions: A Multinational Journal, 68:3, 501-522 (1999).*

72 J. Goniakowski and C. Noguera. Insulating oxide surfaces and nano-structures. *ref*

73 Jacek Goniakowski, Fabio Finocchi and Claudine Noguera. Polarity of oxide surfaces and nanostructures. *Reports on Progress in Physics 71 (2008) 016501.*

74 Claudine Noguera and Jacek Goniakowski. Polarity in oxide nano-objects. *Chemical Review 113 (2013) 4073-4105.*

75 J. Goniakowski, C. Noguera. The concept of weak polarity: an application to the $SrTiO_3$ (001) surface. *Surface Science Letters 365 (1996) L657.*

76 A. Pojani, F. Finocchi, C. Noguera. Polarity on the $SrTiO_3$ (111) and (110) surfaces. *Surface Science 442 (1999) 179-198.*

77 F. Bottin, F. Finocchi, C. Noguera. Stability and electronic structure of the $(1x1)$ $SrTiO_3$ (110) polar surfaces by first-principles calculations. *Physical Review B 68, 035418 (2003).*

78 D. Pesquera, M. Scigaj, P. Gargiani, A. Barla, J. Herrero-Martín, E. Pellegrin, S. M. Valvidares, J. Gázquez, M. Varela, N. Dix, J. Fontcuberta, F. Sánchez, and G. Herranz. Two-Dimensional Electron Gases at $LaAlO_3/SrTiO_3$ Interfaces: Orbital Symmetry and Hierarchy Engineered by Crystal Orientation. *Physical Review Letters 113 (2014). 156802.*

79 Mateusz Scigaj, Jaume Gázquez, María Varela, Josep Fontcuberta, Gervasi Herranz, Florencio Sánchez. Conducting interfaces between amorphous oxide layers and $SrTiO_3$ (110) and $SrTiO_3$ (111). *Solid State Ionics. Volume 281, 15 November 2015, Pages 6872. doi:10.1016/j.ssi.2015.09.002.*

80 Michaela Altmeyer, Harald O. Jeschke, Oliver Hijano-Cubelos, Cyril Martins, Frank Lechermann, Klaus Koepernik, Andres Santander-Syro, Marcelo J. Rozenberg, Roser Valentí, Marc Gabay. Magnetism, spin texture and in-gap states: Atomic specialization at the surface of oxygen-deficient SrTiO3. *arXiv:1511.08614.*

Published articles

1. **Two-Dimensional electron gas with six-fold symmetry at the** (111) **surface of** $KTaO_3$**.**
   C. Bareille, F. Fortuna, T. Rödel, F. Bertran, M. Gabay, O. Hijano Cubelos, A. Taleb-Ibrahimi, P. Le Fèvre, M. Bibes, A. Barthélémy, T. Maroutian, P. Lecoeur, M. J. Rozenberg and A. F. Santander-Syro.
   Scientific Reports. 4:3586. DOI: 10.1038/srep03586.

2. **Orientational tuning of the Fermi sea of confined electrons at the** $SrTiO_3$ (110) **and** (111) **surfaces.**
   T. C. Rödel, C. Bareille, F. Fortuna, F. Bertran, P. Le Fèvre, M. Gabay, O. Hijano Cubelos, M. J. Rozenberg, T. Maroutian, O. Lecoeur and A. F. Santander-Syro.
   Phys. Rev. Applied 1, 051002 (18 June 2014).

3. **Magnetism, spin texture and in-gap states: Atomic specialization at the surface of oxygen-deficient SrTiO3.**
   Michaela Altmeyer, Harald O. Jeschke, Oliver Hijano-Cubelos, Cyril Martins, Frank Lechermann, Klaus Koepernik, Andres Santander-Syro, Marcelo J. Rozenberg, Roser Valenti, Marc Gabay.
   arXiv:1511.08614.

SCIENTIFIC REPORTS

OPEN

SUBJECT AREAS:
SURFACES, INTERFACES AND THIN FILMS
ELECTRONIC PROPERTIES AND MATERIALS

Received
7 August 2013

Accepted
3 December 2013

Published
7 January 2014

Correspondence and requests for materials should be addressed to A.F.S.-S. (andres.santander@csnsm.in2p3.fr)

Two-dimensional electron gas with six-fold symmetry at the (111) surface of $KTaO_3$

C. Bareille[1], F. Fortuna[1], T. C. Rödel[1,2], F. Bertran[3], M. Gabay[4], O. Hijano Cubelos[4], A. Taleb-Ibrahimi[3], P. Le Fèvre[3], M. Bibes[5], A. Barthélémy[5], T. Maroutian[6], P. Lecoeur[6], M. J. Rozenberg[4] & A. F. Santander-Syro[1]

[1]CSNSM, Université Paris-Sud and CNRS/IN2P3, Bâtiments 104 et 108, 91405 Orsay cedex, France, [2]Universität Würzburg, Experimentelle Physik VII, Am Hubland, 97074 Würzburg, Germany, [3]Synchrotron SOLEIL, L'Orme des Merisiers, Saint-Aubin-BP48, 91192 Gif-sur-Yvette, France, [4]Laboratoire de Physique des Solides, Université Paris-Sud and CNRS, Bâtiment 510, 91405 Orsay, France, [5]Unité Mixte de Physique CNRS/Thales, Campus de l'Ecole Polytechnique, 1 Av. A. Fresnel, 91767 Palaiseau, France and Université Paris-Sud, 91405 Orsay, France, [6]Institut d'Electronique Fondamentale, Université Paris-Sud and CNRS, Bâtiment 220, 91405 Orsay, France.

Two-dimensional electron gases (2DEGs) at transition-metal oxide (TMO) interfaces, and boundary states in topological insulators, are being intensively investigated. The former system harbors superconductivity, large magneto-resistance, and ferromagnetism. In the latter, honeycomb-lattice geometry plus bulk spin-orbit interactions lead to topologically protected spin-polarized bands. 2DEGs in TMOs with a honeycomb-like structure could yield new states of matter, but they had not been experimentally realized, yet. We successfully created a 2DEG at the (111) surface of $KTaO_3$, a strong insulator with large spin-orbit coupling. Its confined states form a network of weakly-dispersing electronic gutters with 6-fold symmetry, a topology novel to all known oxide-based 2DEGs. If those pertain to just one Ta-(111) bilayer, model calculations predict that it can be a topological metal. Our findings demonstrate that completely new electronic states, with symmetries not realized in the bulk, can be tailored in oxide surfaces, promising for TMO-based devices.

The realization of 2DEGs at surfaces or interfaces of transition-metal oxides is a field of bursting activity[1–13]. These materials are usually correlated-electron systems presenting a wealth of unique properties, such as high-temperature superconductivity, colossal magnetoresistance, metal-to-insulator transitions, or multiferroic behaviour. In the search for new functionalities and future electronic device applications, a crucial challenge is to find original ways to design the oxide-based 2DEGs, so as to endow them with the exotic physics of their parent compounds, and to tailor novel states of matter.

Research in non-trivial topological edge states is also a very active field[14–19]. The possibility of realizing these in oxide-based 2DEGs, raised in several recent theoretical works[20–24], is attracting much interest. A practical proposal was based on a key insight: that the cubic ABO_3 perovskite structure, common to many correlated oxides, realizes a honeycomb lattice when a bilayer along the [111] direction is considered[20,23,24]. Such artificial structure could, in principle, be digitally engineered as a sandwich between two oxide insulators[20]. However, this approach currently remains a technological challenge.

Here we take an alternative route towards the same goal. Beyond the realization of 2DEGS at $LaAlO_3/SrTiO_3$ interfaces oriented along [001][1], and lately [110] and [111] cristallographic directions[25,26], it was recently discovered that 2DEGs can be simply obtained at the vacuum-cleaved (001) surface of insulating ABO_3 perovskites[10–13] opening an exciting perspective to create novel 2DEGs at the surface of correlated oxides. Following this methodology, here we demonstrate that the Fermi sea of the 2DEG can be crafted by properly choosing the cleaving plane of the perovskite crystal. Specifically, we obtain a 2DEG at the (111) surface of the strong spin-orbit coupled insulator $KTaO_3$ (KTO), and determine directly its electronic structure using angle-resolved photoemission spectroscopy (ARPES). We observe an open Fermi surface of 6-fold symmetry with weakly dispersing branches, which is unique among all other previously known oxide-based 2DEGs. Using model calculations we show that it originates from electron hopping between consecutive layers of Ta atoms along the [111]

direction. Furthermore, by analyzing the symmetries of this electronic structure, we demonstrate that confining this novel 2DEG to a bilayer of Ta atoms, hence a *honeycomb* lattice, will lead to a *topological metal*.

Results

Basic considerations: structure of $KTaO_3$ along the [111] direction. Figure 1(a) presents the crystal structure of $KTaO_3$. Along the [111] direction, the system has 3-fold symmetry, as any cubic system, and consists of alternating layers of Ta and KO_3. There are three different Ta-(111) layers per unit cell, labelled Ta-I, Ta-II and Ta-III. Figure 1(b) shows the Ta atoms in the 3D structure seen from the [111] direction. Arrows represent the lattice vectors of a 2D unit cell in the (111) plane, which corresponds to a centered hexagonal network with 6-fold symmetry. When only two layers are considered (Ta-I and Ta-II, for example), the lattice formed by nearest neighbors is a honeycomb lattice (thick black lines), similar to the bilayer structure proposed in Ref. 20. As we shall see later, our ARPES data are consistent with the formation of a 2DEG with the periodicity and the symmetry of an unresconstructed (111) plane.

Experimental electronic structure. Figure 2(a) shows the Fermi surface (color map) of the 2DEG measured at the (111) surface of *transparent and bulk insulating* KTO, pictured in Fig. 2(b). Experimental details of the extraction of this Fermi surface are given in the Supplementary Material. The black hexagons in figure 2(a) represent the Brillouin zone of the unreconstructed (111) surface. Note that the observed Fermi surface has a well defined 6-fold symmetry and a periodicity corresponding to that of the unreconstructed KTO-(111) layers. By Bloch theorem, we infer that the 2DEG is formed by itinerant conduction electrons experiencing an in-plane potential compatible with unreconstructed (111) layers. In turn, this strongly suggests that, while one might expect that the highly-polar KTO-(111) surface reconstructs, the observed 2DEG is formed by electrons confined in unreconstructed subsurface layers.

More specifically, the Fermi surface of Fig. 2(a) consists of 6 branches extending out from $\overline{\Gamma}$ to the six $\overline{M}$ points. From the area enclosed by this Fermi surface, we obtain a carrier density $n_{2D} \sim 10^{14}$ cm^{-2}. The observation of such a large Fermi surface fully supports the quasi-2D (*i.e.*, confined) character of the electron gas. Indeed, if the Fermi surface was a cross-section of an hypothetical 3D Fermi surface, the ensuing electron density would be, by simple scaling, $n_{3D} \sim n_{2D}^{3/2} \sim 10^{21}$cm^{-3}. For such density, only one order of magnitude smaller than that of pure gold, the sample would be highly conducting and its aspect would be mirror-like, in stark contrast with the transparent character of the bulk crystal shown in figure 2(b), indicative of an insulating state.

Different energy-momentum intensity maps across the Fermi sea provide valuable complementary information about the 2DEG at the (111) surface of KTO. Figures 2(c, d) show the dispersion along the $\langle\bar{1}10\rangle$ direction, dashed green line in figure 2(a), in the form of, respectively, intensity map and stack of momentum distribution curves (MDCs). This dispersion indicates that the Fermi surface branches are formed by electron-like bands coming close to each other near $\overline{\Gamma}$. The effective mass of these electron-like bands, deduced from a parabolic fit (red dashed lines), is $m^*_{\langle\bar{1}10\rangle} \approx 0.3 m_e$ (m_e is the free electron mass). Furthermore, as shown by the stack of energy distribution curves (EDCs) in figure 2 (e), the bottom of each of these electron bands is essentially non-dispersive along the $\overline{\Gamma M}$ direction. Accordingly, the Fermi surface forms a star with six open branches, each branch being composed of two quasi-parallel sheets. In other words, the electronic structure of the 2DEG at the (111) surface of KTO consists of a network of weakly dispersing "electron gutters".

Since we observe only the first subband (E_1) of the 2DEG, we can only estimate an upper limit for the extension L of the 2DEG. We make the reasonable assumptions that $E_1 \approx -V_0$, where V_0 is the depth of the confining potential well, and that the next quantum level (E_2) of the same nature as the measured subband lies at an energy $E_2 - E_1 \approx V_0$, at or above E_F. The result, detailed in the Supplementary Material, is $L < 16$ Å, or equivalently, $L < 7$ Ta-layers along (111).

Note, from figures 2(c–e), that there is an intense background below $E = -260$ meV trailing behind the bands forming the 2DEG. The most likely origin of this background is inelastic scattering of the electrons off impurities or disorder. This can be either in-plane scattering, which will broaden the spectral lines, or scattering of the electron on its way out of the surface during the photoemission process. For instance, we expect that the fractured native surface will be rugged, and will contain a large density of vacancies. Thus, a large number of photo-emitted electrons will loose some kinetic energy, due to inelastic scattering, on their way out of the solid. All these electrons will contribute to an intense inelastic background trailing

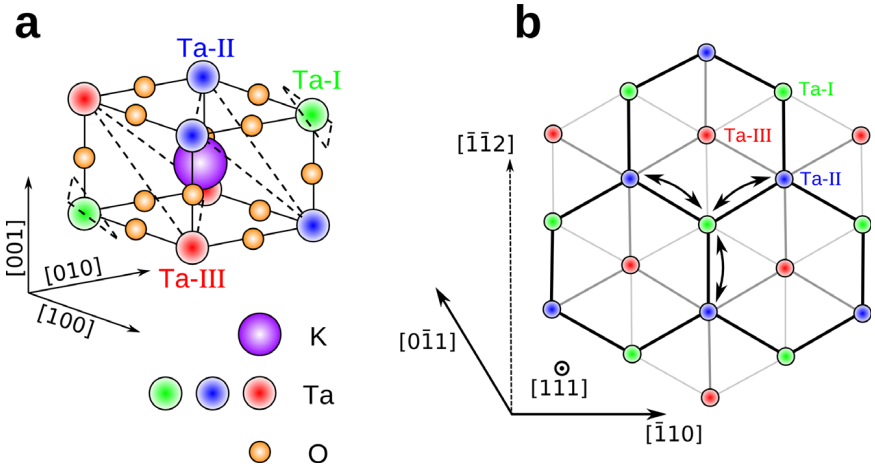

Figure 1 | $KTaO_3$ crystal in real space: schematics of the structure along the [111] direction. (a) Crystal structure of $KTaO_3$. Dashed triangles indicate the three Ta-(111) layers in the unit cell, labeled Ta-I, Ta-II and Ta-III. Ta atoms lying in the same (111) plane have the same shading color (green, blue or red). Note that Ta atoms in consecutive Ta-(111) layers are nearest neighbors. (b) View along the [111] direction of the Ta atoms alone. Lines connecting Ta atoms represent the edges of the 3D unit cell. Thick black lines connect nearest neighbors in layers Ta-I and Ta-II, forming a honeycomb lattice. Curved double arrows represent electron hopping between nearest neighbors. Straight black arrows are the lattice vectors of a 2D unit cell in the (111) plane. Such 2D unit cell is independent of the number of Ta-layers considered.

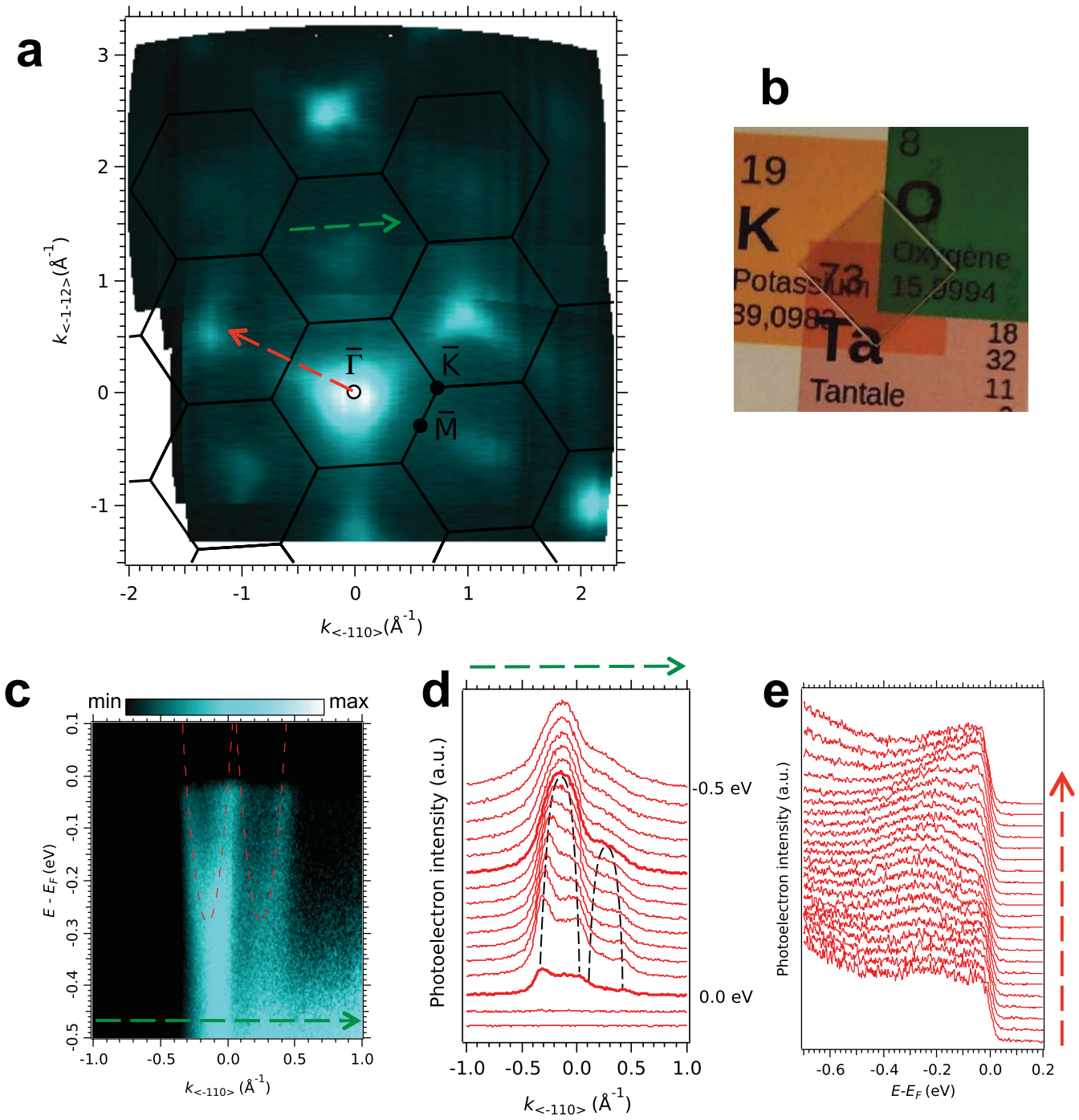

Figure 2 | Electronic structure of the 2DEG at the (111) surface of bulk insulating $KTaO_3$. (a) Fermi surface in the (111) plane, obtained from the superposition of ARPES maps measured at $h\nu = 96$ eV and $h\nu = 50$ eV, and integrated over $[-50, +5]$ meV around E_F. Black hexagons correspond to the surface Brillouin zones. (b) Picture of a measured sample of $KTaO_3$ before fracturing in vacuum. (c) Energy-momentum intensity map of the band structure in the $\langle\bar{1}10\rangle$ direction, measured along the dashed green line in panel (a). The red dashed lines are parabolic fits to the dispersion. (d) Stack of MDCs for the intensity map in (c). Each MDC was integrated over ± 20 meV around its corresponding energy. Thicker lines represent the MDCs at E_F and at the bottom of the bands. Dashed lines are guides to the eye for the peaks of the two observed bands. (e) Stack of EDCs along $\overline{\Gamma M \Gamma}$, dashed red arrow in panel (a). The positions of the peaks at $E \sim -260$ meV correspond to the bottom of the parabolic electron bands, like those of panel (c), forming the quasi-non-dispersive 'gutters'. Data of (c), (d) and (e) were measured at $h\nu = 96$ eV.

behind the broadened parabolic quasi-particle peak. As this background is extrinsic to the electronic structure, it has no effect on the quasi-particle spectral function, in agreement with the observation, noted earlier, that the experimental effective mass of the 2DEG's band is essentially the same as the one given by non-correlated tight-binding calculations (Supplementary Material and Ref. 13).

Discussion

The observed electronic structure can be understood in terms of electron hopping between neighbouring Ta layers. To see how, we modeled the 2DEG using a tight binding (TB) hamiltonian on a Ta-(111) bilayer with the hopping parameters determined from our previous study of KTO-(001)[13] –see details in the Supplementary

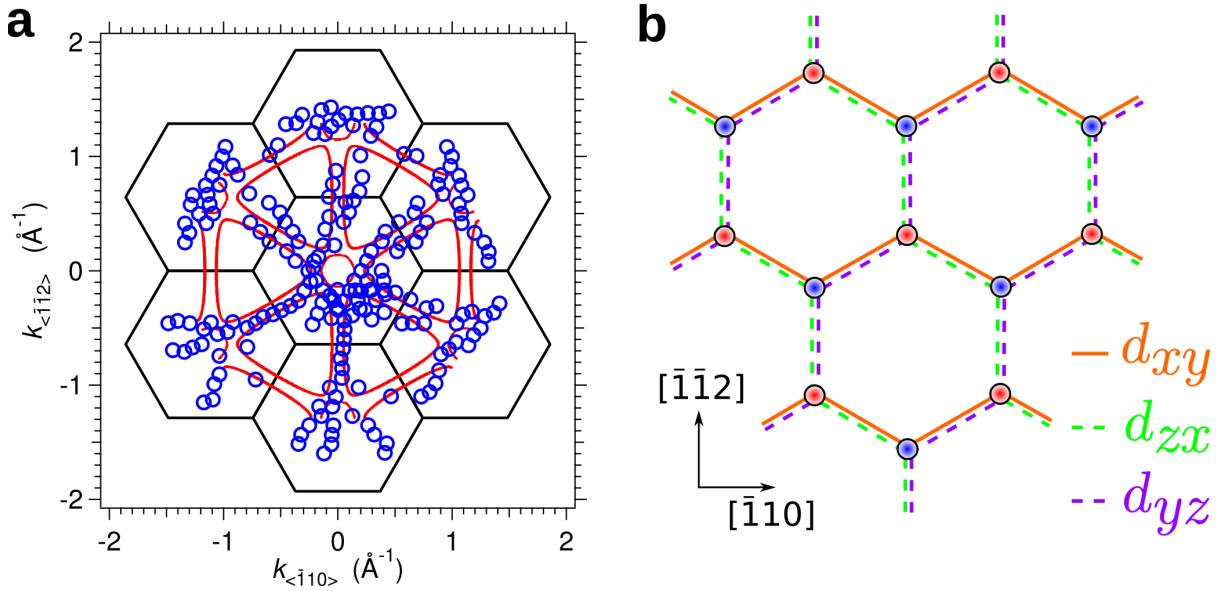

Figure 3 | Comparison of experimental and tight-binding Fermi surfaces of the 2DEG at the (111) surface of $KTaO_3$. (a) Experimental Fermi momenta from the original data after symmetrization (blue open circles) compared to the Fermi surface from a two-layer tight-binding calculation (red lines). The Fermi momenta were determined from the peak positions of the MDCs at E_F, using Lorenzian fits. The inner quasi-circular Fermi surface found in the calculations, of radius ~ 0.15 Å^{-1}, is difficult to compare with the data, due to the experimental resolution. (b) Directional paths, in real space, created by the different t_{2g} orbitals, d_{xy}, d_{zx} and d_{yz}, on a (111) bilayer of Ta atoms. The orange solid lines illustrate hopping channels created by the d_{xy} orbitals, while dashed green and violet lines illustrate the channels created by the d_{zx} and d_{yz} orbitals, respectively.

Material. Indeed, as schematically indicated by the double arrows in figure 1(b), and in Ref. 20, the largest hopping occurs between the Ta atoms of consecutive (111) layers, as they correspond to nearest neighbors along [001] in the cubic 3D lattice. In figure 3(a) we compare the experimental ARPES Fermi surface to the calculated Fermi surface. We observe that the model correctly gives the band-structure of the weakly dispersing electron gutters. The comparison between the data and calculations close to the $\overline{\Gamma}$ point is more difficult due to the experimental resolution. We checked that including extra Ta layers or considering the hopping of electrons between Ta atoms on the same (111) layer, which are next-nearest neighbors, will mainly change the computed band-structure around the $\overline{\Gamma}$ point, but not the structure of the gutters, so that the comparison above remains valid.

The weakly dispersing gutters along the $\overline{\Gamma M \Gamma}$ lines are the most salient feature of the observed Fermi surface. They can be intuitively understood from the directional overlaps between t_{2g} orbitals in neighboring Ta sites, which give rise to large nearest-neighbor hopping amplitudes along the [001] (and equivalent) directions. When seen from the [111] direction, these appear as directional zig-zag chains at 120° from each other, as depicted in Fig. 3(b) for two consecutive Ta (111) layers. Each set of parallel hopping chains on the 2D lattice will lead to *open* weakly dispersing Fermi sheets in reciprocal space, *i.e.*, to the observed gutters.

Our results demonstrate that a 2DEG with hexagonal symmetry can be easily created at the (111) surface of KTO. As an outlook for near-future investigations, an exciting feature arises when such a 2DEG is confined to a Ta-(111) bilayer, which forms a honeycomb lattice –as seen from the lattice formed by layers Ta-I and Ta-II in figure 1(b). In this case, following Ref. 27, one can demonstrate (details in the Supplementary Material) that the electron wave-function of the ground state has an odd parity at one of the $\overline{M}$ points (and its time-reversal partner), but an even parity at all other points, implying a *non trivial* topological index $Z_2 = 1$. In this case, the 2DEG at the KTO (111) surface would correspond to a *topological 2D metal*, similar to some of the non-trivial states predicted in Ref. 20, with the 2DEG itself corresponding to the "bulk" states, and the non-trivial states appearing at the 1D edges of the sample.

From a broader perspective, our results show that different surface orientations can be used to tailor Fermi seas and to radically change the microscopic state, hence the physical properties, of oxide perovskite-based 2DEGs. Of particular interest is the prospect for engineering 2DEGs of strongly correlated insulators on honeycomb lattice-structures, which could lead to correlated topological and edge-states with new physical properties not shown by semiconducting topological insulators. Thus, in perspective, our results provide some initial bridges between the fields of topological matter, correlated electrons and oxide electronics.

Methods

The angle resolved photoemission spectroscopy (ARPES) experiments were done at the Synchrotron Radiation Center (SRC, University of Wisconsin, Madison) and at the Synchrotron SOLEIL (France), using linearly polarized photons in the energy range 20–100 eV and Scienta R4000 detectors with vertical slits (henceforth the k_y direction). The momentum and energy resolutions were 0.25° and 15 meV, respectively. The mean diameter of the incident photon beam was smaller than 50 μm (SOLEIL) and about 150 μm (SRC).

The samples studied were *undoped transparent* high-grade laser crystals of $KTaO_3$ (SurfaceNet, GmbH), of purity 99,9995%, grown by a modified top seeded solution growth (TSSG) using KO_2 as solvent. The estimated amount of oxygen vacancies is less than 10 ppm, being mostly concentrated in the seeding area, which was not used for the final cut crystals. Similarly, the estimated amount of defects is less than 100 cm^{-3}.

The crystals were mounted with $\langle\bar{1}10\rangle \| k_y$ and fractured *in-situ* along the (111) surface at 25 K (SRC) and 10 K (SOLEIL), in pressure lower than 6×10^{-11} Torr. The fractured surfaces had homogeneous electron photo-emittance over a large area.

The results have been reproduced in 6 different cleaves.

1. Ohtomo, A. & Hwang, H. Y. A high-mobility electron gas at the $LaAlO_3/SrTiO_3$ heterointerface. *Nature* **427**, 423 (2004).
2. Okamoto, S. & Millis, A. J. Electronic reconstruction at an interface between a Mott insulator and a band insulator. *Nature* **428**, 630 (2004).
3. Reyren, N. *et al.* Superconducting interfaces between insulating oxides. *Science* **317**, 1196–1199 (2007).
4. Brinkman, A. *et al.* Magnetic effects at the interface between non-magnetic oxides. *Nature Mater.* **6**, 493–496 (2007).

5. Ueno, K. *et al.* Electric-field-induced superconductivity in an insulator. *Nature Mater.* **7**, 855–858 (2008).
6. Caviglia, A. D. *et al.* Tunable Rashba spin-orbit interaction at oxide interfaces. *Phys. Rev. Lett.* **104**, 126803 (2010).
7. Ben Shalom, M., Sachs, M., Rakhmilevitch, D., Palevski, A. & Dagan, Y. Tuning spin-orbit coupling and superconductivity at the $SrTiO_3/LaAlO_3$ interface: a magnetotransport study. *Phys. Rev. Lett.* **104**, 126802 (2010).
8. Li, L., Richter, C., Mannhart, J. & Ashoori, R. C. Coexistence of magnetic order and two-dimensional superconductivity at $LaAlO_3/SrTiO_3$ interfaces. *Nature Phys.* **7**, 762–766 (2011).
9. Bert, J. A. *et al.* Direct imaging of the coexistence of ferromagnetism and superconductivity at the $LaAlO_3/SrTiO_3$. *Nature Phys.* **7**, 767771 (2011).
10. Santander-Syro, A. F. *et al.* Two-dimensional electron gas with universal subbands at the surface of $SrTiO_3$. *Nature* **469**, 189 (2011).
11. Meevasana, W. *et al.* Creation and control of a two-dimensional electron liquid at the bare $SrTiO_3$ surface. *Nature Mater.* **10**, 114 (2011).
12. King, P. D. C. *et al.* Subband structure of a two-dimensional electron gas formed at the polar surface of the strong spin-orbit perovskite $KTaO_3$. *Phys. Rev. Lett.* **108**, 117602 (2012).
13. Santander-Syro, A. F. *et al.* Orbital symmetry reconstruction and strong mass renormalization in the two-dimensional electron gas at the surface of $KTaO_3$. *Phys. Rev. B.* **86**, 121107(R) (2012).
14. Haldane, F. D. M. Model for a quantum Hall effect without Landau levels: condensed-matter realization of the Parity Anomaly" *Phys. Rev. Lett.* **61**, 2015–2018 (1988).
15. Kane, C. L. & Mele, E. J. Z_2 topological order and the quantum spin Hall effect. *Phys. Rev. Lett.* **95**, 146802 (2005).
16. König, M. *et al.* Quantum spin Hall insulator state in HgTe quantum wells. *Science* **318**, 766–770 (2007).
17. Hsieh, D. *et al.* A topological Dirac insulator in a quantum spin Hall phase. *Nature* **452**, 970–974 (2008).
18. Hasan, M. Z. & Kane, C. L. *Colloquium:* Topological insulators. *Rev. Mod. Phys.* **82**, 3045–3067 (2010).
19. Qi, X.-L. & Zhang, S.-C. Topological insulators and superconductors. *Rev. Mod. Phys.* **83**, 1057–1110 (2011).
20. Xiao, D., Zhu, W., Ran, Y., Nagaosa, N. & Okamoto, S. Interface engineering of quantum Hall effects in digital transition metal oxide heterostructures. *Nat. Commun.* **2**, 596; DOI:10.1038/ncomms1602 (2011).
21. Corboz, P., Lajkó, M., Läuchli, A. M., Penc, K. & Mila, F. Spin-orbital quantum liquid on the honeycomb lattice. ArXiv:1207.6029 (2012).
22. Kourtis, S., Venderbos, J. W. F. & Daghofer, M. Fractional Chern insulator on a triangular lattice of strongly correlated t2g electrons. ArXiv:1208.3481 (2012).
23. Rüegg, A., Mitra, C., Demkov, A. A. & Fiete, G. A. Electronic structure of $(LaNiO_3)_2/(LaAlO_3)_N$ heterostructures grown along 111. *Phys. Rev. B* **85**, 245131 (2012).
24. Yang, K.-Y. *et al.* Possible interaction-driven topological phases in (111) bilayers of $LaNiO_3$. *Phys. Rev. B* **84**, 201104 (2011).
25. Herranz, G., Sánchez, F., Dix, N., Scigaj, M. & Fontcuberta, J. High mobility conduction at (110) and (111) $LaAlO_3/SrTiO_3$ interfaces. *Sci. Rep.* **2**, 758; DOI:10.1038/srep00758 (2012).
26. Annadi, A. *et al.* Anisotropic two-dimensional electron gas at the $LaAlO_3/SrTiO_3$ (110) interface. *Nature Communications* **4**, 1838; DOI:10.1038/ncomms2804 (2013).
27. Fu, L. & Kane, C. L. Topological insulators with inversion symmetry. *Phys. Rev. B* **76**, 045302 (2007).

Acknowledgments

We thank R. Weht, J. Guevara, G. Montambaux, F. Piéchon, J.-N. Fuchs and M.-O. Goerbig for discussions. A.F.S.-S. and M.G. acknowledge support from the Institut Universitaire de France. This work was supported by the ANR (project LACUNES) and the LabEX PALM (project ELECTROX).

Author contributions

Project conception: A.F.S.-S.; ARPES measurements: C.B., T.R., F.F., F.B. and A.F.S.-S.; infrastructure for ARPES experiments at Soleil: F.B., A.T.I. and P.L.F.; sample characterizations: M.B., A.B., T.M. and P.L.; data analysis, interpretation, calculations: C.B., A.F.S.-S., M.G., O.H.C. and M.J.R.; writing of the manuscript: A.F.S.-S., with input from C.B., M.G. and M.J.R. All authors discussed extensively the results and the manuscript.

Additional information

Supplementary information accompanies this paper at http://www.nature.com/scientificreports

Competing financial interests: The authors declare no competing financial interests.

How to cite this article: Bareille, C. *et al.* Two-dimensional electron gas with six-fold symmetry at the (111) surface of $KTaO_3$. *Sci. Rep.* **4**, 3586; DOI:10.1038/srep03586 (2014).

SUPPLEMENTARY MATERIAL

Two-dimensional electron gas with six-fold symmetry at the (111) surface of $KTaO_3$

C. Bareille,[1] F. Fortuna,[1] T. C. Rödel,[1,2] F. Bertran,[3] M. Gabay,[4]
O. Hijano Cubelos,[4] A. Taleb-Ibrahimi,[3] P. Le Fèvre,[3] M. Bibes,[5] A. Barthélémy,[5]
T. Maroutian,[6] P. Lecoeur,[6] M. J. Rozenberg,[4] and A. F. Santander-Syro[1,*]

[1]*CSNSM, Université Paris-Sud and CNRS/IN2P3, Bâtiments 104 et 108, 91405 Orsay cedex, France*

[2]*Universität Würzburg, Experimentelle Physik VII, Am Hubland, 97074 Würzburg, Germany*

[3]*Synchrotron SOLEIL, L'Orme des Merisiers, Saint-Aubin-BP48, 91192 Gif-sur-Yvette, France*

[4]*Laboratoire de Physique des Solides, Université Paris-Sud and CNRS, Bâtiment 510, 91405 Orsay, France*

[5]*Unité Mixte de Physique CNRS/Thales, Campus de l'Ecole Polytechnique, 1 Av. A. Fresnel, 91767 Palaiseau, France and Université Paris-Sud, 91405 Orsay, France*

[6]*Institut d'Electronique Fondamentale, Université Paris-Sud and CNRS, Bâtiment 220, 91405 Orsay, France*

PHOTON-ENERGY-DEPENDENT SELECTION RULES

The Fermi surface presented in figure 2(a) of the main text was obtained by superposing two Fermi surfaces measured at $h\nu = 50$ eV and $h\nu = 96$ eV, shown in figures S1(a) and S1(b) respectively. As seen from these figures, one subtle aspect of our data is that while the hexagonal structure in reciprocal space is associated with the 6-fold symmetry of the (111) surface of real space, the observed symmetry of the electronic structure around the $\overline{\Gamma}$ points appears as 3-fold. Two a-priori prominent possibilities are a surface reconstruction, or an effect of photoemission selection rules. A surface reconstruction, which may be expected from the polar (111) surfaces, would imply a longer periodicity of the real space lattice, hence a smaller periodicity in reciprocal space. At odds with this expectation, we actually observe, in figures S1(a, b), a Fermi surface with a periodicity *larger* than the one of the unreconstructed 2D Brillouin zone. An alternative explanation, consistent with the rest of our data, is that the observed 3-fold symmetry results from photoemission selection rules extinguishing 3 out of the 6 Fermi surface branches required by the symmetry of the unreconstructed Brillouin zone. In fact, in the photoemission process [SR1], the absorption of an incident photon induces an energy- and momentum-conserving optical transition of the electron from a bound state in the 2DEG to a non-occupied state. Transitions to bulk final states have a larger cross-section. As shown in the inset of figure S1, these states display the required three-fold symmetry at all momenta along $< 111 >$ (and 6-fold only at a plane passing through a bulk Γ point), effectively "filtering" the 2DEG states that can be detected. A similar effect is observed, for instance, in the topological surface states of Sb(111) [SR2].

The data from figures S1(a, b) fully confirm the above picture: by switching the photon energy from 50 eV (panel a) to 96 eV (panel b), thus changing the final bulk state and its orientation thereof, one selectively turns "on" and "off" the complementary pairs of 3-branches of the Fermi surface. This demonstrates that the *intrinsic* electronic structure at the KTO-(111) surface has the expected 6-fold symmetry.

ESTIMATE OF THE EXTENSION OF THE 2DEG

Following our previous works on the 2DEGs at the (001) surfaces of $SrTiO_3$ and $KTaO_3$ [SR3, SR4], we approximate the effect of the confining potential acting in the [111]

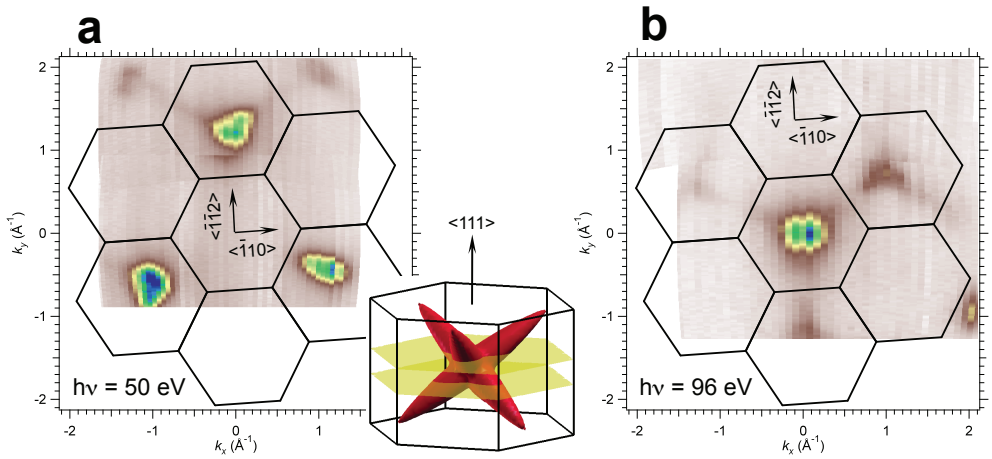

Figure S 1: (a) Experimental Fermi surface in the (111) plane, obtained from the ARPES intensity at $h\nu = 50$ eV, and integrated over the energy range $[-50, +50]$ meV around E_F. Black hexagons correspond to the surface Brillouin zones. (b) Corresponding Fermi surface at $h\nu = 96$ eV. The data were obtained on the same sample. The inset shows an iso-energy surface of the *bulk* t_{2g} states (red surface), illustrating the 3-fold symmetry of the final photoemission state for photon energies inducing transitions to (111) planes above or below a bulk Γ point (yellow planes).

(or z) direction by a potential wedge $V(z) = V_0 + eFz$, where e is the charge of the electron and F is the strength of the electric field along z. The quantized eigenenergies E_n are given in very good approximation by:

$$E_n = -V_0 + \left(\frac{\hbar^2}{2m_z^\star}\right)^{1/3} \left[\left(\frac{3\pi}{2}\right)\left(n - \frac{1}{4}\right) eF\right]^{2/3}, \qquad (1)$$

where n indicates the subband, V_0 is the depth of the confining potential well, and $m_z^\star$ is the bulk effective mass in the (111)-direction. The effective mass is obtained by a bulk tight binding calculation (see next section), yielding $m_z^\star \approx 0.28 m_e$.

By measuring the subband splitting $\Delta E = E_2 - E_1$, we can in principle deduce F. In the data presented in the main text, we observe only one subband. Thus, we can only infer a lower limit for the subband splitting: $\Delta E \geq 0.26$ eV. This gives a lower limit for the strengh of the electric field: $F \gtrapprox 166$ MeV/m. Using this field strength, and the approximation $eFL \approx \Delta E$, we can estimate an upper limit for the depth (L) of the confining potential well. This gives $L \lessapprox 16$ Å, or about 7 Ta layers.

BAND STRUCTURE PROPERTIES AND PERSPECTIVE FOR TOPOLOGICAL NON-TRIVIAL NATURE

In this section we show how the remarkable band-structure geometry of the 2DEG in KTO-(111) can be brought into light using a tight binding modeling, and draw further insight into the nature of the 2DEG by investigating the symmetries of the resulting electronic states.

As discussed in Ref. [SR4], low energy states in KTO pertain to the t_{2g} triplet of d orbitals. In the main text, we deduced from the band structure that the 2DEG is confined to less than 7 Ta-layers. Here, we will demonstrate that, by considering that the conducting sheet is only a single Ta-bilayer thick, the 2DEG gains a topologically non-trivial nature. We follow the derivation of Xiao *et al.* [SR5], and introduce a unit cell consisting of two Ta atoms; that in the top (bottom) layer is denoted with a 1 (2) index. The values of the main hopping amplitudes, which involve like-orbitals, are t and t_δ between nearest neighbour interlayer Ta sites, and t' between nearest neighbour intralayer sites. We may conveniently estimate their values using the Slater-Koster expressions [SR6] and the Solid State Table in Harrison's book [SR7]. We also include the potential energy difference V between the two layers as well as a trigonal crystal field term E_t. Lastly, we account for the large bulk spin-orbit term by adding a $\lambda \vec{L} \cdot \vec{S}$ contribution.

In the absence of spin-orbit terms, a convenient basis to express the Hamiltonian H_0 of the bilayer is $\{X'_{1\sigma}, Y'_{1\sigma}, Z'_{1\sigma}, X'_{2\sigma}, Y'_{2\sigma}, Z'_{2\sigma}\}$, where the states X', Y', Z' have a dominant d_{yz}, d_{xz}, d_{xy} character respectively, and where $\sigma = \uparrow, \downarrow$ is a spin index [SR4]. Using Dirac's notation, the non spin-orbit coupled Hamiltonian for the bilayer is thus:

$$H_0 = \sum_{(I=X',Y',Z'),\sigma} |d_{I,\sigma,1}, d_{I,\sigma,2}\rangle \mathbf{M} \langle d_{I,\sigma,2}, d_{I,\sigma,1}|, \tag{2}$$

where the matrix $\mathbf{M}$ is given by

$$\begin{pmatrix} a_I & e_I \\ e_I^* & b_I \end{pmatrix}. \tag{3}$$

If we define a two-dimensional real space basis parallel to the bilayer [SR5] and Fourier

transform the interactions, the entries of $\mathbf{M}$ are:

$$\begin{aligned} a_{X'} &= -2t'\cos(-\frac{\sqrt{3}}{2}k_x c + \frac{3}{2}k_y c); \\ a_{Y'} &= -2t'\cos(\frac{\sqrt{3}}{2}k_x c + \frac{3}{2}k_y c); \\ a_{Z'} &= E_t - 2t'\cos(\sqrt{3}k_x c); \end{aligned} \tag{4}$$

$$b_I = a_I + V; \tag{5}$$

$$\begin{aligned} e_{X'} &= -t(1+\exp -i(-\frac{\sqrt{3}}{2}k_x c + \frac{3}{2}k_y c)) - t_\delta \exp -i(\frac{\sqrt{3}}{2}k_x c + \frac{3}{2}k_y c); \\ e_{Y'} &= -t(1+\exp -i(\frac{\sqrt{3}}{2}k_x c + \frac{3}{2}k_y c)) - t_\delta \exp -i(-\frac{\sqrt{3}}{2}k_x c + \frac{3}{2}k_y c); \\ e_{Z'} &= E_t - 2t\exp -i(\frac{3}{2}k_y c)\cos(\frac{\sqrt{3}}{2}k_x c) - t_\delta; \end{aligned} \tag{6}$$

with $c = \sqrt{2/3}d$, and d the Ta–Ta interatomic distance.

Inspection of Eq.(6) reveals that all e_I's are real at the $\overline{\Gamma}$ point and at the three $\overline{M}$ points: $\overline{M_1} \equiv (1/c)(\pi/\sqrt{3},\ \pi/3)$, $\overline{M_2} \equiv (1/c)(-\pi/\sqrt{3},\ \pi/3)$, $\overline{M_3} \equiv (1/c)(0,\ 2\pi/3)$. As $t \sim 1.4$ eV is at least one order of magnitude larger than both E_t and t_δ, we see that $e_I < 0$ at $\overline{\Gamma}$, $\overline{M_1}$, $\overline{M_2}$, but $e_I > 0$ at $\overline{M_3}$. If the value of the potential is not too different for layers 1 and 2 (*i.e*, $V \ll 2t'$), then $b_I \sim a_I$. In that limit, the smallest eigenvalue is $a_I - |e_I|$, giving the lowest energy band. The corresponding eigenvectors are $1/\sqrt{2}(|d_{I,\sigma,1}\rangle - \mathrm{sign}(e_I)|d_{I,\sigma,2}\rangle)$. Accordingly, at the $\overline{\Gamma}$ point, we get a four-fold degeneracy of the energy bands, while the eigenvectors, which are of X' or Y' orbital character, have even parity (when we exchange 1 and 2). At $\overline{M_1}$ and $\overline{M_2}$, the minimum energies are $a_{X'} - |e_{X'}|$ and $a_{Y'} - |e_{Y'}|$, respectively, and the corresponding eigenvectors are $1/\sqrt{2}(|d_{X',\sigma,1}\rangle + |d_{X',\sigma,2}\rangle)$ and $1/\sqrt{2}(|d_{Y',\sigma,1}\rangle + |d_{Y',\sigma,2}\rangle)$. Again, eigenvectors have even parity. By contrast, at $\overline{M_3}$, the eigenvector corresponding to the minimum energy $a_{Z'} - |e_{Z'}|$ is given by $1/\sqrt{2}(|d_{Z',\sigma,1}\rangle - |d_{Z',\sigma,2}\rangle)$ and hence has odd parity.

We now consider spin-orbit coupling. The basis which diagonalizes the spin-orbit H_{so} Hamiltonian consists of the Γ_{8c} quartet ($\psi_1 = \frac{1}{\sqrt{2}}(X'_\uparrow + iY'_\uparrow), \psi_3 = \frac{1}{\sqrt{6}}(X'_\uparrow - iY'_\uparrow + 2Z'_\downarrow)$ and their Kramers partners, ψ_2, ψ_4 respectively) and of the Γ_{7c} doublet ($\psi_5 = \frac{1}{\sqrt{3}}(-X'_\uparrow + iY'_\uparrow + Z'_\downarrow)$ and its time-reversed conjugate ψ_6).

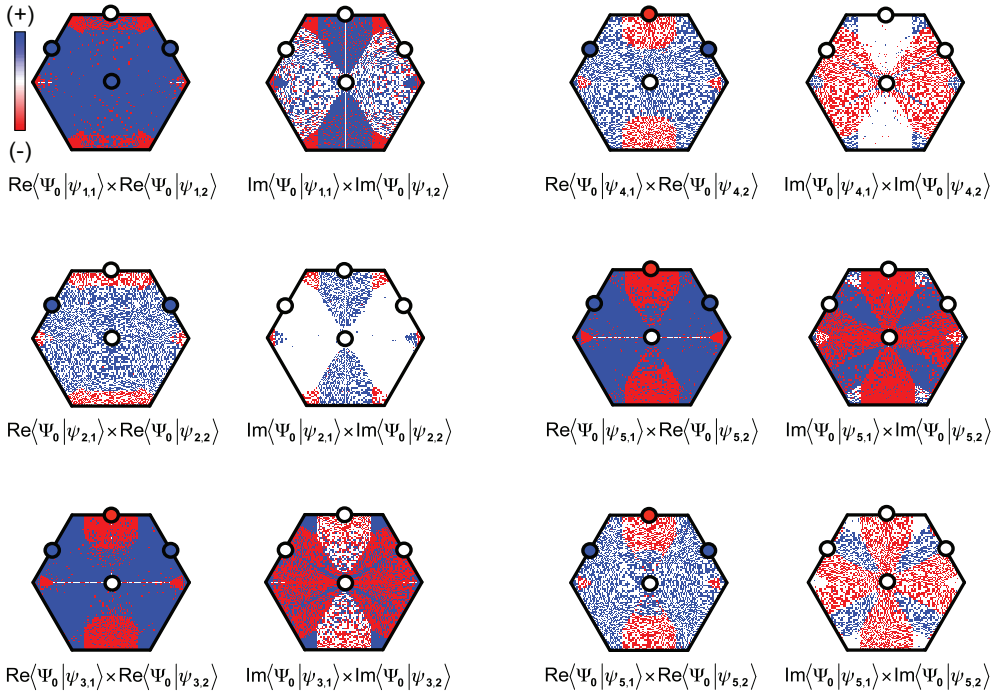

Figure S 2: Colour maps of the products $\mathrm{Re}\langle\Psi_0|\psi_{i,1}\rangle \times \mathrm{Re}\langle\Psi_0|\psi_{i,2}\rangle$ and $\mathrm{Im}\langle\Psi_0|\psi_{i,1}\rangle \times \mathrm{Im}\langle\Psi_0|\psi_{i,2}\rangle$ for the 6 components ($i = 1 \ldots 6$) along the $\{\psi\}$ basis of the ground-state wave-functions at Ta-sites 1 and 2. These scalars serve as "parity-markers": the product is positive (blue hues) if the parities of the wave-functions on the Ta-1 and Ta-2 sites tend to be the same, and negative (red hues) in the opposite case (white is zero). The regions where the colors mix randomly are regions where the absolute value of the plotted scalar is either very small, close to zero within the resolution limits of our computational capabilities, or changing very fast (*i.e.*, near a red/blue boundary). Note that the above scalars become strictly identical to the parity only at the $\overline{\Gamma}$ and $\overline{M}$ points, where Ψ_0 is real. For each color map, the exact values of the corresponding product at the $\overline{\Gamma}$ and three consecutive $\overline{M}$ points are indicated by the filled circles.

As the total Hamiltonian $H_0 + H_{so}$ has time reversal symmetry, we diagonalize it in the $\{\psi\}$ basis. At the special points $\overline{\Gamma}$ and $\overline{M}$, which are their own Kramers partners, we have both parity and time reversal invariance. We focus on the lowest energy band, which shows occupied electronic states in the photoemission data, and exhibits the 6-fold symmetry pattern of electron gutters shown in figure 3(a) of the main text. We denote as Ψ_0 the corresponding lowest-energy eigenstate of the total Hamiltonian. Thus, Ψ_0, and its Kramers partner, have even parity at $\overline{\Gamma}$, $\overline{M_1}$, $\overline{M_2}$ and odd parity at $\overline{M_3}$.

To illustrate this, figure S2 shows momentum-resolved maps of the relative signs for the contributions of the 1 and 2 Ta-sites to Ψ_0. These maps allow one to visualize the basin of attraction of the parity eigenstates at $\overline{\Gamma}$ and the different $\overline{M}$ points. They clearly show that the electron ground-state has an odd parity at one of the $\overline{M}$ points (and its time-reversal partner), but an even parity at all other points, implying a *non trivial* topological index $Z_2 = 1$. Our calculations furthermore indicate that a second, higher-energy band, lies below the Fermi level near the $\overline{\Gamma}$ point (see figure 3(a) of the main text). We find (not shown) that the corresponding state has even parity at $\overline{\Gamma}$.

All the above considerations imply that confining to one Ta-bilayer the 2DEG at the (111) surface of $KTaO_3$ endows it with a topologically non trivial $Z_2 = 1$ nature [SR8]. We checked that, if the conducting sheet is confined within three layers, rather than two, a topological state can still be observed, but for fillings larger than those pertaining to the gutter structure seen in ARPES.

---

* Electronic address: andres.santander@csnsm.in2p3.fr

[SR1] Hüfner, S. Photoelectron spectroscopy: principles and applications. Third edition, Springer (2003).

[SR2] Sugawara, K., Sato, T., Souma, S., Takahashi, T., Arai, M. & and Sasaki, T. Fermi Surface and Anisotropic Spin-Orbit Coupling of Sb(111) Studied by Angle-Resolved Photoemission Spectroscopy. *Phys. Rev. Lett* **96**, 046411 (2006).

[SR3] Santander-Syro, A. F. *et al.* Two-dimensional electron gas with universal subbands at the surface of $SrTiO_3$. *Nature* **469**, 189 (2011).

[SR4] Santander-Syro, A. F. *et al.* Orbital symmetry reconstruction and strong mass renormalization in the two-dimensional electron gas at the surface of $KTaO_3$. *Phys. Rev. B.* **86**, 121107(R) (2012).

[SR5] Xiao, D., , Zhu, W., Ran, Y, Nagaosa, N. & Okamoto, S. Interface engineering of quantum Hall effects in digital transition metal oxide heterostructures. *Nat. Commun.* 2:596 doi: 10.1038/ncomms1602 (2011).

[SR6] Slater, J. C. & Koster, G. F. *Phys. Rev.* **94**, 1498 (1954).

[SR7] Harrison, W. A. Electronic structure and the properties of Solids: the physics of the chemical

bond. Dover Publications, New York (1989).

[SR8] Fu, L. & Kane, C. L. Topological insulators with inversion symmetry. *Phys. Rev. B* **76**, 045302 (2007).

Orientational tuning of the Fermi sea of confined electrons at the $SrTiO_3$ (110) and (111) surfaces

T. C. Rödel,[1,2] C. Bareille,[1] F. Fortuna,[1] C. Baumier,[1] F. Bertran,[2] P. Le Fèvre,[2] M. Gabay,[3] O. Hijano Cubelos,[3] M. J. Rozenberg,[3,4] T. Maroutian,[5] P. Lecoeur,[5] and A. F. Santander-Syro[1,*]

[1] *CSNSM, Université Paris-Sud and CNRS/IN2P3, Bâtiments 104 et 108, 91405 Orsay cedex, France*
[2] *Synchrotron SOLEIL, L'Orme des Merisiers, Saint-Aubin-BP48, 91192 Gif-sur-Yvette, France*
[3] *Laboratoire de Physique des Solides, Université Paris-Sud and CNRS, Bâtiment 510, 91405 Orsay, France*
[4] *Depto. de Física - IFIBA Conicet, FCEN, UBA, Ciudad Universitaria P.1, 1428, Buenos Aires, Argentina*
[5] *Institut d'Electronique Fondamentale, Université Paris-Sud and CNRS, Bâtiment 220, 91405 Orsay, France*

We report the existence of confined electronic states at the (110) and (111) surfaces of $SrTiO_3$. Using angle-resolved photoemission spectroscopy, we find that the corresponding Fermi surfaces, subband masses, and orbital ordering are different from the ones at the (001) surface of $SrTiO_3$. This occurs because the crystallographic symmetries of the surface and sub-surface planes, and the electron effective masses along the confinement direction, influence the symmetry of the electronic structure and the orbital ordering of the t_{2g} manifold. Remarkably, our analysis of the data also reveals that the carrier concentration and thickness are similar for all three surface orientations, despite their different polarities. The orientational tuning of the microscopic properties of two-dimensional electron states at the surface of $SrTiO_3$ echoes the tailoring of macroscopic (*e.g.* transport) properties reported recently in $LaAlO_3/SrTiO_3$ (110) and (111) interfaces, and is promising for searching new types of 2D electronic states in correlated-electron oxides.

Two-dimensional electron gases (2DEGs) in transition-metal oxides (TMOs) present remarkable phenomena that make them unique from a fundamental viewpoint and promising for applications [1, 2]. For instance, heterostructures grown on the (001) surface of $SrTiO_3$, a TMO insulator with a large band-gap of $\sim$ 3.5 eV, can develop 2DEGs showing metal-to-insulator transitions [3], superconductivity [4], or magnetism [5, 6]. Recently, 2DEGs at the (111) and (110) interfaces of $LaAlO_3/SrTiO_3$ were also reported [7]. The latter showed a highly anisotropic conductivity [8] and a superconducting state spatially more extended than the one at the (001) interface [9]. Interestingly, theoretical works have also predicted that exotic, possibly topological, electronic states might occur at interfaces composed of (111) bilayers of cubic TMOs [10–13], as two (111) planes of transition-metal ions form a honeycomb lattice, similar to the one found in graphene. In this context, the discoveries that 2DEGs can also be created at the bare (001) surfaces of $SrTiO_3$ [14–16] and $KTaO_3$ [17, 18], and more recently at the (111) surface of $KTaO_3$ [19], opened new roads in the fabrication and study of different types of 2DEGs in TMOs –in particular using surface-sensitive spectroscopic techniques, which give direct information about the Fermi surface and subband structure of the confined states. The origin of the confinement is attributed to a local doping of the surface region due to oxygen vacancies and/or lattice distortions.

Here we show that new types of 2DEGs can be directly tailored at the bare (110) and (111) surfaces of $SrTiO_3$. Imaging their electronic structure *via* angle-resolved photoemission spectroscopy (ARPES), we find that their Fermi surfaces, subband masses, and orbital ordering are different from the ones of the 2DEG at the $SrTiO_3$ (001) surface [14, 15] and the ones predicted for the bulk, being thus uniquely sensitive to the confining crystallographic direction. This occurs because the crystallographic symmetries of the 2DEG plane, and the electron effective masses along the confinement direction, influence the symmetry of the electronic structure and the orbital ordering of the t_{2g} orbitals. Furthermore, the observed carrier concentrations and 2DEG thicknesses for different surfaces allow us to showcase the impact of oxygen vacancies and of the polar discontinuity on distinctive features of the confined conducting sheet.

The confined states were either created by fracturing the samples in vacuum or by chemically and thermally preparing the surfaces *in situ*, and studied through ARPES at the Synchrotron Radiation Center (SRC, University of Wisconsin, Madison) and the Synchrotron Soleil (France). The sample preparation, similar to the one in references [20, 21], is detailed in the Supplemental Material [22]. All through this paper, we describe the crystal structure in a cubic basis of unit-cell vectors, and note as $[hkl]$ the crystallographic directions in real space, $\langle hkl \rangle$ the corresponding directions in reciprocal space, and as (hkl) the planes orthogonal to those directions.

The major difference between the confined states at various surface orientations of $SrTiO_3$ originates from the different symmetries of the corresponding crystal planes: 4-fold for the (001) plane, 2-fold for the (110) surface, and 6-fold for the (111) surface. Another difference is the polar character of the surface. Thus, while the (001) termi-

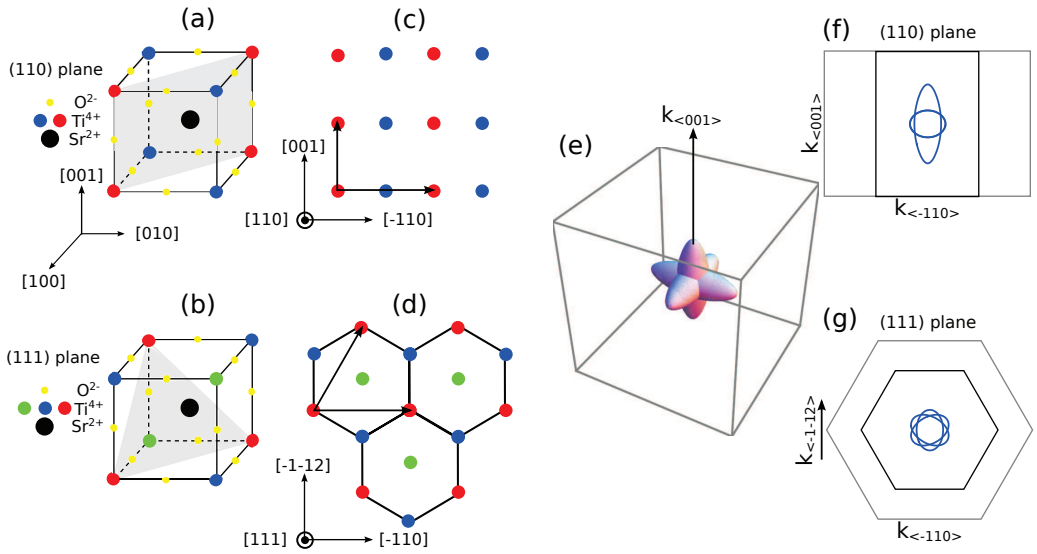

FIG. 1. (a, b) Unit cell of the cubic perovskite lattice of $SrTiO_3$. The grey planes are the (110) and (111) planes, respectively. The yellow dots represent the O^{2-} anions, the black dot in the center the Sr^{2+} cation, and the red/green/blue dots the Ti^{4+} cations in different (110) or (111) planes. Both orientations are highly polar, as the crystal is built of alternating layers of $(SrTiO)^{4+}$ and $(O_2)^{4-}$ or Ti^{4+} and $(SrO_3)^{4-}$. (c, d) Ti^{4+} cations of the crystal lattice at the (110) and (111) planes. The black arrows indicate the lattice vectors of the Ti^{4+} cations in one (110) or (111) plane. As indicated by the black lines in panel (d), a (111)-bilayer of Ti^{4+} cations forms a honeycomb lattice. (e) Bulk Fermi surface, calculated using a tight-binding model with an unrealistically large value of 10^{21} cm^{-3} for the bulk carrier density, intended to make the Fermi surface visible. Such carrier density is at least *three orders of magnitude* higher than the bulk carrier density of the samples prepared for this study. (f, g) Cross section of the bulk Fermi surface in (e) along the (110) and (111) planes, respectively. The grey lines show the cross section of the bulk 3D Brillouin zone through a Γ point, while the black lines correspond to the surface Brillouin zone.

nations, namely SrO or TiO_2, are nominally non-polar, the (110) terminations are alternatively $(SrTiO)^{4+}$ and $(O_2)^{4-}$, and the (111) terminations are either Ti^{4+} or $(SrO_3)^{4-}$. These different surface symmetries and their polarity are illustrated in figures 1(a-d). Note in particular, from figure 1(d), that a (111)-type bilayer of Ti^{4+} cations forms a honeycomb lattice, as noted in Ref. [10].

For our discussion later, it will be instructive to contrast the observations at the (110) and (111) $SrTiO_3$ surfaces with both the 2DEG at the (001) surface and a model bulk electronic structure. Figure 1(e) shows the bulk Fermi surface from a simplified tight-binding (TB) model where the electron hopping amplitudes between the three t_{2g} orbitals of neighboring Ti^{4+} are $t_\pi = 0.236$ eV and $t_{\delta'} = 0.035$ eV [23], and we neglect spin-orbit coupling and tetragonal distortions. Near the Γ point, this gives effectives masses listed in the first row of table I for various directions. Figures 1(f, g) show cross sections of the bulk Fermi surface along the (110) and (111) planes through the Γ point, illustrating their respective 2-fold and 6-fold symmetries. The *experimental* spectra at the $SrTiO_3$ (001) surface [14], on the other hand, fit well to a TB form where the hopping amplitudes are $\bar{t}_\pi = 0.36$ eV and $\bar{t}_{\delta'} = 0.025$ eV, leading to values of the effective masses near the Γ point shown in the second rows of table I. Note that all these masses differ by about 30% from the bulk theoretical ones.

We now present our experimental results. Figure 2(a) shows the Fermi surface measured at the *fractured* (110) surface of an undoped *insulating* $SrTiO_3$ sample. As we will see, our observations are similar to another recent study of the 2DEG at the $SrTiO_3$(110) surface in a Nb-doped sample prepared *in situ* by Wang *et al.* [24]. The metallic states we observe present the same 2-fold symmetry of the unreconstructed (110) surface Brillouin

TABLE I. Effective light (L) and heavy (H) masses predicted by a TB model in the bulk (first row) and experimental in-plane masses of the 2DEGs at the (001), (110), and (111) surfaces (other rows) along the different high-symmetry directions of the crystal lattice (columns) of $SrTiO_3$. In the bulk, all the effective masses along ⟨111⟩ are identical.

	m_{100}/m_e		m_{110}/m_e		$m_{11\bar{2}}/m_e$		m_{111}/m_e
	L	*H*	*L*	*H*	*L*	*H*	
Theory bulk[a]	1.06	7.16	1.06	1.85	1.24	2.46	1.48
$SrTiO_3$(001)	0.7[b]	10.0[b]	0.7[c]	1.3[c]	0.8[c]	1.8[c]	1.0[c]
$SrTiO_3$(110)	1.0	8.5	1.6	6.0	–	–	–
$SrTiO_3$(111)	–	–	0.27	1.08	0.33	8.67	–

[a] From Ref. [23] [b] From Ref. [14]

[c] From TB model using experimental masses along ⟨100⟩

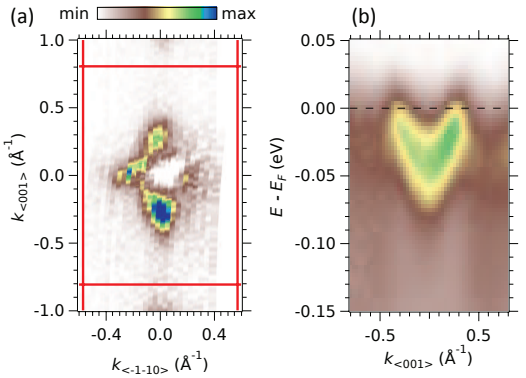

FIG. 2. (a) ARPES Fermi surface map (second derivative) at $h\nu = 91$ eV in the (110) plane of a fractured insulating $SrTiO_3$ sample. The map is a superposition of intensities measured in the bulk Γ_{130} and Γ_{131} Brillouin zones [22]. The red lines indicate the edges of the unreconstructed (110) Brillouin zones. (b) Energy-momentum intensity map at a Γ point along the $k_{\langle 001\rangle}$ direction.

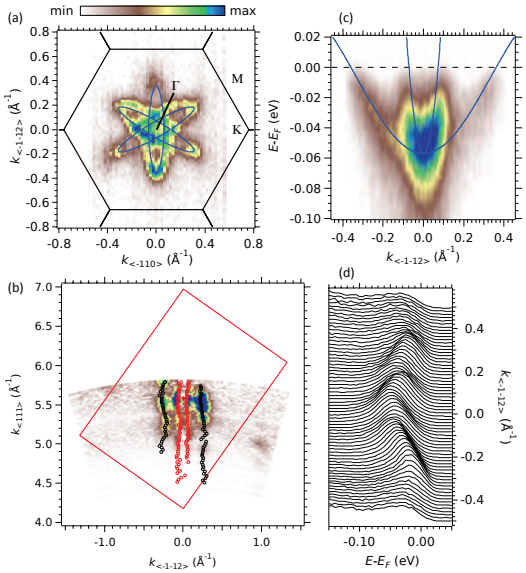

FIG. 3. (a) Fermi surface map measured at $h\nu = 110$ eV on a $SrTiO_3$ (111) surface prepared *in-situ*. The black lines indicate the edges of the unreconstructed (111) Brillouin zones around Γ_{222}. (b) Fermi surface map (second derivative of ARPES intensity, negative values) in the $k_{\langle 111\rangle} - k_{\langle \bar{1}\bar{1}2\rangle}$, or $(1\bar{1}0)$ plane, acquired by measuring at normal emission while varying the photon energy in 1 eV steps between $h\nu_1 = 67$ eV and $h\nu_2 = 120$ eV. The experimental Fermi momenta, represented by the black and red circles, were obtained by fitting the momentum distribution curves (MDCs) integrated over $E_F \pm 5$ meV. The red rectangle is the bulk Brillouin zone in the $(1\bar{1}0)$ plane. (c) Energy-momentum map across the Γ point along the $\langle \bar{1}\bar{1}2\rangle$ direction. The dispersions of a heavy band and light bands are visible. (d) Raw energy distribution curves of the dispersions shown in panel (c). In panels (a) and (c), the blue lines are simultaneous TB fits to the Fermi surface and dispersions.

zone (BZ), represented by red rectangles. This implies that *(i)* the macroscopic properties of this 2DEG should be highly anisotropic, echoing the observed anisotropic transport characteristics reported in 2DEGs at (110) $LaAlO_3/SrTiO_3$ interfaces [8], and *(ii)* any surface roughness or reconstructions, expected in this highly polar surface, do not affect the 2DEG, which must then reside in the sub-surface layers –in agreement with our previous conclusions on fractured (111) surfaces of $KTaO_3$ [19]. Figure 2(b) shows the dispersion along the $k_{\langle 001\rangle}$ direction, giving rise to the longest of the two ellipsoidal Fermi surfaces in figure 2(a). The band forming the shortest ellipsoid is eclipsed by photoemission selection rules along this direction (see the Supplemental Material [22]). The band bottom and Fermi momenta are about -40 meV and 0.3 Å^{-1}, respectively.

From the data above, we model the Fermi surface of the 2DEG at the $SrTiO_3$ (110) surface as two orthogonal ellipses, one along along $\langle 001\rangle$ with semi-axes of 0.3 Å^{-1} and 0.1 Å^{-1}, the other along $\langle 1\bar{1}0\rangle$ with semi-axes 0.25 Å^{-1} and 0.13 Å^{-1}. From the area A_F enclosed by the Fermi surfaces, we obtain a carrier density $n_{2D}^{(110)} = A_F/2\pi^2 \approx 1\times10^{14}$ cm^{-2}. The electronic states associated to such a high charge carrier density *must be confined to the region near the surface* –otherwise the bulk would be highly conductive, in contradiction with the insulating nature of the samples studied. Similarly, from the band bottom and Fermi momenta, using a parabolic approximation, we obtain the effective band masses along $\langle 001\rangle$ and $\langle \bar{1}\bar{1}0\rangle$ (and equivalent directions), listed in the third row of table I. These effective masses are similar to the ones determined in the aforementioned study [24] of the 2DEG at the $SrTiO_3$(110) surface. In our study, the band bottom of the heavy band, *c.f.* figure 2(b), and the carrier density of the 2DEG are slightly lower, probably due to the different surface preparation techniques.

Henceforth, we focus on new experimental results at the (111) surface of $SrTiO_3$, which as we will see presents the hexagonal symmetry of the unreconstructed surface, and could thus be an interesting platform for the quest of new electronic states and macroscopic properties at oxide surfaces.

Figure 3(a) shows the Fermi surface measured at the $SrTiO_3$ (111) surface prepared *in-situ*, as described in the Supplemental Material [22]. It consists of three ellipses forming a six-pointed star, thus strongly differing from the Fermi surface at the $SrTiO_3$ (110) surface, shown in figure 2(a), or the one at the $SrTiO_3$ (001) surface, discussed in previous works [14–16]. Additional experiments show that for surfaces prepared *in-situ* with either (1×1) or (3×3) reconstructions, the band structure and periodicity of the confined states are *identical*, and correspond to the one expected from an *unreconstructed surface* [22]. This indicates that the 2DEG at the $SrTiO_3$(111) surface is also located in the sub-surface layers, and is at best weakly affected by the surface reconstructions at the po-

lar (111) surface.

The 2D-like character of the electronic states is strictly demonstrated from the Fermi surface map in the $\langle 111\rangle - \langle \bar{1}\bar{1}2\rangle$ plane, shown in figure 3(b). Here, one sees that the bands do not disperse along $k_{\langle 111\rangle}$ over more than half a bulk Brillouin zone, thereby confirming the confined (*i.e.*, localized) character of the electrons along the [111] direction in real space. The modulation of the intensity in the Fermi surface map, a typical feature of quantum well states [25, 26], is discussed in the Supplemental Material [22]. Interestingly, note that the red rectangles in figures 2(a) and 3(b) represent the Brillouin zone in the (110) (or equivalent) plane. Yet, as seen from those figures, the shapes of the corresponding Fermi surfaces are completely different. This directly shows the orientational tuning of the Fermi surface due to different confinement directions.

Figure 3(c) shows the energy-momentum map at the Γ point along the $\langle \bar{1}\bar{1}2\rangle$ direction, corresponding to the major axis of the ellipsoids forming the 6-pointed-star Fermi surface. The dispersions of one light band and one heavy band are clearly visible. These constitute the ground state of the 2DEG. Additional subbands are not observed, implying that the band bending at the surface is too low to populate the upper quantum-well states. Within our resolution, the heavy and light bands are degenerate at Γ, with their band bottom located at about -57 meV. We fit simultaneously these dispersions and the whole Fermi surface of figure 3(a) using a simple tight-binding model [22]. The fit, shown by the continuous blue lines, yields Fermi momenta of about 0.07 Å^{-1} and 0.36 Å^{-1} for, respectively, the light and heavy bands along $\langle \bar{1}\bar{1}2\rangle$. This gives an electron concentration $n_{2D}^{(111)} \approx 1.0 \times 10^{14}$ cm^{-2}, and effective masses listed in the third row of table I.

We now draw some comparisons between the effective masses and thicknesses of the 2DEGs at the $SrTiO_3$ (001), (110) and (111) surfaces. Table I shows that, while the masses along the "natural" electron-hopping directions in the bulk ([001] and equivalent) are comparable between the 2DEGs at the $SrTiO_3$ (001) and (110) surfaces, the masses along [110] at the (110) surface, and all the masses of the 2DEG at the (111) surface, are very different from the ones expected from the tight-binding parameters describing the bulk or the 2DEG at the (001) surface. In this respect, note that if the confinement direction is [110] or [111], then the electrons moving in the 2DEG plane along a direction *other than* [001] will experience the confining potential gradient and the modified crystal field outside the surface, as they will hop in staircase patterns between first neighbors along [001] (or equivalent) directions –see figures 1(a-d) and Ref. [8, 19]. The understanding of these mass differences, also reported in quantum well states at thin films of simple-metals [27] or strongly-correlated oxides [28], should be the subject of further theoretical works.

The maximal spatial extension d_{max} of the 2DEGs at the $SrTiO_3$ (110) and (111) surfaces can be estimated using a triangular potential well model [22]. We obtain $d_{max}^{110} \approx 1.7$ nm, which amounts to 6 2D-layers or 3 bulk unit cells along [110], and $d_{max}^{111} \approx 1.9$ nm, corresponding to ~ 9 layers of Ti (111), or again about 3 bulk unit cells along [111].

Finally, we note that the orbital ordering of the electronic states at the (110) and (111) surfaces of $SrTiO_3$ is different from the one at the (100) surface. In the first two cases, the bands are degenerate within our experimental resolution, whereas at the (001) surface the smallest observed splitting between bands of different orbital character is of 50 meV [14]. As the confinement energy of each band is inversely proportional to its effective mass along the confinement direction [14], different surface orientations result in different orbital ordering. But along the [111] direction the effective masses of the three t_{2g} bands are identical, and so their degeneracy at the Γ point is not lifted by the confinement. Similarly, the effective masses of bands of different orbital character along [110] are quite similar (see table I). Hence, the degeneracy lift is rather small, and cannot be observed in our data. This demonstrates the influence of the confinement direction on the orbital ordering.

Several scenarios have been proposed to explain the origin of the 2DEG at the $LaAlO_3/SrTiO_3$ (001) interface. According to one of these, the formation of a conducting sheet prevents the occurrence of a polar catastrophe in the material. Yet, the discovery of a confined 2DEG at the (001) surface of $SrTiO_3$, with characteristics similar to those of the above heterostructure, suggests that the driving mechanism may not be unique, as in the bare $SrTiO_3$ all the layers are electrically neutral. Instead, in the latter case, surface oxygen vacancies are believed to cause and to confine the gas [14, 15, 24]. Additionally, for the (110) and (111) $SrTiO_3$ surfaces, of nominal polar charge $4e$, one would expect a much larger carrier concentration in the 2DEG, and a very strong electric field confining the electrons in a narrow sheet at the surface. However, we observe that the carrier concentrations and thicknesses of the 2DEGs are quite comparable for all three orientations (this work and Ref. [14]): $n_{2D} \sim 10^{14}$ cm^{-2}, $d_{max} \sim 2$ nm. In fact, in the polar $SrTiO_3$ surfaces studied here, the polar catastrophe does not seem to be compensated by the electrons of the 2DEG but by surface reconstructions or relaxations, while the 2DEG lies in the subsurface layers. Thus, although the 2D electronic structure (effective masses, orbital ordering) depends on the surface orientation, the thickness and carrier concentration of the 2DEG might be controlled by another factor, probably oxygen vacancies and/or lattice distortions induced by the synchrotron light irradiation, as discussed in the Supplemental Material [22].

In conclusion, our results show that the symmetries, electronic structure, and orbital ordering of the con-

fined states at the surface of TMOs can be tailored by confining the electrons along different directions in the *same* material. Such orientational tuning echoes the differences of transport properties reported recently in $LaAlO_3/SrTiO_3$ (110) and (111) interfaces [7–9]. In particular, from our data, the highly anisotropic transport behavior observed in the (110) interfaces [8] can be directly related to the 2-fold symmetry of the Fermi surface measured by ARPES. More generally, our results provide an exciting route for obtaining new types of 2D electronic states in correlated-electron oxides.

We thank V. Pillard for her contribution to the sample preparation. T.C.R. acknowledges funding from the RTRA Triangle de la Physique (project PEGASOS). A.F.S.-S. and M.G. acknowledge support from the Institut Universitaire de France. This work is supported by public grants from the French National Research Agency (ANR) (project LACUNES No ANR-13-BS04-0006-01) and the "Laboratoire d'Excellence Physique Atomes Lumière Matière" (LabEx PALM project ELECTROX) overseen by the ANR as part of the "Investissements d'Avenir" program (reference: ANR-10-LABX-0039).

SUPPLEMENTAL MATERIAL

ARPES Experiments

The ARPES measurements were conducted at the Synchrotron Radiation Center (SRC, University of Wisconsin, Madison) and the Synchrotron Soleil (France). We used linearly polarized photons in the energy range $20 - 120$ eV, and Scienta R4000 electron detectors with vertical slits. The angle and energy resolutions were 0.25° and 25 meV at SRC, and 0.25° and 15 meV at Soleil. The mean diameter of the incident photon beam was smaller than 100 μm. The samples were cooled down to 10-30 K before fracturing or measuring, in pressure lower than 6×10^{-11} Torr. The confined states were either created by fracturing the samples in vacuum or by chemically and thermally preparing the surfaces *in situ*, as detailed in the next section. The results were reproduced for at least five different samples for each surface orientation.

Surface preparation

The non-doped, polished crystals of $SrTiO_3$ were supplied by CrysTec GmbH and Aldrich. To prepare the surface, the samples were ultrasonically agitated in deionized water, subsequently etched in buffered HF and annealed at 950°C for several hours in oxygen flow. Depending on the annealing time, this treatment yields a Ti-rich, single-terminated or mixed-terminated step-and-terrace structured surface of $SrTiO_3$ (111) [20]. Figure 4(a) shows the atomic-force microscopy (AFM) image of the single-terminated (111) surface of a sample annealed for 3h. This treatment produces a (1×1) unreconstructed surface, shown by RHEED image in figure 4(b). Longer annealing (10h) results in a mixed-terminated surface [21], as shown in the AFM friction image in figure 4(c), measured in contact mode. The surface prepared in such a way is (3×3) reconstructed, as displayed in the RHEED image in figure 4(d). The surface state of the cleaved samples was not determined by imaging or diffraction techniques.

To perform the surface-sensitive ARPES measurements, one needs pristine and crystalline surfaces. To clean the surface of contaminations, the samples prepared as described above were further annealed *in-situ* in vacuum at a pressure of approximately $p = 3 \times 10^{-9}$ mbar at a temperature of $T = 550$°C for about 2 hours. This annealing step cleans the surface, does not change the surface reconstruction, and also introduces oxygen vacancies in the bulk of the $SrTiO_3$ samples. Note that the introduced bulk charge carrier density is at least three orders of magnitude lower than the one observed for the confined states in the ARPES measurements, as detailed in the main text. Moreover, Plumb *et al.* demonstrated that various *in-situ* sample preparations, including annealing in an O_2-rich atmosphere which results in a non-doped bulk, create identical confined states at the (001) surface of TiO_2-terminated $SrTiO_3$ [16]. Recall also, from figure 3(b), that the states observed in our experiments do not disperse along the confinement direction, which demonstrates their quasi-2D character.

For the confined states at the (111) surface, the quality of the obtained ARPES data is better for the surface prepared *in-situ*. This might be due to the strong polar nature of the (111) surface of $SrTiO_3$. Hence, fracturing a sample along a (111) plane might yield a partly disordered surface.

The electronic structure of the 2DEG at the $SrTiO_3$ (111) surface is similar for the cleaved and the two differently prepared surfaces (unreconstructed and (3×3) reconstructed). In fact, for all three types of surfaces the periodicity of the electronic structure in reciprocal space, shown in figure 5(a) for the prepared, (3×3) reconstructed surface, corresponds to the one expected of an unreconstructed surface. By Bloch theorem, the very existence of dispersive bands and well-defined Fermi surfaces implies the existence of a periodic in-plane potential acting on the confined electrons, hence of crystalline order at the layer(s) where the 2DEG is located. As the electronic structure has the periodicity of the *unreconstructed* surface, the 2DEG seems to stabilize in a sub-surface region, where it is not affected by any surface reconstructions or superstructures related to vicinal surfaces or terraces. A possible explanation for this observation would be that the electrons of the Ti cations in the topmost layer are localized, while the itinerant elec-

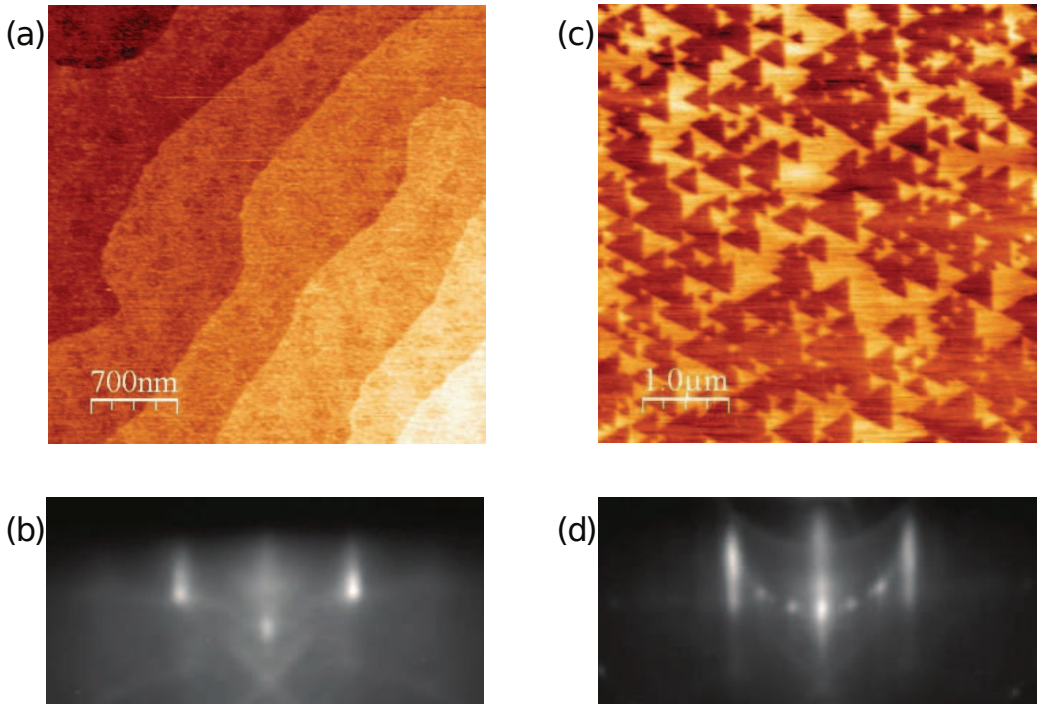

FIG. 4. (Color online) (a) Atomic force microscope (AFM) image of a chemically and thermally prepared $SrTiO_3$ (111) surface. The surface is single terminated and unreconstructed, as shown in the RHEED image in (b). Longer annealing times result in a mixed terminated surface, as demonstrated in the AFM friction image (c) measured in contact mode. A 3×3 reconstruction of the surface can be deduced from the corresponding RHEED image in (d).

trons exist in the subsurface layers. For the (110) surface, a surface preparation similar to the one described above for the (111) surface was conducted. The data quality of fractured and prepared samples are quite similar as the chemical etching step is not perfectly adapted to the (110) surface. Sr and Ti are both situated in one of the alternating (110) layers of $(SrTiO)^{4+}$ and O_2^{4-} building up the crystal lattice. Thus, the selective etching of Sr-related species might result in a rather rough surface.

Photon energy dependence

The photon energy dependence of the electronic states at the $SrTiO_3$ (111) surface is displayed in the main text in figure 3. Although the states do not disperse, confirming their confined nature, the intensity of the states drops rather quickly moving away from Γ_{222}. This observation is similar to the intensity modulation as a function of the photon energy reported previously at the (001) surface of $SrTiO_3$ [14] and $KTaO_3$ [18], as well as in quantum well states of metals [25, 26]. This modulation is due to photoemission dipole selection rules: the optical excitation of the electrons occurs from initial states in the near surface region that do not disperse along the confinement direction (the confined electrons) to dispersing bulk final states. Moreover, if the wave function of the confined states is not exactly localized in a 2D layer, but exists over several unit cells, the dispersion along the confinement direction will be affected. This can be intuitively understood from Heisenberg uncertainty principle: only a strict 2D confinement in real space yields a complete indetermination of the electron momentum along the confinement direction, hence an exactly cylindrical Fermi surface. Some delocalization along the confinement direction, as in quantum-well states, implies a small dispersion of the Fermi surface along that direction.

Bearing these effects (selection rules in quantum wells, finite delocalization) in mind, one can comprehend the data in figure 5(a), which shows a superposition of Fermi surface maps measured at different photon energies, for a (111) surface prepared *in-situ*. The black hexagons are the Brillouin zones assuming an unreconstructed surface. Thus, due to selection rules, the intensity of the photoemission peak from the confined states is highest close to positions corresponding to Γ points of the bulk, where final states at the same $k_{\langle 111 \rangle}$ momentum are available for the optical transition. But this intensity will decrease rapidly by moving along $k_{\langle 111 \rangle}$, away from the bulk Γ points [25]. Experimentally, this is done by changing the photon energy. This results in the necessity to measure in-plane Fermi surface maps at different photon energies,

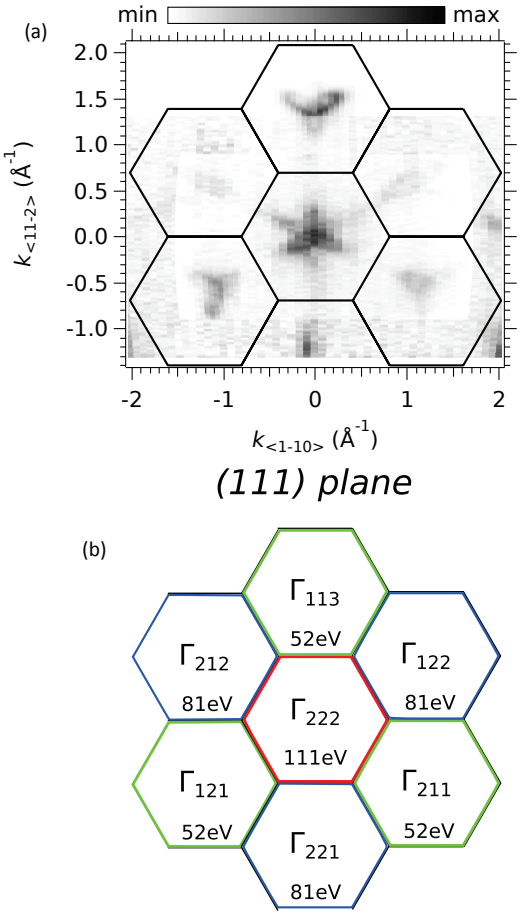

FIG. 5. (Color online) (a) Superposition of Fermi surface maps measured for the chemically and thermally prepared $SrTiO_3$ (111) sample ((3×3) reconstructed surface) at photon energies of $h\nu = 47$ eV and $h\nu = 96$ eV. (b) Reciprocal 2D space in the (111) plane. Inside each Brillouin zone the projections of the different bulk Γ points corresponding to available final states during the photoemission process at the specified photon energy are indicated. This diagram helps understanding the Fermi-surface intensities shown in panel (a). The color (red, blue, green) of the hexagons indicates which Γ points are located in the same (111) plane in reciprocal space.

and then superpose them to retrieve the complete periodicity of the electronic states, as illustrated in figure 5(b). This figure shows the positions of the experimentally observed Γ points projected in the (111) plane. The photon energy inside each Brillouin zone corresponds to the $k_\perp$ value of the Γ points assuming a work function of $W = 4.25$ eV and an inner potential of $V_0 = 12$ eV.

Fermi surface of $SrTiO_3$(110)

As stated in the main text, the Fermi surface map shown in figure 2 is a superposition of intensities measured in the bulk Γ_{130} and Γ_{131} Brillouin zones. Figure 6

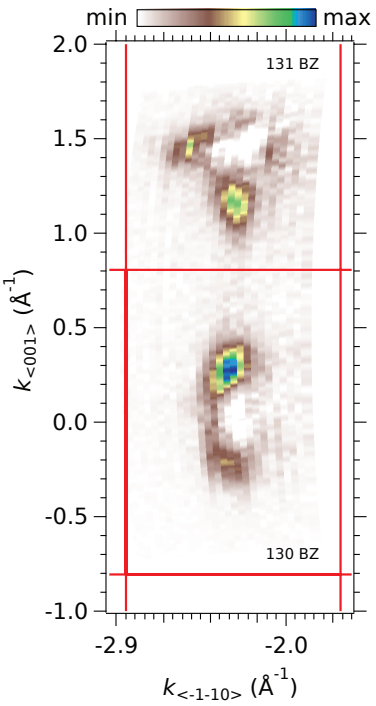

FIG. 6. (Color online) Second derivative of ARPES Fermi surface map at $h\nu = 91$ eV in the (110) plane of a cleaved insulating $SrTiO_3$ sample. The map spans the Γ_{130} (bottom) and Γ_{131} (top) Brillouin zones. The red lines indicate the edges of the unreconstructed (110) Brillouin zones.

shows the intensities measured in those Brillouin zones. Due to photoemission matrix elements, only the vertical ellipsoidal Fermi surface is observed around the Γ_{130} point, while both the vertical and the smaller horizontal ellipsoidal Fermi surfaces are observed around the Γ_{131} point.

Estimate of the spatial extensions of the 2DEGs at the $SrTiO_3$ (110) and (111) surfaces.

In our data, figures 2 and 3 of the main text, only the lowest-energy subbands are observed. To estimate the maximal extension d_{max} of the corresponding confined states, we follow the same strategy of Ref. [19]. We assume that the second subbands are slightly above the Fermi level, hence unoccupied and not detectable by ARPES. We then use a triangular potential well model, and take as effective masses along the [110] and [111] confinement directions, respectively, $m_{110} \approx 1.6 m_e$ (the lightest of the masses gives the largest 2DEG thickness) and $m_{111} = 1.0 m_e$ (given by extrapolating the experimental masses at the (001) surface to the bulk [111] direction) –see table I of the main text. This gives $d^{110}_{max} \approx 1.7$ nm, amounting to 6 2D-layers or 3 bulk unit cells along [110], and $d^{111}_{max} \approx 1.9$ nm, corresponding to

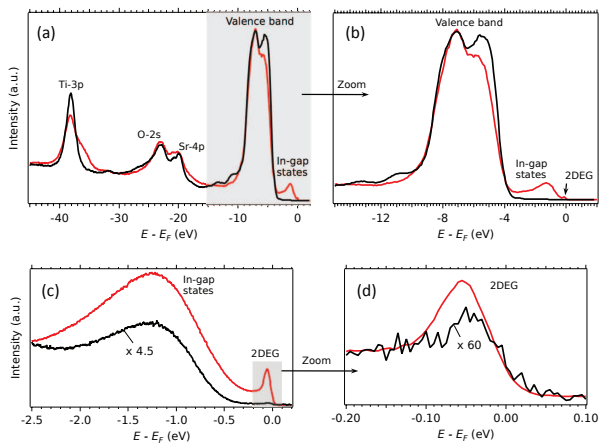

FIG. 7. (Color online) (a) Angle-integrated spectra of an $SrTiO_3$ sample prepared *in-situ*, measured at a photon energy of hv = 110 eV, with a step size of 50 meV, showing the density of states for binding energies between −45 eV and 2 eV. The black curve was measured shortly after the first exposure of the sample to the UV light, and the red curve at the end of the measurements (about 36 hours later). (b) Zoom over the valence band region. (c) Angle-integrated spectra showing the in-gap states and the confined states at the Fermi level, measured at hv = 110 eV with a step size of 5meV. (d) Zoom over the confined states at the Fermi level.

∼ 9 layers of Ti (111), or again about 3 bulk unit cells along [111].

UV dose dependence: enhancement of Ti^{3+} signal

Understanding the influence of the UV synchrotron illumination on the observed confined states is important to determine the origin of such states. Recent photoemission studies on the 2DEGs at the (001) or (110) surface of $SrTiO_3$ proposed that the UV light creates oxygen vacancies [15, 24] or, respectively, ferroelectric lattice distortions [16] in the surface region. The two effects are difficult to disentangle using photoemission, as in both cases charge is transferred from O to Ti. Figure7(a) shows the angle-integrated spectra, measured at hv = 110 eV, of a $SrTiO_3$ sample prepared *in-situ* for binding energies between −45 eV and 2 eV. The black curve was measured shortly after the first exposure of the sample to the UV light, while the red curve was recorded at the end of the measurements (36 hours later). The spectra are normalized to the intensity of the Sr 4*p*-peak, which should be rather independent of the concentration of oxygen vacancies and/or ferroelectric lattice distortions. Figure 7(b) is a zoom over the valence band region, while figures 7(c, d) show the in-gap states and the confined states at the Fermi level. The change of various features under UV irradiation is obvious: first, the formation of a shoulder in the Ti-3*p* peak at lower binding energies, indicating electron transfer from Ti^{4+} to a lower valency state. Second, the decrease in intensity of the valence band in its low binding energy region. Third, the increase in intensity of the in-gap states and of the peak corresponding to the confined states. All these observations could be explained by both scenarios: the creation of oxygen vacancies and the ferroelectric lattice distortions.

In contrast to samples prepared *in-situ*, cleaved samples show a different behavior regarding the UV light exposure. The subbands of the 2DEG in all the *cleaved* $SrTiO_3$ surfaces we have studied so far, *i.e.* (001), (110) and (111), are all observed essentially *immediately after cleaving*, with no or little time delay after the first exposure to UV light. A more detailed study on the UV induced effects is beyond the scope of this paper.

Tight-binding calculations of the 2DEG at the $SrTiO_3(111)$ surface

The band dispersions shown in the main text correspond to the bottom of the conduction band of $SrTiO_3$, which is formed by Ti-3*d* orbitals hybridized with O-2*p* orbitals. The interaction between the oxygen anions forming an octahedron and the Sr cation generates a large crystal field which splits the *d* states in a lower t_{2g} triplet and an higher e_g doublet. Hence, only the t_{2g} orbitals are considered in our tight-binding model, which is based on the calculations of reference [10]. Our model for the $SrTiO_3(111)$ surface is limited to a bilayer of Ti atoms. This approach is sufficient to fit the experimental data as shown in the main text, but does not necessarily imply the confinement of the electrons to a bilayer.

The Hamiltonian H of the system in the basis $\{d_{I,n}\}$, where $I = (X, Y, Z)$ correspond to the orbital character (yz, zx, xy) of the t_{2g} orbitals and $n = 1, 2$ indicates the number of the layer of Ti cations, is given by:

$$H = \begin{pmatrix} d^\dagger_{X,1} \\ d^\dagger_{Y,1} \\ d^\dagger_{Z,1} \\ d^\dagger_{X,2} \\ d^\dagger_{Y,2} \\ d^\dagger_{Z,2} \end{pmatrix}^T \begin{pmatrix} \tilde{\epsilon}_X & & & \epsilon_X & & \\ & \tilde{\epsilon}_Y & & & \epsilon_Y & \\ & & \tilde{\epsilon}_Z & & & \epsilon_Z \\ \epsilon^*_X & & & \tilde{\epsilon}_X & & \\ & \epsilon^*_Y & & & \tilde{\epsilon}_Y & \\ & & \epsilon^*_Z & & & \tilde{\epsilon}_Z \end{pmatrix} \begin{pmatrix} d_{X,1} \\ d_{Y,1} \\ d_{Z,1} \\ d_{X,2} \\ d_{Y,2} \\ d_{Z,2}. \end{pmatrix}$$

Here, $\tilde{\epsilon}_I$ describes the hopping of electrons between next nearest neighbors of Ti cations (intra-layer hopping), characterized by the hopping amplitude $t_{\sigma''}$, whereas ϵ_I describes the hopping between nearest neighbors (inter-layer hopping) with hopping amplitudes t_π and t'_δ:

$$\tilde{\epsilon}_X = -2t_{\sigma''}\cos(-\frac{\sqrt{3}}{2}\tilde{a}\ k_x + \frac{3}{2}b\ k_y)$$
$$\tilde{\epsilon}_Y = -2t_{\sigma''}\cos(\frac{\sqrt{3}}{2}\tilde{a}\ k_x + \frac{3}{2}b\ k_y)$$
$$\tilde{\epsilon}_Z = -2t_{\sigma''}\cos(\sqrt{3}\tilde{a}\ k_x)$$
$$\epsilon_X = -t_\pi e^{-i\tilde{a}\ k_y}\left[1 + e^{i\frac{\tilde{a}}{2}(-\sqrt{3}k_x+3k_y)}\right] - t_{\delta'}e^{i\frac{\tilde{a}}{2}(\sqrt{3}k_x+k_y)}$$
$$\epsilon_Y = -t_\pi e^{-i\tilde{a}\ k_y}\left[1 + e^{i\frac{\tilde{a}}{2}(\sqrt{3}k_x+3k_y)}\right] - t_{\delta'}e^{i\frac{\tilde{a}}{2}(-\sqrt{3}k_x+k_y)}$$
$$\epsilon_Z = -2t_\pi e^{\frac{i}{2}\tilde{a}\ k_y}\cos(\frac{\sqrt{3}}{2}\tilde{a}\ k_x) - t_{\delta'}e^{-i\tilde{a}\ k_y}.$$

In the above expressions, k_x corresponds to $k_{\langle 1\bar{1}0\rangle}$, k_y to $k_{\bar{1}\bar{1}2}$, and $\tilde{a}$ to the cubic lattice constant a projected in the (111) plane $\tilde{a} = \sqrt{2/3}a$. Compared to the calculations of reference [10], our data can be fitted rather well using a simplified model. We neglect in our model the spin-orbit coupling, the trigonal crystal field, the layer potential difference, crystal distortions at low temperature, and the hopping ($t_{\pi'}$) between next nearest neighbors of different orbital symmetry. The fits shown in figures 3(a) and 3(c) of the main text are based on such a simplified model using fitting parameters of $t_\pi = 1.6$ eV, $t_{\delta'} = 0.07$ eV and $t_{\sigma''} = 0.05$ eV.

Note that such value of t_π, which quantifies the hopping energy between nearest neighbors along the [100] (and equivalent) directions, is here over 4 times larger than the same parameter inferred from the 2DEG at the $SrTiO_3$ (001) surface (namely, $t = 0.36$ eV, see the main text). This shows again that the effective masses of the 2DEG at the $SrTiO_3$ (111) surface strongly differ from what would be expected from a model based on the 2DEG at the (001) surface. As discussed in the main text, the electrons moving along any direction in the (111) plane will actually hop in zig-zag patterns between first neighbors along [001] (or equivalent) directions, and thus will experience the confining potential gradient and the modified crystal field outside the surface. These effects are not accounted by our minimalist TB model. Additionally, our TB model only considers one bilayer of Ti atoms. However, it is known that in quantum well states the effective masses of the confined electrons depend on the width of the quantum well or, equivalently, the number of layers [27, 28]. All these effects should be taken into account in future theoretical works addressing the 2DEGs at the different surfaces of $SrTiO_3$. On the other hand, while distortions of the crystal lattice, and thereby of the overlap between the different t_{2g} orbitals, might exist at the surface and be slightly different depending on the surface orientations, they should bear a negligible effect on the 2DEGs reported here, as we have seen that their electronic structure is essentially insensitive to surface polarity or reconstructions.

* andres.santander@csnsm.in2p3.fr

[1] H. Takagi and H. Y. Hwang, An Emergent Change of Phase for Electronics, Science **327**, 1601 (2010).

[2] J. Mannhart and D.G. Schlom, Oxide Interfaces–An Opportunity for Electronics, Science **327**, 1607 (2010).

[3] S.Thiel, G. Hammerl, A. Schmehl, C. W. Schneider, J. Mannhart, Tunable Quasi-Two-Dimensional Electron Gases in Oxide Heterostructures, Science **313**, 1942 (2006).

[4] A.D. Caviglia, S. Gariglio, N. Reyren, D. Jaccard, T. Schneider, M. Gabay, S. Thiel, G. Hammerl, J. Mannhart, J.-M. Triscone, Electric field control of the $LaAlO_3/SrTiO_3$ interface ground state, Nature (London) **456**, 624 (2008).

[5] A. Brinkman, M. Huijben, M. van Zalk, J. Huijben, U. Zeitler, J.C. Maan, W.G. van der Wiel, G. Rijnders, D.H.A. Blank, H. Hilgenkamp, Magnetic effects at the interface between non-magnetic oxides, Nat. Mater. **6**, 493 (2007).

[6] M. Salluzzo, S. Gariglio, X. Torrelles, Z. Ristic, R. Di Capua, J. Drnec, M. Moretti Sala, G. Ghiringhelli, R. Felici, N.B. Brookes, Structural and Electronic Reconstructions at the $LaAlO_3/SrTiO_3$ Interface, Adv. Mater. **25**, 2333 (2013).

[7] G. Herranz, F. Sánchez, N. Dix, M. Scigaj, J. Fontcuberta, High mobility conduction at (110) and (111) $LaAlO_3/SrTiO_3$ interfaces, Sci. Rep. **2**, 758 (2012).

[8] A. Annadi *et al.*, Anisotropic two-dimensional electron gas at the $LaAlO_3/SrTiO_3$ (110) interface,Nat. Commun. **4**, 1838 (2013).

[9] G. Herranz, N. Bergeal, J. Lesueur, M. Scigaj, N. Dix, J. Fontcuberta, Orientational tuning of the 2D-superconductivity in $LaAlO_3/SrTiO_3$ interfaces, arXiv:1305.2411 (2013).

[10] D. Xiao, W. Zhu, Y. Ran, N. Nagaosa, S. Okamoto, Interface engineering of quantum Hall effects in digital transition metal oxide heterostructures, Nat. Comm. **2**, 596 (2011).

[11] K.-Y. Yang, W. Zhu, D. Xiao, S. Okamoto, Z. Wang, Y. Ran, Possible interaction-driven topological phases in (111) bilayers of $LaNiO_3$, Phys. Rev. B **84**, 201104 (2011).

[12] A. Rüegg and G.A. Fiete, Topological insulators from complex orbital order in transition-metal oxides heterostructures, Phys. Rev. B **84**, 201103 (2011).

[13] D. Doennig, W.E. Pickett, R. Pentcheva, Massive Symmetry Breaking in $LaAlO_3/SrTiO_3$(111) Quantum Wells: A Three-Orbital Strongly Correlated Generalization of Graphene, Phys. Rev. Lett. **111**, 126804 (2013).

[14] A.F. Santander-Syro *et al.*, Two-dimensional electron gas with universal subbands at the surface of $SrTiO_3$, Nature (London) **469**, 189 (2011).

[15] W. Meevasana, P.D.C. King, R.H. He, S.-K. Mo, M. Hashimoto, A. Tamai, P. Songsiriritthigul, F. Baumberger, Z.-X. Shen, Creation and control of a two-dimensional electron liquid at the bare $SrTiO_3$ surface, Nat. Mater. **10**, 114 (2011).

[16] N.C. Plumb *et al.*, Mixed dimensionality of confined conducting electrons tied to ferroelectric surface distortion on an oxide, arXiv:1302.0708, (2013).

[17] P.D.C. King *et al.*, Subband Structure of a Two-

Dimensional Electron Gas Formed at the Polar Surface of the Strong Spin-Orbit Perovskite $KTaO_3$, Phys. Rev. Lett. **108**, 117602 (2012).

[18] A.F. Santander-Syro *et al.*, Orbital symmetry reconstruction and strong mass renormalization in the two-dimensional electron gas at the surface of $KTaO_3$, Phys. Rev. B **86**, 121107 (2012).

[19] C. Bareille *et al.*, Two-dimensional electron gas with six-fold symmetry at the (111) surface of $KTaO_3$, Sci. Rep. **4**, 3586 (2014).

[20] A. Biswas, P.B. Rossen, C.-H. Yang, W. Siemons, M.-H. Jung, I.K. Yang, R. Ramesh, Y.H. Jeong, Universal Ti-rich termination of atomically flat $SrTiO_3$ (001), (110), and (111) surfaces, Appl. Phys. Lett. **98**, 051904 (2011).

[21] J. Chang, Y.-S. Park, S.-K. Kim, Atomically flat single-terminated $SrTiO_3$ (111) surface, Appl. Phys. Lett. **92**, 152910 (2008).

[22] See Supplemental Material [URL] for more details on the sample preparation, photon energy dependent matrix elements, the Fermi surface of $SrTiO_3$(110), spatial extensions of the 2DEGs and the UV dose dependence of the photoemission spectra.

[23] G. Khalsa and A.H. MacDonald, Theory of the $SrTiO_3$ surface state two-dimensional electron gas, Phys. Rev. B **86**, 125121 (2012).

[24] Z. Wang, Z. Zhong, X. Hao, S. Gerhold, B. Stoger, M. Schmid, J.Sanchez-Barriga, A. Varykhalov, C. Franchini, K. Held, U. Diebold, Anisotropic two-dimensional electron gas at $SrTiO_3$(110),PNAS **111**, 3933 (2014).

[25] A. Mugarza, J. Ortega, A. Mascaraque, E. Michel, K. Altmann, F. Himpsel, Periodicity and thickness effects in the cross section of quantum well states, Phys. Rev. B **62**, 12672 (2000).

[26] E.D. Hansen, T. Miller, T.C. Chiang, Quantum-well or bulklike behaviour of Cu layers on Co, J. Phys.: Condens. Matter **9**, L435 (1997).

[27] Y.Z. Wu, C.Y. Won, E. Rotenberg, H.W. Zhao, F. Toyoma, N.V. Smith, Z.Q. Qiu, Dispersion of quantum well states in Cu/Co/Cu(001), Phys. Rev. B **66**, 245418 (2002).

[28] K. Yoshimatsu, K. Horiba, H. Kumigashira, T. Yoshida, A. Fujimori, M. Oshima, Metallic Quantum Well States in Artificial Structures of Strongly Correlated Oxide, Science **333**, 319 (2011).

Atomic specialization at the surface of oxygen-deficient $SrTiO_3$

Michaela Altmeyer,[1] Harald O. Jeschke,[1] Oliver Hijano-Cubelos,[2] Cyril Martins,[2] Frank Lechermann,[3] Klaus Koepernik,[4] Andres Santander-Syro,[5] Marcelo J. Rozenberg,[2] Roser Valentí,[1] and Marc Gabay[2]

[1] *Institut für Theoretische Physik, Goethe-Universtät Frankfurt, 60438 Frankfurt am Main, Germany*
[2] *Laboratoire de Physique des Solides, Bat 510, Université Paris-Sud, 91405 Orsay, France*
[3] *I. Institut für Theoretische Physik, Universität Hamburg, 20355 Hamburg, Germany*
[4] *IFW Dresden, Helmholtzstraße 20, 01069 Dresden, Germany*
[5] *CSNSM IN2P3/CNRS, Bats 104&108, Université Paris Sud, 91405 Orsay, France*

Motivated by recent spin- and angular-resolved photoemission measurements (SARPES) performed on the two-dimensional electronic states confined near the (001) surface of $SrTiO_3$ in the presence of oxygen vacancies, we explore their spin structure by means of *ab initio* density functional theory (DFT) calculations of slabs. Relativistic non-magnetic DFT calculations display Rashba-like spin winding with a splitting of a few meV and when surface magnetism on the Ti ions is included, bands become spin-split with an energy difference ~ 100 meV at the Γ point, consistent with SARPES findings. While magnetism tends to suppress the effects of the relativistic Rashba interaction, signatures of it are still clearly visible in terms of complex spin textures. Furthermore, we observe an *atomic specialization* phenomenon, namely two types of electronic contributions; one is from Ti atoms neighboring the oxygen vacancies that acquire rather large magnetic moments and mostly create in-gap states; another comes from the partly polarized t_{2g} itinerant electrons of Ti atoms lying further away from the oxygen vacancy which form the two-dimensional electron system and are responsible for the Rashba spin winding and the spin splitting at the Fermi surface.

Introduction.- Transition metal oxides constitute a major topic of interest in the scientific community as these materials are endowed with a broad range of significant electronic properties, i.e. functionalities, ranging from ferroelectricity to metal-insulator transitions as well as from magnetism to superconductivity. Many of these compounds exhibit structural instabilities, strong electronic correlations and complex phase diagrams with competing ground states. Artificial structures of transition metal oxides therefore seem ideal to explore interfacial effects that could possibly lead to new phases. In this respect, the two-dimensional electronic system (2DES) at the interface between the wide band-gap insulators $LaAlO_3$ (LAO) and $SrTiO_3$ (STO) that was observed by Ohtomo and Hwang [1, 2] a decade ago has attracted a considerable amount of attention. It was found that the 2DES hosts gate-tunable insulator to metal, insulator to superconductor transitions, magnetism [3] and a large interfacial spin-orbit effect [4]. The mechanisms responsible for these special properties are still under debate. Questions include the intrinsic (i.e. electronic reconstruction) versus extrinsic (e.g. oxygen vacancies) mechanism [5] responsible for the formation of the 2DES, and also the role and spatial distribution of the various d orbitals which could contribute selectively to a specific charge or spin property.

Angular-resolved photoemission (ARPES) measurements revealed the existence of 2DES with similar features to those seen at the LAO-STO interface at *bare surfaces* of several insulating perovskite oxide crystals, and among them (001) oriented STO [6, 7]. For this compound, the origin of the carriers can be plausibly ascribed to oxygen vacancies since constitutive layers of the structure are charge neutral. These vacancies are likely created during the sample preparation process and also when the sample is illuminated during the measurement [8]. Spin resolved ARPES (SARPES) of the 2DES at the (001) oriented STO surface [9] have highlighted the existence of sizable Rashba-like spin textures along with a large energy splitting that has been interpreted as a signature of ferromagnetism. Their simultaneous occurrence is puzzling since the two effects *a priori* compete with each other and estimates of the respective energy scales give about 100 meV for magnetism and a few meV for surface spin-orbit coupling.

A number of density functional theory (DFT) studies pertaining to bulk STO and including local correlation effects found in-gap bound states below the conduction band and magnetism, when isolated oxygen vacancies or pairs of vacancies are present [10–12] in the bulk. The reported location of the bound state and the size of the spin polarization depend strongly on the computational details. Recent DFT calculations for slab geometries [13–15] found qualitative agreement with the bulk case. In addition, in the latter case DFT finds a 2DES as soon as oxygen vacancies are incorporated in the slab, as evidenced by the presence of dispersive t_{2g} bands at the Fermi energy. Effects of spin orbit coupling [16, 17], correlation [18] have also been studied at the model level.

In the present work, we investigate via first principles DFT the spin textures and magnetism of the 2DES states at the (001) oriented surface of STO and we determine how these emerge from the electronic states that are formed in the presence of oxygen single- and divacancies near the surface. Further insight into the origin of the in-gap states and of the 2DES states is obtained

through tight-binding modelling of divacancies. As the preexistent literature on this problem is already large, let us emphasize that the new results reported here are relevant for the interpretation of the following experimental facts: (i) ARPES spectra pertaining to 2DES at interfaces and also at surfaces all seem to appear concomitant with a universal non-dispersive feature at an energy of about 1.3 eV below the Fermi energy [19–21]; and (ii) spin-ARPES appears to highlight the occurrence of both Rashba-like textures and ferromagnetism [9].

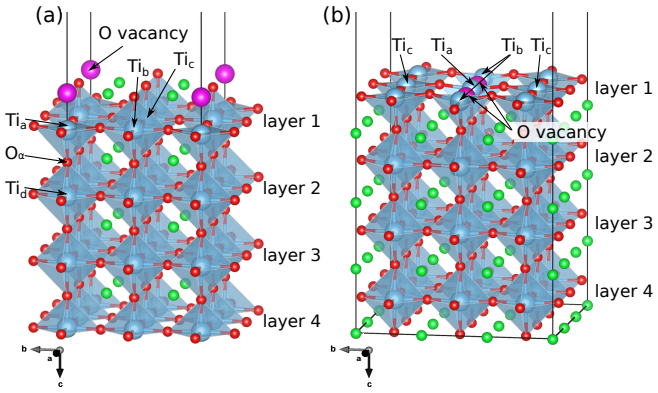

FIG. 1. (a) SrO-terminated 2×2×4 slab with one oxygen vacancy at the topmost level. O_α denotes the position where a second vacancy is introduced for divacancy 2×2×4 calculations (see text). (b) TiO_2-terminated 3×3×4 slab with two vertically positioned oxygen vacancies. Other slab geometries are included in the Supp. Inf.

Methods.- For our DFT calculations we considered various slabs of (001) oriented STO with different oxygen vacancy concentrations. From the large range of possible slab structures and vacancy configurations we have selected three representative cases; a single vacancy at the topmost level of a SrO-terminated 2×2×4 slab (Fig. 1 (a)), a vertical divacancy at the topmost level of a SrO-terminated 2×2×4 slab (Fig. 1 (a)), and a horizontal divacancy sandwiching a Ti atom located at the topmost level of a TiO_2-terminated 3×3×4 slab (Fig. 1 (b)). These slabs are chosen as test cases for investigating the effects of surface reconstruction, in-gap states, Rashba spin-orbit coupling and magnetism. In all slabs we included a vacuum layer of at least 20 Å to avoid any spurious interactions between the periodic images. The trade-off between considering large enough slabs to avoid boundary effects and computational efficiency dictated our choice of supercell sizes. Note, that our single vacancy 2×2×4 and divacancy 3×3×4 slabs have realistic carrier densities of about 1.5×10^{14} cm^{-2} as obtained by integrating occupied densities of states and of about 3×10^{14} cm^{-2} as estimated from Fermi surface areas.

In order to account for possible surface reconstructions, the internal coordinates of the slabs were relaxed with the projector-augmented wave basis [22] as implemented in VASP [23, 24]. For the relaxations and electronic structure calculations we used the generalized-gradient approximation (GGA) [25] in the Dudarev [26] GGA+U scheme as described in Ref. 13. The electronic structure was analyzed with the all-electron full-potential local orbital (FPLO) [27] method and GGA+U functional [28]. Checks were also performed with the all-electron full-potential linearized augmented plane wave method as implemented in Wien2k [29]. Spin textures for the various slabs were obtained from full relativistic calculations in FPLO (GGA+SO+U) with a newly implemented subroutine.

Results and discussion.- We start first with the analysis of spin textures in the absence of magnetism. In Figs. 2 (a) and 2 (d) we show the spin textures at the Fermi surface ($k_z = 0$) obtained for non-magnetic ground states in GGA+SO+U calculations for the single vacancy 2×2×4 and the divacancy 3×3×4 slabs, respectively (results for the divacancy 2×2×4 are shown in the Suppl. Mat.). We used typical values for the parameters (U=5 eV and J_H=0.64 eV on Ti 3d orbitals [30]). In all cases, every two bands show a small energy splitting of a few meV at the Fermi surface, due to the spin-orbit interaction. Spins on the Fermi surface ($k_z = 0$) are fully polarized parallel to the surface xy plane, aligned in opposite direction to each other in the split bands. On some of the bands the spins are pointing clock- and anti-clockwise around the center of the Brillouin zone, which is a clear signature of the relativistic Rashba effect due to the breaking of inversion symmetry at the surface of $SrTiO_3$. On other bands we additionally notice a more complex texture of rotating spins, born out of the interplay between spin and orbital degrees of freedom [8, 31]. The rather small size of the spin-splitting contrasts with the large value reported in recent SARPES experiments [9].

Next, we consider solutions with ferromagnetic order and spin-orbit interactions; first for the 2×2×4 slab. Fig. 2 (b) displays the spin-projected bandstructure obtained from spin-polarized GGA+SO+U calculations for the 2×2×4 slab with one vacancy (similarly, results for the divacancy 2×2×4 slab are shown in the Suppl. Inf.). We adopt the magnetic moment quantization axis along z but below we also discuss the case of a quantization along x. The size of the magnetic splitting can be inferred from the black arrows connecting the majority and minority spin bands. For a comparison to the experiment we have to consider the splitting of the light bands of d_{xy} character, as heavy bands have been silenced in the measurements [9]. The energy separation at the Γ point of the two spin-splitted d_{xy} bands originating from Ti_d (Fig. 1(a)) is of the order of 60 meV and therefore in qualitative agreement to the experimental data (Ref. 9, $\Delta E \approx 100$ meV).

In order to identify the microscopic origin of the peculiar electronic and magnetic features described above

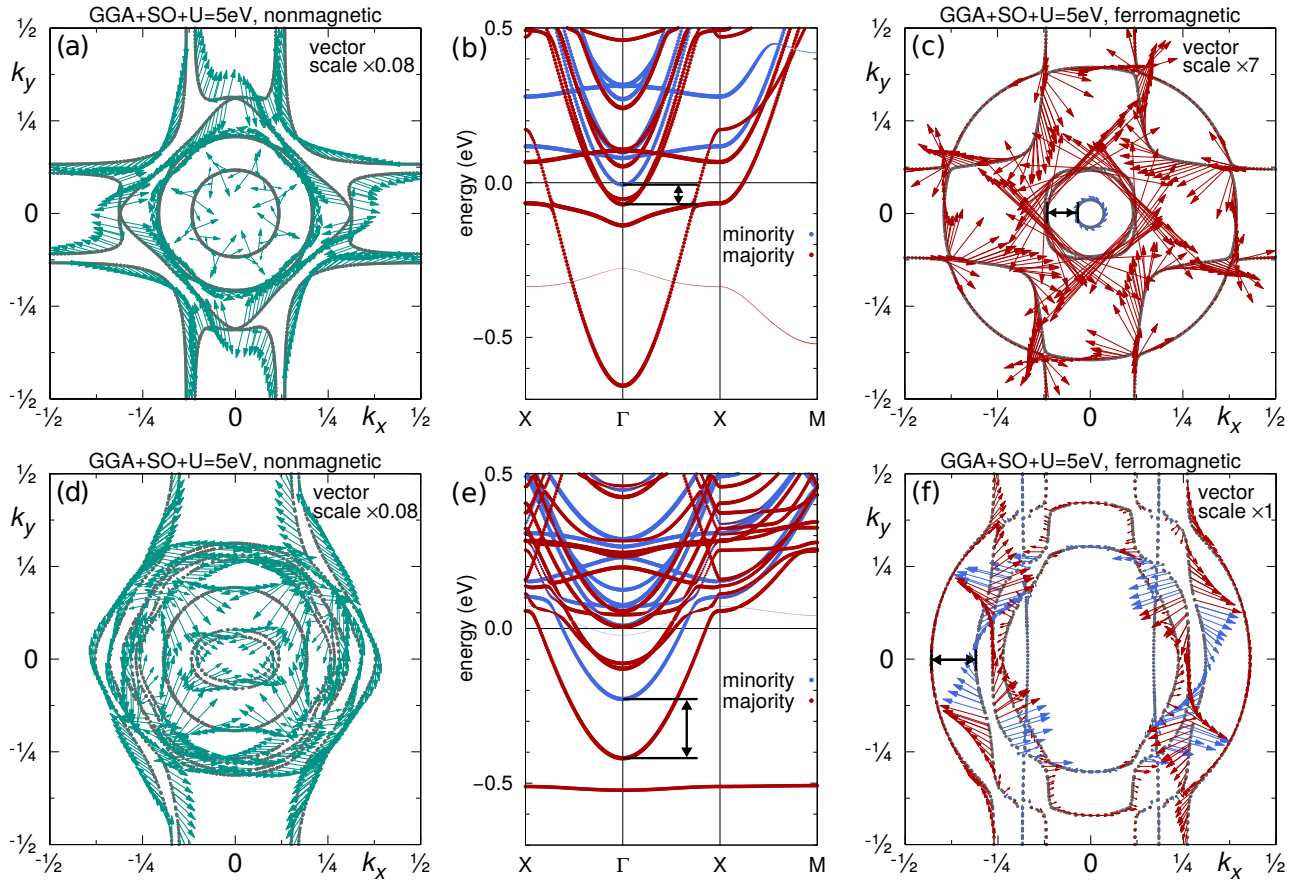

FIG. 2. Spin-textures and spin-polarized bandstructures for the relaxed 2×2×4 slab with one O vacancy (a)-(c) and for the relaxed 3×3×4 slab with an oxygen divacancy in the surface TiO_2 layer (d)-(f). (a) and (d) are based on nonmagnetic GGA+SO+U calculations with $U = 5$ eV, and (b), (c), (e), (f) are obtained from ferromagnetic GGA+SO+U calculations with $m \parallel \hat{z}$. Reciprocal space units are 0.402 $Å^{-1}$ for (a) and (c), 0.268 $Å^{-1}$ for (d) and (f).

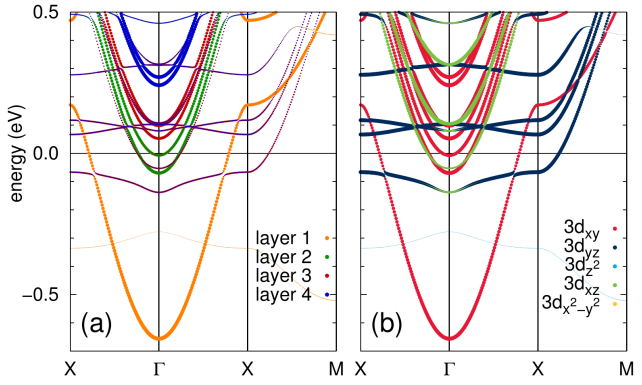

FIG. 3. Ferromagnetic GGA+SO+U Ti 3d bandstructure for the relaxed 2×2×4 slab with one O vacancy with an $m \parallel \hat{z}$ setup. (a) Layer resolved. (b) Orbitally resolved. Note, that the thickness of lines is proportional to the strength of the 3d character on the bands.

we plot in Fig. 3 the layer and orbitally resolved GGA+SO+U bandstructure near E_F for the one-vacancy 2×2×4 slab (similar plots are shown in the Suppl. Inf for the divacancy 2×2×4 slab) and in Fig. 4 (a) we display the Ti $t_{2g} - e_g$ resolved magnetic moments as a function of the distance between Ti and O vacancy. We find that (i) the magnetic splitting of the light d_{xy} bands at the Fermi level is caused by itinerant electrons belonging to Ti located not in the immediate vicinity of the oxygen vacancy (e.g. Ti_d in Fig. 1 (a)) with magnetic moments of the order of 0.1 μ_B (see Fig. 4 (a)). (ii) Ti atoms neighboring the oxygen vacancy in the uppermost layer (Ti_a, Ti_b, Ti_c in Fig. 1(a)) have the largest magnetic moment (Fig. 4 (a)) and are mostly responsible for the heavy bands and occupied states at higher binding energies (see Fig. 3). In particular, we observe an in-gap band of Ti e_g (d_{z^2}) character hybridizing with Ti 4s and 4p corresponding to Ti_a. It sits at -0.4 eV in the single vacancy case and is shifted to about -1 eV in the divacancy case (see Suppl. Inf.) The position of this band depends on the parameters U and J_H chosen for the GGA+U calculations and on the concentration and position of vacancies in the slab (see Suppl. Mat. and Ref. 15). Note that this band has some dispersion due to the fact that the slab is too small and e_g Bloch states

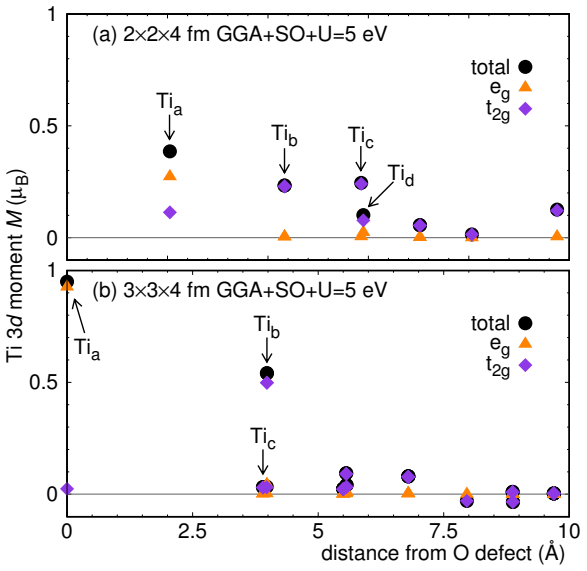

FIG. 4. t_{2g}-e_g resolved magnetic moments in GGA+SO+U=5 eV for the relaxed (a) 2×2×4 and (b) 3×3×4 slab in the ferromagnetic $m \parallel \hat{z}$ setup (magnetic moment of the closest neighbor smaller than total moment on Ti, as $4s$ and $4p$ are also contributing to the magnetic moment).

between neighboring unit cells are formed.

Interestingly, already with this minimal slab, we find a phenomenon of *atomic specialization*, i.e. there are two types of electronic contributions to magnetism: one from Ti atoms neighboring the oxygen vacancy that acquire rather large magnetic moments and are mostly located below the Fermi surface inducing in-gap states; and another, from those Ti atoms lying further away from the oxygen vacancies, that correspond to polarized t_{2g} itinerant electrons with small magnetic moments, which are responsible for the Rashba spin winding and the spin splitting at the Fermi surface. These remarkable effects will be even more pronounced in larger slabs.

In the 3×3×4 slab (Fig. 1(b)) the loss of symmetry due to the presence of the vacancies induces a ladder of bands at E_F corresponding to inequivalent Ti atoms (Fig. 2 (f)) and a breaking of the xy symmetry as also observed in the Fermi surface topography (Fig. 2 (d)). In experiment, such an asymmetry is not observed and is here a consequence of considering an individual divacancy realization. This asymmetry is expected to decrease when larger slab geometries and a disorder average are considered, which is beyond our computational possibilities.

The Ti atom in between the oxygen vacancies (Ti_a in Fig. 1 (b)) gives rise to a heavy e_g band of $d_{x^2-y^2}$ character which appears at the Fermi surface, while the neighboring Ti_b, due to the very special divacancy geometry, create dominantly d_{xz} in-gap states at -0.5 eV. Note, that a different arrangement of the divacancy in this slab has been found [15] to shift the heavy e_g state to the gap region consistent with experimental observations.

We observe here the same phenomenon of atomic specialization as in the smaller 2×2×4 slab; Ti atoms neighboring the oxygen vacancies (Ti_a and Ti_b in Fig. 1 (b)) acquire large magnetic moments (see Fig. 4 (b)) and are responsible for the in-gap states located at higher binding energies; while Ti atoms lying further away from the oxygen vacancy (Ti_c and beyond) contribute to the 2DES with itinerant electrons carrying small magnetic moments, which are responsible for the Rashba spin winding and the spin splitting at E_F.

Further insight into the atomic dichotomy can be gained through tight-binding cluster diagonalization (see Suppl. Inf.) of structures with various configurations of vacancies. In order to monitor the formation of the 2DES conduction band states and of the in-gap states, we adiabatically turn on the energy contributions that represent the effect of introducing a vacancy into the cluster. Features seen in DFT are qualitatively reproduced.

We now examine how magnetism and surface spin-orbit coupling interplay with each other. Based on our above discussion of each individual effect, we may infer that spin textures and spin splitting compete with each other in the t_{2g} bands. Fig. 2 (c) displays the spin texture at $k_z = 0$ obtained from spin-polarized GGA+SO+U calculations for the 2×2×4 slab with one vacancy. The spin texture shows signs of the Rashba winding but it is less pronounced than in the nonmagnetic case. Taking a closer look at the inner pockets in Fig. 2 (c) (blue and red circles centered at Γ) corresponding to the spin up and spin down projections (compare Fig. 2 (b)), we observe a significant Fermi momentum shift of the bands ($\sim 0.1\text{Å}^{-1}$), which is of the same order of magnitude as the one observed in SARPES experiments [9]. As can be seen from the now very small in-plane spin component ($P_{\parallel} \leq 0.04$), ferromagnetism is dominating the arrangement of the spins. Inclusion of magnetism in GGA+SO+U calculations for the 3×3×4 slab with an oxygen divacancy also yields a shift of ~ 0.1 Å^{-1} at E_F (Fig. 2 (f)) and while the spin winding is still visible, the in-plane spin component is small. In contrast to the nonmagnetic calculations, inclusion of correlation effects as implemented in the GGA+U functional is important for describing the Ti magnetic moments. All these observations are in agreement with the results of the smaller 2×2×4 slab and confirm the general validity of the results.

Note that while SARPES spectra show that the spin polarization vectors have the largest component parallel to the surface plane, we find that the (ferro-)magnetic moments should point out of the plane, leading to a small in-plane component of the spin polarization vectors, in agreement with previous theoretical considerations [32]. We also performed calculations with the magnetization axis along x; in this case spins are aligned in the plane and the Rashba interaction is unable to rotate the spins

to achieve a sign change for opposite k points; in view of the experimental observation, this orientation might not be preferred.

Conclusions.- By performing full relativistic non-magnetic and magnetic density functional theory calculations in the framework of GGA+SO+U on representative oxygen deficient $SrTiO_3$ slabs, we find the magnetic state to be the ground state and we observe clear signatures of *atomic specialization* of the electronic and magnetic contributions. Ti atoms neighboring the oxygen vacancies create e_g localized wavefunctions with large magnetic moments and are responsible for the presence of in-gap states at energies around -0.5 to -1 eV. The position of the in-gap states is influenced by the slab termination, the depth of the oxygen vacancy below the surface and by possible oxygen clustering. On the other hand, Ti atoms lying further away from the oxygen vacancy contribute with polarized t_{2g} itinerant electrons to the conducting 2DES and are responsible for the Rashba spin winding and the spin splitting at the Fermi surface observed in SARPES. Our calculations show that magnetism masks the Rashba effect by increasing the spin splitting of the t_{2g} orbitals and by modifying the individual spin orientation but it does not eliminate spin winding. The disagreement on the orientation of the magnetic moment between the spin-polarized GGA+SO+U calculations and SARPES may suggest inhomogeneities near the surface in the sample, e.g. a sea of 2DES interspersed with islands of magnetism perhaps mirroring a mixture of TiO_2 and SrO in the termination layer.

ACKNOWLEDGMENTS

We would like to thank Vladislav Borisov for performing test calculations with Quantum Espresso. We especially thank Domenico di Sante and Silvia Picozzi for useful discussions. M.A., H.O.J. and R.V. gratefully acknowledge the Deutsche Forschungsgemeinschaft (DFG) for financial support through grants SFB/TR 49, FOR 1346. M.A. and R.V. were partially supported by the Kavli Institute for Theoretical Physics at the University of California, Santa Barbara under National Science Foundation grant No. PHY11-25915.

[1] A. Ohtomo and H. Y. Hwang, *A high-mobility electron gas at the $LaAlO_3/SrTiO_3$ heterointerface*, Nature **427**, 423–426 (2004).

[2] S. Thiel, G. Hammerl, A. Schmehl, C. W. Schneider, and J. Mannhart, *Tunable quasi-two-dimensional electron gases in oxide heterostructures*, Science **313**, 1942 (2006).

[3] Julie A. Bert, Beena Kalisky, Christopher Bell, Minu Kim, Yasuyuki Hikita, Harold Y. Hwang, and Kathryn A. Moler, *Direct imaging of the coexistence of ferromagnetism and superconductivity at the $LaAlO_3/SrTiO_3$ interface*, Nat. Phys. **7**, 767 (2011).

[4] J. A. Sulpizio, S. Ilani, P. Irvin, and J. Levy, *Nanoscale phenomena in oxide heterostructures*, Ann. Rev. Mater. Res. **44**, 117 (2014).

[5] G. Berner, A. Müller, F. Pfaff, J. Walde, C. Richter, J. Mannhart, S. Thiess, A. Gloskovskii, W. Drube, M. Sing, and R. Claessen, *Band alignment in $LaAlO_3/SrTiO_3$ oxide heterostructures inferred from hard x-ray photoelectron spectroscopy*, Phys. Rev. B **88**, 115111 (2013).

[6] A. F. Santander-Syro, O. Copie, T. Kondo, F. Fortuna, S. Pailhes, R. Weht, X. G. Qiu, F. Bertran, A. Nicolaou, A. Taleb-Ibrahimi, P. Le Fevre, G. Herranz, M. Bibes, N. Reyren, Y. Apertet, P. Lecoeur, A. Barthelemy, and M. J. Rozenberg, *Two-dimensional electron gas with universal subbands at the surface of $SrTiO_3$*, Nature **469**, 189 (2011).

[7] W. Meevasana, P. D. C. King, R. H. He, S-K. Mo, M. Hashimoto, A. Tamai, P. Songsiriritthigul, F. Baumberger, and Z-X. Shen, *Creation and control of a two-dimensional electron liquid at the bare $SrTiO_3$ surface*, Nat. Mater. **10**, 114 (2011).

[8] S. McKeown Walker, A. de la Torre, F. Y. Bruno, A. Tamai, T. K. Kim, M. Hoesch, M. Shi, M. S. Bahramy, P. D. C. King, and F. Baumberger, *Control of a two-dimensional electron gas on $SrTiO_3$* (111) *by atomic oxygen,* Phys. Rev. Lett. **113**, 177601 (2014).

[9] A. F. Santander-Syro, F. Fortuna, C. Bareille, T. C. Roedel, G. Landolt, N. C. Plumb, J. H. Dil, and M. Radovic, *Giant spin splitting of the two-dimensional electron gas at the surface of $SrTiO_3$*, Nat. Mater. **13**, 1085 (2014).

[10] D. D. Cuong, B. Lee, K. M. Choi, H.-S. Ahn, S. Han, and J. Lee, *Oxygen vacancy clustering and electron localization in oxygen-deficient $SrTiO_3$: LDA+U study*, Phys. Rev. Lett. **98**, 115503 (2007).

[11] Z. Hou and K. Terakura, *Defect states induced by oxygen vacancies in cubic $SrTiO_3$: First-principles calculations*, J. Phys. Soc. Jpn. **79**, 114704 (2010).

[12] A. Lopez-Bezanilla, P. Ganesh, and P. B. Littlewood, *Magnetism and metal-insulator transition in oxygen-deficient $SrTiO_3$*, Phys. Rev. B **92**, 115112 (2015).

[13] J. Shen, H. Lee, R. Valenti, and H. O. Jeschke, *Ab initio study of the two-dimensional metallic state at the surface of $SrTiO_3$: Importance of oxygen vacancies*, Phys. Rev. B **86**, 195119 (2012).

[14] J. C. Li, J. I. Beltrán, and M. C. Mu noz, *Multiorbital structure of the two-dimensional electron gas in $LaAlO_3/SrTiO_3$ heterostructures: The formation of a d_{xy} ferromagnetic sheet*, Phys. Rev. B **87**, 075411 (2013).

[15] H. O. Jeschke, J. Shen, and R. Valenti, *Localized versus itinerant states created by multiple oxygen vacancies in $SrTiO_3$*, New J. Phys. **17**, 023034 (2015).

[16] Z. Zhong, A. Tóth, and K. Held, *Theory of spin-orbit coupling at $LaAlO_3/SrTiO_3$ interfaces and $SrTiO_3$ surfaces*, Phys. Rev. B **87**, 161102 (2013).

[17] Guru Khalsa, Byounghak Lee, and A. H. MacDonald, *Theory of t_{2g} electron-gas rashba interactions*, Phys. Rev. B **88**, 041302 (2013).

[18] C. Lin and A. A. Demkov, *Electron correlation in oxygen vacancy in $SrTiO_3$*, Phys. Rev. Lett. **111**, 217601 (2013).

[19] Y. Aiura, I. Hase, H. Bando, T. Yasue, T. Saitoh, and D. S. Dessau, *Photoemission study of the metallic state of*

lightly electron-doped $SrTiO_3$, Surf. Sci. **515**, 61 (2002).

[20] R. Courths, *Ultraviolet photoelectron spectroscopy (UPS) and LEED studies of $BaTiO_3$ (001) and $SrTiO_3$ (100) surfaces*, J. Phys. Stat. Sol. B **100**, 135 (1980).

[21] Y. S. Kim, J. Kim, S. J. Moon, W. S. Choi, Y. J. Chang, J.-G. Yoon, J. Yu, J.-S. Chung, and T. W. Noh, *Localized electronic states induced by defects and possible origin of ferroelectricity in strontium titanate thin films*, Appl. Phys. Lett. **94**, 202906 (2009).

[22] P. E. Blöchl, *Projector augmented-wave method*, Phys. Rev. B **50**, 17953 (1994).

[23] G. Kresse and J. Furthmüller, *Efficiency of ab-initio total energy calculations for metals and semiconductors using a plane-wave basis set*, Comp. Mater. Sci. **6**, 15 (1996).

[24] J. Hafner, *Ab-initio simulations of materials using VASP: Density-functional theory and beyond*, J. Comp. Chem. **29**, 2044 (2008).

[25] J. P. Perdew, K. Burke, and M. Ernzerhof, *Generalized gradient approximation made simple*, Phys. Rev. Lett. **77**, 3865 (1996).

[26] S. L. Dudarev, G. A. Botton, S. Y. Savrasov, C. J. Humphreys, and A. P. Sutton, *Electron-energy-loss spectra and the structural stability of nickel oxide: An LSDA+U study*, Phys. Rev. B **57**, 1505 (1998).

[27] K. Koepernik and H. Eschrig, *Full-potential nonorthogonal local-orbital minimum-basis band-structure scheme*, Phys. Rev. B **59**, 1743 (1999).

[28] A. I. Liechtenstein, V. I. Anisimov, and J. Zaanen, *Density-functional theory and strong interactions: Orbital ordering in Mott-Hubbard insulators*, Phys. Rev. B **52**, R5467 (1995).

[29] P. Blaha, K. Schwarz, G. K. H. Madsen, D. Kvasnicka, and J. Luitz, *WIEN2k, An Augmented Plane Wave and Local Orbitals Program for Calculating Crystal Properties* (Techn. Universität Wien, Austria, 2001).

[30] S. Okamoto, A. J. Millis, and N. A. Spaldin, *Lattice relaxation in oxide heterostructures: $LaAlO_3/SrTiO_3$ superlattices*, Phys. Rev. Lett. **97**, 056802 (2006).

[31] P. D. C. King, S. McKeown Walker, A. Tamai, A. de la Torre, T. Eknapakul, P. Buaphet, S.-K. Mo, W. Meevasana, M. S. Bahramy, and F. Baumberger, *Quasiparticle dynamics and spinorbital texture of the $SrTiO_3$ two-dimensional electron gas*, Nat. Commun. **5**, 3414 (2014).

[32] S. E. Barnes, J. Ieda, and S. Maekawa, *Rashba Spin-Orbit Anisotropy and the Electric Field Control of Magnetism*, Sci. Rep. **4**, 4105 (2014).

Atomic specialization at the surface of oxygen-deficient $SrTiO_3$

Michaela Altmeyer,[1] Oliver Hijano-Cubelos,[2] Harald O. Jeschke,[1] Cyril Martins,[2] Klaus Koepernik,[3] Andres Santander-Syro,[4] Marcelo J. Rozenberg,[2] Roser Valentí,[1] and Marc Gabay[2]

[1] *Institute of Theoretical Physics, Goethe University Frankfurt am Main, 60438 Frankfurt am Main, Germany*
[2] *Laboratoire de Physique des Solides, Bat 510, Université Paris-Sud, 91405 Orsay, France*
[3] *IFW Dresden Helmholtzstraße 20, 01069 Dresden, Germany*
[4] *CSNSM IN2P3/CNRS, Bats 104&108, Université Paris Sud, 91405 Orsay, France*

(Dated: November 18, 2015)

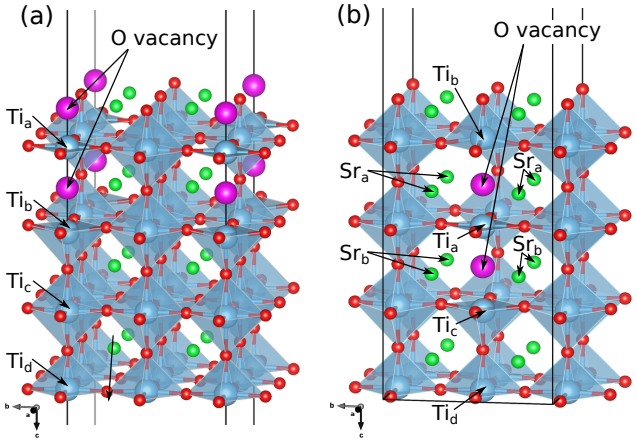

FIG. 1. SrO terminated $2 \times 2 \times 4$ slab with two apically positioned oxygen vacancies (a) at the surface and (b) buried in the slab.

For completeness, we present here the results on the electronic and magnetic properties for further slabs considered in our study (see Fig. 1); an SrO-terminated $2 \times 2 \times 4$ slab with a vertically placed surface divacancy and a SrO-terminated $2 \times 2 \times 4$ slab with a divacancy buried inside the slab.

I. SRO TERMINATED $2 \times 2 \times 4$ SLABS WITH OXYGEN DIVACANCIES

Our analysis of the single-vacancy SrO terminated $2 \times 2 \times 4$ slab in the main text has already shown the presence of an in-gap state at ~ -0.4 eV (see Fig. 2(b), main text) of d_{z^2} character that originates from the Ti atom closest to the vacancy. Here we explore the effects of an additional vacancy in the slab located on the opposite side of this Ti atom (Fig. 1 (a)), as we would expect this additional vacancy to shift the in-gap states to higher binding energies. Furthermore, we also analyze the case, where this apically ordered divacancy is embedded in the slab (Fig. 1 (b)).

Note: Considering two vacancies in a slab of this size corresponds to a carrier concentration far above realistic values. The observations in actual measurements can therefore be expected to be a lot less drastic than the results presented in the next sections. The cases presented in the main text (a mono-vacancy in a $2 \times 2 \times 4$ slab and a divacancy in a $3 \times 3 \times 4$ slab), however, are in the regime of vacancy densities measured in experimental observations; $2.9 \cdot 10^{14}$ cm^{-2} for $3 \times 3 \times 4$ compared to estimates by King, Baumberger (2015) of $2.7 \cdot 10^{14}$ cm^{-2}) and are therefore yielding a better description of the experimental situation.

In Fig. 2 we present the relativistic nonmagnetic GGA+SO and ferromagnetic GGA+SO+U spin texture calculations for the two slabs in Fig. 1. As also found in the slabs considered in the main text, the non-magnetic calculations (Fig. 2 (a) and (d)) show a characteristic Rashba spin texture with splittings of only a few meV.

In the magnetic calculations in a ferromagnetic $m \parallel \hat{z}$ setup we find the same trends as observed in the slabs of the main text; i.e. an atomic specialization with in-gap states (Fig. 2 (c) and (f)) originating from Ti located in the immediate vicinity of the divacancy (Ti$_a$ in Fig. 1) and spin winding at the Fermi surface with a small in-plane component (Fig. 2 (b) and (e)).

Three comments are in order: (i) All in-gap states obtained for the SrO-terminated $2 \times 2 \times 4$ slabs are of d_{z^2} nature (Fig. 3 and 4). Please note that the in-gap states in the $3 \times 3 \times 4$ slab in the text correspond to a very special TiO_2 surface arrangement of the vacancies. (ii) We observe that the position of the e_g in-gap states is very sensitive to the position and nature of the divacancy, as already commented in the main text. While the in-gap states lie at -1 eV in the slab with surface divacancies, it lies at -0.6 eV in the slab with the divacancies buried inside the slab. (iii) Due to the small size of the slab, the magnetic moments induced by the introduction of charge through the two vacancies distributes to all Ti in the slab, so that, not only the Ti$_a$ e_g in-gap states acquire large magnetic moments but also the itinerant t_{2g} states and the spin splittings of the t_{2g} bands are considerable. This has as a consequence that the up and down spin textures are not visible at the Fermi level (Figs. 2 (b) and (e). As mentioned above, these $2 \times 2 \times 4$ divacancy slabs probably represent an unrealistically large amount of vacancy concentration. Nonetheless, the results are instructive, especially concerning the in-gap states and the fact that in-gap states at the experimentally observed -1.3 eV energies come from clustered vacancies near the surface.

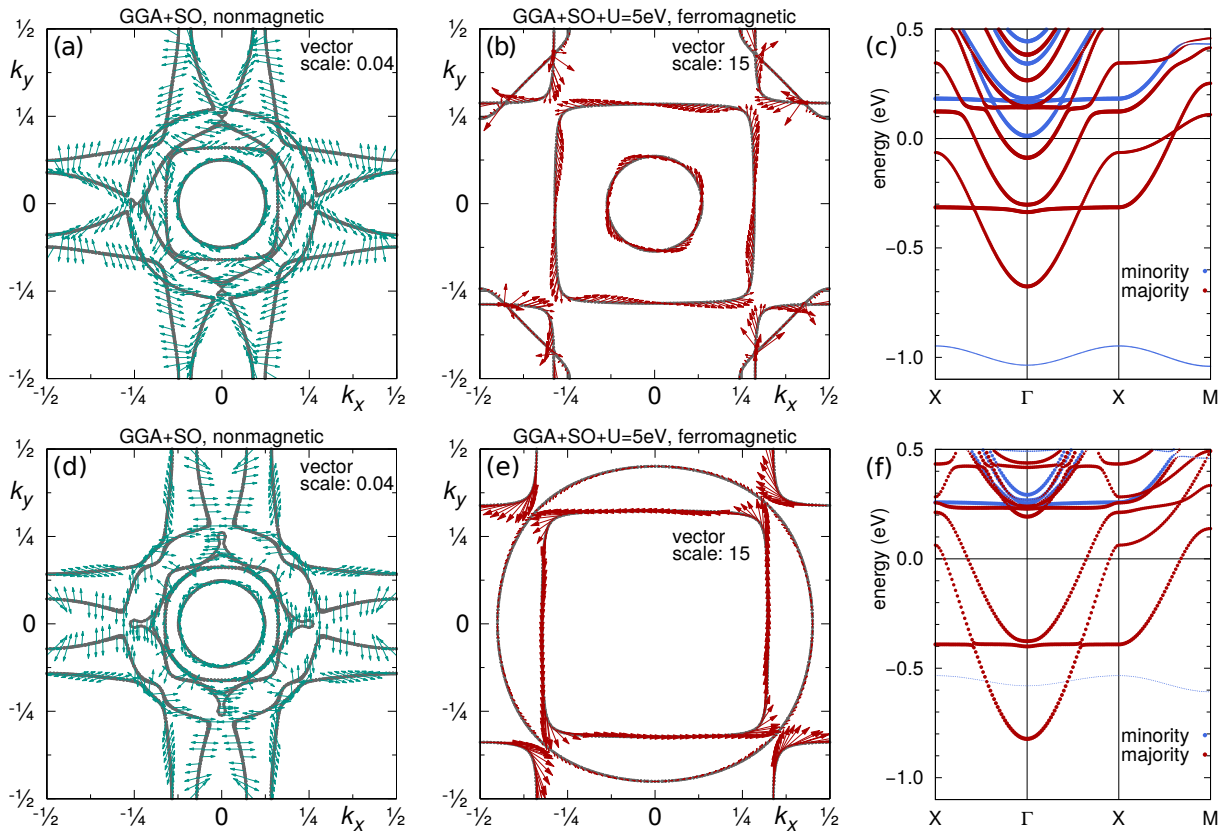

FIG. 2. Spin-textures and spin-polarized bandstructures for the relaxed $2 \times 2 \times 4$ slabs with a divacancy (a)-(c) at the surface of the slab and (d)-(f) buried inside the slab.

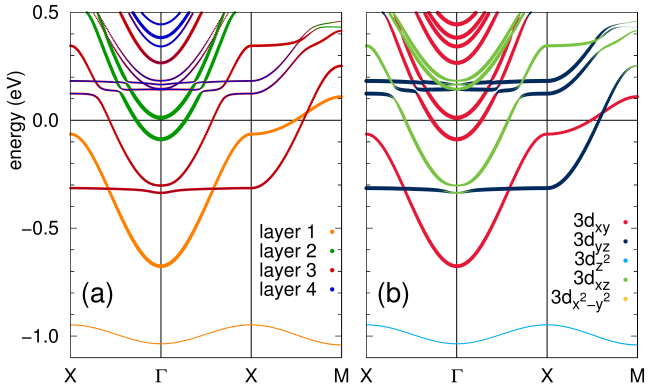

FIG. 3. Ferromagnetic GGA+SO+U Ti $3d$ bandstructure for the relaxed $2 \times 2 \times 4$ slab with two oxygen vacancies at the surface of the slab with a $m \parallel \hat{z}$ setup. (a) Layer resolved. (b) Orbital resolved.

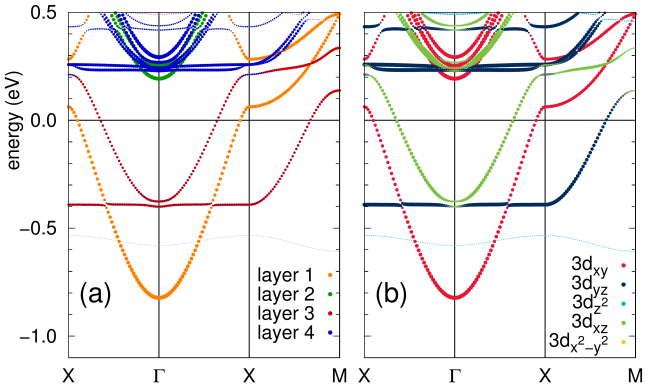

FIG. 4. Ferromagnetic GGA+SO+U Ti $3d$ bandstructure for the relaxed $2 \times 2 \times 4$ slab with two oxygen vacancies buried in the slab with a $m \parallel \hat{z}$ setup. (a) Layer resolved. (b) Orbital resolved.

II. CLUSTER CALCULATION

To gain further insight into the atomic and orbital specializations of the electronic states in the 2DES, we performed tight-binding calculations on $2 \times 2 \times 4$ clusters where we only retain Ti 3d and O 2p states. For the structure shown in Fig. 5 there are a priori 472 such states, including spin. The O layer at the bottom is removed when we construct slabs containing an integer number of $SrTiO_3$ unit cells.

The Hamiltonian reads

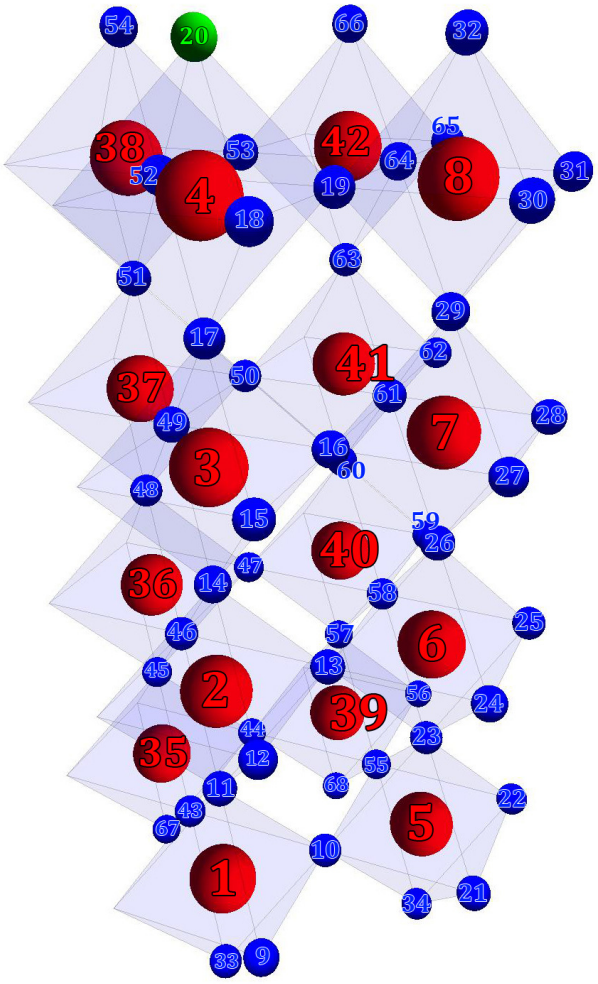

FIG. 5. Representation of the cluster of 68 sites considered in the tight-binding study. Ti (O) atoms are shown in red (blue). A vacancy is present (in green) in the topmost SrO layer at site 20

$$H = H_O + H_{int} + H_{SO}$$

where

$$H_o = \sum_{i(Ti)} \sum_{d} \sum_{\sigma=\uparrow,\downarrow} E_d a^{\dagger}_{i(Ti),d,\sigma} a_{i(Ti),d,\sigma} + \sum_{j(O)} \sum_{p} \sum_{\sigma=\uparrow,\downarrow} E_p b^{\dagger}_{j(O),p,\sigma} b_{j(O),p,\sigma} \quad (1)$$

H_o is a diagonal matrix that contains the information of the on-site energies of the different atomic orbitals. $a^{\dagger}_{i(Ti),d,\sigma}$ creates an electron in the Ti d orbital at position i(Ti), with spin σ and $b^{\dagger}_{j(O),p,\sigma}$ creates an electron in the O p orbital at position j(O) with spin σ.

Electronic site to site hops give rise to the kinetic contribution

$$H_{int} = \sum_{<i(Ti_1),j(Ti_2)>} \sum_{d_1,d_2} \sum_{\sigma=\uparrow,\downarrow} T_{d_1,d_2,i(Ti_1),j(Ti_2)} \times e^{i\vec{k}\vec{v}_{i(Ti_1)j(Ti_2)}} a^{\dagger}_{i(Ti_1),d_1,\sigma} a_{j(Ti_2),d_2,\sigma} + \sum_{<i(Ti),j(O)>} \sum_{d,p} \sum_{\sigma=\uparrow,\downarrow} T_{d,p,i(Ti),j(O)} \times e^{i\vec{k}\vec{v}_{i(Ti)j(O)}} a^{\dagger}_{i(Ti),d,\sigma} b_{j(O),p,\sigma} + \sum_{<i(O_1),j(O_2)>} \sum_{p_1,p_2} \sum_{\sigma=\uparrow,\downarrow} T_{p_1,p_2,i(O_1),j(O_2)} \times e^{i\vec{k}\vec{v}_{i(O_1)j(O_2)}} b^{\dagger}_{i(O_1),p_1,\sigma} b_{j(O_2),p_2,\sigma} + H.C.$$

The most general case involves hops between neighboring Titanium atoms (first term), between neighboring Titanium-Oxygen atoms (second term) and lastly between neighboring Oxygen atoms (third term). Since the d and p orbital lobes are directional hopping amplitudes depend on the relative positions and the orbitals of the two atoms involved in the path. Calculation of these amplitudes follow the Slater-Koster rules.

$$H_{SO} = \lambda \vec{L} \cdot \vec{S}$$

H_{SO} is the bulk spin-orbit coupling term. It lifts the spin degeneracy.

Values assigned to the various parameters are chosen such that in the absence of O vacancies the energy spectrum compares favorably with LDA calculations for slabs in the subspace of of d-p states.

Modeling the presence of a vacancy in the cluster is achieved by changing the on-site energy of the missing O,

and the hopping amplitudes between the vacancy and the neighboring atoms. Furthermore, the presence of the missing oxygen may cause shifts in the positions of neighboring Ti atoms which in turn impact their on-site and kinetic contributions: locally the octaedral symmetry is broken and this changes the crystal field energy of the Ti d orbitals; ab initio calculations suggest that the relative variation of the O-Ti-O bond angle for the shifted Ti is on the order of 3-4% and this affects the values of the local hopping amplitudes. In order to monitor the evolution of the states in the presence of the vacancy is present, we adiabatically "turn on" the defect in the cluster, i.e. we change incrementally the different energy terms pertaining to the perturbation. We multiply these by a parameter α which varies between 1 (no vacancy present) and zero (vacancy present). Fig. **??** (a) shows the variations in the band energies at the Γ point with α. Beyond the expected changes within the valence and conduction band groupings, one sees that several states emerge from the valence band manifold and give rise to (i) in-gap states (ii) new states in the t_{2g} conduction band group. In the case of a single vacancy on the topmost position of a SrO terminated cluster, the distance

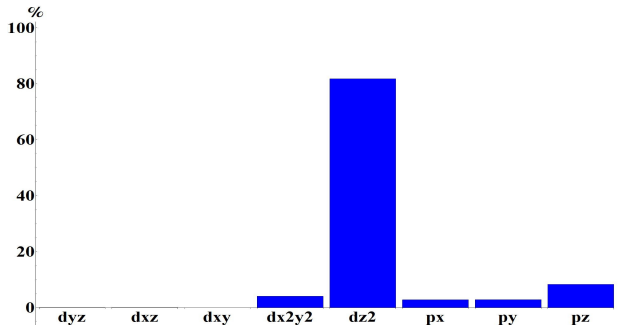

FIG. 6. Orbital weights of the in-gap state for the $2 \times 2 \times 4$ slab with one apical oxygen vacancy in the topmost SrO layer at site 20 (see Fig. 5).

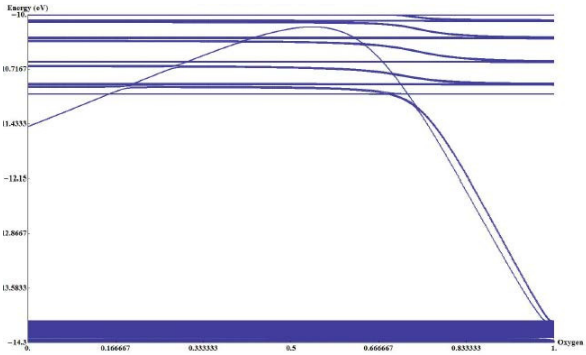

FIG. 7. Energy states at the Γ point for the $2 \times 2 \times 4$ slab with one apical oxygen vacancy in the topmost SrO layer at site 20 (see Fig. 5).

between the in-gap states and the conduction band bottom is ~ 0.42eV (Fig. 7) which compares favorable with the LDA results. For that same configuration, Fig. 6 (b) shows that the orbital character of this in-gap state is a mixture of d_{z^2} and p_z states coming from the hybridization of the Ti orbital just below the vacancy (atom 4 in Fig. 5) with the O orbital below that Ti (atom 17 in Fig. 5). Investigation of various configurations of di-vacancies, yields a similar picture, namely that in-gap states emerge from the valence band, that they mix e_g states of Ti atoms sandwiched by the di-vacancy or sitting on either side of it with p orbitals of neighboring O atoms. For a di-vacancy in the topmost SrO layer, an in-gap state with energy ~ -1.3eV is found.